MORPHOMETRIC ANALYSIS OF THE RAT LOWER LIMB NERVES

ANATOMICAL DATA FOR NEURAL PROSTHESIS DESIGN

MORPHOMETRIC ANALYSIS OF THE RAT LOWER LIMB NERVES

ANATOMICAL DATA FOR NEURAL PROSTHESIS DESIGN

PROEFSCHRIFT

ter verkrijging van

de graad van doctor aan de Universiteit Twente,

op gezag van de rector magnificus,

prof. dr. W.H.M. Zijm,

volgens besluit van het College voor Promoties

in het openbaar te verdedigen

op donderdag 26 januari 2006 om 16.45 uur

door

Dimiter Petkov Prodanov

geboren op 16 maart 1975

te Sofia, Bulgarije

Dit proefschrift is goedgekeurd door de promotors en assistent promotor

prof. dr. E. Marani (promotor)

prof. dr. P. Veltink (promotor)

dr. H.K.P. Feirabend (assistent promotor)

For the less even as for the greater there is some deed that he may accomplish but once only; and in that deed his heart shall rest.

J.R.R. Tolkien, The Silmarillion, ch. 9

To my parents

and to my friends Luc, Dani, and Ivo

TABLE OF CONTENTS

LIST OF FIGURES

LIST OF TABLES

CHAPTER 1

General Introduction

1.1 Neural prostheses

NEural prostheses[1] (i.e. neuroprostheses) can be defined as a class of medical devices that replace lost or improve impaired motor or sensory functions by electrical stimulation of the *Peripheral Nervous System* (PNS). The underlying approach for stimulation is commonly referred to as *Functional Electrical Stimulation* (FES), the term itself introduced by Moe and Post (1962). Current clinical applications and future perspectives of neuroprostheses and the state of art of the FES are discussed in Chapter 2. Implantable neural prostheses can turn out to be the most efficient treatment of medical conditions, such as blindness, diaphragm arrest, and spinal cord injury (SCI) (Heiduschka and Thanos, 1998). In SCI, less than 1% of the patients are discharged from hospital with complete neurological recovery while the majority discharge with tetraplegia or paraplegia (Fig. 1.1). With an annual incidence of persons surviving SCI of approximately 27.4 cases per million of population (Schonherr et al., 1996) in the Netherlands or 40 cases per million in the USA (NSCISC, 2005) such distribution of clinical outcomes imposes a growing social and economic burden on society. Neuroprostheses can enable mobility in individuals with low cervical or thoracic SCI and restore abilities such as standing, performing transfers, and walking, which were previously unobtainable with injuries at these levels (Chapter 2).

In SCI patients, the spinal reflex arches are intact distally from the site of injury (Fig. 1.2), but the interaction of the cortical control circuitry (primary motoneuron) with the secondary motoneuron in the spinal cord is lost. Therefore, the central issue in the application of loco-motion neural prostheses is the substitution of the primary motoneuron function by electrical stimulation using proper electrodes interfacing PNS. Current advances in the neuroprosthetic field are aimed at development of implantable electrodes for stimulation and recording (Agnew and McCreery, 1990; Heiduschka and Thanos, 1998; Popovič et al., 2001; Prodanov et al., 2003).

---

[1]Definition derived from Owens (2005).
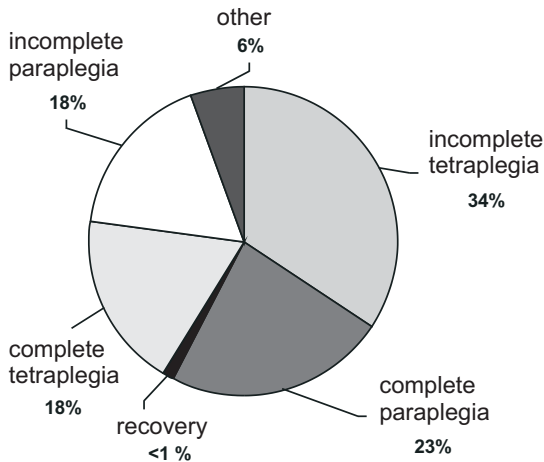
Figure 1.1: Medical condition at discharge from hospital after SCI
Data are obtained from the National Spinal Cord Injury Statistical Center, USA (NSCISC, 2005)

1.2 Structure of the nerves and their stimulation using implantable electrodes

SEveral anatomical factors contribute to the excitability of the peripheral nerves and, thus, to the overall efficiency of stimulation using implantable electrodes. These are: (i) spatial distribution of the targeted population of fibers (i.e. functional topography) with respect to the stimulating electrode; (ii) the diameter of the myelinated fiber being stimulated and its relation to the internal diameter of axon (i.e. g-ratio); (iii) the distribution of the nodes of Ranvier along the nerve fibers (i.e. the internodal distance distribution).

There are two interrelated requirements for the obtained functionality of stimulation using a neural prosthesis. *First*, stimulation should be topically selective in view of the target effect. Functional topography of axons is important for the topical selectivity of stimulation. In the case of a motor prosthesis, topical selectivity translates into *muscle-selectivity*. While for sensory neuroprostheses, such as the cochlear implant, topical selectivity translates into positional selectivity of stimulation inside the cochlea. *Second*, stimulation should be specific for the physiological type of the nerve fibers being excited. Since functionally different fibers often have very different sizes (Boyd and Davey, 1968), the second aspect translates into *size-selectivity* of stimulation. For the majority of myelinated nerve fibers, the internodal distance correlates with the external nerve fiber diameter (Rushton, 1951). Therefore, it is an important parameter for determining the recruitment order during stimulation (Veltink, 1988)[2] and the obtained size-selectivity (Rutten, 2002), respectively.

Both aspects of selectivity depend on the type of electrode that is used. Many different electrodes have been developed to explore selectivity experimentally, such as: cuff electrodes (Agnew and McCreery, 1990), intraneural wire electrodes (Veltink et al., 1989; Malagodi et al., 1989; Yoshida and Horch, 1993), or intraneural microelectrode arrays (Rutten et al., 1991; 1995; Branner and Normann, 2000; McDonnall et al., 2004). Experiments using intraneural stimulation electrodes outlined both the influence of the functional motor fiber topography on the efficiency of the electrical stimulation and the limitations of the intrafascicular electrodes im-

---

[2]PhD thesis from the Biomedical Signals and Systems group, Twente University
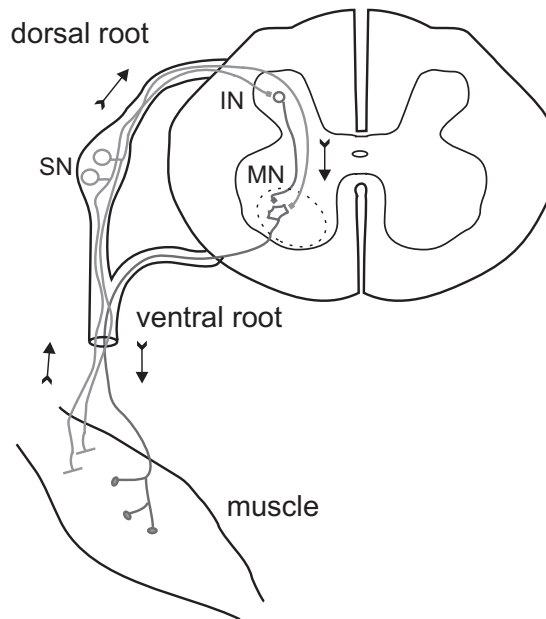
Figure 1.2: The spinal reflex arch

The spinal reflex arch consists of efferent and afferent parts. The **efferent part** comprises: the spinal cord *motor neuron* (MN) that extends its axon throughout a spinal *ventral root*, (usually via a nerve plexus) and a distal nerve; a *striated muscle*, where the *axon* of the spinal cord motoneuron forms extensive arborization and ends up in a number of *motor endplates*. The **afferent part** comprises: a *(stretch) receptor* (Golgi tendon organ or muscle spindle); a *peripheral axonal processus* of the dorsal ganglion sensory neuron (SN) that extends from the *sensory neuron soma* in the dorsal root ganglion; a *central axonal processus* of the dorsal ganglion neuron that forms a synapse in the dorsal horn of the spinal cord and, in multisynaptic reflexes, *intermediate neuron(s)* (IN) that connects synaptically with the motor neuron. A dashed line outlines the motor nucleus in the spinal cord gray matter; arrows show the flow of information.

L4
L5
S1
S2
S3

N. Ischiadicus

1 - n. ischiadicus
2 - n. peroneus prof.
3 - n. peroneus superf
4 - n. tibialis.
5 - n. suralis
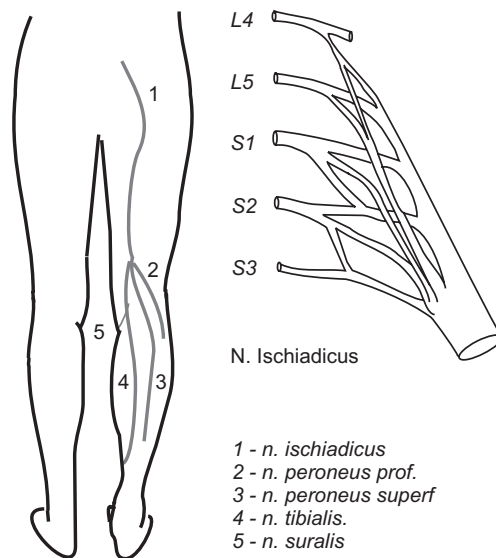
Figure 1.3: Anatomy of the sciatic nerve in man. Modified from Gray (1918) and Marani et al. (1993).

posed by the random distribution of the nodes of Ranvier (Smit, 1996)[3]. With the development of better means to control the excited area inside a nerve cross-section using cuff electrodes (Deurloo, 1999)[4] the functional topography of motor fibers inside the ventral roots rose as the next point that needs to be addressed for further development of implantable neural prostheses.

1.3 Comparative anatomy of the sciatic nerve in man and in rat

Lumbar spinal cord and the sciatic nerve have a common plan of organization in mammals, such as man, simian primates, cat, and rat. In man, the sciatic nerve originates from L4 - S3 spinal levels (Gray, 1918) (Fig. 1.3). In some primates (Janjua and Leong, 1984; 1987) and the cat (Romanes, 1964), the sciatic nerve originates from L4 - L7 segments with some involvement of S1. In the rat, the sciatic nerve originates from the spinal nerve L4 - L6 (Fig. 1.4) (Brunner et al., 1980; Swett et al., 1986). In all of the mentioned mammals, its major branches are the tibial, the common peroneal, and the sural nerves.

The columnar organization of the motoneurons in the spinal cord is also common across different mammals (Rexed, 1952; Nieuwenhuys, 1964). In mammals, musculotopic organization of the peripheral nervous system has been proposed for the first time by Romanes (1964) for the motor neuronal columns in the spinal cord. Motor neurons form distinct motor nuclei, which are organized in a medio-lateral manner and project topographically onto the flexor and extensor muscle groups in the leg. Motor nuclei for different muscles are comparable across mammals,

---

[3]PhD thesis from the same group
[4]PhD thesis from the same group

1 - n. pudendus
2,2' - nn. glutei cran.et caud.
3 - n. ischiadicus
4 - n. cut. surae med.
5 - n. gastrocnemius lat
6 - n. tibialis
7 - n. peroneus prof.
    sv. fibularis prof.
8 - n. peroneus superf.
    sv. fibularis superf.
9 - n. gastrocnemius med.
10 - n. peroneus comm.
    sv. fibularis. comm.
11 - n. suralis
    sv. n. cut. surae lat.
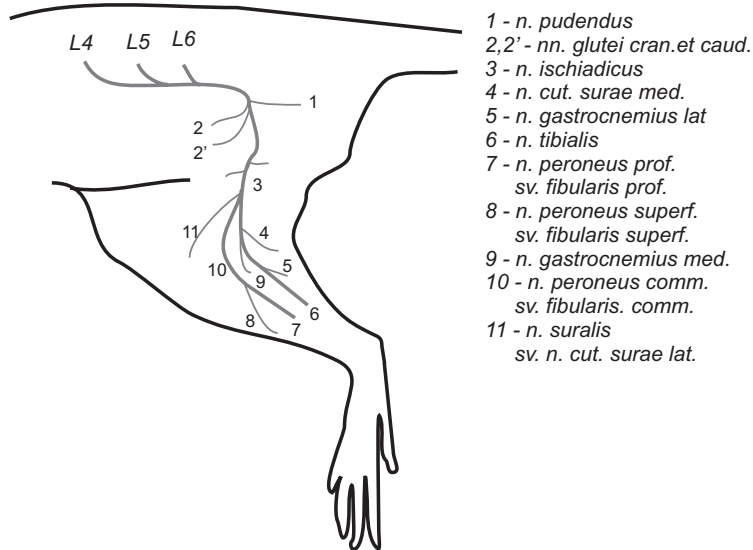
Figure 1.4: Anatomy of the sciatic nerve in rat

Modified from Hebel and Stromberg (1986). To facilitate comparisons with the human, the terms "peroneal nerve" and "sural nerve" are used throughout the thesis.

although with some shifts in their spinal levels (see for example Romanes (1964); Janjua and Leong (1987); Yeong et al. (1998)). Due to these outlined principal similarities of the rat spinal cord to the human spinal cord and the good availability of the rat as an experimental animal in the Netherlands (Beynen et al., 2001), its PNS can be considered a suitable model to study the structure and the function of human PNS. The rat sciatic nerve and its tributary branches (Fig. 1.4) are frequently used as model systems for studying the mechanisms of the regeneration of nerve fibers (Navarro and Kennedy, 1991; Vleggeert-Lankamp et al., 2004; Negredo et al., 2004), developmental and induced cell death (Greensmith et al., 1996; Prodanov et al., 1998; Puigdellivol-Sanchez et al., 2002; Iwasaki et al., 2004), and for establishing the performance and biocompatibility of implanted neuroprostheses (recent overviews in Heiduschka and Thanos (1998) and Prodanov et al. (2003), i.e. Chapter 2).

1.4 Aims of the thesis

This thesis aims to establish the topography of the motor fibers in the spinal roots of the rat according to their muscle destination in view of the topical selectivity of stimulation. As a *second aim*, the thesis intends to provide quantitative data on the structural organization of the nerve fibers in the sciatic nerve, its tributary branches, and its founding spinal roots for the purposes of their size-selective electrical stimulation. Therefore, with regard to the stated aims, two particular research questions arise:

1. Which are the suitable places for stimulation throughout the course of the sciatic nerve, its tributary branches, and its founding spinal roots from an anatomical point of view?

2. Are the motor fibers innervating a given muscle spatially organized in the nerve or the spinal root? In particular, are they clustered in a certain compartment of a ventral root or a peripheral nerve, respectively; or are they dispersed?

1.5   Outline of the thesis

Chapter 2 Functional Electric Stimulation for sensory and motor functions: Progress and problems[5]

This chapter gives an overview on the neuroprosthetic field (e.g. Functional Electrical Stimulation). A brief historical overview is presented in the light of its relevance for the development of the major clinical applications of the implantable neuroprostheses, such as pacing of the heart and diaphragm, the restoration of locomotion and grasping, and the restoration of bladder and bowel functions. Critical analysis is performed on the neuroprosthetic restoration of lost locomotor functions. The structural and functional information needed for further development of the neuroprostheses for locomotion and for urological functions is identified based on the analysis of their contemporary clinical applications.

Chapter 3 Three-dimensional topography of the motor endplates of the rat gastrocnemius muscle[6]

This chapter presents a three-dimensional (3D) map of the motor endplates in the medial and the lateral gastrocnemius muscles of the rat assembled from thick histological sections. Recommendations are given for optimal placement of tracer injections in these muscles based on the presented 3D maps. Gastrocnemius muscles are used further in the retrograde tracing experiments described in Chapters 6 and 7 to label the sciatic nerve and its founding ventral roots. In addition, the use of the presented 3D maps for the realistic simulation of surface EMG recordings is discussed.

Chapter 4 Morphometric analysis of the fiber populations of the rat sciatic nerve, its spinal roots, and its major branches[7]

This chapter provides reference values for the fiber density, interspace, and cross-sectional area. The sciatic nerve, its founding dorsal and ventral spinal roots, and its major branches, the *tibial*, *peroneal*, and *sural* nerves, were measured (semi-) automatically on semi-thin histological sections. Fiber diameter distributions are modeled statistically using multi-component lognormal models and an optimal model for each nerve or root is selected using information theory criteria. The functional identities of so modeled fiber populations are established using calculations of conduction velocities and anatomical considerations for each studied nerve or root. Findings are discussed in view of their importance for development of neural prostheses.

---

[5]Published as D. Prodanov, E. Marani, and J. Holsheimer, Biomedical Reviews (2003) 14, 23-50
[6]Published as D. Prodanov, M.-A. Thil, J. Delbeke, E. Marani, and J. Holsheimer, Muscle & Nerve (2005), 32(3), 292-302
[7]In preparation for publication in the Journal of Comparative Neurology

Chapter 5 Automatic morphometry of synaptic boutons of cultured cells using granulometric analysis of digital images[8]

This chapter presents a novel technique for automatic identification and morphometry of fluorescently labeled neuronal structures based on non-linear filtering of digital images. The algorithm is tested in a task for automatic identification of synaptic boutons in microscopic images of cultured cells and further compared to the performance of human observers. Its further use for morphometric analysis of nerve fibers is discussed. A brief overview of the *mathematical morphology*, the underlying theory used for the algorithm development, is given in an appendix.

Chapter 6 Automated morphometric analysis of the nerve fiber population innervating the rat gastrocnemius muscles[9]

In this part, the method presented in Chapter 5 is elaborated further to encompass automatic identification of tracer in axonal profiles in histological cross sections. Using paired sets of measurements of the tracer signal within the axonal profile and of the corresponding fiber diameter (i.e. axonal profile and its myelin sheath) in sections of ventral roots and peripheral nerves, a relationship between the fiber diameter and the signal diameter is established. Using this relationship the total fiber population is reconstructed from the axonal fluorescence measurements and the functional type of the predominantly labeled fibers is identified.

Chapter 7 Local spatial analysis of the motor axonal clustering in rat ventral spinal roots[10]

This chapter presents the functional topography of the motor axons in the L6 ventral spinal root revealed from the performed tracing experiments using rat gastrocnemius muscles. Maps of the locations of the tracer-positive fibers in the ventral root L6 were automatically constructed using the method developed in Chapter 6. A new spatial statistical function is introduced to test for the occurrence of clusters locally and its behavior is tested on simulated data by means of serial Monte-Carlo simulations. The function is further applied to the spatial data from the retrograde tracing experiments and used to reveal the locations of the clusters of labeled fibers. A brief overview on the theory and methodology of spatial statistics is given in an appendix.

Finally, the thesis is concluded with a general discussion of the findings in view of future neuroprosthetic applications (**Chapter 8**).

Bibliography

Agnew, W. F. and D. B. McCreery (1990) Neural Prostheses: Fundamental Studies. Prentice Hall Advanced Reference Series. Englewood Cliffs: Prentice Hall.

Beynen, A. C., V. Baumans, and L. F. M. V. Zutphen (2001) Principles of Laboratory Animal Science: A contribution to the humane use and care of animals and to the quality of experimental results. Amsterdam: Elsevier, 2nd edn.

Boyd, I. A. and M. R. Davey (1968) Composition of Peripheral Nerves. Edinburgh: Livingstone.

---

[8]D. Prodanov, J. Heeroma, and E. Marani, Journal of Neuroscience Methods (2005), in press
[9]Submitted to BMC Neuroscience
[10]Submitted to the Journal of Neuroscience Methods

Branner, A. and R. A. Normann (2000) A multielectrode array for intrafascicular recording and stimulation in sciatic nerve of cats. Brain Res. Bull. *51*:293–306.

Brunner, R., P. Zimmermann, and F. W. Klussmann (1980) Localization and neurophysiological properties of motoneurones of the m. triceps surae of the rat after retrograde labelling with Evans Blue. Cell Tissue Res. *212*:73–81.

Deurloo, K. (1999) Selectivity in extraneural stimulation of peripheral nerves. Ph.D. thesis, Twente University.

Gray, H. (1918) Anatomy of the Human Body. Philadelphia; http://www.bartleby.com/107: Lea & Febiger, 20th edn.

Greensmith, L., J. Dick, A. O. Emanuel, and G. Vrbová (1996) Induction of transmitter release at the neuromuscular junction prevents motoneuron death after axotomy in neonatal rats. Neuroscience *71*:213–220.

Hebel, R. and M. W. Stromberg (1986) Anatomy and Embryology of the Laboratory Rat. Worthsee: BioMed. Verlag.

Heiduschka, P. and S. Thanos (1998) Implantable bioelectric interfaces for lost nerve functions. Prog. Neurobiol. *55*:433–461.

Iwasaki, Y., Y. Ichikawa, O. Igarashi, S. Konno, J. Aoyagi, K. Ikeda, S. Marabuchi, S. Ono, H. Iguchi, K. Kawabe, and T. Fujioka (2004) T-588 protects motor neuron death following axotomy. Neurochem. Res. *29*:403–406.

Janjua, M. Z. and S. K. Leong (1984) Organization of neurons forming the femoral, sciatic, common peroneal, and tibial nerves in rats and monkeys. Brain Res. *310*:311–323.

Janjua, M. Z. and S. K. Leong (1987) Sensory, motor, and sympathetic neurons forming the common peroneal and tibial nerves in the macaque monkey (macaca fascicularis). J. Anat. *153*:63–76.

Malagodi, M. S., K. W. Horch, and A. A. Schoenberg (1989) An intrafascicular electrode for recording of action potentials in peripheral nerves. Ann. Biomed. Eng. *17*:397–410.

Marani, E., M. E. Pijl, M. C. Kraan, G. A. Nijeholt, and A. C. Videleer (1993) Interconnections of the upper ventral rami of the human sacral plexus: a reappraisal for dorsal rhizotomy in neurostimulation operations. Neurourol. Urodyn. *12*:585–598.

McDonnall, D., G. A. Clark, and R. A. Normann (2004) Selective motor unit recruitment via intrafascicular multielectrode stimulation. Can. J. Physiol. Pharmacol. *82*:599–609.

Moe, J. H. and H. W. Post (1962) Functional Electrical Stimulation for ambulation in hemiplegia. J. Lancet *82*:285–288.

Navarro, X. and W. R. Kennedy (1991) The effects of autologous nerve transplants on motor and sudomotor reinnervation by regenerative axons. Brain Res. *565*:181–187.

Negredo, P., J. Castro, N. Lago, X. Navarro, and C. Avendano (2004) Differential growth of axons from sensory and motor neurons through a regenerative electrode: a stereological, retrograde tracer, and functional study in the rat. Neuroscience *128*:605–615.

Nieuwenhuys, R. (1964) Comparative anatomy of the spinal cord. In J. C. Eccles and J. P. Schadé (eds.), *Organization of the spinal cord*, Amsterdam: Elsevier, chap. 1, pp. 1–57.

NSCISC (2005) Spinal cord injury. Facts and figures at a glance. Tech. rep., U.S. National Spinal Cord Injury Statistical Center.

Owens, T. A. (2005) Prosthesis (definition). In *Medical Encyclopedia*, http://www.nlm.nih.gov/medlineplus/ency/article/002286.htm: U.S. National Library of Medicine.

Popovič, M. R., A. Curt, T. Keller, and V. Dietz (2001) Functional Electrical Stimulation for grasping and walking: Indications and limitations. Spinal Cord. *39*:403–412.

Prodanov, D., G. Mantchev, A. Iliev, V. Traykov, K. Yakimova, R. Kaneva, and I. Krushkov (1998) Effects of Dexamethasone in rat neonatal model of axotomy-induced motoneuronal cell death. Arch. Physiol. Biochem. *106*:355–361.

Prodanov, D., E. Marani, and J. Holsheimer (2003) Functional Electric Stimulation for sensory and motor functions: Progress and problems. Biomed. Rev. *14*:23–50.

Puigdellivol-Sanchez, A., A. Valero-Cabre, A. Prats-Galino, X. Navarro, and C. Molander (2002) On the use of Fast Blue, Fluoro-Gold and Diamidino Yellow for retrograde tracing after peripheral nerve injury: Uptake, fading, dye interactions, and toxicity. J. Neurosci. Methods *115*:115–127.

Rexed, B. (1952) The cytoarchitectonic organization of the spinal cord in the cat. J. Comp. Neurol. *96*:414–495.

Romanes, G. J. (1964) The motor pools of the spinal cord. In *Organization of the spinal cord*, Amsterdam: Elsevier, chap. 11, pp. 93–119.

Rushton, W. A. (1951) A theory of the effects of fibre size in medullated nerve. J. Physiol. (Lond) *115*:101–122.

Rutten, W. L. (2002) Selective electrical interfaces with the nervous system. Annu. Rev. Biomed. Eng. *4*:407–452.

Rutten, W. L., T. A. Frieswijk, J. P. Smit, T. H. Rozijn, and J. H. Meier (1995) 3D neuro-electronic interface devices for neuromuscular control: Design studies and realisation steps. Biosens. Bioelectron. *10*:141–153.

Rutten, W. L., H. J. van Wier, and J. H. Put (1991) Sensitivity and selectivity of intraneural stimulation using a silicon electrode array. IEEE Trans. Biomed. Eng. *38*:192–198.

Schonherr, M. C., J. W. Groothoff, G. A. Mulder, and W. H. Eisma (1996) Rehabilitation of patients with spinal cord lesions in The Netherlands: an epidemiological study. Spinal Cord. *34*:679–683.

Smit, J. P. A. (1996) Selective Motor Stimulation using Endoneural Prostheses. Ph.D. thesis, Twente University.

Swett, J. E., R. P. Wikholm, R. H. Blanks, A. L. Swett, and L. C. Conley (1986) Motoneurons of the rat sciatic nerve. Exp. Neurol. *93*:227–252.

Veltink, P. H. (1988) Recruitment of myelinated nerve fibers during artificial electrical nerve stimulation. Ph.D. thesis, Twente University.

Veltink, P. H., J. A. van Alste, and H. B. Boom (1989) Multielectrode intrafascicular and extraneural stimulation. Med. Biol. Eng. Comput. *27*:19–24.

Vleggeert-Lankamp, C. L., R. J. van den Berg, H. K. Feirabend, E. A. Lakke, M. J. Malessy, and R. T. Thomeer (2004) Electrophysiology and morphometry of the $A\alpha$- and $A\beta$-fiber populations in the normal and regenerating rat sciatic nerve. Exp. Neurol *187*:337–349.

Yeong, S. O., K. Subramaniam, and G. Vrbova (1998) Organization of common peroneal nerve motoneurones in the rat and monkey: a comparative study. Neuroreport *9*:1085–1088.

Yoshida, K. and K. Horch (1993) Selective stimulation of peripheral nerve fibers using dual intrafascicular electrodes. IEEE Trans. Biomed. Eng. *40*:492–494.

CHAPTER 2

Functional Electric Stimulation for sensory and motor functions: Progress and problems [†]

Abstract

Functional Electrical Stimulation (FES) endeavours to restore the lost functions of the nervous system by means of electrical stimulation. It is a multidisciplinary field on the interface between the neuroscience, engineering, rehabilitation, and the clinic. In this review, the principal notions behind FES are outlined together with the relevant moments of its history. The specific research problems encountered in the development of FES applications are extensively covered. From an engineering perspective a special attention is given to the electrodes for selective stimulation. The major clinical applications of FES are overviewed: pacing of the heart, respiratory pacing of the diaphragm, cochlear neuroprostheses for restoration of hearing, the rehabilitation and restoration of locomotion and hand functions, and the restoration of bladder and bowel functions. An analysis of the current FES applications is performed from the perspective of the evidence-based clinical approach. Currently, FES for restoration of the lost locomotor functions is a rapidly developing area that is on the verge of broadening its acceptance in the clinic. Evidence for this is the increasing number of various neuroprosthetic devices, some of them already beyond the prototype stage, that have been developed recently. The present FES treatments combined with conventional occupational and physical therapy remain the most promising approach in rehabilitation of the spinal cord injury and the stroke patients. FES in combination with neuromodulation, which is however still in a rather empirical state of operation, becomes a viable option in the treatment of various urological disorders. The analysis indicates that pacing of the heart and cochlear neuroprostheses remain the most developed applications of FES. The presented overview of the FES applications shows that a number of fundamental scientific problems have to be solved before a comparable degree of effectiveness and penetration in common medical practice is achieved for the locomotion neuroprostheses and urological FES appliances. Finally, a summary is given of the major clinical and fundamental directions of research needed for further improvement of FES.

2.1 History of electrical stimulation

Functional Electrical Stimulation (FES)[1] is a part of the broader field of electrotherapy. The term was introduced relatively late in the history of FES by Moe and Post (1962). The history of electrical stimulation follows the theoretical and technological breakthroughs in the study of electricity and magnetism together with the developments in Neuroanatomy and Neurophysiology, since the stimulation is mainly an application of electro-magnetic theory in the nervous system. Nevertheless, the history of electrical stimulation has its own milestones of which the major ones, related to the nervous system, are given in this review. In the field of Neuroanatomy, the application of ethanol to fix brain tissue by Felix Vicq d'Azyr (1748 - 1794) opened the microscopic approach for the study of the brain, ending up with the detection of the sub-cellular protrusions of the neuron and its supporting cells. One should notice that the detection of the micro-architecture of peripheral nerves (Van Leeuwenhoek, 1719) was remarkably accurate but forgotten for nearly a century. The descriptions of Dutrochet (1824) and Remak (1838) once again depicted the tubular structure of the entities in the nerve, together with the detection of myelinated and non-myelinated fibers. Albrecht Haller (1708 - 1777) described the "*irritation phenomenon of muscles*", in fact, the contraction and relaxation of a muscle. In his notion, it was a "force" that passed along the nerves and that could induce excitation of muscles. In addition, Haller introduced the first concept on sensibility. He found that tissues by themselves lack sensations, but the latter were perceived and relayed by the nerves and their endings. After extensive studies of the muscle contractions in cadavers, Luigi Galvani (1737 - 1798) developed the theory of the "*animal electricity*"- an electric fluid contained in the nerves, which caused contractions of muscles. Later on in 1792, Allesandro Volta (1745 - 1827), who developed the so-called "*galvanic*" element, could demonstrate that the galvanic element used electricity (Fig. 2.1). These theories interfaced Neuroanatomy and Neurophysiology with the study of electricity, so that the nerves could be regarded as the electric cabling of the body. In the mean time, friction electricity was in use and the first capacitor, "*de Leidse fles*" (1746), was developed by Muschenbroeck. From 1784 to 1791, the biggest friction-electrical machine was build by John Cuthbertson (Fig. 2.2). Martinus van Marum (1750 - 1837), biologist, physician, and botanist used this machine to do electrophysiological research for ten years. This shows that around the beginning of the XIXth century systematic application of electricity in research and medicine had already started.

By the middle of the XIXth century, with the discovery of static electricity, capacitance, and electromagnetic inductance, physiologists could study muscle contractions, nerve conduction, and cell excitation. During the same period, Johannes Müller (1801 - 1858) introduced the law of Specific Nerve Energies, which stated: "*the kind of sensation, following the stimulation of a sensory nerve, depends not on the mode of stimulation but on the nature of the sense organ with which the nerve is linked*". His disciple Hermann von Helmholtz (1821 - 1894) measured the velocity of the nervous impulse and Emil DuBois-Reymond (1818 - 1896), another disciple of Müller, proved the existence of the resting membrane potential in the nerve fibers and also demonstrated that each impulse is directly related to a change in potentials. Sir Charles Bell (1774 - 1842) and François Magendie (1783 - 1855) established the neuronal basis for the reflex that the dorsal roots relay afferent, sensory information, while the ventral roots control the motor function. Finally, the idea that the central nervous system is the controller of the

---

[1]In the American literature, FES is referred to as Functional Neuromuscular Stimulation, FNS. However, the approach is limited only to the restoration of motor functions.
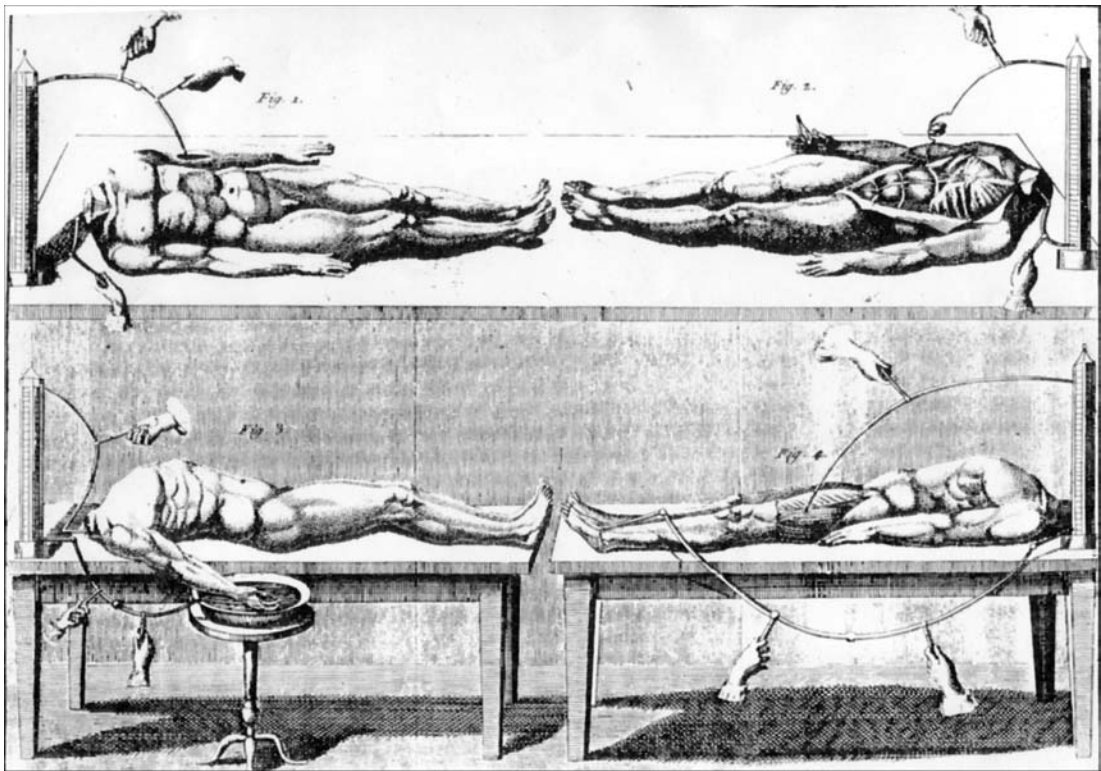
Figure 2.1: The experiments of L. Galvani

The experiments of Luigi Galvani on human muscles: muscles of a cadaver contracted when a metal object closed the loop with a nerve. From G. Aldini, *Essai théorique en experimental sur le Galvanisme, avec série d'experiences* ... Paris, Fournier fils, 1804. Courtesy: Prof. H. Beukers, Leiden University

organism was brought forward by Thomas H. Huxley (1825 - 1895) in his Manual of the Anatomy of the Invertebrate Animals (1817) and became generally accepted. This concept became the fundament for the effective application of electrical stimulation. Throughought this period, medical applications were numerous but short lived and poorly understood. Electricity was reported to cure rheumatism, neuralgia, insomnia, and even cold feet, as reviewed by Rattay (1990).

In XXth century, the major technological advances in electronics and computing (the discoveries of diode, triode, transistor, and integrated circuits) lead to the development of contemporary FES appliances. The main push in the applications of FES was the successful development and clinical applications of the heart pacemakers. Literature shows controversy about who was the first inventor of the artificial heart pacemaker (Gold, 1984). In 1932, Dr. Albert Hyman described an "*artificial pacemaker*" he had used with experimental animals to resuscitate the arrested heart. About that time, the Australian physician Mark C. Lidwill, along with the physicist Major Edgar Booth, built a portable pacemaking unit. It was demonstrated in 1931,
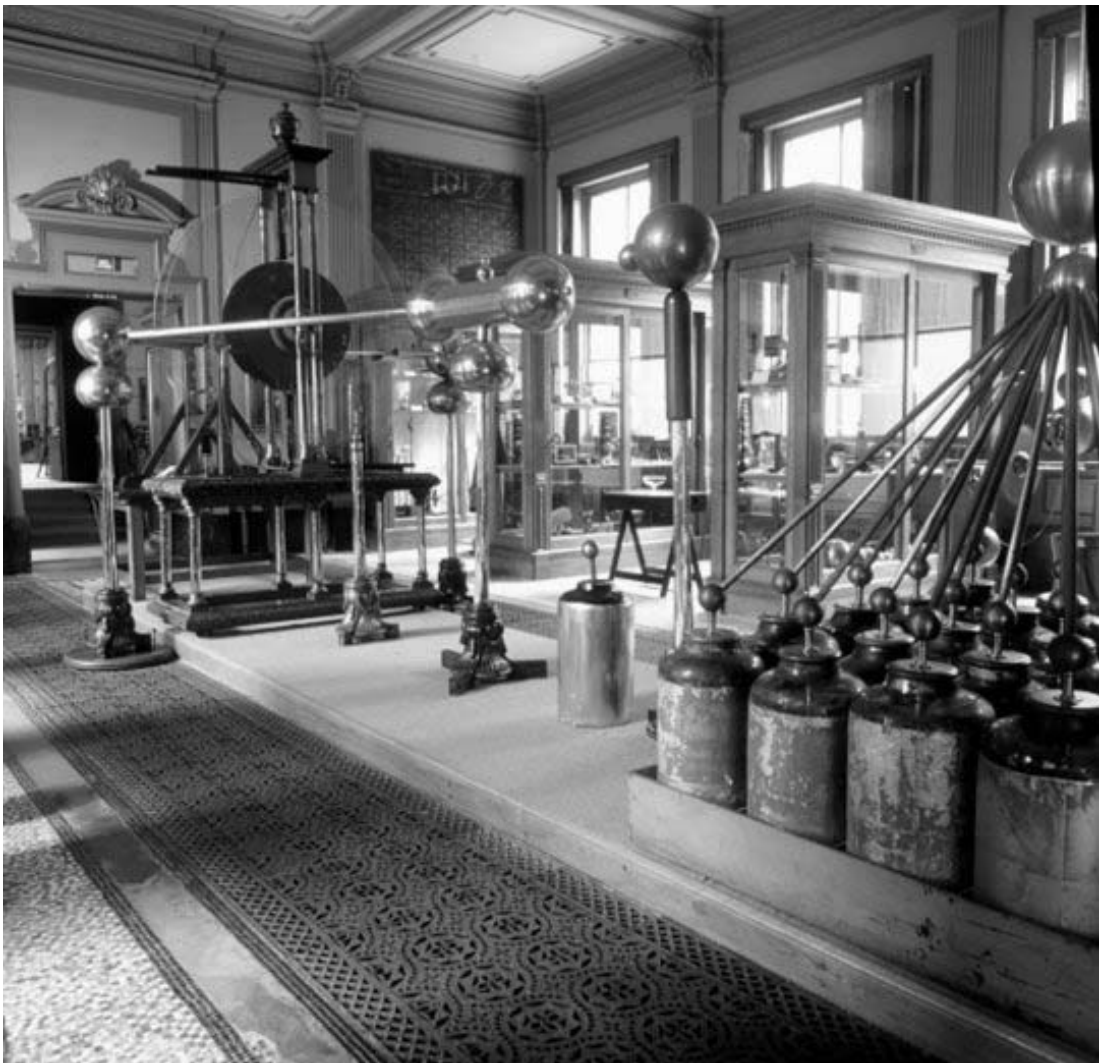
Figure 2.2: The enormous friction electrical machine together with the Leiden jars built by J. Cuthbertson

For its operation, two men had to move two enormous glass discs. Each disc was fractioned by four cushions. The electricity on the glass discs had to be induced into the conductors by an array of Leiden jars. The potential difference reached nearly 330 kV. Courtesy: Teylers Museum

while Hyman developed his device in 1930-31. Lidwill's apparatus had one pole applied to the skin and another into the appropriate cardiac chamber (Greatbatch, 1991). Later on, the Hyman device was successfully used in patients.

Chronic application of the cardiac pacemakers dates as far back as 1954. However, it was not until the 1960s when pacemakers were adopted on a great scale in clinical practice. Their potential for different applications in the beginning was not recognized by both the medical profession and the industry. Another reason was the immaturity of both technologies and implantation techniques. Stimulation was carried out by skin electrodes, which left uncomfortable burns when used for more than a couple of days. Later, electrode wires leading through the skin were tried but infections along the wires remained an unsolvable problem (Greatbatch, 1991). This could be circumvented by the implantation of the entire pacemaker. Dr. Rune Elmqvist designed the world's first implantable pacemaker. The first 10 patients for the implantable pacemaker were operated in 1960 (Chardack et al., 1961). In the 1970s, heart pacemakers demonstrated the reliability of implanted electronic devices and showed the benefits in terms of improved quality of life.

In parallel to the development of cardiac pacemakers went the attempts to apply stimulation of the diaphragm for *respiratory pacing*. For some 200 years, electricity has been applied to the phrenic nerves to activate the diaphragm. However, the actual therapeutic opportunity arose in the 1950s, by the time the heart pacemakers were developed. The first attempts to pace the diaphragm with implanted electrodes were carried out between 1948 and 1950 by Sarnoff et al. One of the most important prerequisites of the routine clinical applications was the introduction of the long-term electrical stimulation by the radio frequency inductive method introduced around the end of the 1950s (Glenn et al., 1964). In 1966, Dr William Glenn at Yale University, USA, performed the first clinical application to patients with *hypoventilation* of central origin. The ventilation support was made by radio frequency pacing of the diaphragm. Pacing for total ventilatory support in patients with *respiratory paralysis* was applied in 1971. The first commercial phrenic nerve pacers were introduced in the early 1980s .

As a result of the successful application of the pacing of the heart, the technological advances achieved during the development of the pacemakers were also successfully applied in the development of other neural prostheses. *Restoration of hearing* to the profoundly deaf was an early target. A report by Gersuni and Volokhov (1937) indicated that hearing could be produced over a normal frequency range and that it persisted following the surgical removal of the tympanic membrane and ossicles. One of the first recorded attempts to stimulate the auditory nerve was made by Lundberg in 1950, who employed sinusoidal currents during a neurosurgical operation. The patient could only hear noise. However, the milestone for the development of auditory prosthesis was the electrical stimulation of the acoustic nerve of a deaf man by an implanted electrode achieved by Djourno and Eyries (1957). They used an implanted induction coil connected with one end to the inner ear electrode and with the other to an indifferent electrode at the temporal muscle. Another coil, outside the body was held over the implanted coil to inductively transmit the signal from a microphone. The usefulness of the device was very limited since the patient could recognize only few words from the transmitted signal (*papa*, *maman*, and *allo*). This operation, however, opened the doors for further attempts to interface the sense organs. The early investigators were subjected to severe criticism by both neuroscientists and clinical professionals for the insufficient safety studies and the unsatisfactory design of the implants used. The safety of the cochlear implantation improved in the late 1950s with the evolution and developments of microsurgical techniques and stapes surgery. The indications and contraindications for this implantation were elaborated in a broad debate between the clinicians and the promoters of the cochlear prostheses. Questions were also raised about which device should be used and about the safety of the electrical stimulation. The 1970s could be

considered as a decade of controversy concerning the implant itself and its use. Finally, in 1984, after more than twenty years of on-going experimentation, the cochlear implant received Food and Drug Administration (FDA) approval for use in adults in USA. Nowadays the cochlear implant is a historical example of how a neural prosthesis can revolutionize treatment.

In 1929, Foerster described the effects of electrical stimulation of the human visual cortex (Foerster, 1929). The subjects reported for "*perception of a small point of light during stimulation*", which was later called phosphene. This result was reproduced many times in both sighted and blind subjects. The idea that concurrent stimulation of many sites in the brain could produce a single coherent image was postulated by Krieg (1953), based on the retinotopy in the visual cortex. As a second milestone for the development of neural prostheses can be considered the implantation of a *prosthesis in the visual cortex* of a blind woman in 1968 by Brindley and Lewin. The prosthesis did not benefit much the patient (she reported only about occasional phosphenes in her visual field) but demonstrated that it is possible to transfer large amount of information into the visual system. Giles Brindley, one of the greatest protagonists in the FES field, attained recognition and acceptance of the applications of neural prostheses in the clinical field. The results obtained by the Brindley implant and the early cochlear stimulator showed the need to stimulate selectively small groups of neurons or fibers in order to transmit meaningful information into the central nervous system.

Attempts to restore the lost functions of the paralyzed leg muscles were performed for the first time in 1961 by Liberson et al. The system was developed to compensate for the "drop foot" problem in hemiplegic stroke patients. By stimulating the peroneal nerve, the prosthesis triggered ankle dorsiflexion, eversion, and inversion. Since then, a number of neuroprostheses for restoration of walking, hand, and arm functions have been designed and tested in various patients and with different levels of success.

Apart from these well-endorsed success stories, other applications of FES still suffer from major difficulties regarding the clinical acceptance and patient compliance. Two such examples will be given here. Long and Masciarelli (1963) introduced prosthesis for the hand that could not meet the expectations of the patients and was later on abandoned. In the 1970s, attempts to treat refractory epilepsy were also carried out by means of stimulation of the cerebellar cortex. Later on, the performed double blind clinical trials did not confirm the claimed effects (Hambrecht, 1990).

In conclusion, history of FES shows that pacing of the heart emerged at different places and its success stimulated pacing of the diaphragm. The criticism of the early cochlear prostheses could be surmounted by tenacious research. However, one may consider these first successful applications as "lucky shots" based on the simple reactions of the involved organs: for the cardiac muscle and the diaphragm - the simple contraction response to stimulation; and for the inner ear - the linear tonotopical organization allowing simple positional encoding of the stimulating signal. On the other hand, neuroprostheses for locomotion as well as those for reaching and grasping require selective stimulation of those myelinated fibers in the nerves, which innervate the muscles performing the movements. Therefore, in the case of selective nerve stimulation, the research should be directed towards localization of the different physiological types of myelinated axons and their spatial organization within particular nerves.

As the abovementioned clinically recognized "success stories" of electrical stimulation motor neuroprostheses comprise a rapidly developing area that is on the verge of broadening its applications. Evidence for this is the increasing number of various neuroprosthetic devices that have been developed recently. Some of them are already beyond the prototype stage. That is why this paper will deal further on primarily with the electrical stimulation of the motor

system.

2.2 Principal notions in FES

FES aims at restoring the lost functions of the nervous system by means of *electrical stimulation.* This can be achieved by either performing rehabilitation, thus improving recovery, or by use of a prosthesis[2] to substitute for the lost function or an orthosis[3] to support the diminished function. Example of the former is the stimulator of the phrenic nerve and of the latter is the peroneal stimulator for foot-drop.

2.2.1 Electrochemical processes at the tissue-electrode interface

Electrical stimulation of biological tissues with metal electrodes requires the flow of charge in the biological tissue. This flow is induced by both capacitive and faradic mechanisms. The capacitive mechanism involves periodic charge and discharge of the electrode double layer. There is no charge transfer across the electrode/electrolyte interface. This is an ideal mechanism for charge injection, but it is limited by the maximal amount of charge that can be transferred before the dielectric breaks down, approximately 20 μC/cm^2. Because the charge required for physiological stimulation exceeds this limit, all electrical stimulation is performed by faradic charge injection. The faradic mechanism involves charge transfer across the electrode/tissue interface and, therefore, electrochemical reduction/oxidation processes. These reactions can be either reversible or irreversible. All irreversible electrochemical reactions are undesirable since they alter the chemical composition of the extracellular fluid by producing cytotoxic products or bringing about large changes in pH. For every material used in the production of electrodes, there is a charge limit for the reversibility of the electrochemical process. This charge limit depends on the particular properties of the material, the shape of the electrode, its size, and the stimulation waveform. According to Robblee and Rose (1990), the most important factor is the temporal shape of the stimulation wave.

In order to diminish the oxidation and dissolution of the electrodes, generally a noble metal like **Pt**, **Ir**, or **Au** is used as material for the anode. Of the non noble metals, 316L stainless steel is also used for intramuscular electrodes (Bhadra and Peckham, 1997). At the cathode O_2 molecules are reduced to O_2^-, which in turn react to produce free radicals. The free radicals are known to damage the cell membranes and DNA molecules. During a typical neurostimulation pulse, a substantial amount of the O_2 molecules is reduced to anions (Morton et al., 1994). Part of the free radicals generated near the cathode can be neutralized by oxidation when an anodic pulse follows the cathodic pulse. Morton et al. (1994) concluded that the reduction of oxygen, and thus the generation of free radicals are restricted most when the cathodic pulse has a small width and when an anodic pulse with the same charge immediately follows the cathodic pulse. This principle is known as *biphasic charge-balanced stimulation* (Lilly and Hughes, 1955). The continuous stimulation with biphasic, charge-balanced pulses without delay between the pulses is more beneficial with regard to avoiding nerve degeneration than that with delays (McCreery et al., 1992) and was shown not to have harmful effects to sciatic nerves (McCreery et al., 1995).

---

[2]artificial substitute of a dysfunctional organ
[3]device supporting the function of an organ in the case of impairment

2.2.2   Voltage-controlled and current-controlled stimulation

Historically, the implantable FES systems in clinical applications have been voltage-controlled (for example cardiac pacemakers). In contrast, the current-controlled devices dominate in experimental set-ups. In the voltage-controlled devices, the output voltage V of the pulse generator is regulated. Generally V is kept constant, thus creating a rectangular voltage pulse, the related current obeying Ohm's Law. In contrast, in the current-controlled devices the current I is kept constant, whereas V is automatically adapted according to the value of the impedance Z, which may vary over time due to the reaction of the surrounding tissue to the implant. The current needed for stimulation does not change chronically and thus no corrections are needed. In the voltage-controlled systems, however, the voltage needed for stimulation is influenced by the changing value of Z over time and, thus, the amplitude of stimulation has to be adapted at least in the first two months after implantation when the fibrous encapsulation layer develops. Since the current consumption determines battery life of an implanted pulse generator it is important that the stimulation current is determined in the first place. This is, however, not possible when a voltage- controlled pulse generator is used, since I depends on the unknown value of Z. Therefore, the battery life cannot be accurately predicted from the value of V. Nevertheless, it is often erroneously assumed that a reduction of V reflects a reduction of I and *vise-versa*.

2.2.3   Monopolar, bipolar, and tripolar stimulation

Since the cathodic threshold for nerve fibers is 3-7 times lower than the anodic threshold current, cathodic stimulation is by far the most efficient way (Ranck, 1975). In monopolar stimulation, therefore, the active electrode (in or near the neuronal target) is the cathode and the distant, indifferent electrode, is the anode. In that situation, the current injected by the cathode is distributed more or less evenly in all directions. In bi-, tri-, and multipolar stimulation, activation of nerve fibers always happens near the cathode and, therefore, its position is more important than the position of the anode for the optimal stimulation. In the clinical applications of FES, phenomena, such as cathodic block, anodic excitation, and anodic block are not likely to occur (Wee et al., 2000; Wee, 2001). The threshold current for stimulation of a nerve fiber increases with the distance between the cathode and the fiber and is inversely related to the fiber diameter. The preferential stimulation of large fibers is favored most when short pulses ($\approx$ 60 ms) are applied. Smaller fibers can be activated more easily when pulses are wider. The current consumption is minimized when stimulation is given with a "guarded" cathode parallel to the fiber bundle as in peripheral nerve stimulation and Spinal Cord Stimulation (SCS).

2.2.4   Cable properties of the nerve fibers

The theory of the current flow in electric cables was developed for submarine cables by lord Kelvin (1855). It was applied in studies on excitable cells for the first time towards the end of XIXth century. Cable theory allows to derive equations for the current flow in cylindrical nerve or muscle fibers subjected to voltage changes small enough so that the membrane properties are linear. Finite cables, such as the axons, could be described by the theory equations and the behavior of the impulse in an axon could be predicted.

2.2.5 Active properties of the nerve fibers

The nerve fibers conduct information by means of action potentials propagating at almost constant velocity (Table 2.1). In the myelinated nerve fibers, the velocity of the action potential is proportional to the fiber diameter (Hursh, 1939; Rushton, 1951) and the mode of conduction is saltatory. Moreover, the threshold of excitations also depends of the fiber type (Blair and Erlanger, 1933). Action potential of the non-myelinated fibers could be described quantitatively for the first time by Hodkin and Huxley (1952). The electrical behavior of the myelinated nerve fiber can be represented by a similar cable network involving two types of elements: the passive internodal regions and the active nodes of Ranvier having a Hodgkin-Huxley electrical behavior (Frankenhaeuser and Huxley, 1964). For the mammalian nerve fibers, this model was introduced by McNeal (1976) in order to calculate how a stimulation-induced extracellular field affects nodal transmembrane voltages (Fig. 2.3). According to the McNeal model, the node of Ranvier that is closest to the cathode will be excited first when the stimulus current is sufficiently high. The McNeal model is the basis of the most of the theoretical research performed in FES. The results of this theoretical approach are in accordance with the general observation that the threshold stimulus of nerve fiber excitation is smallest near the cathode and rises with the increase of the distance (Ranck, 1975). As a result, cathodic stimulation gives rise to a depolarization of several nodes, whereas a larger number on both sides of the cathode are hyperpolarized to a lesser extent, thus creating a *virtual anode.*

During anodic stimulation, the opposite effects occur. The virtual anode and virtual cathode effects underlay phenomena, such as cathodic block and anodic excitation. *Anodic excitation* is possible when the anodic current is so large that the virtual cathodic depolarization on either side of the hyperpolarized membrane generates action potential. For the *cathodic block*, the opposite is true — if the cathodic current is large enough the induced virtual anodic hyperpolarizations can block the propagating action potential.

2.2.6 Selectivity concepts

There are two interrelated aspects of the obtained functionality of stimulation using a neural prosthesis: (i) stimulation should be topically selective in view of the target effect and (ii) it should be specific for the physiological type of the nerve fibers being excited. Different aspects of selectivity may be distinguished depending on the structures being stimulated. Here we propose modification of the classification used by Smit (1996):

Spatial selectivity is the possibility to stimulate a particular region inside a nervous structure. However, it does not always guarantee specificity of the functional effect.
Peripheral and spinal nerves generally consist of several morphologically distinct suborgans, called fascicles. Therefore, a suitable definition of **fascicle selectivity** is the stimulation of only one fascicle in a multifascicular peripheral nerve without spread of the activation to other fascicles. It is a special case of the spatial selectivity.

Muscle selectivity is the possibility to activate a specific muscle by peripheral nerve stimulation, i.e. to control an individual muscle. It is a particular aspect of the spatial selectivity.

Fiber selectivity is another special case of the spatial selectivity. It can be defined as activation of single nerve fibers.
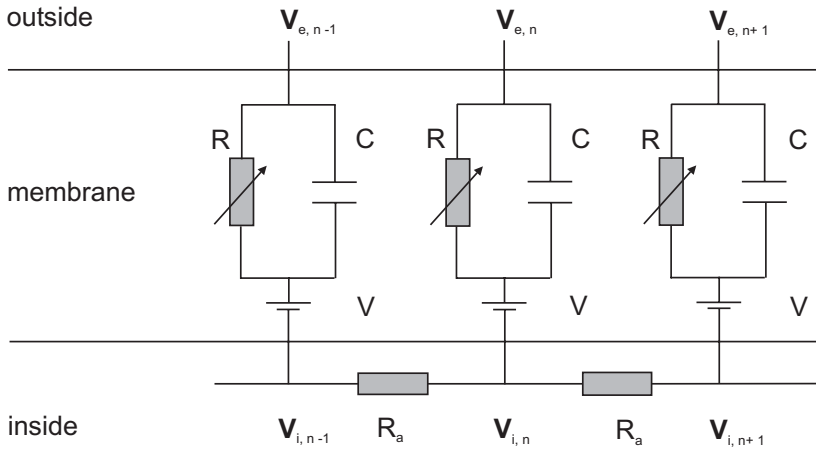
Figure 2.3: The McNeal cable model for the myelinated axon

Each node of Ranivier is represented by an equivalent electric scheme. Only resistive and capacitive elements are considered. V_i intramembrane potential, V_e extamembrane potential, R_a intraaxonal resistance, R variable membrane resistance, C - membrane capacity, V resting membrane potential

Size selectivity can be defined as activation of fibers of a particular size group. Since functionally different fibers often have very different sizes (Table 2.1) size selectivity can deliver the desired selectivity of stimulation with regard to the physiological type of fibers.

Spatially selective stimulation of the nerve fibers within a given peripheral nerve is important, because the different muscles are innervated by fibers having a specific localization within a nerve bundle. In the paradigm of the implantable devices, selective stimulation of individual components of multifascicular nerves would allow control of several muscles using less hardware (Grill and Mortimer, 1996). In general, a mixture of efferent and afferent fibers is present in the nerve. Such mixed populations may lead to undesirable sensations during stimulation. To avoid this, size selectivity of stimulation is required.

2.2.7   Stimulation Electrodes

To improve different aspects of selectivity of stimulation, many different designs of electrodes employing different materials and geometries of the contacts have been developed. Most of them are used only in animal experiments and only few are employed in clinical FES applications. FES electrodes can be classified in: (i) surface (skin) electrodes; (ii) intramuscular and epimysial electrodes; (iii) extraneural electrodes (cuff or helical electrode around a peripheral nerve); (iv) intraneural wire electrodes; (v) intraneural linear, 2D and 3D multi-electrode arrays. An extensive account on the cuff, intrafascicular, and sieve electrodes designs and fabrication technology can be found in Heiduschka and Thanos (1998) and Rutten (2002).

Table 2.1: Morphology and electrophysiology of the fibers in the Peripheral Nervous System

Type	class	MCV[a]	d[b]	Function
$A\alpha$	myelinated	70 - 120	12 - 20	somatic motor, proprioception, muscle spindle annulospiral
$A\beta$	myelinated	30 - 70	5 - 12	proprioception, muscle spindle flower spray, exteroception, touch, pressure
$A\gamma$	myelinated	15 - 30	3 - 6	somatic motor muscle spindle
$A\delta$	myelinated	12 - 30	2 - 5	exteroception, pain temperature, touch
B	thin myelinated	3 - 14	< 3	motor autonomic preganglionic
C	unmyelinated	0.5 - 2.5	0.4 - 1.2	exteroception, pain reflex responses; motor autonomic postganglionic sympathetic

[a]Mean Conduction Velocity [m/s]; MCV values for $A\beta$ and $A\gamma$ fiber classes are corrected.
[b]diameter [μm]; fiber class borders presented for the cat; see Chapter 4 for the rat values

Surface electrodes

Transcutaneous stimulation is performed with self-adhesive or non-adhesive electrodes that are placed on the skin of the subject, above the peripheral nerve. The metal electrode is connected to the skin with a saline bridge. Desired features for surface electrodes are low impedance with an even current spread, flexibility, ease of application and removal, and lack of skin irritation (McNeal and Bowman, 1985). The application is simple. Nevertheless, damage of the skin can only occur by the diffusion of soluble electrochemical products. The large distances to the stimulation targets and the insulation of the skin and the fat tissue demand high stimulation strengths, which in turn results in low selectivity. Complications are rare and include burns, skin irritation, erythema, and local pain.

Intramuscular and epimysial electrodes

Muscle electrodes have their stimulating surfaces onto or inside a striated muscle. In the former case, they are sutured to the epimysium of the muscle (hence the name epimysial). If terminal motor branches are present, the electrodes exert their action by stimulating the nerve endings. Therefore, they can be considered also as nerve electrodes. In comparison with the transcutaneal electrodes, they produce contractions with lower currents and with greater selectivity. For these reasons, muscle-based electrodes are preferable for situations that require independent control of several isolated muscles.

Depending on their intended application, intramuscular electrodes can be introduced either percutaneously (Marsolais and Kobetic, 1983) or in an open surgical procedure (Wuolle et al., 1994). However, intramuscular electrodes can also activate other than intended neural structures near their stimulating tips thus recruiting other muscles besides the ones targeted (Marsolais et al., 1994). Nevertheless, intramuscular electrodes are considered safe and effective means to produce strong and isolated contractions of single muscles. Complications include infections and wire breakdowns. In an effort to avoid the use of percuataneous leads for muscle electrodes Cameron et al. (1997) and Loeb et al. (2001) developed implantable muscle stimula-

cuff

flap

slit

contact
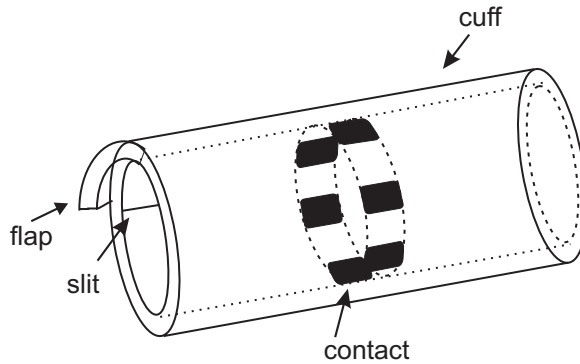
Figure 2.4: A schematic view of a cuff electrode. Courtesy: K. Deurloo, from (Deurloo, 1999, p. 66)

tors that can be controlled telemetrically and are inductively powered from external magnetic devices in order to overcome infections. According to the promoters of this approach, this would ultimately alleviate the burdens involved with maintenance of the awkward external electronic equipment.

Cuff electrodes

Cuff electrodes circumscribe the nerve (Fig. 2.4). They were introduced in the 1970s. The first cuff electrodes had a very simple cylindrical rigid design and could stimulate only the most superficial fibers of the nerves (Heiduschka and Thanos, 1998). Modern cuff electrodes, on the other hand, use flexible materials and adaptable geometries. Cuff electrodes are implanted by a simple surgical procedure and their size can be adapted to the diameter of the nerve of interest. If needed, they can be surgically fixed to adjacent tissues. Various designs, such as the *helix-shaped electrode* (Naples et al., 1990), the *spiral-cuff* (Naples et al., 1988a), and the so-called *half-cuff electrode* of Kim et al. (1983), have been developed and applied. Another particular design is the arrangement of flexible interdigitating sub-units with microelectrodes along a backbone-like carrier (Klepinski, 1994). The use of silicone and helical designs in cuff electrodes has improved surgical access and reduced nerve damage (Tarver et al., 1992; Loeb and Peck, 1996; Veraart et al., 1993). The main push for their continuing development was the inadequate spatial and fiber selectivity, which they provided at first.

With a sufficient number of electrodes within the cuff, high spatial selectivity of stimulation can be achieved by combinations of longitudinal and transversal currents produced by appropriately switched electrodes (Veraart et al., 1993). Longitudinally aligned tripolar dot electrodes on the surface of a nerve trunk restrict excitation to superficial nerve trunk regions more successfully than monopolar dot electrodes (Sweeney et al., 1990). Using a 12 contact cuff, the selectivity is dependent on the relative location of the electrode contacts and the nerve fascicles and the size and relative spacing of the neighboring fascicles (Grill and Mortimer, 1996). On the basis of computer modeling results, Deurloo and Holsheimer (2003) concluded that transverse steering provides better selective stimulation than longitudinal steering. However, the fiber size selectivity during stimulation could not be improved by these methods. Goodall et al. (1996) found that large fibers were activated before smaller with a cuff electrode containing

12 electrodes arranged in 4 longitudinal tripoles irrespective of the fiber position. Transverse current from an anode positioned opposite to the stimulating cathode was found to improve spatial selectivity, and position selectivity was enhanced when the ratio of transverse current to longitudinal current was increased.

Intraneural wire electrodes

Intraneural electrodes that directly contact nerve fibers within a given nerve bundle were developed in an attempt to overcome the selectivity problems occurring during cuff electrode stimulation. Intraneural wire electrodes are also referred to as penetrating electrodes. The first penetrating electrodes were simply thin metal wires or needles, which were inserted into the nervous tissue. They are used for both recording and stimulation.

An interesting, non-silicon approach for intrafascicular stimulation is the use of tethered platinum microwires. Nannini and Horch (1991) tested the performance of **Pt-Ir** intrafasicular electrodes (25 µm wire diameter) implanted in nerves innervating the gastrocnemius and soleus muscles. Originally developed for recording purposes, these electrodes proved also suitable for simulation. Yoshida and Horch (1993) used dual intrafascicular electrodes to study activation of nerve fibers by pairs of **Pt-Ir** wire electrodes implanted within single fascicles of the nerve innervating the gastrocnemius muscle in cats. They aimed to determine whether intrafascicular electrodes could activate nerve fibers in different fascicles independently of each other and whether they could be used to activate separate subsets of axonal populations within a single fascicle.

Intraneural multi-electrode arrays (MEAs)

MEAs can be classified into linear multielectrodes (1D), two-dimensional (2D-), and three-dimensional (3D-) arrays. Linear multielectrodes are 1D MEAs consisting of wedge-shaped microprobes carring lines of electrode sites suitable for recording and stimulation purposes (BeMent et al., 1986). 2D-arrays consist of electrodes with tips ending in the same plane. Each tip is configured either as a bundle of wires or as a galvanically grown needle. The substrate carrying the electrodes is either needle- or wedge-shaped in order to allow penetration into the nervous tissue. This makes recording and stimulation of axons possible not only on the surface but also in a certain well-defined depth within the tissue, e.g. within a fiber bundle. If the needles of the array have variable lengths, the device is called a 3D-array. Implantation of MEAs is always associated with some damage of the nervous tissue, cell death of neurons, and disruption of axons. Moreover, stiffness of many models may lead also to a chronic mechanical damage of the nervous tissue. Thus, the efforts are directed to miniaturize the penetrating parts of the implant and to use materials that are more flexible. Rutten et al. (1995) produced a 3D needle array with 128 recording sites on one electrode placed on the tip of a needle intended to serve as interface to peripheral nerves (Fig. 2.5). The different lengths of the needles allowed stimulation in the volume of the peripheral nerve. Design of the array was based on calculations for optimal stimulation assuming uniform random distribution of the nodes of Ranvier along the myelinated peripheral nerve fibers.

For recording and stimulation of a larger area, e.g. within the cortex, 2D-MEAs are necessary. An example of such 2D array is the Utah Electrode Array (Nordhausen et al., 1996). It was designed for implantation in the human visual cortex and was intended to be a prototype in the development of visual prostheses (Branner and Normann, 2000). It provides a multichannel
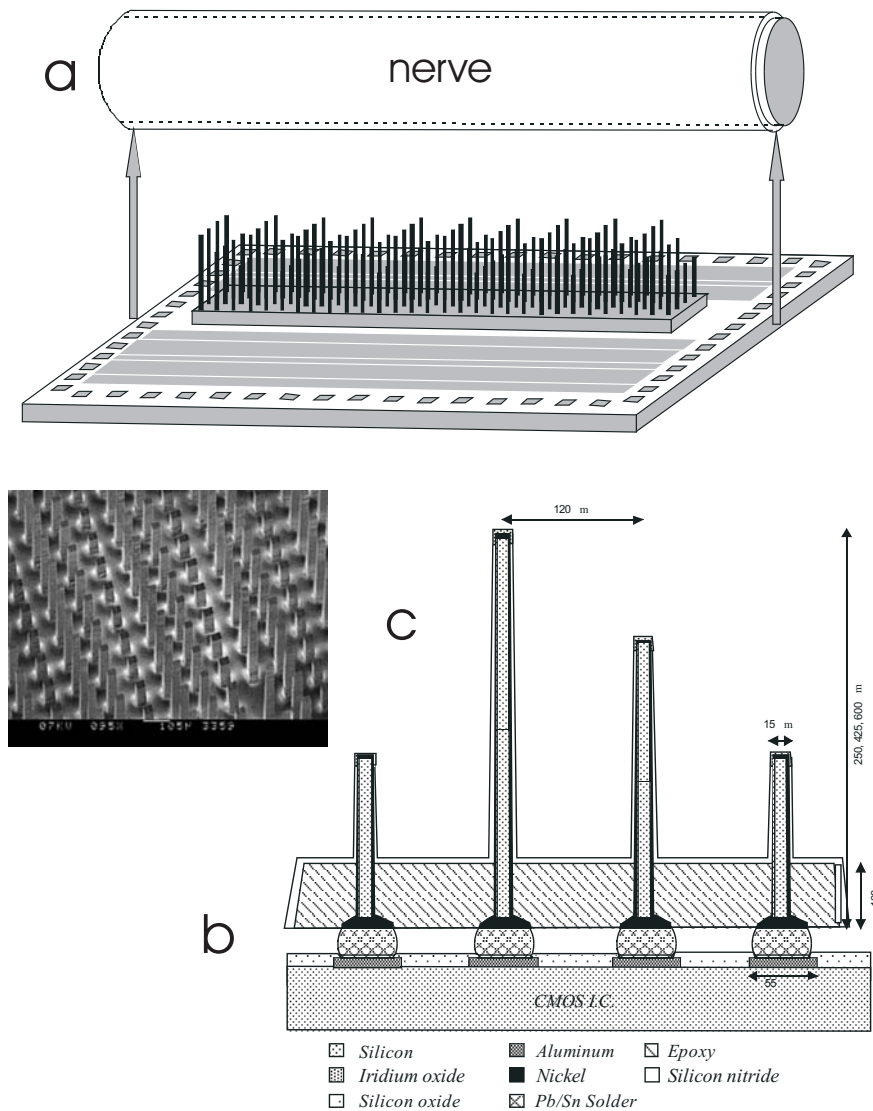
Figure 2.5: The Twente array

(a) Scheme of the University of Twente 128-electrode 3-D glass-silicon array (UT-128 array) mounted on a CMOS mixed mode processing chip with dimensions 4x4 mm. Needle lengths are 600 µm, 425 µm or 250 µm; width at tip is 15 µm; needle spacing is 120 µm. (b) Details of the dimensions and materials used for the UT-128 array. (c) A 'sea' of sawn and etched silicon needles of three different lengths, embedded in a glass matrix. Courtesy: W. Rutten, from (Rutten, 2002).

interface with the visual cortex using a large number of 1.5 mm long electrodes (typically 100 in a 10 x 10 square grid) projecting from a very thin (200 µm) substrate and separated from each other by 400 µm. With the technological advance in the field of the flexible polymeric

substrates, so-called "flexible nerve plates"came into development (Meyer et al., 1995). They consist of a flexible substrate, which carries the MEA and it is possible to add other elements of a microelectronic circuitry.

In general, the silicon microtechnology based fabrication leads to improvement of recording structures, which made possible to create not only planar 2D MEAs but also intraneural electrode structures for *in vivo* measurements. Alike the cuff electrodes, geometry and arrangement of the intraneural electrode arrays are currently optimized to fit the geometrical characteristics of the nerve fibers (fiber position in a bundle, diameter of the fibers, and their orientation). While Smit (1996) argues for intrafascicular stimulation, the proposed approach could be employed only in acute experiments, thus limiting the use of the obtained knowledge for clinical applications. In theory, intraneural electrodes should give better spatial selectivity than the cuff electrodes (Rutten et al., 1991; Yoshida and Horch, 1993). However, the random distribution of the nodes of Ranvier in the peripheral nerves makes the stimulation a probabilistic process. The implanted intraneural electrode may simply miss the target fiber population when the topography of the nerve fibers is unknown. Further, since during implantation these intraneural electrodes must penetrate the relatively tough epineurium and the perineurium of the nerve, they can cause short- and long-term nerve damage during the electrode insertion procedure (Fried et al., 1989; Rice and McMahon, 1992; Rice et al., 1993; 1994). Nevertheless, histological results suggest that intraneural electrodes can be used chronically in peripheral nerves (Bowman and Erickson, 1985; Hallin et al., 1986; Lefurge et al., 1991). Moreover, a reliable fixation of the cuff must be achieved because otherwise the cuff may rotate around the nerve or shift along the nerve, both leading to a serious loss of selectivity.

To summarize, the implantable electrodes are surgically set in around, within, or adjacent to a nerve trunk or root. By means of transcutaneous electrodes it is difficult or impossible to selectively activate individual muscles, especially deep muscles, such as the hip flexors (Stanič et al., 1977; Petrofsky and Phillips, 1985). Large currents may be required to drive sufficient charge through the skin and intervening tissues between the electrode and the peripheral nerve. In many cases, cutaneous pain receptors are excited and patients with preserved or heightened sensation may find it difficult to tolerate surface stimulation at the levels required to produce a functional motor response. Advantages of the implantable electrodes over the superficial, epimysial, and intramuscular include:

- The current needed to excite an action potential in the target fibers is smaller by at least an order of magnitude over the current required for the latter designs.

- Muscle length and limb position are expected to have substantially less effect on the recruitment characteristics in the case of an implantable electrode. Cuff-electrodes are easy to implant and are generally less invasive to the nerve than intraneural electrodes are.

Despite all new developments in electrodes, the robustness of obtained stimulation is hampered by the the random distribution of the nodes of Raniver and the fasciculation, typically present in the nerve. Therefore, the main prerequisite for successful application of the modern sophisticated electrode designs and stimulation protocols is the detailed knowledge of the topography of the nerve fibers within the nerve bundle and their function (i.e. functional topography). An ideal peripheral nerve electrode array should have the neural selectivity of the intraneural electrode and the ease of implantation, stability, and biocompatibility of the extraneural electrode.

2.3 Research Problems

Major issues in the development of a neural prosthesis from the neuroscientist's point of view are: (i) the biocompatibility of the materials, which determines the long-term use of the device; (ii) the amount of detailed neuroanatomical and neurophysiological knowledge of the system, which in the end determines the effectiveness of the device.

2.3.1 Biocompatibility of implantable devices: general considerations

Implantable devices should be able to survive in the rather aggressive internal milieu of the body without causing significant tissue reaction. The major prerequisite for the application of implants is that the organism accepts the implant, i.e. that the implant is biocompatible. This also holds for objects that come in close contact with the skin or mucose. An accepted definition of biocompatibility is "*the ability of a material to perform with an appropriate host response in a specific application*" (Williams, 1987). The selection and evaluation of materials and devices intended for use in humans requires a structured program of assessment to establish biocompatibility and safety. Current regulations, whether in accordance with the U.S. FDA (ISO 10993-1/EN 30993 standard, since 1995), the International Organization for Standardization (ISO), or E.U. regulation bodies (The EU council directive - 93/42/EEC, since 1993), as part of the regulatory clearance process require conduction of adequate safety testing of the finished devices through pre-clinical and clinical phases (Bollen and Svendsen, 1997). An extensive account on the biocompatibility may be found in the standard ISO 10993-1/EN 30993. In brief, the notion of biocompatibility encloses non-toxicity, non-immunogenity, non- carcinogenicity, non-mutagenity, and haemocompatibility. An implant can be considered biocompatible if it gives negative results on the following tests: *cytotoxicity; sensitisation; genotoxicity; implantation; chronic toxicity; carcinogenicity; intracutaneous irritation; acute systemic toxicity; and subchronic toxicity.*

According to Heiduschka and Thanos (1998), the "*biosafety*" and the "*biofunctionality*" also have to be considered. Biosafety means that the implant does not harm its host in any way, and biofunctionality means that the implant acts in the body as it was intended. In addition, "*biostability*" is important which means that the implant must not be susceptible to attack of biological fluids, proteases, macrophages, or any metabolic substances. For example, implants may be subject to continuous attack by hydrolytic enzymes (Salthouse, 1976) or free radicals produced by monocytes and/or cell lysis. Stability of implanted material is important not only for a stable function but also because degradation products may be harmful to the host organism. Overview on the biological reactions to implanted materials can be found in Ratner et al. (1996).

2.3.2 Chemical biocompatibility

Chemically appropriate implant materials are designed to be as inert as possible. If chemical reactions are to be expected, they should be minimal and all resulting products should be inert. Candidate materials for use in neuroprotheses pass especially rigorous testing since they must remain inert not only passively but also when subjected to electrical stimulation. Typical materials for nerve electrode arrays include **Pt-Ir** alloys or stainless steel for the conducting parts and epoxy resins, polytetrafluoroethylene (PTFE, Teflon), silicone rubbers, and polyimides for

the insulators (Agnew and McCreery, 1990; Heiduschka and Thanos, 1998). These polymers are biocompatible, electrically insulating and stable.

The amount of **Pt** ions released into the surrounding tissue may be neglected even after long-term stimulation. During the last years, **Ir** has been of increasing importance because a stable oxide film can be formed on the surface of iridium electrodes. This oxide film has a big charge delivery capacity and is, for this reason, well suited for stimulating electrodes. **Pt** and **Ir** are established materials in microelectronics and carbon can be deposited onto microelectronic structures. Glassy carbon or carbon fibers are also used as electrode materials, and they are biocompatible and stable, though they have a higher roughness than metals. The bulk properties of polymers as backbones for electrodes can be modified to a certain degree and also surface modification procedures are performed in order to improve biocompatibility. However, certain surface modifications like autologous protein coatings also enhance the adhesion of pathogenic bacteria to the implant surface (Vaudaux et al., 1995; Wassall et al., 1998). A review on the chemical modifications employed in the production for neural prostheses can be found in Heiduschka and Thanos (1998).

2.3.3 Mechanical biocompatibility

The mechanical biocompatibility of an implant depends on the basic mechanical properties of the tissue and the implant. Ideally, the implantable device should have mechanical properties similar to the tissue in which it is implanted. This includes flexibility, strength, and durability. It is also important to consider the tissue motion within the implantation site. For example, flexibility is important in the peroneal foot-drop stimulator and not in the devices for spinal cord stimulation and anterior lumbo-sacral root stimulation. For any implant, the allowable size must be defined relative to its function. It is not necessarily true that increased function is associated with larger size. The geometrical characteristics of an implant are of great importance too. For example, sharp edges and blunt corners should be avoided. The primary goal for a cuff electrode design is to minimize the size as any constriction injury in the implanted site should be avoided. Such designs have been associated with incidence of morphological changes in neural tissue like axonal degeneration, demyelinization, and fibrosis (Naples et al., 1990). Thus, the recommendation had been to implant cuffs with an internal diameter equal to 150% of the nerve diameter (AAMI, 1984). However, this recommendation was criticized as to be actually more likely to create neuronal trauma (Naples et al., 1990). It also limits the degree of selectivity that is obtained during extraneural stimulation (McNeal and Bowman, 1985; Veraart et al., 1993).

2.3.4 Implantation and Nerve damage

The key factor determining the damage of electrode implantation is the disruption of the microcirculation of the nerve, which results in edema. This holds especially for intrafascicular electrodes. Another factor is the damage to the endoneurium and the disruption of the homeostasis, maintained by the blood-nerve barrier. The mechanisms of the damage during implantation are still debatable. According to Agnew and McCreery (1990) on the first place stands direct mechanical interaction between the electrode and the nerve. Other mechanisms that may play a role during implantation are:

- Surgical trauma to either the neural microvasculature or the nerve itself.

- Pressure caused by post-surgical edema, seroma formation, or excessive fibrous encapsulation of the implant.

- Reduced mobilization of the nerve caused by excessive scar tissue formation, which could fuse the nerve to the surrounding tissues.

- Undue tension in the electrode leads.

- The transmission of forces from muscles to the electrode array and the nerve.

- Obstruction of the microcirculation.

For epineural and intraneural designs, though, the most important factors are the implant procedure itself and transmission of tension via the leads.

2.3.5   Tissue reaction to implantation

Implantation usually causes foreign body reaction involving the natural inflammatory defensive response of the body. The *acute response* starts with protein adsorption onto the surface of the implant. Therefore, the surface properties like roughness and surface chemical composition, which depend on the production process, are important for the grade of the subsequent response (Romero, 2000). The late response produces the typical cellular and humoral reaction including tissue edema, cytokines secretion, neutrophil, lymphocyte, and macrophage migration and adhesion. This is a complex process mediated by the secreted cytokines. The *chronic reaction* includes formation of a fibrotic capsule consisting of collagen fibers and fibroblasts around the foreign body. The thickness and the structure of the capsule are generally a measure of the severity of the response. The severity of the reactions can be determined by the amount of the giant Langerhans cells and macrophages. The electrical properties of this fibrotic capsule were studied by Grill and Mortimer (1994). They found that resistivity of the encapsulating tissue had a frequency dependency between 10 Hz and 1 kHz and decreased from 454 ± 123 to $193 \pm 98 \ \Omega \cdot cm$ and was frequency -independent between 1 kHz and 100 kHz with a mean value of $195 \pm 88 \ \Omega \cdot cm$. Moreover, the fibrotic capsule may lead to displacement of the electrode positions and changes in the tissue impedance (Grill and Mortimer, 1994).

The results from early experiments indicated that nerves implanted with snuggly fitting spiral cuffs showed signs of sustained trauma (Naples et al., 1988b; 1990). The typical pattern was a crescent-shaped region containing thinly myelinated axons, proliferation of subperineurial connective tissue, and a reduced axon density. In a more extensive study of the tissue reaction to the spiral cuff, 4 out of 44 nerves exhibited peripheral crescent-shaped areas, which contained thinly myelinated fibers with an apparent reduction in axon density, but there was no correlation between the cuff-to-nerve diameter ratio and the presence of morphological abnormalities. Similar results have been found in cuff electrode studies conducted by researchers at the Huntington Medical Research Institutes (Agnew et al., 1989). Recently, Grill and Mortimer (2000) reported focal areas of abnormal neural morphology including perineurial thickening, endoneurial fibrosis, thinly myelinated axons, and focal reduction in the density of myelinated axons in chronic implantation experiments with cuff electrodes.

Intrafascicular electrodes can also produce morphological changes in neural tissue (Lefurge et al., 1991). Chronic implantations of intraneural coiled-wire electrodes showed endoneurial fibrosis and edema, loss of nerve fibers (the large myelinated fibers being the most susceptible),

and variable shifts in the excitation threshold. However, there were no changes in conduction velocities indicating that no significant damage occurred due to implantation (Bowman and Erickson, 1985). The bulbous enlargement formed at the point where the electrode penetrated the perineurium was associated with focal nerve fiber compression, demyelination, edema, and fibrosis (McNeal et al., 1977; Bowman and Erickson, 1985). Electrodes sutured to the epineurium have also led to neural damage including endoneurial edema, endoneurial fibrosis, loss of axons, and reduction of myelin (Girsch et al., 1991; Koller et al., 1992). In general, intraneural electrodes are associated with greater risk of trauma than the cuff-electrodes (Agnew et al., 1990).

2.3.6 Nervous tissue reaction to electrical stimulation

Brief stimulation of the peripheral (Liang and Jones, 1996) or the cranial nerves results in increased expression of Immediate Early Genes (IEG) in the neuronal cell bodies, such as *c-fos* (Nakamura et al., 2003). IEG family consists of approximately 30 genes, whose protein products act as transcription factors (Lanahan and Worley, 1998). IEG are activated shortly after cell stimulation and without the requirement for *de novo* protein synthesis. Brief unilateral electrical stimulation of the cochlear nerve (120-250 mA, 5 Hz, 30 min) in anaesthetized rats with a biphasic current resulted in increased expression of c-Fos in the ipsilateral ventral and in the dorsal cochlear nuclei bilaterally (Nakamura et al., 2003). Intracochlear electrical stimulation with a cochlear implant in rats lead to changes in the phosphorylation state of the cAMP response element binding protein (CREB) and the expression of the IEG family members *c-fos* and *egr-1* in a tonotopically precise pattern in the central auditory neurons (Illing et al., 2002), which resided in nearly all auditory brainstem nuclei. Moreover, effects of electrical stimulation were identified in the medial vestibular nucleus and the lateral parabrachial nucleus. Regionally, CREB was dephosphorylated, wherever immediate-early gene expression went up. These massive stimulation-dependent modulations of transcription factors in the ascending auditory system indicate ongoing plastic changes as a consequence of the stimulation of the inner ear.

In the spinal cord, Molander et al. (1992) showed that in chronically axotomized nerves, *c-fos* was expressed after electrical stimulation of the fibers. Stimulation of the normal sciatic nerve at C-fiber intensity resulted in *c-fos* protein-positive cells within the sciatic projection territory in the ipsilateral dorsal horn (lamina I and outer lamina II), while stimulation of A/B fibers had little effect. The expression was delimited to the projection areas of the sensory A/B-fibers (ipsilateral laminae II, III, and IV and in the gracile nucleus) in young animals. This suggests that the excitability of these neurons is increased by nerve injury. The role of the IEG is implied in the structural plasticity of the nervous systems (Illing, 2001; Platenik et al., 2000). One may speculate that the continuous improvement of the responses of the individuals after early rehabilitation, in contrast with late rehabilitation, is due to FES being able to guide the plastic phenomena occurring after injury in a direction towards restoration of function. This line of thought is supported also by Muir and Steeves (1997) in a review showing accumulation of physiological and behavioral data that adaptive (plastic) processes also occur within spinal circuits. The potential ability of the spinal cord to "learn" has obvious implications for altering and improving locomotor function after injury. Recent studies in man indicate that a significant population of stroke and SCI patients could also benefit from FES rehabilitation (Wieler et al., 1999; Popovič et al., 2002). In particular, it was found that stroke patients and incomplete

SCI patients subjected to intensive FES treatment were able to recover grasping or walking function faster and better compared to patients who did not participate in the FES treatment post injury.

In the peripheral nervous system, prolonged high-frequency (f > 20-50 Hz) electrical stimulation of a peripheral nerve induces a typical pattern of neural injury, called early axonal degeneration, with a characteristic "salt-and-pepper" like mixture of "normal" and damaged fibers. The primary damage is observed as collapse of the myelin into the axoplasm and is restricted primarily to the large caliber axons (i.e. $A\alpha$, $A\beta$). It is followed by degradation and phagocytosis of the axon (Agnew et al., 1989; 1990; 1999). The neuronal injury originating from electrical stimulation has two mechanisms of occurrence:

Direct injury resulting from the electrochemical process near the electrodes. Brummer and Turner (1972) have shown that the rate of production of compounds by electrochemical reactions and the type of compounds produced are directly related to the charge density (charge transferred per unit area of the electrode surface). The charge density near the surface of an electrode determines the extent of depolarization and hyperpolarization induced in the neurons close to the electrodes. If such depolarization is abundant and going on for a long time the second mechanism of injury comes into play.

Excitotoxic neuronal injury that is caused by the excitatory neurotransmitter glutamate through its NMDA receptors. This view is supported also by the finding that MK-801, a potent NMDA receptor antagonist, is a neuroprotective factor during prolonged electrical stimulation (Agnew et al., 1993). The mechanism of the induced neuronal cell death is necrotic. Such damage occurs when the stimulus charge density or the charge per phase are large.

In summary, implantation of a FES device induces acute, late, and chronic inflammatory response. The smallest effect is caused by the chemical reaction due to the inert materials used for the implantable parts production. The largest damage comes from the mechanical stress during movement or is due to the surgery.

2.3.7 Surface stimulation vs. Implantation

An important advantage of the surface FES systems is that they do not require surgical intervention with its inherent risks. They also can be removed at any time if contraindications arise. Another advantage is that the transcutaneous electrode can be placed directly above the target muscle and, thus, muscle-selective stimulation can be achieved (Deurloo, 1999). A typical example where surface stimulation can be used is the restoration of hand function. Surface FES can be applied at a very early stage of the rehabilitation, during the recovery and reorganization period of the central and peripheral nervous systems (plasticity), allowing early benefit for the patient. FES training during recovery may help a subject to restore a function to the point that he/she no longer needs a neuroprosthesis.

Popovič et al. (2002) advocate an early start of FES as part of the rehabilitation in stroke patients. This benefits the use of surface FES systems since the objective of the treatment is to help patients to relearn the grasping task rather than to provide them with a permanent assisting system. In SCI subjects, there are two possibilities: implantation and surface stimulation. For the implantation, the patient should have reached stable neurological status. Surface FES

is also preferred in treatment of spasticity in order to strengthen the antagonistic muscles and in recovery of simple movements, which requires stimulation by few electrodes with easy positioning (Rattay, 1990). A disadvantage is that only a small part of a muscle can be stimulated, causing a rapid development of muscle fatigue. Furthermore, the reproducibility of muscle force is insufficient due to changes in the muscle geometry during contraction. Another issue is the displacement of the electrodes, which may occur during use of the FES device (Deurloo, 1999).

The advantages of the implantable FES systems are that the stimulation does not depend on the geometry of the muscle and a single electrode can stimulate several muscles with low energy consumption. Therefore, implantable stimulation is preferred in the following cases: (i) when deep muscles that are difficult to stimulate by surface electrodes have to be recruited; (ii) for complex movements, which require a large number of electrodes in a limited space; and (iii) to avoid pain and burns caused by stimulation of the pain receptors and the skin (Rattay, 1990). The disadvantages are that (i) the existing implantable FES systems still do not provide enough selectivity of stimulation; (ii) the implantation is associated with surgical trauma; and (iii) there are some unresolved issues in the geometry of the electrodes (Popovič et al., 2001a).

2.4 Contemporary Clinical applications of FES

2.4.1 The cochlear implant

The cochlear implant relies on the assumption that there are enough auditory nerve fibers left for stimulation near the electrodes. Although the first fully implantable cochlear prostheses preceded the fully implantable heart pacemakers, in the 1970's, heart pacemakers achieved high reliability and improved quality of life of the patients. In the USA, FDA nevertheless approved the first cochlear implant device for clinical use not earlier than 1984. Over the past 20 years of clinical experience, more than 20,000 people worldwide have received cochlear implants. Cochlear implantation has a profound impact on hearing and speech perception in postlingually deafened adults. Most individuals demonstrate significantly enhanced speech reading capabilities attaining scores of 90-100 percent correct on everyday sentence materials (NIH, 1995). Moreover, according to the NIH Consensus Statement the cochlear implant is the first, and still the only, neural prosthesis that is aiding a significant portion of a disabled population. In recapitulation, while the cochlear implant has reached wide acceptance and maturity as device, most of the other neuroprosthetic applications are still in childhood.

2.4.2 The drop-foot stimulator

The first neuroprosthesis for walking was developed by Liberson et al. (1961) to compensate for the "drop-foot" problem. The drop-foot is a pathological condition, caused by diminished ability to use the muscles that lift the foot. It may be caused by stroke, cerebral palsy, multiple sclerosis, or neurological trauma. By stimulating the peroneal nerve, the prosthesis elicited ankle dorsiflexion, eversion, and/or inversion, thus allowing the subject to make a step with the disabled leg. Since then, a multitude of devices has been developed, mostly in former Yugoslavia. The *Fepa system* was proposed by Vodovnik et al. (1978). Currently there are several commercial systems all based on surface stimulation: *MikroFES* (Jozef Stefan Institute of Science, Slovenia), *Odstock 2* (Salisbury District Hospital, UK) (Burridge et al., 1997), and *WalkAide* (Neuromotion, Canada) (Wieler et al., 1996). The drop-foot stimulators are

commonly controlled by a foot switch. A recent overview on the different FES systems can be found in Popovič et al. (2001a). So far, most systems are external with a surface electrode placed over the peroneal nerve just below the head of the fibula. *Odstock 2* is a surface stimulation system that has been used mostly in the clinical environment. It is based on the stimulator proposed by Liberson. The device can be used as an assisting aid or as a training device to strengthen muscles and improve voluntary control. Additionally, the device has a role in physiotherapy in gait re-education allowing isolated components of the gait cycle to be practiced under therapist control (Taylor et al., 1999a;b). *Odstock 2* was perceived by its users to be of a considerable benefit (Lyons et al., 2002). *Odstock 2* and the *MikroFES*, have been fitted to more than 500 subjects. So far, only the *WalkAid* has been approved by the US FDA.

More recently, implantable stimulators have been developed. For example, an experimental implantable two-channel system was made by the University of Twente and further commersially developed by Finetech, UK (Fig. 2.6). By 2002, it was tested in 10 patients (Kenney et al., 2002). It has the ability to stimulate independently the deep and the superficial branch of the peroneal nerve, thus allowing the correction for excessive eversion and inversion.
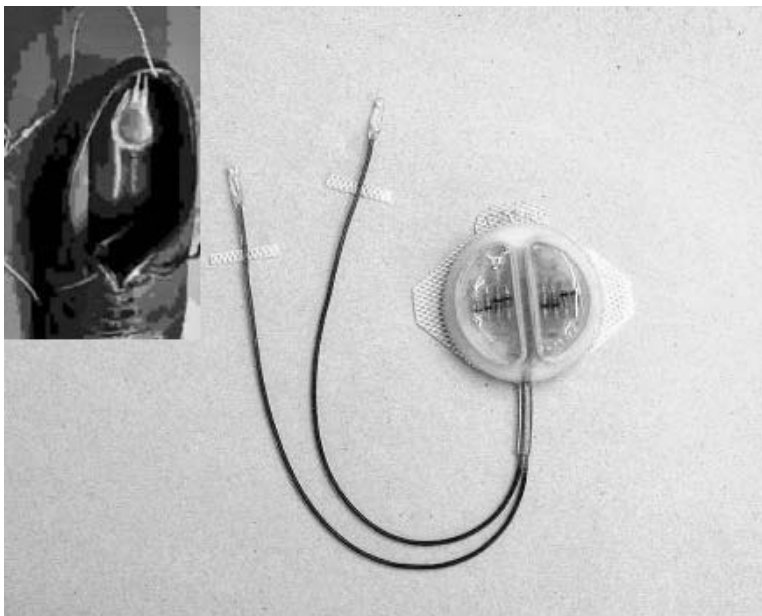
Figure 2.6: The Twente implantable drop-foot stimulator

This implantable stimulator is currently produced by Finetech, UK. The prosthesis has a radio-frequency transmitter and subepineural electrodes for the *N. Peroneus profundus* and *N. Peroneus superficialis*; inset - the heel switch placed in a shoe. Courtesy: G. Bulstra and H. E. van der Aa

2.4.3 Restoration of Lower limb Function

In 1963, Kantrowitz reported the first application of FES to a T-3 paraplegic patient who achieved standing for brief periods by surface stimulation of the gluteus and the quadriceps. The first systems were external devices enabling walking and were developed by Bajd and Kralj in

the 1970s through 1980s in Lublijana, Slovenia (Kralj et al., 1980). The initial devices only used two surface stimulation channels for each leg to produce standing and walking. The stimulation was delivered to the knee extensors. Devices with 4 channels have been proposed later (Bajd et al., 1983). Systems used by patients included stationary bikes for exercise, transfer systems to enable the patient to move between a wheelchair and a bed, transfer systems between standing and sitting, and walking aids (Kralj et al., 1980). The targeted patients were paraplegics after SCI. Patients used a rolling walker frame or crutches for support. About 50 patients successfully used the system (Kralj et al., 1988).

One of the first implantable multichannel stimulators was developed by Brindley with electrodes applied on the femoral and the gluteal nerves (Brindley et al., 1979). An overview of the contemporary devices, such as *Parastep*, *LARSI* (Donaldson et al., 1997), *FESmate*, *HAS*, *RGO*, *Praxis24*, and the implanted FES system of Kobetic et al. (1997), can be found in Popovič et al. (2001a). The only commercialized system, developed initially by Graupe et al. (1998), is *Parastep* (Sigmedics Inc., USA). It is based on the earlier work of Kralj et al. (1980). The target patient group consists of the complete or almost complete T4-T12 SCI patients. The system uses surface electrodes and no orthotic aids. The *Parastep* system was applied to more than 400 subjects and was the first FDA-approved FES system.

Although FES of locomotion gains clinical acceptance, it is still in its experimental phase of development and is, so far, incapable to deliver a complete treatment for the target groups of patients. Only in several cases, it may provide pathogenetic treatment. The main impediment of its development is the insufficient selectivity of stimulation and the small number of applications in patients, which hinders assessment of any beneficial clinical outcome.

2.4.4 Hand disabilities - reaching and grasping

In tetraplegic and stroke patients, the most important target for achieving a high level of independence in active daily life is the restoration of the hand function. Thus, the main objective in applying FES in such patients is to improve the hand function by creating a reliable and long lasting power grasp, or a smooth pulp-pinch grasp that is needed to manipulate small objects. Neuroprostheses for grasping are used to restore or improve grasping function in tetraplegic and stroke subjects. The patients that would benefit most from such a neuroprosthesis would be C5-7 quadriplegics. The available neuroprostheses for grasping enable the restoration of the two most frequently used grasping styles, the palmar and the lateral grasp (Popovič et al., 2001b). The best known grasping neuroprostheses are the *Freehand* system (Scott et al., 1995), *Handmaster NMS* (Snoek et al., 2000), *Bionic Glove* (Prochazka et al., 1997), *NEC FESMate* system (Handa et al., 1992), *ETHZ-ParaCare* neuroprosthesis (Popovič et al., 2001b), the systems developed by Rebersek and Vodovnik (1973) and the *Belgrade Grasping System* (Popovič et al., 1998). A recent overview of these can be found in Popovič et al. (2002).

In 1997, FDA approved for clinical use the **Freehand** system (NeuroControl Corp., Cleveland, Ohio) for restoration of the hand grasp in quadriplegics. The research and development process took 25 years, mostly carried out by the researchers at the Case Western Reserve University, Ohio. The device consists of a stimulator and electrodes implanted in wrist and forearm muscles, a "joystick" controller implanted in the opposite shoulder, and an external processing unit (Scott et al., 1995). The joystick-like sensor placed on the chest relaxes and tightens the hand as the shoulder moves back and forth. A detailed description of the prosthesis can be found in Keith (2001). This prosthesis has been experimentally

implanted in more than 130 people. With training, most patients with this device can open and close their hand in two different grasping movements and lock the grasp in place by moving their shoulder in different ways. A recent small clinical study with 6 patients in Australia (Carroll et al., 2000) is a sign of increasing acceptance and application of the Freehand system outside USA. Researchers reported that, within the 30s test period, all subjects were able to grasp, move, and release more objects with the neuroprosthesis than without it. In 85% of the occasions, the six subjects expressed a preference for using the neuroprosthesis to perform these activities in daily living. Twelve months after rehabilitation, five of them still used the neuroprosthesis regularly. One of the main advantages of the *Freehand* system is that the time needed to put on and to take off the system is significantly shorter compared to most surface stimulation FES systems. On the other hand, the Freehand system can be applied only 18-24 months after the injury and is only suitable for SCI subjects and not for individuals suffering from stroke (Popovič et al., 2001b).

Bionic Glove is a hybrid system that utilizes a glove with FES electrodes. The detection of wrist extension stimulates finger flexion; therefore, the control of the device is directly related to the normal grasping sequence. Only patients who have sufficient wrist extension strength can use this type of device. The controls of the *Freehand* system and the *Handmaster* are not related to the normal movements included in the motor function, whereas the *Bionic Glove* uses mechanical sensors to detect wrist extension and the control is therefore directly coordinated by the grasping sequence. Reported as a part of a multicenter clinical trial, *Bionic Glove* could significantly improve independence in patients with C5-C7 spinal cord injury (Popovič et al., 1999).

Handmaster is an orthosis for grasping with three pairs of surface stimulation electrodes. This system can be used to generate a grasping function in tetraplegic and stroke patients. Originally, this system was envisioned as an exercise and rehabilitation tool, but it is also used as a permanent prosthetic system. One of the advantages of the *Handmaster* is that it is easy to put on and to take off. *Handmaster* is predominately used as an exercise tool for stroke subjects and is commercially available in a limited number of countries.

An interesting attempt is the **MeCFES** system (myoelectrical controlled functional electrical stimulator) where the residual myoelectric signals from the paretic wrist extensor (m. extensor carpi radialis) are used to control stimulation of either the wrist extension (i.e. the same muscle) or thumb flexion. Initial results of six spinal cord lesion patients and one stroke patient show improvement of the wrist extension (Thorsen et al., 2001).

With the exception of the *Freehand* and *NEC-FES* systems, all other neuroprostheses for grasping use surface stimulation. Only the *Freehand* and *Handmaster* systems are currently available on the market while the other neuroprostheses are produced in research laboratory environments.

All of the discussed neuroprostheses for grasping have demonstrated improvement of the grasping function in clinical trials including stroke or SCI subjects. These systems confirmed that, in principle, FES technology could facilitate comfortable and secure grasp. However, the grasp strategies that can be provided with the existing neuroprostheses for grasping are very limited and can only be used for a restricted set of grasping and holding tasks. In conclusion, it is too early to consider as a success any of the existing systems, including *Freehand* and

Handmaster, because of the small number of patients using the systems (about 150 for *Freehand* and a comparable amount for *Handmaster*).

2.4.5 Phrenic stimulation

Of those patients who sustain a high cervical spinal cord injury, a substantial number initially require some form of mechanical ventilation of their lungs. Most of them are able to breathe spontaneously with recovery, but 25% remain dependent upon some form of ventilation support for the remainder of their lives. Most of these injuries occur in young, otherwise healthy people, with a life expectancy of 20 years or more, assuming they have access to appropriate medical care. In patients with cervical lesions of the spinal cord, direct stimulation of the phrenic nerve can be applied for respiratory pacing. This is one of the earliest clinical applications of FES.

Diaphragm pacing is useful for conditions where the brain stem respiratory centers provide little or no activation of the respiratory muscles, such as central hypoventilation syndrome, Arnold-Chiari malformation/brain stem dysfunction, and high quadriplegia. Suitable patients are those with bilaterally intact phrenic nerve motor neuron pools in their cervical spinal cord. This can be checked by measuring the phrenic nerve conduction velocity and the diaphragm electromyogram (EMG). To do this, phrenic nerves are stimulated by needle or surface electrodes in the neck and EMG of the diaphragm is recorded from electrodes placed low on the chest at the front. The patient wears an external radio-frequency transmitter over an implanted receiver so that a stimulating current is induced without the need for any percutaneous wires. The introduction of phrenic nerve pacing more than three decades ago by Dr William Glenn and associates at Yale University has provided many ventilator-dependent tetraplegic patients with freedom from mechanical ventilation (Glenn et al., 1964; 1984; 1986). More than 1,200 phrenic nerve stimulator implantations have been performed throughout the world since 1968. Patients from several months of age to over 80 years of age have been successfully implanted and paced for long periods. Many patients have been successfully helped for more than 10 years; the longest period of pacing in a patient has been more than 20 years. In patients with ventilator-dependent quadriplegia, phrenic nerve pacing provides significant clinical advantages compared to mechanical ventilation. This technique, however, requires a thoracotomy with its associated risks and in-patient hospital stay and it carries some risk of phrenic nerve injury.

During the past decade, diaphragm pacing has also been attempted in small infants. The appropriate stimulation parameters are low stimulus frequency, short inspiration time and moderate respiratory rate. In a clinical trial in 33 pediatric patients, the mean time to failure was 56 months, which is acceptable for limited application of the pacemakers (Brouillette and Marzocchi, 1994). Among the benefits of the phrenic nerve pacing can be outlined: *increased mobility of the patients; improved speech; improved sense of well-being and reduced anxiety due to elimination of fear of ventilator disconnection; elimination of ventilator tubing and of ventilator noise; more physiological breathing and tracheostomy closure in some patients; and reduced incidence of respiratory tract infections.*

To recapitulate, one may consider the phrenic stimulator as a major improvement of the quality of life of the patient, which also reduces the overall costs for nursing.

2.5   Evidence based evaluation of the FES applications

2.5.1   Efficacy of FES after stroke

M<small>ETA</small> analysis showed that FES promotes recovery of muscle strength in post-stroke hemiparetic patients if included in rehabilitation. The study was based on the results of clinical trials dating between 1978 and 1992 (Glanz et al., 1996). There is, however, more evidence for improvement of the motor control of the upper extremity after stroke (de Kroon et al., 2002). The meta analysis was based on six randomized controlled trials on the therapeutic electrical stimulation on motor control and functional abilities. After stroke, up to 81% of the individuals develop shoulder subluxation, a condition frequently associated with poor upper limb function. FES on the shoulder muscles has been used in treatment of this condition. The results of seven (four early and three late) trials indicate that, when added to conventional therapy, FES is beneficial early after stroke for prevention of shoulder subluxation (Ada and Foongchomcheay, 2002). In a randomized controlled trial in subacute single stroke patients, Burridge et al. (1997) measured the effect of the Odstock Dropped Foot Stimulator as a supplement to physiotherapy. The results of 32 subjects showed increase in walking speed and beneficial Physiological Cost Index, if the stimulator had been used.

2.5.2   Efficacy of FES in urological conditions

Stimulation of the sacral spinal nerves, the sacral spinal roots, or the pelvic nerves can be used to restore bladder function in patients with voiding disorders. Several therapeutic techniques have become established in clinical urology as part of the therapy at increasing number of specialized centers. As part of the treatment of different kinds of lower urinary tract dysfunctions refractory to conservative treatment Tanagho and Schmidt introduced sacral nerve neuromodulation in the 1970s (Schmidt and Tanagho, 1979). Neuromodulation is now carried out by stimulation of the S3 sacral nerve. To do so, an electrode is placed in S3 foramen. The electrode has to be brought into the ventral side of the opening in front of the S3 ventral ramus. This procedure is minimally invasive, as compared to sacral neurostimulation. As part of an evaluation test, the patient is sent home with an external pulse generator for a few days. Responders are then implanted with a permanent implant in the sacral foramen and a pulse generator (Groen and Bosch, 2001). Since its early applications, neuromodulation has grown in popularity and the indications for this procedure are multiplying. Among them are now urge incontinence and sensory urgency, idiopathic chronic urinary retention, pelvic pain, and interstitial cystitis (Hassouna et al., 2000). Complications, in general, are minimal and included electrode migration, electrode failure and pain at the implantable pulse generator site (Bosch and Groen, 1995). The sacral neurostimulation approach proposed in the 1980s by Brindley et al. (1982) consists of intradural implantation of a so-called book electrode to stimulate S2-S3 ventral roots, combined with S2-S4 posterior rhizotomy. The primary purpose of the Brindley bladder stimulator is to improve bladder emptying, thereby eliminating urinary infection and preserving kidney function in suprasacral SCI patients. It also assists in defecation and enables male patients to have a sustained full erection. Nowadays, the Brindley bladder stimulator is being developed by the company Finetech in UK.

Detrusor sphincter dysynergia - The suprasacral SCI patients develop detrusor sphincter dyssinergia, which imposes serious health risks. The results from the first 500 patients implanted with the Brindley stimulator show usage in 424 after a mean follow up of 4 years (Brindley, 1994). Another study reported 38 patients with a complete spinal cord lesion (van der Aa et al., 1999). During the follow-up period ranging up to 12 years, all patients had increased bladder capacity and reduced residual urine volumes; 31 patients were continent; 29 males could achieve a sustained full erection; 27 patients used the implant for bowel function. The long-term favorable effects of the stimulator were also confirmed in follow-up studies on urodynamics (Kerrebroeck et al., 1997) and cost-effectiveness (Wielink et al., 1997) in 52 patients.

The Overactive Bladder comprises a spectrum of conditions ranging from urgency-frequency syndrome to urge incontinence. The incidence of the overactive bladder increases with age, with a prevalence ranging from 4% to 5.5% of the population. The efficacy of the neuromodulation therapy was evaluated in a prospective 12-center study in Europe, Canada, and the United States conducted from 1993 to 1999 with the *InterStim* system (Medtronic Inc., Minneapolis, Minnesota). The study enrolled 184 patients for urinary urge incontinence, 220 for urgency-frequency, and 177 for retention up to a total of 581 patients (Siegel et al., 2000).

Urge Incontinence and Sensory Instability - Neuromodulation is used in patients with urge incontinence and with therapy-resistant idiopathic detrusor instability where, in a follow-up trial, results showed clinically significant improvement of the quality of life (Hassouna et al., 2000). In patients with detrusor hyperactivity, implantable neuroprosthetic devices also lead to improvement in the urodynamic parameters (Bosch and Groen, 1998). Out of 20 patients with urge urinary incontinence, presented by Thon et al. (2003), 17 showed an improvement of more than 50% compared to the baseline, which persisted for more than one year of follow-up. Elabbady et al. (1994) presented their results in 9 patients with urgency frequency and/or urge incontinence: frequency improved by 73%, urgency by 42%, and incontinence by 50%. However, the number of patients is small to derive statistically valid conclusions for the success rate of the operation. On the other hand, the outcome of the multi-center trial is promising. Results demonstrate that after 3 years, 59% of 41 urinary urge incontinent patients showed greater than 50% reduction in leaking episodes per day and 46% of them became completely dry. After 2 years, 56% of the urgency-frequency patients showed greater than 50% reduction in voids per day (Siegel et al., 2000).

Idiopathic Non-Obstructive Chronic Urinary Retention was addressed in the multicenter trial (Jonas et al., 2001). A total of 177 patients with urinary retention refractory to standard therapy were enrolled in the study. Compared to the control group, patients implanted with the *InterStim* system had statistically and clinically significant reductions in the catheter volume per catheterization. Successful results were achieved in 83% of the implant group with retention compared to 9% of the control group at 6 months. Temporary inactivation of sacral nerve stimulation therapy resulted in a significant increase in residual volumes but effectiveness of sacral nerve stimulation was sustained through 18 months after implantation. In another study, Thon et al. (2003) reported that, from 33 patients with chronic urinary retention implanted permanently with neuroprosthesis, 23

showed a long-lasting significant improvement but in the remaining 10 the improvement did not reach 50% compared to baseline. In 7 patients with chronic retention, Vapnek and Schmidt (2003) reported success in 5 cases and Elabbady et al. (1994) - in 8 of 8 cases. Results of the presented studies demonstrate that sacral nerve stimulation is effective for restoring voiding in patients with retention who are refractory to other forms of treatment.

Pelvic pain and discomfort are very common symptoms associated with other storage or voiding dysfunctions. In the available literature on sacral root neuromodulation, associated pelvic pain has improved from 85% to 90% when postimplant status was compared to baseline (Bosch and Groen, 1995; Thon et al., 2003).

In conclusion, the correlation between the clinical outcome and the urodynamic test results is poor. The results of the presented studies on neuromodulation show that 40% of the selected patients do not qualify for the procedure and the effect of treatment is not enduring: voiding dysfunctions return as soon as the neuroprosthesis is switched off. It is considered that the effect is based on antidromic stimulation of the inhibitory neurons in the spinal cord. However, because the used stimulators are voltage-controlled and the amount of injected current into the tissue is unknown, both the type of fibers which are stimulated (i.e. myelinated or non-myelinated) and the direction of stimulation (i.e. ortho- or antidromic) are not known. Therefore, additional basic and clinical research needs to be performed before this treatment can be introduced as a routine procedure in patients with serious voiding dysfunction refractory to conservative measures (Marani, 2002).

2.6   Experimental and theoretical research

2.6.1   Visual prostheses

Blindness can result when any step of the optical pathway - the optics, the retina, the optic nerve, visual cortex, or other cortical areas involved in the processing of vision - sustains damage. Public discussion of the effects of electricity on vision dates back to 1751, when it was addressed by Benjamin Franklin following his celebrated kite-and-key experiment. Despite some advocacies then, the idea of treating blindness by electrical stimulation did not catch on.

In Germany, 17,000 patients become blind every year for whom there is no effective treatment or cure (Moe and Post, 1962). In the last 30 years, extensive experimental research for development of visual prostheses has been performed. In 1967-68, the experiments of Brindley and Lewin showed the feasibility of the long-term interface with the visual system. The approach of the cortical prostheses has its foundations in the observations of the visuotopic organization of electrically evoked phosphenes in the occipital cortex. This led a number of investigators to propose that electrical stimulation of visual cortex via arrays of electrodes might provide the profoundly blind with a limited form of functional vision. Several groups investigated the stimulation with cortical prostheses - the cortical surface electrodes of Brindley and Lewin (1968) and Dobelle and Mladejovsky (1974); the cortical penetrating electrodes of Bartlett and Doty (1980), and the electrodes of Schmidt et al. (1996). Influential as it is, so far, this idea has very little practical progress. Neurons in the visual cortex recognize textures, depth (displacements), angles, and the brightness /color of the object. The perception of images is not based on pixelation; therefore, all of the bitmap-based stimulation approaches are

doomed to fail. On the other hand, the cortical stimulation approach may provide the only therapeutic option for individuals with non-functional retinas and/or optic nerves. Recently, Dobelle (2000) reported for the development of a visual prosthesis providing a sort of "artificial vision"to a blind volunteer by connecting a digital video camera, computer, and associated electronics to the visual cortex of his brain. As an alternative to the cortical stimulation, two other approaches have also been investigated.

The idea to make a *visual prosthesis stimulating the optic nerve* was conceived by Veraart and Mortimer in the beginning of the 1990s. The first implantation was carried out in 1998 and the patient was able to perceive phosphenes. Nevertheless, high spatial resolution cannot be expected with such a stimulation arrangement (Veraart et al., 1998). Although ingenious, so far, the approach does not take into account the information processing steps taking places in the retinal ganglionic cells. However, it still may offer some promise if thousands of intraneural electrodes as part of an electrode array are implanted in the optic nerve to provide better selectivity of stimulation.

In the end of the 1980s, an entirely new approach was undertaken by the teams of M. Humayun (John Hopkins University) (Schmidt et al., 1996) and that of J. Rizzo (Harvard University) (Rizzo et al., 2003) in association with the Massachusetts Institute of Technology. They developed an implantable electrode array for the retina itself, a *retinal implant*, in order to stimulate the retinal ganglionic cells (Grumet et al., 2000), which axons form the optic nerve. This prosthesis is referred to as *epiretinal implant*. Another kind of retinal implant is the *subretinal implant* developed by Chow and Chow (1997) in Chicago and Zrenner et al. (1997) in Tübingen. Both teams have stimulated retinas of blind patients with epiretinal electrodes that were transiently inserted into the eye through a scleral opening. Although both groups reported for sensations of light patterns by the patients (Weiland et al., 1999; Rizzo et al., 2003), perception of geometric patterns was reported in only few instances. Recently a permanent implantation has been made in a blind volunteer (Humayun et al., 2003).

To summarize, results in the field in the past 30 years are still far from true object recognition. However, they do demonstrate the feasibility of generating perception of light patterns in blind people.

2.6.2   Spinal Cord stimulation after SCI

Apart from the pain suppression of chronic intractable pain, peripheral vascular disease, and angina pectoris, spinal cord stimulation has been employed in motor disorders for control of spasticity in SCI patients. Attempts in this direction have been carried out for the first time by Richardson et al. (1979). Recently, Pinter et al. (2000) stimulated the L2-L3 dorsal roots of the spinal cord in SCI patients. Results demonstrated reduction of the muscle hypertonia of the lower extremities. A possible future application of SCS is to contribute to the restoration of the motor functions of the lower extremity (Barbeau et al., 1999; Kargo and Giszter, 2000). There is accumulating evidence for the existence of a Central Pattern Generator (CPG) of locomotion in both primates and men (Dimitrijevič et al., 1998). Therefore, if one is able to control the CPG in the motor spinal cord many of the selectivity problems pointed out so far would be circumvented. This requires a Multi Electrode Array to be placed in the spinal cord such that it is able to stimulate the musculotopically-organized motor neuronal pools of the lower limbs.

2.7 Modeling studies on selectivity

As part of the design of different types of electrodes for stimulation, a substantial amount of theoretical and experimental research on selectivity has been performed. The electrical behavior of the myelinated nerve fiber can be represented by a simple cable network (Fig. 2.3). The first to introduce this model for the mammalian nerve fiber was McNeal (1976) in order to calculate how a stimulation-induced extracellular field affects nodal transmembrane voltages. All of the research commented in the subsequent sections is based on the McNeal model.

2.7.1 Research on spatially-selective nerve stimulation

The feasibility of selective activation of peripheral nerve fascicles was demonstrated by McNeal and Bowman (1985), who found that with proper fit and positioning a single circumneural sleeve with multiple electrode contacts could control selectively the activation of two antagonist muscle groups innervated by a common nerve trunk. In their study, Sweeney et al. (1990) performed numerical modeling and experimental testing of a nerve cuff technique for selective stimulation of superficial peripheral nerve trunk regions. Two basic electrode configurations ("snug" cuff monopolar and tripolar longitudinally aligned dots) were considered. Both modeling and experimentation suggested that longitudinally aligned tripolar dot electrodes on the surface of a nerve trunk would restrict excitation to superficial nerve trunk regions more successfully than monopolar dot electrodes would do. Transverse anodal "steering" improved the spatial selectivity of both monopolar and tripolar electrode configurations (Sweeney et al., 1990).

With a sufficient number of electrodes within a cuff electrode, high selectivity of stimulation could be achieved by either longitudinal or transversal currents produced using appropriately switched electrodes (Veraart et al., 1993). Goodall et al. (1996) found that transverse current from an anode positioned opposite the stimulating cathode improved spatial selectivity and position selectivity was enhanced when the ratio of transverse current to longitudinal current was increased. Based on computer modeling, Deurloo and Holsheimer (2003) concluded that transverse steering provides more selective stimulation than longitudinal steering. Selectivity was dependent on the relative location of the electrode contacts and the nerve fascicles, as well as on the size and the relative spacing of neighboring fascicles (Grill and Mortimer, 1996).

Deurloo et al. (1998) performed theoretical research on how to improve the selectivity of multi-contact cuff electrodes obtained during stimulation of peripheral nerves. As the combination of controlled fiber size and spatial selectivity was hard to achieve, the focus was set primarily on spatial selectivity. They found that the transverse tripole was the only configuration that maximized selectivity for a small cylindrical bundle of fibers in the periphery of a monofascicular nerve trunk (Fig. 2.7). Inverse recruitment was less pronounced than that for the other configurations. They recommended transverse tripolar stimulation since it did not change the shape of the recruitment contours despite the lowering of the excitation threshold, which might occur in chronic implantation fibrosis on the implantation site. However, in acute animal experiments, where the recruitment characteristics of muscle selective nerve stimulation by a multi-contact nerve cuff electrode was studied, the results showed that only in few cases transverse bi- and tripolar stimulation provided a better selectivity than monopolar stimulation (Deurloo et al., 2000). In accordance with the results of the modeling studies, bi- and tripolar stimulation required higher stimulus currents than monopolar stimulation, whereas maximum recruitment and slopes of recruitment curves were lower. Due to the variability in the num-
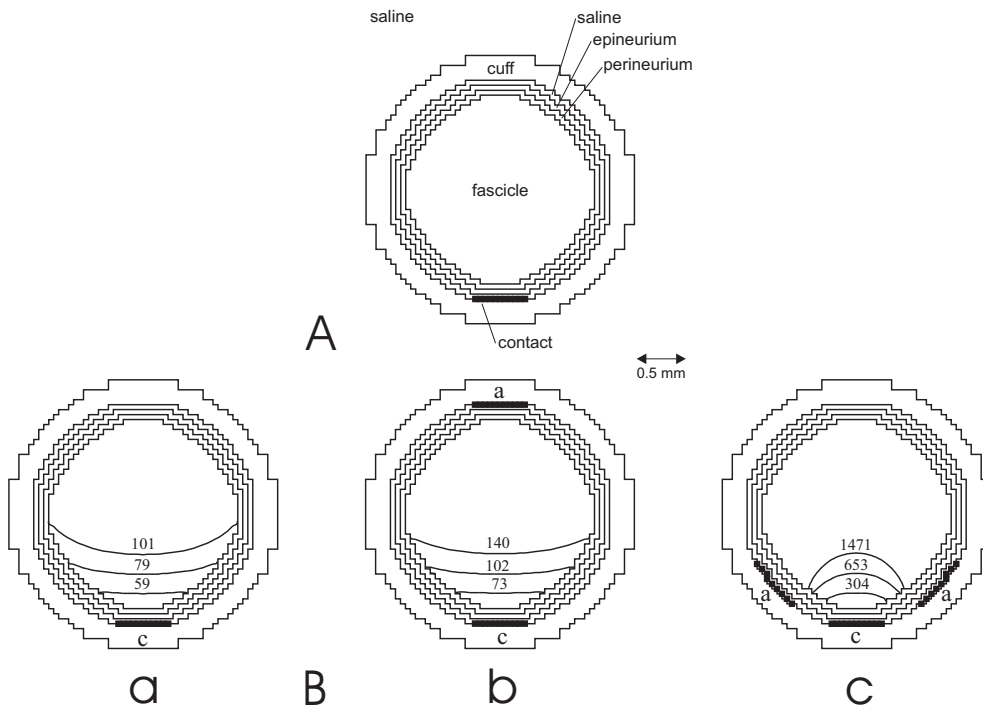
Figure 2.7: Modeling of selectivity in stimulation by cuff electrodes

A - Transverse section of the 3D volume conductor model of a monofascicular nerve surrounded by an insulating cuff with an electrode contact on its inner surface. B - Recruitment contours showing excitation regions in the nerve trunk; c - cathode, a - anode. Subfigures: **a**: central cathode **b**: longitudinal tripole + additional anode **c**: transverse tripole. Courtesy: K Deurloo, from (Deurloo, 1999, A p. 15 and B p. 30)

ber and size of the fascicles and their position in this nerve sufficient reproducibility for the selectivity could not be obtained.

The theoretical research performed by Rutten et al. (1991) and Yoshida and Horch (1993) suggested that intraneural electrodes should give better spatial selectivity than cuff electrodes. In this line of reasoning, Rutten et al. (1999) argued that the best way to control individual fibers would be to stimulate in close proximity of the nodes of Ranvier, which implied use of intrafascicular electrodes. However, the random distribution of the nodes of Ranvier along the myelinated nerve fibers makes the stimulation a probabilistic process. The experimental studies show that, despite the theoretical expectations, when the topography of the motor nerve fibers is unknown, the implanted intraneural electrode may simply miss the target fiber population. Several attempts for such stimulation have been made so far with 1D arrays. The obtained information gave insight on how to improve the design (the shape and the distance between the electrodes) of the later on produced 3D arrays. In acute nerve implantation experiments, 5- to 24-wire-MEAs were used in order to investigate whether the electrodes could selectively stimulate single motor units. The results revealed partial blocking of neural conduction, similar to

that reported with microneurographic insertion of single needle electrodes (Smit et al., 1999). The arrays were capable of evoking threshold forces selectively with an average efficiency of 81%. Frieswijk et al. (1998) performed animal experiments and model simulations of monopolar intrafascicular nerve stimulation in order to study muscle recruitment (i.e. force-current relationships). They found that the conductivity of the extraneural medium was of prime importance for the shape of the resulting recruitment curves: an insulating extraneural medium generally lead to steeper curves with lower threshold currents than a well-conducting extraneural medium. Statistical comparison between the experimental and the modeling results suggested possible clustering of the motor fibers innervating the *extensor digitorum longus* muscle within the peroneal nerve.

In conclusion, the insufficient neuroanatomical knowledge of the spatial organization and topography of fibers in the peripheral nerve hampers the definitive choice for the type and the design of electrodes for functional stimulation.

2.7.2   Research on fiber size selective stimulation

In myelinated axons, there is a positive correlation between the internodal distance and the axonal diameter (Rushton, 1951). Thus, the large fibers (A, B) have nodes further apart than the small fibers. As a result, in an electric field the larger fibers have a larger potential difference between adjacent nodes. This leads to a lower threshold of the large fibers in comparison with the small ones. Therefore, during stimulation, the large myelinated fibers fire first. Unfortunately, this is the reverse to the natural order of recruitment, and it results in fast development of muscle fatigue. By activating/blocking stimuli delivered by multiple cuff electrodes the order of recruitment can be reversed (Zhou et al., 1987). Better fiber size selectivity can be achieved by intraneural stimulation, as outlined by Rutten et al. (1999). The order in which the nerve fibers in a peripheral nerve or a spinal root are excited by a stimulus pulse is predominantly related to both the fiber diameter and the distance between the fiber and the cathode (Feirabend et al., 2002). In the conducting media around the electrode, the current density is inversely proportional to 2nd- 3rd power of the distance. Accordingly, the threshold current is increased at the same rate as shown empirically (Ranck, 1975). In clinical applications, due to the generally limited amplitude range, only the large fibers will be recruited. For example in spinal cord stimulation, the maximal therapeutic amplitude should not exceed 170% of the paresthesia threshold perception. Calculations show that the nerve fibers smaller than 9 µm in diameter will not be recruited. Another relevant aspect of the recruitable large fibers is their density within the fascicle (Feirabend et al., 2002).

Fang and Mortimer (1991a;b) studied selective activation of small fibers without activating larger fibers in the same nerve trunk. In the proposed nerve stimulation system, quasi-trapezoidal shaped current pulses were delivered through a tripolar cuff electrode to effect differential block by membrane hyperpolarization. The quasi-trapezoidal shaped pulses with a square leading edge, a 350 µs plateau, and an exponential trailing phase ensured the block of propagating action potentials and prevented the occurrence of anodal break excitation. The tripolar cuff electrode restricted current flow inside the cuff and, thus, eliminated the undesired nerve stimulation due to the *virtual cathode* effect. Subsequent animal experiments confirmed that large Aα motor axons could be blocked at lower current levels than smaller Aα motor axons,

Aα fibers could be blocked at lower current levels than Aγ fibers, and the blocking threshold correlated with the fiber diameter (Fang and Mortimer, 1991b). For the same purpose, van Bolhuis et al. (2001) suggested the use of two pulse generators independently supplying short supramaximal cathodal stimulating pulses (0.5 ms) and long subthreshold cathodal inactivating pulses (1.5 s). Results showed that propagation of action potentials was blocked size-selectively by adjusting the strength of the inactivating current. It was shown that cathodal pre-pulses inversed the recruitment order (Grill and Mortimer, 1997; Deurloo et al., 2001). Grill and Mortimer (1997) demonstrated that subthreshold membrane depolarization generated a transient decrease in neural excitability and, thus, an increase in the threshold for stimulation by a subsequent stimulus pulse. When a depolarizing stimulus pulse was applied immediately after the subthreshold depolarization nerve fibers far from the electrode could be stimulated without stimulating fibers close to the electrode. Thus, subthreshold depolarizing pre-pulses allowed selective stimulation of nerve fibers far from the electrode. In a realistic model of a nerve surrounded by a cuff electrode, Deurloo et al. (2001) showed that it is also possible to stimulate small fibers without exciting large ones. The applied model requires that, in the case of monopolar stimulation with a cuff electrode, the cuff length should not exceed twice the internodal distance of the fibers to be blocked. Similarly, the distance between cathode and anodes should not exceed the internodal distance of these fibers when tripolar stimulation is used (Deurloo et al., 2001).

2.8 Conclusions

PRincipal requirements to any substituting structure are features mimicking some of the biological functions of nerves and replacing these functions depending on the scope of implantation. Profound knowledge about the development, functional and structural organization of the nervous system is a prerequisite for any attempt to establish meaningful recording or stimulation in order to substitute for a given function or modality. A number of proposed ideas for electronic implants are based, however, on a more "engineer-like" way of thinking rather than considering the complexity of the biological systems. The necessary for engineering development reductionistic approach often substitutes basic problems for secondary ones. For example, the concept of spatial selectivity in stimulation is often substituted for fascicle selectivity, which equalizes the fiber representation of a particular muscle contraction (dynamic view) to a coincidentally delimited anatomical region along the course of a nerve (static view).

During the last 50 years, a substantial amount of basic and applied research was performed in the field of FES, which led to successful development of the cardiac and the phrenic pacemakers, and the cochlear prostheses. Nevertheless, a number of fundamental scientific problems still remain to be solved before one sees a comparable degree of effectiveness and penetration in common medical practice for the locomotion neuroprostheses and urological FES appliances. Although FES of locomotion gains clinical acceptance, it is still in its experimental phase of development due to several interrelated but different issues, such as: *effectiveness and reliability of the devices; available technical support; the place of the devices in the complex treatments of stroke, SCI, multiple sclerosis etc.*

Despite the significant technical progress achieved in the last 10 - 15 years in the FES field, there is a consensus that these systems are not sufficiently advanced and that they need further development. Complexity of human motion greatly diminishes the area of the animal experi-

mentation in the field and puts the stress on computer modeling. This complexity, however, makes the leap from a model to a patient even more difficult than from an animal model to human, and is reflected in the performance of many implantable FES systems. The leap has only been done in a limited number of cases, which in turn diminishes the validity of the obtained results and leads to case descriptions rather than generalizations. This in turn increases the interval between trial and error (the most prominent approach in experimentation) and as a result slows down the research and development process for new applications. Nevertheless, present FES treatments combined with conventional occupational and physical therapy still remain the most promising approach in rehabilitating SCI patients and stroke patients. The need of training, which is seen by some as a shortcoming of FES (Popovič et al., 2001a), in our opinion may be turned into advantage if it is integrated in the overall treatment and rehabilitation process.

The mechanism of action of electrical neuromodulation is still poorly understood, which leaves it in a rather empirical state of operation. Until now, hundreds of patients have been successfullyt reated using the Brindley approach for bladder voiding disorders. However, the required posterior rhizotomy is a rather crude approach towards blocking the spinal reflexes. Nevertheless, FES is effective in improving the bladder function in the overactive bladder states and in SCI patients it gives long-term favorable results, which makes it a viable therapeutical option for the indicated groups of patients. The research performed in the field of the visual prostheses showed the complexity of the information processing by the (human) visual system. Even the modest goals of the projects so far are ambitious compared to the information content of the reported visual phenomena. We would like to finish with a quotation from Dobelle (2000), which applies in the end to any prosthetic treatment:

> *Development of implanted medical devices such as this artificial vision system progresses in three stages. First there is speculation, then there is hope, and finally there is promise.*

Bibliography

AAMI (1984) American National Standard for Implantable Peripheral Nerve Stimulators ANSI/AAMI NS15-1984. Association for the Advancement of Medical Instrumentation.

Ada, L. and A. Foongchomcheay (2002) Efficacy of electrical stimulation in preventing or reducing subluxation of the shoulder after stroke: a meta-analysis. Aust. J. Physiother. *48*:257–267.

Agnew, W. F. and D. B. McCreery (eds.) (1990) Neural Prostheses: Fundamental Studies. Prentice Hall Advanced Reference Series. Englewood Cliffs: Prentice Hall.

Agnew, W. F., D. B. McCreery, L. Bullara, and T. G. Yuen (1990) Effects of prolonged electrical stimulation of peripheral nerve. In W. F. Agnew and D. B. McCreery (eds.), *Neural Prostheses: Fundamental Studies*, Englewood Cliffs: Prentice Hall, chap. 9, pp. 147–168.

Agnew, W. F., D. B. McCreery, T. G. Yuen, and L. A. Bullara (1989) Histologic and physiologic evaluation of electrically stimulated peripheral nerve: Considerations for the selection of parameters. Ann. Biomed. Eng. *17*:39–60.

Agnew, W. F., D. B. McCreery, T. G. Yuen, and L. A. Bullara (1993) MK-801 protects against neuronal injury induced by electrical stimulation. Neuroscience *52*:45–53.

Agnew, W. F., D. B. McCreery, T. G. Yuen, and L. A. Bullara (1999) Evolution and resolution of stimulation-induced axonal injury in peripheral nerve. Muscle Nerve *22*:1393–1402.

Bajd, T., A. Kralj, R. Turk, H. Benko, and J. Sega (1983) The use of a four-channel electrical stimulator as an ambulatory aid for paraplegic patients. Phys. Ther. *63*:1116–1120.

Barbeau, H., D. A. McCrea, M. J. O'Donovan, S. Rossignol, W. M. Grill, and M. A. Lemay (1999) Tapping into spinal circuits to restore motor function. Brain Res. Rev. *30*:27–51.

Bartlett, J. R. and R. W. Doty (1980) An exploration of the ability of macaques to detect microstimulation of striate cortex. Acta Neurobiol. Exp. (Wars.) *40*:713–727.

BeMent, S. L., K. D. Wise, D. J. Anderson, K. Najafi, and K. L. Drake (1986) Solid-state electrodes for multichannel multiplexed intracortical neuronal recording. IEEE Trans. Biomed. Eng. *33*:230–241.

Bhadra, N. and P. H. Peckham (1997) Peripheral nerve stimulation for restoration of motor function. J. Clin. Neurophysiol. *14*:378–393.

Blair, E. A. and J. Erlanger (1933) A comparison of the characteristics of axons through their individual electrical responces. Am.J.Physiol. *106*:524–564.

Bollen, L. S. and O. Svendsen (1997) Regulatory guidelines for biocompatibility safety testing. Medical Plastics and Biomaterials pp. 1–16.

Bosch, J. L. and J. Groen (1995) Sacral (S3) segmental nerve stimulation as a treatment for urge incontinence in patients with detrusor instability: Results of chronic electrical stimulation using an implantable neural prosthesis. J. Urol. *154*:504–507.

Bosch, J. L. and J. Groen (1998) Neuromodulation: Urodynamic effects of sacral (S3) spinal nerve stimulation in patients with detrusor instability or detrusor hyperflexia. Behav. Brain Res. *92*:141–150.

Bowman, B. R. and R. C. Erickson (1985) Acute and chronic implantation of coiled wire intraneural electrodes during cyclical electrical stimulation. Ann. Biomed. Eng. *13*:75–93.

Branner, A. and R. A. Normann (2000) A multielectrode array for intrafascicular recording and stimulation in sciatic nerve of cats. Brain Res. Bull. *51*:293–306.

Brindley, G. S. (1994) The first 500 patients with sacral anterior root stimulator implants: General description. Paraplegia *32*:795–805.

Brindley, G. S. and W. S. Lewin (1968) The visual sensations produced by electrical stimulation of the medial occipital cortex. J. Physiol. (Lond) *194*:54–5P.

Brindley, G. S., C. E. Polkey, and D. N. Rushton (1979) Electrical splinting of the knee in paraplegia. Paraplegia *16*:428–437.

Brindley, G. S., C. E. Polkey, and D. N. Rushton (1982) Sacral anterior root stimulators for bladder control in paraplegia. Paraplegia *20*:365–381.

Brouillette, R. T. and M. Marzocchi (1994) Diaphragm pacing: Clinical and experimental results. Biol. Neonate *65*:265–271.

Brummer, S. B. and M. Turner (1972) Electrochemical aspects of neuromuscular stimulation. Tech. rep., National Academy of Sciences, Washington, DC.

Burridge, J. H., P. N. Taylor, S. A. Hagan, D. E. Wood, and I. D. Swain (1997) The effects of common peroneal stimulation on the effort and speed of walking: a randomized controlled trial with chronic hemiplegic patients. Clin. Rehabil. *11*:201–210.

Cameron, T., G. E. Loeb, R. A. Peck, J. H. Schulman, P. Strojnik, and P. R. Troyk (1997) Micromodular implants to provide electrical stimulation of paralyzed muscles and limbs. IEEE Trans. Biomed. Eng. *44*:781–790.

Carroll, S., C. Cooper, D. Brown, G. Sormann, S. Flood, and M. Denison (2000) Australian experience with the freehand system for restoring grasp in quadriplegia. Aust. N. Z. J. Surg *70*:563–568.

Chardack, W. M., A. A. Gage, and W. Greatbatch (1961) Experimental observations and clinical experiences with the correction of complete heart block by an implantable, self-contained pacemaker. Trans. Am. Soc. Artif. Intern. Organs *7*:286–295.

Chow, A. Y. and V. Y. Chow (1997) Subretinal electrical stimulation of the rabbit retina. Neurosci. Lett. *225*:13–16.

de Kroon, J. R., J. H. van der Lee, M. J. IJzerman, and G. J. Lankhorst (2002) Therapeutic electrical stimulation to improve motor control and functional abilities of the upper extremity after stroke: A systematic review. Clin. Rehabil. *16*:350–360.

Deurloo, K. (1999) Selectivity in extraneural stimulation of peripheral nerves. Ph.D. thesis, Twente University.

Deurloo, K. and J. Holsheimer (2003) Fascicular selectivity in transverse stimulation with a nerve cuff electrode: A theoretical approach. Neuromodulation *6*:258–269.

Deurloo, K. E., J. Holsheimer, and P. Bergveld (2000) Nerve stimulation with a multi-contact cuff electrode: Validation of model predictions. Arch. Physiol. Biochem. *108*:349–359.

Deurloo, K. E., J. Holsheimer, and P. Bergveld (2001) The effect of subthreshold prepulses on the recruitment order in a nerve trunk analyzed in a simple and a realistic volume conductor model. Biol. Cybern. *85*:281–291.

Deurloo, K. E., J. Holsheimer, and H. B. Boom (1998) Transverse tripolar stimulation of peripheral nerve: A modelling study of spatial selectivity. Med. Biol. Eng. Comput. *36*:66–74.

Dimitrijevič, M. R., Y. Gerasimenko, and M. M. Pinter (1998) Evidence for a spinal central pattern generator in humans. Ann. N. Y. Acad. Sci. *860*:360–376.

Djourno, A. and C. Eyries (1957) Prothese auditive par excitation electrique a distance du nerf sensoriel a l'aide d'un bodinage inclus a demeure. Presse Med. *35*:14–17.

Dobelle, W. H. (2000) Artificial vision for the blind by connecting a television camera to the visual cortex. ASAIO J. *46*:3–9.

Dobelle, W. H. and M. G. Mladejovsky (1974) Phosphenes produced by electrical stimulation of human occipital cortex, and their application to the development of a prosthesis for the blind. J. Physiol. (Lond) *243*:553–576.

Donaldson, N. D., T. A. Perkins, and A. C. Worley (1997) Lumbar root stimulation for restoring leg function: Stimulator and measurement of muscle actions. Artif. Organs *21*:247–249.

Dutrochet, R. J. H. (1824) Recherches Anatomiques Et Physiologiques Sur La Structure Intime Des Animaux Et Vegétax Et Sur Leur Mobilité. Paris: Bailliére.

Elabbady, A. A., M. M. Hassouna, and M. M. Elhilali (1994) Neural stimulation for chronic voiding dysfunctions. J. Urol. *152*:2076–2080.

Fang, Z. P. and J. T. Mortimer (1991a) A method to effect physiological recruitment order in electrically activated muscle. IEEE Trans. Biomed. Eng. *38*:175–179.

Fang, Z. P. and J. T. Mortimer (1991b) Selective activation of small motor axons by quasi-trapezoidal current pulses. IEEE Trans. Biomed. Eng. *38*:168–174.

Feirabend, H. K., H. Choufoer, S. Ploeger, J. Holsheimer, and J. D. van Gool (2002) Morphometry of human superficial dorsal and dorsolateral column fibres: Significance to spinal cord stimulation. Brain *125*:1137–1149.

Foerster, O. (1929) Beitrage zur pathophysiologie der sehbahn und der sehsphare. J. Psychol. Neurol. (Lpz) *39*:463–485.

Frankenhaeuser, B. and A. F. Huxley (1964) The action potential in the myelinated nerve fiber of xenopus laevis as computed on the basis of voltage clamp data. J. Physiol. (Lond) *171*:302–315.

Fried, K., J. Frisen, and M. Mozart (1989) De- and regeneration of axons after minor lesions in the rat sciatic nerve. Effects of microneurography electrode penetrations. Pain *36*:93–102.

Frieswijk, T. A., J. P. Smit, W. L. Rutten, and H. B. Boom (1998) Force-current relationships in intraneural stimulation: Role of extraneural medium and motor fibre clustering. Med. Biol. Eng. Comput. *36*:422–430.

Gersuni, G. and A. Volokhov (1937) On the effect of alternating currents on the cochlea. J. Physiol. (Lond). *89*:113–121.

Girsch, W., R. Koller, H. Gruber, J. Holle, C. Liegl, U. Losert, W. Mayr, and H. Thoma (1991) Histological assessment of nerve lesions caused by epineurial electrode application in rat sciatic nerve. J. Neurosurg. *74*:636–642.

Glanz, M., S. Klawansky, W. Stason, C. Berkey, and T. C. Chalmers (1996) Functional electrostimulation in poststroke rehabilitation: a meta-analysis of the randomized controlled trials. Arch. Phys. Med. Rehabil. *77*:549–553.

Glenn, W. W., J. H. Hageman, A. Mauro, L. Eisenberg, S. Flanagan, and B. M. Harvard (1964) Electrical stimulation of excitable tissue by radiofrequency transmission. Ann. Surg. *160*:338–350.

Glenn, W. W., J. F. Hogan, J. S. Loke, T. E. Ciesielski, M. L. Phelps, and R. Rowedder (1984) Ventilatory support by pacing of the conditioned diaphragm in quadriplegia. N. Engl. J. Med. *310*:1150–1155.

Glenn, W. W., M. L. Phelps, J. A. Elefteriades, B. Dentz, and J. F. Hogan (1986) Twenty years of experience in phrenic nerve stimulation to pace the diaphragm. Pacing Clin. Electrophysiol. *9*:780–784.

Gold, G. R. (1984) Cardiac pacing-from then to now. Medical Intsrumentation *18*:15–21.

Goodall, E. V., J. F. de Breij, and J. Holsheimer (1996) Position-selective activation of peripheral nerve fibers with a cuff electrode. IEEE Trans. Biomed. Eng. *43*:851–856.

Graupe, D., R. Davis, H. Kordylewski, and K. H. Kohn (1998) Ambulation by traumatic T4-12 paraplegics using functional neuromuscular stimulation. Crit. Rev. Neurosurg. *8*:221–231.

Greatbatch, W. (1991) Origins of the implantable cardiac pacemaker. J. Cardiovasc. Nurs. *5*:80–85.

Grill, W. M. and J. T. Mortimer (1994) Electrical properties of implant encapsulation tissue. Ann. Biomed. Eng. *22*:23–33.

Grill, W. M. and J. T. Mortimer (1996) Quantification of recruitment properties of multiple contact cuff electrodes. IEEE Trans. Rehabil. Eng. *4*:49–62.

Grill, W. M. and J. T. Mortimer (1997) Inversion of the current-distance relationship by transient depolarization. IEEE Trans. Biomed. Eng. *44*:1–9.

Grill, W. M. and J. T. Mortimer (2000) Neural and connective tissue response to long-term implantation of multiple contact nerve cuff electrodes. J. Biomed. Mater. Res. *50*:215–226.

Groen, J. and J. L. Bosch (2001) Neuromodulation techniques in the treatment of the overactive bladder. BJU. Int. *87*:723–731.

Grumet, A. E., J. J. L. Wyatt, and I. J. F. Rizzo (2000) Multi-electrode stimulation and recording in the isolated retina. J. Neurosci. Methods *101*:31–42.

Hallin, R. G., Z. Wiesenfeld-Hallin, and R. Duranti (1986) Percutaneous microneurography in man does not cause pressure block of almost all axons in the impaled nerve fascicle. Neurosci. Lett. *68*:356–361.

Hambrecht, F. T. (1990) The history of neural stimulation and its relevance to future neural prostheses. In W. F. Agnew and D. B. McCreery (eds.), *Neural Prostheses: Fundamental Studies*, Englewood Cliffs: Prentice Hall, chap. 1, pp. 1–25.

Handa, Y., T. Handa, M. Ichie, H. Murakami, N. Hoshimiya, S. Ishikawa, and K. Ohkubo (1992) Functional Electrical Stimulation (FES) systems for restoration of motor function of paralyzed muscles–versatile systems and a portable system. Front Med. Biol. Eng. *4*:241–255.

Hassouna, M. M., S. W. Siegel, A. A. Nyeholt, M. M. Elhilali, P. E. van Kerrebroeck, A. K. Das, J. B. Gajewski, R. A. Janknegt, D. A. Rivas, H. Dijkema, D. F. Milam, K. A. Oleson, and R. A. Schmidt (2000) Sacral neuromodulation in the treatment of urgency-frequency symptoms: a multicenter study on efficacy and safety. J. Urol. *163*:1849–1854.

Heiduschka, P. and S. Thanos (1998) Implantable bioelectric interfaces for lost nerve functions. Prog. Neurobiol. *55*:433–461.

Hodkin, A. L. and A. F. Huxley (1952) A quantitative description of membrane current and its application to conduction and excitation in nerve. J. Physiol. (Lond) *117*:500–544.

Humayun, M. S., J. D. Weiland, G. Y. Fujii, R. Greenberg, R. Williamson, J. Little, B. Mech, V. Cimmarusti, G. V. Boemel, G. Dagnelie, and E. de Juan (2003) Visual perception in a blind subject with a chronic microelectronic retinal prosthesis. Vision Res. *43*:2573–2581.

Hursh, J. B. (1939) Conduction velocity and diameter of nerve fibers. Am.J. Physiol. *127*:131–139.

Illing, R. B. (2001) Activity-dependent plasticity in the adult auditory brainstem. Audiol. Neurootol. *6*:319–345.

Illing, R. B., S. A. Michler, K. S. Kraus, and R. Laszig (2002) Transcription factor modulation and expression in the rat auditory brainstem following electrical intracochlear stimulation. Exp. Neurol. *175*:226–244.

Jonas, U., C. J. Fowler, M. B. Chancellor, M. M. Elhilali, M. Fall, J. B. Gajewski, V. Grunewald, M. M. Hassouna, U. Hombergh, R. Janknegt, P. E. van Kerrebroeck, A. A. Nijeholt, S. W. Siegel, and R. A. Schmidt (2001) Efficacy of sacral nerve stimulation for urinary retention: Results 18 months after implantation. J. Urol. *165*:15–19.

Kargo, W. J. and S. F. Giszter (2000) Rapid correction of aimed movements by summation of force-field primitives. J. Neurosci. *20*:409–426.

Keith, M. W. (2001) Neuroprostheses for the upper extremity. Microsurgery *21*:256–263.

Kenney, L., G. Bultstra, R. Buschman, P. Taylor, G. Mann, H. Hermens, J. Holsheimer, A. Nene, M. Tenniglo, H. van der Aa, and J. Hobby (2002) An implantable two channel drop foot stimulator: Initial clinical results. Artif. Organs *26*:267–270.

Kerrebroeck, E. V. V., H. E. van der Aa, J. L. Bosch, E. L. Koldewijn, J. H. Vorsteveld, and F. M. Debruyne (1997) Sacral rhizotomies and electrical bladder stimulation in spinal cord injury. Part I: Clinical and urodynamic analysis. Dutch study group on sacral anterior root stimulation. Eur. Urol *31*:263–271.

Kim, J. H., E. E. Manuelidis, W. W. Glenn, Y. Fukuda, D. S. Cole, and J. F. Hogan (1983) Light and electron microscopic studies of phrenic nerves after long-term electrical stimulation. J. Neurosurg. *58*:84–91.

Klepinski, J. R. (1994) Implantable neural electrode, Patent N 5,282,468: U. S. Patent Office.

Kobetic, R., R. J. Triolo, and E. B. Marsolais (1997) Muscle selection and walking performance of multichannel FES systems for ambulation in paraplegia. IEEE Trans. Rehabil. Eng. *5*:23–29.

Koller, R., W. Girsch, C. Liegl, H. Gruber, J. Holle, U. Losert, W. Mayr, and H. Thoma (1992) Long-term results of nervous tissue alterations caused by epineurial electrode application: an experimental study in rat sciatic nerve. Pacing Clin. Electrophysiol. *15*:108–115.

Kralj, A., T. Bajd, and R. Turk (1980) Electrical stimulation providing functional use of paraplegic patient muscles. Med. Prog. Technol. *7*:3–9.

Kralj, A., T. Bajd, and R. Turk (1988) Enhancement of gait restoration in spinal injured patients by Functional Electrical Stimulation. Clin. Orthop. pp. 34–43.

Krieg, W. (1953) Functional Neuroanatomy, New York: Blakiston, pp. 207–208. 2nd edn.

Lanahan, A. and P. Worley (1998) Immediate-early genes and synaptic function. Neurobiol. Learn. Mem. *70*:37–43.

Lefurge, T., E. Goodall, K. Horch, L. Stensaas, and A. Schoenberg (1991) Chronically implanted intrafascicular recording electrodes. Ann. Biomed. Eng. *19*:197–207.

Liang, F. and E. G. Jones (1996) Peripheral nerve stimulation increases Fos immunoreactivity without affecting Type II Ca^{2+}/Calmodulin-dependent protein kinase, Glutamic acid Decarboxylase, or $GABA_A$ receptor gene expression in cat spinal cord. Exp. Brain Res. *111*:326–336.

Liberson, W. T., H. J. Holmquest, D. Scot, and M. Dow (1961) Functional electrotherapy: Stimulation of the peroneal nerve synchronized with the swing phase of the gait of hemiplegic patients. Arch. Phys. Med. Rehabil. *42*:101–105.

Lilly, J. C. and J. R. Hughes (1955) Brief, noninjurious electric waveform for stimulation of the brain. Scince *121*:468–469.

Loeb, G. E. and R. A. Peck (1996) Cuff electrodes for chronic stimulation and recording of peripheral nerve activity. J. Neurosci. Methods *64*:95–103.

Loeb, G. E., R. A. Peck, W. H. Moore, and K. Hood (2001) BION system for distributed neural prosthetic interfaces. Med. Eng. Phys. *23*:9–18.

Long, C. and V. Masciarelli (1963) An electrophysiological splint for the hand. Arch.Phys.Med. Rehabil. *44*:449–503.

Lyons, G. M., T. Sinkjaer, J. H. Burridge, and D. J. Wilcox (2002) A review of portable FES-based neural orthoses for the correction of drop foot. IEEE Trans. Neural Syst. Rehabil. Eng. *10*:260–279.

Marani, E. (2002) Innervation of the Mature Human Pelvis, Enschede: Twente University Press, chap. 7, pp. 95–112.

Marsolais, E. B. and R. Kobetic (1983) Functional walking in paralyzed patients by means of electrical stimulation. Clin. Orthop. pp. 30–36.

Marsolais, E. B., A. Scheiner, P. C. Miller, R. Kobetic, and J. J. Daly (1994) Augmentation of transfers for a quadriplegic patient using an implanted FNS system. Case report. Paraplegia *32*:573–579.

McCreery, D. B., W. F. Agnew, T. G. Yuen, and L. A. Bullara (1992) Damage in peripheral nerve from continuous electrical stimulation: Comparison of two stimulus waveforms. Med. Biol. Eng. Comput. *30*:109–114.

McCreery, D. B., W. F. Agnew, T. G. Yuen, and L. A. Bullara (1995) Relationship between stimulus amplitude, stimulus frequency and neural damage during electrical stimulation of sciatic nerve of cat. Med. Biol. Eng. Comput. *33*:426–429.

McNeal, D. R. (1976) Analysis of a model for excitation of myelinated nerve. IEEE Trans. Biomed. Eng. *23*:329–337.

McNeal, D. R. and B. R. Bowman (1985) Selective activation of muscles using peripheral nerve electrodes. Med. Biol. Eng. Comput. *23*:249–253.

McNeal, D. R., R. Waters, and J. Reswick (1977) Experience with implanted electrodes. Neurosurgery *1*:228–229.

Meyer, J.-U., C. Blau, and T. Stieglitz (1995) Multikontaktierung von nerven mit mikrostrukturen. Spektrum d. Wissensch. pp. 98–102.

Moe, J. H. and H. W. Post (1962) Functional Electrical Stimulation for ambulation in hemiplegia. J. Lancet *82*:285–288.

Molander, C., J. Hongpaisan, and G. Grant (1992) Changing pattern of c-fos expression in spinal cord neurons after electrical stimulation of the chronically injured sciatic nerve in the rat. Neuroscience *50*:223–236.

Morton, S. L., M. L. Daroux, and J. T. Mortimer (1994) The role of oxygen reduction in electrical stimulation of neural tissue. J. Electrochem. Soc. *141*:122–130.

Muir, G. D. and J. D. Steeves (1997) Sensorimotor stimulation to improve locomotor recovery after spinal cord injury. Trends Neurosci. *20*:72–77.

Nakamura, M., S. K. Rosahl, E. Alkahlout, A. Gharabaghi, G. F. Walter, and M. Samii (2003) C-fos immunoreactivity mapping of the auditory system after electrical stimulation of the cochlear nerve in rats. Hearing Res. *184*:75–81.

Nannini, N. and K. Horch (1991) Muscle recruitment with intrafascicular electrodes. IEEE Trans. Biomed. Eng. *38*:769–776.

Naples, G. G., J. T. Mortimer, A. Scheiner, and J. D. Sweeney (1988a) A spiral nerve cuff electrode for peripheral nerve stimulation. IEEE Trans. Biomed. Eng. *35*:905–916.

Naples, G. G., J. T. Mortimer, A. Scheiner, and J. D. Sweeney (1988b) A spiral nerve cuff electrode for peripheral nerve stimulation. IEEE Trans. Biomed. Eng. *35*:905–916.

Naples, G. G., J. T. Mortimer, and T. G. H. Yuen (1990) Overview of peripheral nerve electrode design and implantation. In W. F. Agnew and D. B. McCreery (eds.), *Neural Prostheses: Fundamental Studies*, Englewood Cliffs: Prentice Hall, pp. 107–145.

NIH (1995) Cochlear implants in adults and children. Tech. rep., National Institutes of Health, Bethesda, USA.

Nordhausen, C. T., E. M. Maynard, and R. A. Normann (1996) Single unit recording capabilities of a 100 microelectrode array. Brain Res. *726*:129–140.

Petrofsky, J. S. and C. A. Phillips (1985) Discharge characteristics of motor units and the surface EMG during fatiguing isometric contractions at submaximal tensions. Aviat. Space Environ. Med. *56*:581–586.

Pinter, M. M., F. Gerstenbrand, and M. R. Dimitrijevič (2000) Epidural electrical stimulation of posterior structures of the human lumbosacral cord: 3. Control of spasticity. Spinal Cord. *38*:524–531.

Platenik, J., N. Kuramoto, and Y. Yoneda (2000) Molecular mechanisms associated with long-term consolidation of the NMDA signals. Life Sci. *67*:335–364.

Popovič, D., M. Popovič, A. Stojanovič, A. Pjanovič, S. Radosavljevič, and D. Vulovič (1998) Clinical evaluation of the Belgrade Grasping System. In *Proc. 6th Vienna Int. Workshop on Functional Electrical Stimulation*. pp. 247–250.

Popovič, D., A. Stojanovič, A. Pjanovič, S. Radosavljevič, M. Popovič, S. Jovič, and D. Vulovič (1999) Clinical evaluation of the Bionic Glove. Arch. Phys. Med. Rehabil. *80*:299–304.

Popovič, M. R., A. Curt, T. Keller, and V. Dietz (2001a) Functional electrical stimulation for grasping and walking: Indications and limitations. Spinal Cord. *39*:403–412.

Popovič, M. R., T. Keller, I. P. Pappas, V. Dietz, and M. Morari (2001b) Surface-stimulation technology for grasping and walking neuroprosthesis. IEEE Eng. Med. Biol. Mag. *20*:82–93.

Popovič, M. R., D. B. Popovič, and T. Keller (2002) Neuroprostheses for grasping. Neurol. Res. *24*:443–452.

Prochazka, A., M. Gauthier, M. Wieler, and Z. Kenwell (1997) The Bionic Glove: an electrical stimulator garment that provides controlled grasp and hand opening in quadriplegia. Arch. Phys. Med. Rehabil. *78*:608–614.

Ranck, J. B. J. (1975) Which elements are excited in electrical stimulation of mammalian central nervous system: a review. Brain Res. *98*:417–440.

Ratner, B. D., A. Hoffman, J. E. Lemons, and F. J. Schoen (1996) Biomaterials Science - An Introduction to Materials in Medicine. New York: Academic Press.

Rattay, F. (1990) Electrical Nerve Stimulation: Theory, Experiments and Applications. Wien: Springer-Verlag.

Rebersek, S. and L. Vodovnik (1973) Proportionally controlled functional electrical stimulation of hand. Arch. Phys. Med. Rehabil. *54*:378–382.

Remak, R. (1838) Observationes Anatomicae Et Microscopiscae De Systematis Nervosi Structura. Berolini: Reimerans.

Rice, A. S. and S. B. McMahon (1992) Peripheral nerve injury caused by injection needles used in regional anaesthesia: Influence of bevel configuration, studied in a rat model. Br. J. Anaesth. *69*:433–438.

Rice, A. S. C., N. Y. Andreev, and S. B. McMahon (1994) The consequences of microneurography electrode-induced injury of peripheral nerves observed in the rat and man. Pain *59*:385–393.

Rice, A. S. C., S. B. McMahon, and P. D. Wall (1993) The electrophysiological consequences of electrode impalement of peripheral nerves in the rat. Brain Res. *631*:221–226.

Richardson, R. R., L. J. Cerullo, D. G. McLone, F. A. Gutierrez, and V. Lewis (1979) Percutaneous epidural neurostimulation in modulation of paraplegic spasticity. Six case reports. Acta Neurochir. (Wien.) *49*:235–243.

Rizzo, J., J. Wyatt, J. Loewenstein, S. Kelly, and D. Shire (2003) Methods and perceptual thresholds for short-term electrical stimulation of human retina with microelectrode arrays. Invest Ophthalmol. Vis. Sci. *44*:5355–5361.

Robblee, L. S. and T. L. Rose (1990) Electrochemical guidelines for selection of protocols and electrode materials for neural stimulation. In W. F. Agnew and D. B. McCreery (eds.), *Neural Prostheses: Fundamental Studies*, Englewood Cliffs: Prentice Hall, pp. 26–66.

Romero, E. (2000) Feasibility of Long-term Nerve Stimulation with the Self-sizing Spiral Cuff Electrode: Histological and Physiological Study. Ph.D. thesis, Universite catholique du Louvain, Brussels.

Rushton, W. A. (1951) A theory of the effects of fibre size in medullated nerve. J. Physiol. (Lond) *115*:101–122.

Rutten, W. L. (2002) Selective electrical interfaces with the nervous system. Ann. Rev. Biomed. Eng. *4*:407–452.

Rutten, W. L., T. A. Frieswijk, J. P. Smit, T. H. Rozijn, and J. H. Meier (1995) 3D neuro-electronic interface devices for neuromuscular control: Design studies and realisation steps. Biosens. Bioelectron. *10*:141–153.

Rutten, W. L., J. P. Smit, T. A. Frieswijk, J. A. Bielen, A. L. Brouwer, J. R. Buitenweg, and C. Heida (1999) Neuro-electronic interfacing with multielectrode arrays. IEEE Eng. Med. Biol. Mag. *18*:47–55.

Rutten, W. L., H. J. van Wier, and J. H. Put (1991) Sensitivity and selectivity of intraneural stimulation using a silicon electrode array. IEEE Trans. Biomed. Eng. *38*:192–198.

Salthouse, T. N. (1976) Cellular enzyme activity at the polymer-tissue interface: a review. J Biomed. Mater. Res. *10*:197–229.

Sarnoff, S. J., E. A. Gaensler, and J. V. Maloney (1950) Electrophrenic respiration: the effectiveness of contralateral ventialtion during activity of one phrenic nerve. J. Thoracic. Surg. *19*:929.

Schmidt, E. M., M. J. Bak, F. T. Hambrecht, C. V. Kufta, D. K. O'Rourke, and P. Vallabhanath (1996) Feasibility of a visual prosthesis for the blind based on intracortical microstimulation of the visual cortex. Brain *119 (Pt 2)*:507–522.

Schmidt, R. A. and E. A. Tanagho (1979) Feasibility of controlled micturition through electric stimulation. Urol Int. *34*:199–230.

Scott, T. R., P. H. Peckham, and M. W. Keith (1995) Upper extremity neuroprostheses using functional electrical stimulation. Baillieres Clin. Neurol. *4*:57–75.

Siegel, S. W., F. Catanzaro, H. E. Dijkema, M. M. Elhilali, C. J. Fowler, J. B. Gajewski, M. M. Hassouna, R. A. Janknegt, U. Jonas, P. E. van Kerrebroeck, A. A. Nijeholt, K. A. Oleson, and R. A. Schmidt (2000) Long-term results of a multicenter study on sacral nerve stimulation for treatment of urinary urge incontinence, urgency-frequency, and retention. Urology *56*:87–91.

Smit, J. (1996) Selective Motor Stimulation using Endoneural Prostheses. Ph.D. thesis, Twente University.

Smit, J. P., W. L. Rutten, and H. B. Boom (1999) Endoneural selective stimulating using wire-microelectrode arrays. IEEE Trans. Rehabil. Eng. *7*:399–412.

Snoek, G. J., M. J. IJzerman, F. A. in 't Groen, T. S. Stoffers, and G. Zilvold (2000) Use of the NESS Handmaster to restore handfunction in tetraplegia: Clinical experiences in ten patients. Spinal Cord. *38*:244–249.

Stanič, U., T. Bajd, V. Valenćič, M. Kljajič, and R. Acimovič (1977) Standardization of kinematic gait measurements and automatic pathological gait pattern diagnostics. Scand. J. Rehabil. Med. *9*:95–105.

Sweeney, J. D., D. A. Ksienski, and J. T. Mortimer (1990) A nerve cuff technique for selective excitation of peripheral nerve trunk regions. IEEE Trans. Biomed. Eng. *37*:706–715.

Tarver, W. B., R. E. George, S. E. Maschino, L. K. Holder, and J. F. Wernicke (1992) Clinical experience with a helical bipolar stimulating lead. Pacing Clin. Electrophysiol. *15*:1545–1556.

Taylor, P. N., J. H. Burridge, A. L. Dunkerley, A. Lamb, D. E. Wood, J. A. Norton, and I. D. Swain (1999a) Patients' perceptions of the Odstock dropped foot stimulator (ODFS). Clin. Rehabil. *13*:439–446.

Taylor, P. N., J. H. Burridge, A. L. Dunkerley, D. E. Wood, J. A. Norton, C. Singleton, and I. D. Swain (1999b) Clinical use of the Odstock dropped foot stimulator: Its effect on the speed and effort of walking. Arch. Phys. Med. Rehabil. *80*:1577–1583.

Thon, W. F., L. S. Baskin, U. Jonas, E. A. Tanagho, and R. A. Schmidt (2003) Neuromodulation of voiding dysfunction and pelvic pain. World J. Urol *9*:138.

Thorsen, R., R. Spadone, and M. Ferrarin (2001) A pilot study of myoelectrically controlled FES of upper extremity. IEEE Trans. Neural Syst. Rehabil. Eng. *9*:161–168.

van Bolhuis, A. I., J. Holsheimer, and H. H. Savelberg (2001) A nerve stimulation method to selectively recruit smaller motor-units in rat skeletal muscle. J. Neurosci. Methods *107*:87–92.

van der Aa, H. E., E. Alleman, A. Nene, and G. Snoek (1999) Sacral anterior root stimulation for bladder control: Clinical results. Arch. Physiol. Biochem. *107*:248–256.

Vapnek, J. M. and R. A. Schmidt (2003) Restoration of voiding in chronic urinary retention using neuroprothesis. World J. Urol *9*:142.

Vaudaux, P. E., c. P. Fran R. A. Proctor, D. McDevitt, T. J. Foster, R. M. Albrecht, D. P. Lew, H. Wabers, and S. L. Cooper (1995) Use of adhesion-defective mutants of staphylococcus aureus to define the role of specific plasma proteins in promoting bacterial adhesion to canine arteriovenous shunts. Infect. Immun. *63*:585–590.

Veraart, C., W. M. Grill, and J. T. Mortimer (1993) Selective control of muscle activation with a multipolar nerve cuff electrode. IEEE Trans. Biomed. Eng *40*:640–653.

Veraart, C., C. Raftopoulos, J. T. Mortimer, J. Delbeke, D. Pins, G. Michaux, A. Vanlierde, S. Parrini, and M. C. Wanet-Defalque (1998) Visual sensations produced by optic nerve stimulation using an implanted self-sizing spiral cuff electrode. Brain Res. *813*:181–186.

Vodovnik, L., A. Kralj, U. Stanič, R. Acimovič, and N. Gros (1978) Recent applications of Functional Electrical Stimulation to stroke patients in Ljubljana. Clin. Orthop. pp. 64–70.

Wassall, M. A., M. Santin, G. Peluso, and S. P. Denyer (1998) Possible role of α-1-microglobulin in mediating bacterial attachment to model surfaces. J. Biomed. Mater. Res. *40*:365–370.

Wee, A. S. (2001) Anodal excitation of intact peripheral nerves in humans. Electromyogr. Clin. Neurophysiol. *41*:71–77.

Wee, A. S., A. A. Leis, A. R. Kuhn, and R. W. Gilbert (2000) Anodal block: Can this occur during routine nerve conduction studies? Electromyogr. Clin. Neurophysiol. *40*:387–391.

Weiland, J. D., M. S. Humayun, G. Dagnelie, de Juan E Jr, R. J. Greenberg, and N. T. Iliff (1999) Understanding the origin of visual percepts elicited by electrical stimulation of the human retina. Graefes Arch. Clin. Exp. Ophthalmol. *237*:1007–1013.

Wieler, M., S. Naaman, and R. B. Stein (1996) WalkAid: An improved functional electrical stimulator for correcting foot-drop. In *Proc 1st Ann. Conf. Int. Functional Electrical Stimulation Society*. pp. 101–104.

Wieler, M., R. B. Stein, M. Ladouceur, M. Whittaker, A. W. Smith, S. Naaman, H. Barbeau, J. Bugaresti, and E. Aimone (1999) Multicenter evaluation of electrical stimulation systems for walking. Arch. Phys. Med. Rehabil. *80*:495–500.

Wielink, G., M. L. Essink-Bot, P. E. van Kerrebroeck, and F. F. Rutten (1997) Sacral rhizotomies and electrical bladder stimulation in spinal cord injury. 2. Cost-effectiveness and quality of life analysis. Dutch study group on sacral anterior root stimulation. Eur. Urol *31*:441–446.

Williams, D. F. (1987) Definitions in Biomaterials, Amsterdam: Elsevier, chap. 4, p. 54.

Wuolle, K. S., C. L. V. Doren, G. B. Thrope, M. W. Keith, and P. H. Peckham (1994) Development of a quantitative hand grasp and release test for patients with tetraplegia using a hand neuroprosthesis. Am. J. Hand Surg. *19*:209–218.

Yoshida, K. and K. Horch (1993) Selective stimulation of peripheral nerve fibers using dual intrafascicular electrodes. IEEE Trans. Biomed. Eng. *40*:492–494.

Zhou, B. H., R. Baratta, and M. Solomonow (1987) Manipulation of muscle force with various firing rate and recruitment control strategies. IEEE Trans. Biomed. Eng. *34*:128–139.

Zrenner, E., K. D. Miliczek, V. P. Gabel, H. G. Graf, E. Guenther, H. Haemmerle, B. Hoefflinger, K. Kohler, W. Nisch, M. Schubert, A. Stett, and S. Weiss (1997) The development of subretinal microphotodiodes for replacement of degenerated photoreceptors. Ophthalmic Res. *29*:269–280.

Three-dimensional Topography of the Motor Endplates of the Rat Gastrocnemius Muscle [†]

Abstract

Spatial distribution of motor endplates affects the shape of the electrical activity recorded from muscle. In order to provide information for realistic models of action potential propagation within muscles, we assembled three-dimensional maps of the motor endplates of the rat medial gastrocnemius (MGM) and lateral gastrocnemius (MGL) muscles. The maps were assembled from histological cross sections stained for acetylcholinesterase activity. Within MGL, the motor endplates formed three columns along its longitudinal axis. Within MGM, the motor endplates were arranged in a leaf-like body that shifted obliquely from proximal to distal. As inferred from the proximo-distal distribution of the cross-sectional projection area, the majority of the motor endplates were concentrated in the middle of MGL and in the distal third of MGM. Regions of maximal motor endplate concentration are considered most suitable for injections of neuroactive substances, such as neuronal tracers. The assembled maps of the gastrocnemius muscles can be used as guides for such injections within the motor endplate zones.

3.1 Introduction

The rat gastrocnemius muscle consists of two main heads that are considered to be distinct muscles - the tripennate gastrocnemius lateralis (MGL) and the unipennate gastrocnemius medialis (MGM). MGL comprises lateral, intermediate, and medial subheads (Bennett et al., 1986; Bennett and Ho, 1988). MGL and MGM are innervated by separate motor branches arising from the tibial nerve (Hebel and Stromberg, 1986). Rostrally, the gastrocnemius muscle is attached to the femur; caudally, its tendon joins the tendon of the soleus muscle in order to form the common calcaneal tendon (Achilles tendon) (Hebel and Stromberg, 1986).

The rat gastrocnemius muscle is often used as a model in the electrophysiological and functional assessment of recovery during peripheral nerve regeneration (Liu et al., 2003; Rafiuddin and Jayakumar, 2003; Thomas et al., 2003; Valero-Cabre et al., 2004; Varejao et al., 2004). A common approach for such assessment is to inject retrograde tracers into the muscle and count the number of retrogradely labeled motoneurons (Brushart et al., 1998; Popratiloff et al., 2001; Valero-Cabre et al., 2004). Water-soluble retrograde tracers, such as Horseradish peroxidase (HRP) and Fluoro-Gold, are mainly taken up by the motor endplates (Kobbert et al., 2000; Swett et al., 1986). Since the motor endplates are not restricted to a single spot inside the muscle and uptake depends on the availability of the tracer near them, "blind" injections may result in underestimation of the number of innervating motoneurons in the spinal cord (Swett et al., 1986; Janjua and Leong, 1981; McHanwell and Biscoe, 1981). Therefore, topographic description of the motor endplates will allow placement of the tracer injections in a specific and reproducible manner, which in turn will increase the quantity and reproducibility of labeling in the spinal cord.

Variations of single anatomical or physiological parameters are difficult to study in the electromyogram (EMG) *in vivo*. Therefore, numerous studies addressing the manifestation of different anatomical and physiological features of normal and pathological muscles have been performed in simulated EMGs (Miller-Larsson, 1986; Stalberg and Karlsson, 2001a;b;c; Dimitrova et al., 2002; Zalewska et al., 2004). Theoretically, features such as the duration, area, and amplitude of the motor unit action potentials are determined by the geometry of muscle fibers within different parts of the motor unit territory (Nandedkar et al., 1988). Moreover, the presence of even a single muscle fiber close to a concentric needle electrode could lead to the occurrence of serrated motor unit potentials (Zalewska et al., 2004). Accordingly, precise anatomical descriptions of the three-dimensional (3D) geometry of the muscle fibers and motor endplates of different muscles may help to model their electrical activity more realistically.

Morphology and topography of the motor endplates in various muscles are typically revealed at the light-microscopic level by acetylcholinesterase (AChE) histochemistry (see, for example, the classic works of Coërs and Woolf (1959) and Koelle and Friedenwald (1949)). In the present study, motor endplates were visualized by means of the Karnovsky-Roots thiocholine iodide method (Karnovsky and Roots, 1964). The locations of the motor endplates were reconstructed three-dimensionally using specialized software as previously described by Fiala and Harris (2002).

The present study aims to provide a guide for both modeling studies and experimental procedures requiring the precise localization of the endplate zones within the gastrocnemius muscle in the rat. We assembled maps of the locations of motor endplates and quantified the longitudinal distribution of their projection area within the rat gastrocnemius muscles. Three columns of motor endplates were present within MGL, while within MGM the motor endplates were arranged in a structure resembling a curved plant leaf.

3.2   Materials and Methods

3.2.1   Animals

Experiments were performed in accordance with international (EU Directive 86/609/ EEC) and national laws governing the protection of animals used for experimental purposes[1]. Four female Wistar Albino-Glaxo rats, weighing on average 250 g, were deeply anesthetized with Nembutal (Ceva Sante Animale, Libourne, France) and then perfused transcardially with 250 ml 0.9% sodium chloride solution, followed by 250 ml modified Karnovsky fixative (1% paraformaldehyde, 1.25% glutaraldehyde, 0.1 M phosphate buffer, pH 7.2), and finally by 250 ml 0.1 M phosphate-buffered saline (PBS), pH 7.2 (Feirabend et al., 1994). Under a surgical microscope, the right gastrocnemic muscles were dissected free from the surrounding tissues and collected in the same fixative. In three cases, MGM and MGL were dissected separately.

3.2.2   AChE histochemistry

Motor endplates were visualized by means of AChE histochemistry, employing the Karnovsky and Roots (1964) modified thiocholine iodide method. The tissue was stained twice, once as a whole mount (*in toto*) prior to sectioning and once after sectioning and mounting. The first AChE staining procedure was performed to visualize the superficial motor endplates. The muscles were incubated for 2 h at 37 °C in a reaction medium containing 0.17 mM thiocholine iodide (Sigma-Aldrich, St. Louis, Missouri), 0.53 mM sodium citrate, 0.34 mM copper sulfate, and 0.05 mM potassium ferricyanide (Sigma-Aldrich) dissolved in a 0.05 M sodium maleate buffer (pH 6.0) (see also Marani (1981)). Photographs of the entire muscles were taken to assist in the 3D-map reconstruction process (Fig. 3.1).

Subsequently the muscles were embedded in 13% gelatin. In order to orient and align future sections, the gelatin blocks were trimmed obliquely so that an asymmetric shape was formed in the section plane. The gelatin blocks were serially sectioned on a freezing microtome (Leica Jung 1205, Leica Microsystems, Bensheim, Germany). One of the muscles was sectioned parallel to its longitudinal axis, whereas the others were sectioned perpendicularly. The muscles were sectioned at a thickness of 120 μm and each 5th section was mounted and air-dried. The remaining sections were kept until the end of the second staining procedure. During the second AChE staining, the sections on the slides were incubated in the reaction medium at 37 °C for 3 to 5 h under microscopic control until a brownish-red reaction product was formed. Finally, the sections were rinsed in distilled water, passed through ascending series of alcohols, cleared in xylene, and permanently cover-slipped using Fluoromount (Merck, Darmstadt, Germany).

3.2.3   Reconstruction procedure

Three specimens of each muscle were used for assembly of the 3D map. The reconstructions were derived from 15 - 17 sections evenly spaced at 1.2 mm from each other (i.e., every 10th section in the series). This allowed for replacement of a section with an adjacent one with a minimal displacement error in space (10%) if a tissue defect was introduced in the motor endplate zone during clearing. Each cross-section was photographed with an CyberShot 5Mpix digital camera (Olympus Imaging Corp., Tokyo, Japan) under identical lighting conditions. The subsequent

---

[1]Leiden University Animal Care and Experimentation Commission UDEC 02076A
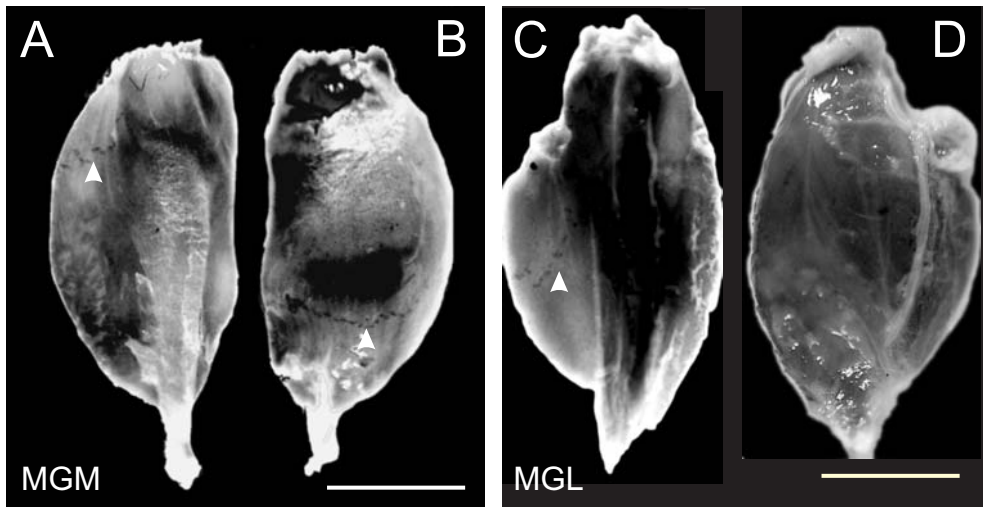
Figure 3.1: Superficial AChE staining of the gastrocnemius muscle

Superficial AChE staining of the gastrocnemius muscle. Photographs of right MGM (tibial aspect, A; dorsmedial aspect, B) and right MGL (tibial aspect, C; dorslateral aspect, D). The innervation bands of MGM appear as punctuated arches (A and B; arrow heads); the innervation band of MGL is present only on its lateral subhead (C; arrow head). Muscle aponeurosis appears as a white translucent band beginning from the Achilles tendon (A). Top, proximal end; scale bar, 1 cm.

pre-processing and reconstruction steps were performed using the specialized software for 3D reconstructions *sEM Align* and *IGL Trace* (Boston University, Boston, Massachussetts; http://synapses.bu.edu/tools/) as previously described (Fiala and Harris, 2002). The digital images of the sections were aligned by performing translations and rotations, i.e., "rigid" geometric transformations only.

Three classes of objects were defined and represented by contours in the images - muscle borders, motor endplate clusters, and motor endplate zones (Coërs's terminal innervation bands (Coërs and Woolf, 1959)). In every image, the muscle border was manually outlined and the motor endplates were traced by circles, each representing a single cluster. Each motor endplate zone was defined as the minimal enclosing convex outline around a macroscopically distinct cluster of motor endplates (Figs. 3.2 A and C) and manually drawn. The tracings of the objects were compared to the original sections by microscopic examination and improved if necessary. The objects were further exported to a common format for 3D data (Virtual Reality Modeling Language; VRML, ISO/IEC 14772) and assembled as solid bodies by surface rendering with the *Actify Spinfire* software program (Actify Inc., San Francisco, CA). Hereafter this composite 3D representation is referred to as the 3D map. In the 3D map, the muscle tissue boundaries were represented by their planar contours and the motor endplate clusters by spheres situated on the section planes. The motor endplate zones were connected by surfaces so that solid bodies could be formed. The 3D map was interactively inspected by rotations and translations in 3D space. The resulting muscle surfaces were compared to photographs of the original muscles and the alignment and assembly procedures were repeated if necessary.
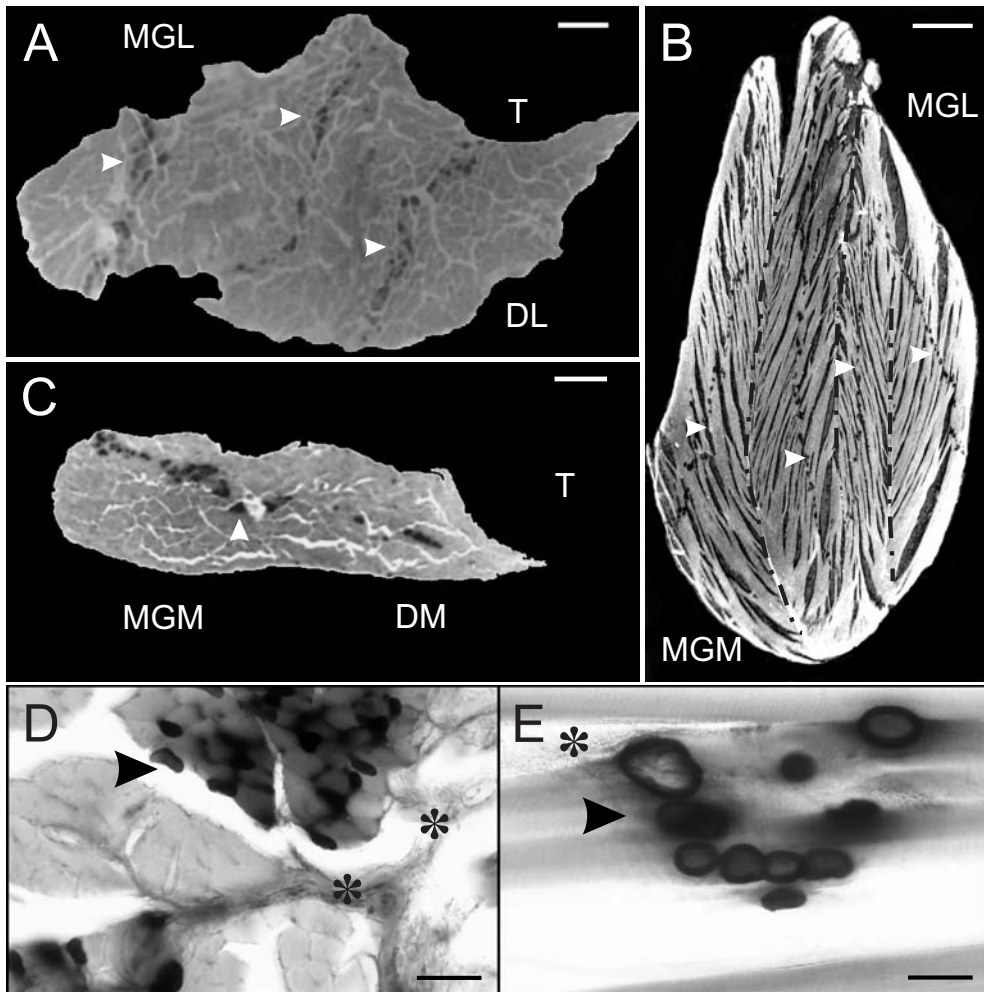
Figure 3.2: AChE staining of cross and longitudinal sections of the gastrocnemius muscle

A - Cross section of MGL, case A1066. Three bands of motor endplates are visible (arrow heads). Offset from the beginning of the series: 6.0 mm. Orientation: left, medial; right, lateral; T, tibial surface; DL, dorsolateral surface. Scale bar, 1 mm. B - Longitudinal section, case A1135. The complex pennate structure of the muscle can be seen. Note the presence of three aponeuroses, enhanced by black dash-dot lines and the N-like configuration of the motor endplate bands within MGL (arrow heads). The motor endplate clusters can be seen as dark dots of approximately equal size. Top, proximal pole; bottom, Achilles tendon; scale bar, 0.25 cm. C - Cross section of MGM, case A1066. One punctated band of motor endplates is visible across the muscle section (arrow head). Offset from the beginning of the series: 10.8 mm. Orientation: left, medial; right, lateral; T, tibial surface; DL, dorsolateral surface; DM, dorsomedial surface. Scale bar, 1 mm. D - Cross section of MGL. A terminal nerve branch (asterisks) approaches a cluster of motor endplates (arrowhead). Scale bar, 50 µm. E - Longitudinal section of MGL. A cluster of motor endplates of the *en plaque* type (arrowhead) is situated on top of several transversely striated muscle fibers (asterisk). Scale bar, 50 µm.

3.2.4   Image processing and morphometric analysis

All of the processing and measurement steps employed in the morphometric analysis were performed by means of the freeware image analysis software package *ImageJ* (NIH, Bethesda, Massachusetts; http://rsb.info.nih.gov/ij/) (Abramoff et al., 2004). Based on their color histograms, the digital images of the cross-sections of the gastrocnemius muscle were thresholded. Depending on its red, green and blue intensities, a foreground label was interactively assigned to every pixel in the image, so that a maximal overlap between the AChE-positive particles and the foreground was obtained. In such a way, binary images were produced where each foreground pixel represented an AChE-positive spot in the original section. The individual particles in the binary images were then automatically identified and measured. The total AChE-positive particle area per section (TPA) was calculated as the arithmetic sum of the individual particle areas obtained from the automatic measurements in each section. The close spacing of the individual motor endplates inside the bands resulted in merging of particles in the derived binary images. Therefore, TPA was chosen over the number of particles as a better measure for the quantity of motor endplates. The TPA of each section was plotted against its position along the longitudinal axis of the series. Hereafter this plot is referred to as the *proximodistal axial distribution.*

The numerical values are reported as mean ± standard deviation. Data were compared by performing Student's t-test. Probability levels less than 0.05 were considered significant.

3.3   Results

3.3.1   Macroscopic observations

In the living animal, the length of the muscle belly was on average 22 mm. For descriptive purposes, we distinguished a proximal end, distal end, dorsolateral aspect, and tibial aspect of MGL. In MGM, we distinguished proximal end, distal end, dorsomedial aspect, and lateral aspect. The lateral aspect of MGM overlapped the medial third of the dorsolateral surface of MGL. The *parva saphenous vein* and *sural nerve* crossed obliquely the dorsolateral surface of MGL. After their removal, a shallow sulcus could be recognized on the surface of the muscle.

The *in toto* staining of MGM revealed punctated bands of motor endplates on both dorsomedial and tibial surfaces (arrow heads, Figs. 3.1 A and B). On the tibial surface, the innervation band was situated at 1 cm from the proximal end of the muscle (arrow head, Fig. 3.1A), whereas dorsmedially it was situated 1.25 cm from the distal end of the muscle tendon (arrow head, Fig. 3.1B).

The *in toto* staining of MGL revealed a faint oblique band of motor endplates on the surface of its lateral subhead, situated near the rim of the tibial surface at 1.4 cm from the distal end of the muscle tendon (arrow head, Fig. 3.1C).

3.3.2   Microscopic anatomy of the motor endplates

In cross sections and longitudinal sections alike, the motor endplates formed clusters, typically 150 - 200 μm in diameter (Figs. 3.2 D and E). The clusters were arranged along imaginary straight lines (Figs. 3.2 A, B, and C), each one representing an individual motor endplate zone.

Figure 3.3 (legend): Section planes are perpendicular to the longitudinal axis of muscle (Z-axis). Sections are 1.2 mm apart. The X-axis points in a medial direction; the Y-axis, to the tibial side of the muscle; the Z-axis, to the Achilles tendon. Boundaries of the muscle tissue are represented by planar contours. The motor endplate clusters are represented by spheres. A - Isometric projection of the 3D map (dorsal view). Three columns of motor endplates, boundaries indicated by blue space filling, are present within the muscle. The map is rotated so that the N-shaped figure is best seen (compare to Fig. 3.1C). B - Coronal projection. Top, tibial surface; bottom, dorsolateral surface. C - Frontal projection from the side of the tibia. The angle between the lateral and the central column is 18°. The angle between the medial and the central column is 20°. Scale bars are 2 mm.

In most sections of MGL, there were three motor endplate zones separated by the muscle aponeuroses. The distance between motor endplates in the different motor endplate zones was substantially larger than between individual motor endplates (Fig. 3.2A). Conversely, in the cross sections of MGM the motor endplates were arranged along a single line (i.e., in one motor endplate zone; Fig. 3.2C), which in some sections had a dashed appearance. At the proximal end of the series, the motor endplate zone was situated peripherally near the dorsomedial surface of the muscle (Fig. 3.1A). Further in the series, the motor endplate zone shifted its position and through the center of the section it eventually reached the tibial surface (Fig. 3.1B).

Microscopic examination of the cross sections revealed that the motor endplate zones were larger in the middle of MGL and in the distal third of MGM. The terminal arborizations formed clusters of motor endplates of the *en plaque* type (Figs. 3.2 D and E) as previously described for mammals (Zacks, 1964). In the longitudinal sections, the motor endplates were situated at the middle of the muscle fiber (Fig. 3.2B) in most instances.

3.3.3 3D map representation

Lateral, central, and medial columns of motor endplates could be discerned in the 3D map of MGL. The columns remained separated throughout their course in all of the animals. Comparison with the longitudinal sections of MGL demonstrated a single column in every muscle subhead. The central column was situated bellow the sulcus left from the saphenous vein (Fig. 3.3).

On a frontal projection, the medial and central columns formed a sharp angle pointing towards the Achilles tendon (Fig. 3.3C). In the same projection, the medial and lateral columns formed a sharp angle pointing towards the proximal pole of the muscle (Fig. 3.3C). The entire constellation resembled a broad "N"-shaped structure (Fig. 3.3A). On a coronal projection, the lateral and the central columns formed a sharp angle, pointing towards the dorsolateral surface; the medial and central columns formed a sharp angle pointing in the direction of the tibia (Fig. 3.3B).

In the 3D map of MGM, motor endplates were arranged in a structure resembling a plant leaf (Fig. 3.4). The longitudinal axis of this arrangement formed a sharp angle with both the muscle longitudinal axis and the aponeurosis (Figs. 3.4A and 3.2B). The leaf-like arrangement extended from the tibial surface of the muscle cranially to the dorsomedial surface caudally. The surface innervation bands corresponded to the 3D bodies of motor endplates inside the muscles. For MGM, this relationship can be demonstrated in Figs. 3.1 A, B, and 3.4, where the motor endplates touch the dorsomedial surface of the muscle. Only in the lateral compartment of MGL, the motor endplates could be revealed on the surface. The VRML versions of the 3D
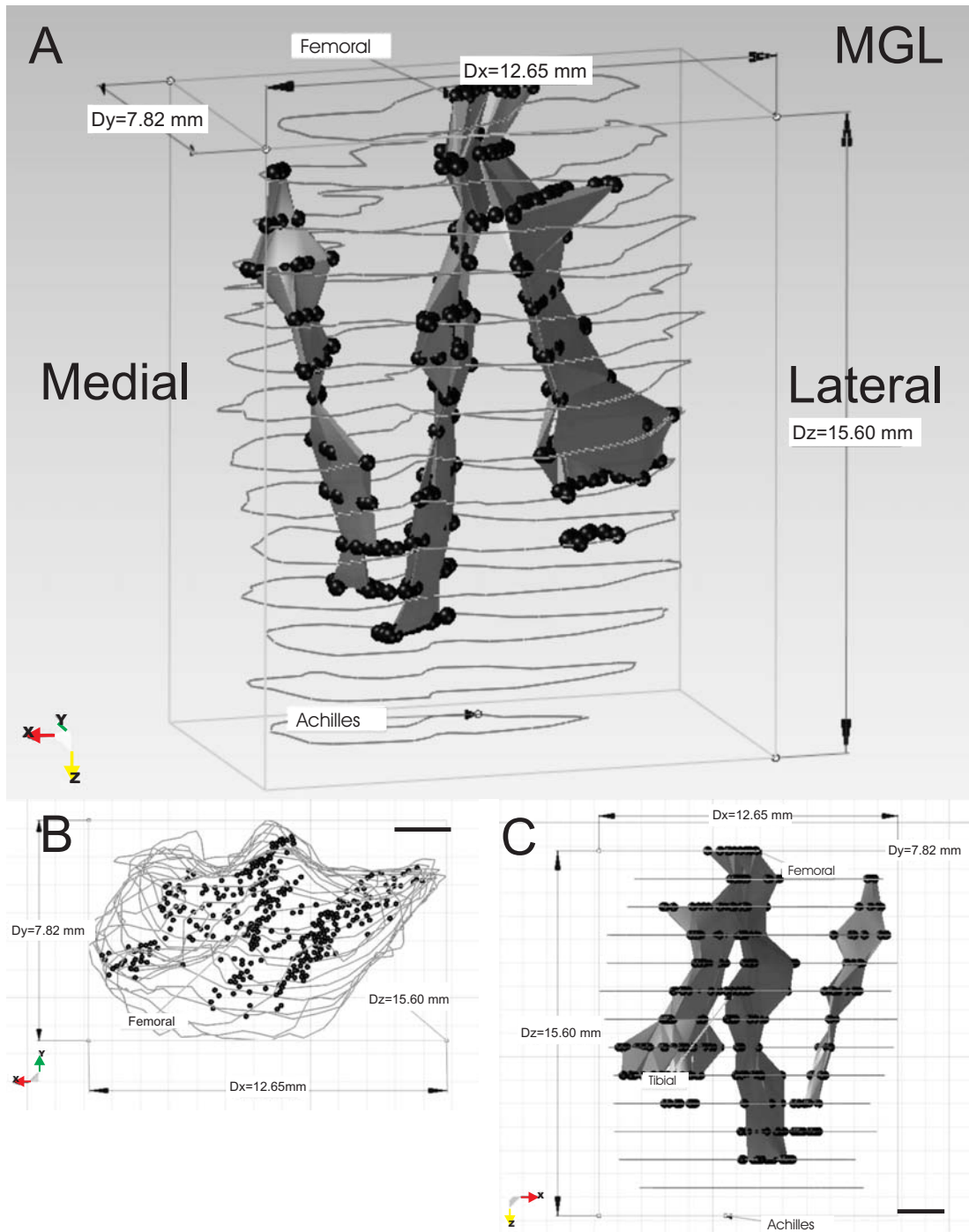
Figure 3.3: 3D map of MGL, case A1066; full color p. 179
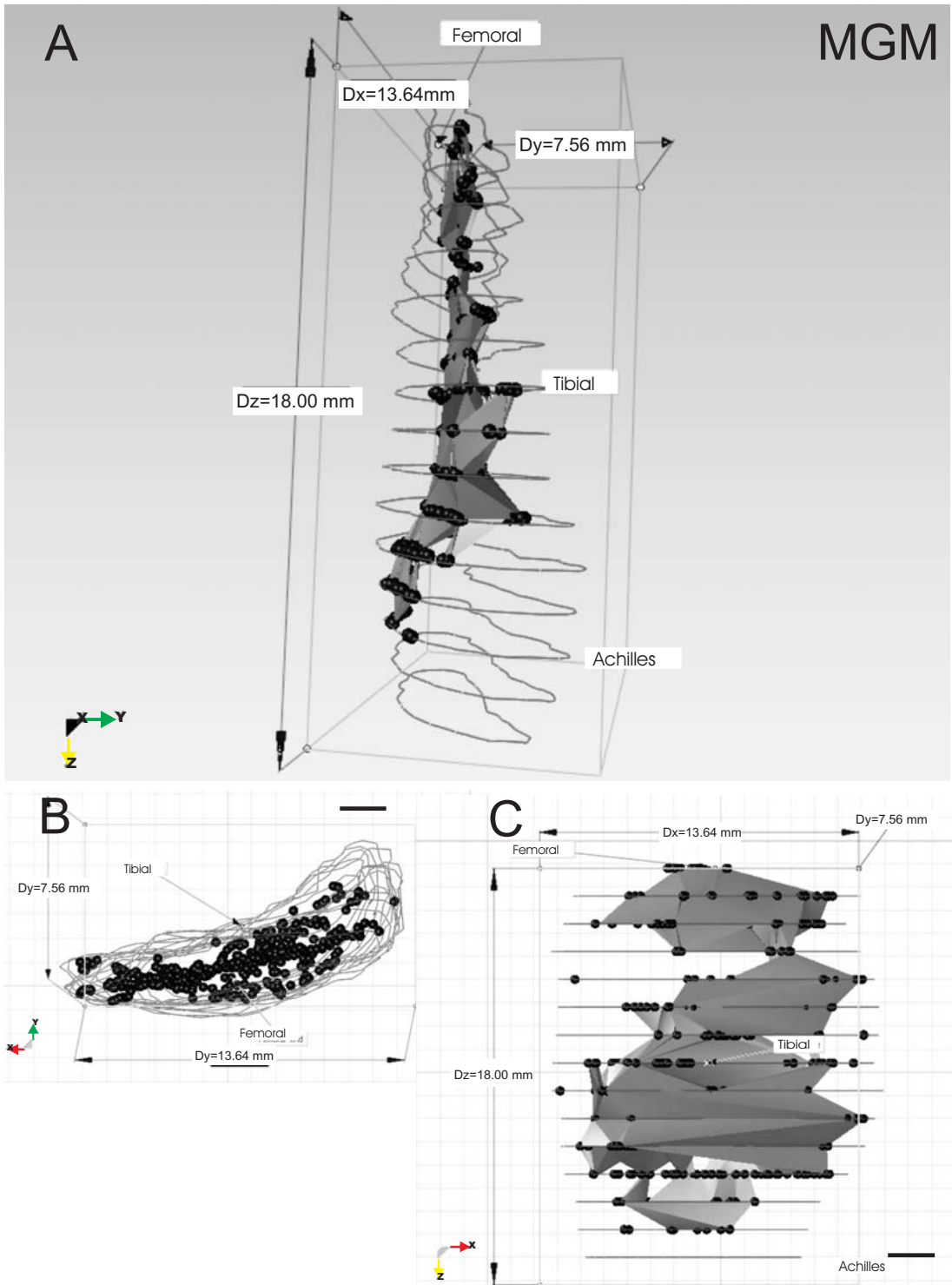
Figure 3.4: 3D map of MGM, case C6221; full color p. 180

Figure 3.4 (continued): Motor endplate clusters are represented by spheres. Boundaries of the muscle tissue are represented by planar contours. Section planes are perpendicular to the longitudinal axis of the muscle (Z-axis). Sections are 1.2 mm apart. The X-axis points in a medial direction; the Y-axis, to the tibial side of the muscle and the Z-axis, to the Achilles tendon. A - Isometric projection of the 3D map (medial view). The motor endplates form a leaf-like structure. The 3D map is rotated so that the configuration of the motor endplates in space is best observed. B - Coronal projection. C - Frontal projection from the side of the tibia. Scale bars are 2 mm.
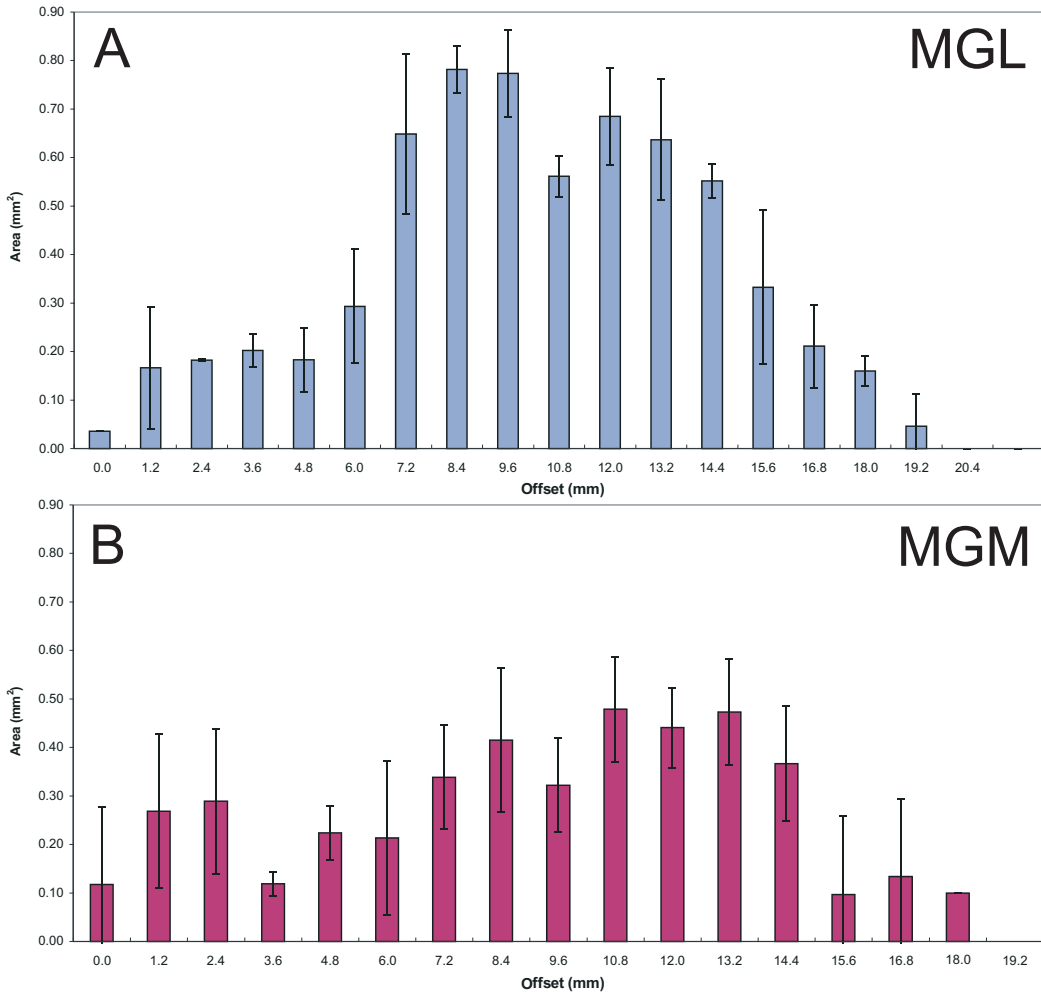
Figure 3.5: Total particle area per section

Data are presented as mean $\pm$ SD. Proximal end of the C6221 case series is taken for offset 0 mm. A - MGL, the TPA ranged from 0.0360 mm^2 to 0.7817 mm^2. The peak spanned from 7.2 mm to 14.4 mm. B - MGM, inter-animal variation was larger than for MGL. A broad peak is present from 10.8 to 14.4 mm.

maps are available for inspection at http://www.neuromorf.com/models.php.

3.3.4   Morphometric analysis of the motor endplates

TPA was calculated as a measure for the quantity of motor endplates in each section. The mean TPA for MGL (0.412 mm^2 $\pm$ 0.263 mm^2) was larger than for MGM (0.295 mm^2 $\pm$ 0.178 mm^2; $p < 0.05$, t-test). In order to compare and collate the axial distributions in the different muscles, we had to account for the variability caused by trimming before and during sectioning. To do so, the MGL series were aligned to each other by the mid-belly point of muscle. Each mid-belly point was identified by the maximum of the cross-section projection area of the muscle in the series. The same alignment minimized the case to case *similarity measure* of the individual TPA distribution curves, defined as the negative of the sum of the squared differences between the corresponding individual data points. The mean axial TPA distribution is represented in Figure 3.5. The axial distribution of MGL showed a broad peak with a 3.7-fold increase of TPA in the center of the series compared to the median value (from L=7.2 to L=14.4 mm; where L is the distance from the proximal end of the series; Fig. 3.5A).

For MGM the variation in data was larger. Nevertheless, a broad peak in the TPA could also be discerned starting from L=10.8 to L=14.4 mm from the proximal end of the series (Fig. 3.5B). The increase was 2.2-fold compared to the median value of the series.

3.4   Discussion

3.4.1   Relationship between the 3D map and muscle compartmental-ization

MGL is divided in different physiological compartments that can contract separately, each supplied by a distinct motor branch (English and Letbetter, 1982; Bennett et al., 1986; Bennett and Ho, 1988). The N-shape arrangement of the motor endplate columns is in good accordance with the tri-pennate structure of MGL. Surprisingly, the functional compartmentalization dictated by the motor branch pattern corresponds only partly to columnar architecture. We can only relate the medial column to the previously described medial muscle compartment (Bennett and Ho, 1988). Little is known about the course and the pattern of the motor branches of MGL in the rat. Previous studies suggest similarity with the anatomy of cat MGL where five primary muscle nerve branches were described (English and Letbetter, 1982). Therefore, we can possibly relate the central column of motor endplates to two of the centrally situated primary branches, and the lateral column to the distal lateral primary branch (English and Letbetter, 1982). MGM is innervated by up to four primary nerve branches, of which the proximal and distal ones are the largest (Ruiter et al., 1995). This pattern can be recognized in the 3D map of the motor endplate zone that resembled a curved plant leaf with its veins probably corresponding to the pattern of the nerve branches.

3.4.2   Relationship between the 3D-map and TPA distribution

Observed concentration of the motor endplates in the 3D map corresponded to the location of the maxima in TPA distribution (Figs. 3.5 and 3.6). It is unlikely that the observed pattern of TPA distribution is caused by regional variations in density or numbers of muscle fibers, as that would imply a 2- to 4-fold increase in either of these parameters (Fig. 3.5). Regional differences in 3D fiber geometry (orientation and alignment of the muscle fibers) are more likely to explain
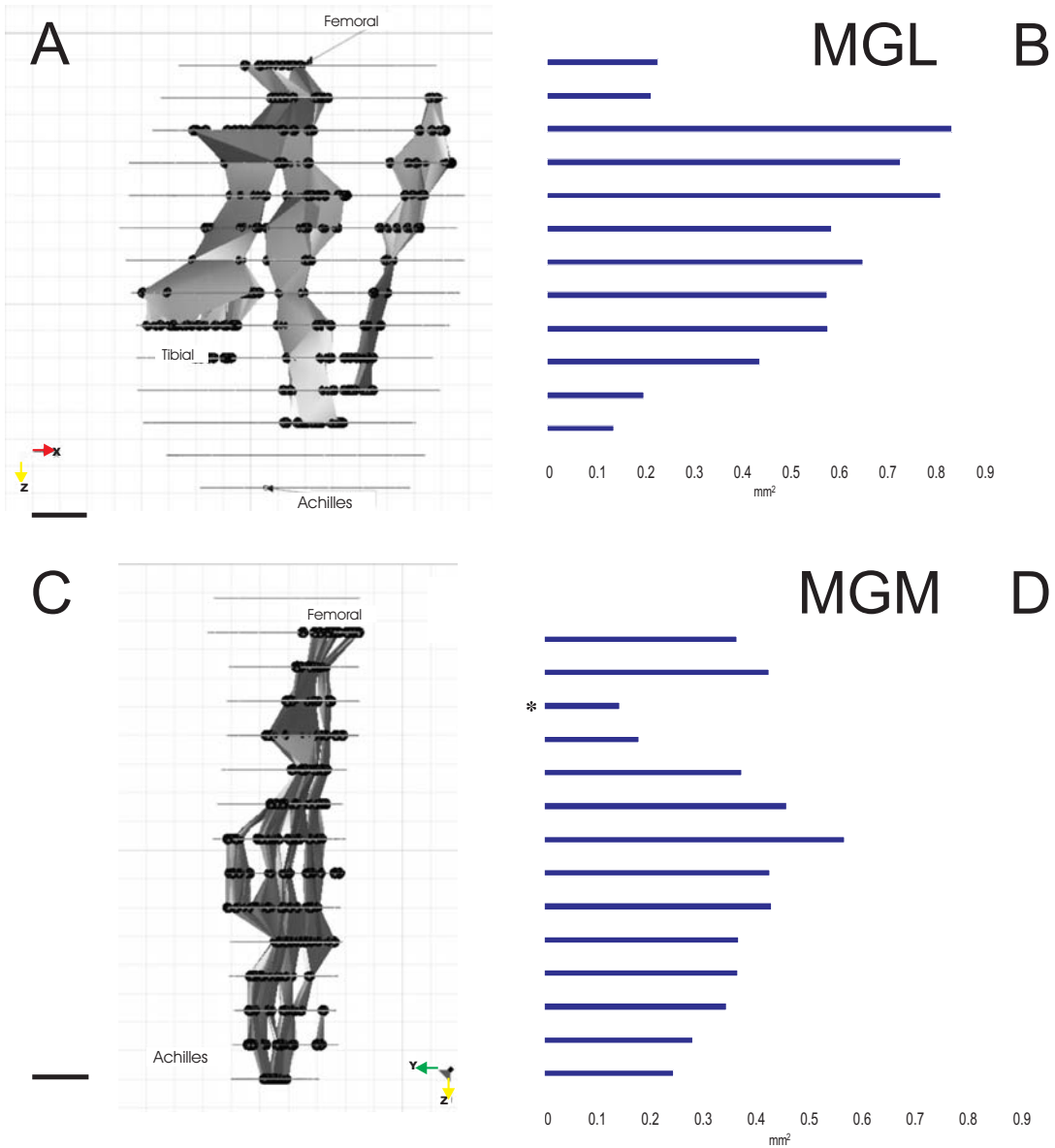
Figure 3.6: Relationship between the 3D map and the TPA distribution, Case A1066

A - Dorsolateral view of the 3D map of MGL; B - corresponding TPA, horizontal bars are aligned to the section planes; C - lateral view of the 3D map of MGM; D - corresponding TPA, with horizontal bars aligned to the section planes. Microscopic inspection showed that the notch in the TPA distribution of MGM (asterisk) was due to nerve branches present in the cross sections at that level. Scale bars are 2 mm.

the observed maxima in the projection area. Differences in size of motor endplates may also contribute, because the fiber composition varies in MGM (Holewijn et al., 1984; Ruiter et al., 1995) and the motor endplate size is related to the fiber type (Coërs and Woolf, 1959).

3.4.3 Applicability in modeling research

The shape, amplitude, and duration of recorded motor unit potentials are highly dependent on the distance between the electrode and the motor endplates (Dekhuijzen et al., 1986; Zalewska et al., 2004) and therefore on the spatial configuration of the endplate zones. Complex motor endplate distributions, such as reported in the present study, will result in an increase in variation of these parameters of motor unit potentials. Indeed, such variability in the maximum-to-minimum time interval of the biphasic potential and in the peak-to-peak amplitude of potentials was shown experimentally in recordings from single motor units from the rat MGM (Grottel et al., 1986). However, even the most realistic EMG modeling studies performed so far have assumed only simple motor endplate spatial distributions (Stalberg and Karlsson, 2001b;c). Therefore, realistic modeling of EMG requires that the geometry of the motor endplate zones is incorporated into models.

3.4.4 Applicability in tracing studies

Three-dimensional reconstructions of different muscles (*biceps brachii*, *tibialis anterior*, *sartorius* (Aquilonius et al., 1984), and *thyroarytenoid* (Rosen et al., 1983)) have been utilized primarily in the clinic as guides for Botulinum toxin injections. We propose similar approach to be used for the application of substances, such as retrograde tracers, in the gastrocnemius muscle of rat. In our experience, this muscle is best approached for injections *ad dorsum* after small incision of the skin along the midline of the calf. In Figure 3.6, muscles are displayed as approximately seen in such a surgical approach. Based on the depicted relationship between the topography and the area of motor endplates, we recommend injections to be made as following:

MGM - in a rostral direction along the longitudinal axis of the muscle at a depth of 2-2.5 mm, preferably in the caudal third of the muscle;

MGL - in a rostral direction oblique to the longitudinal axis of the muscle at a depth of 4-6 mm. For the lateral column, in a lateral direction; for the central column, parallel to the course of the saphena parva vein and the sural nerve; and for the medial column, in a medial direction.

3.5 Conclusions

THe volumetric representation of the anatomical objects by means of VRML models provides better understanding of the topographical anatomy of muscle and the relationship with its innervation. A major benefit of the presented 3D map is the user interactivity, which enables a thorough examination of the 3D arrangement of the motor endplates and their relation to the muscle surface. The 3D map will facilitate precise injections close to the motor endplates, such as those needed in retrograde tracing experiments. Secondly, the spatial distribution of the motor endplates in the 3D map can be incorporated into EMG simulation models of the

gastrocnemius muscle so that it can increase our understanding of the influence of the motor endplate geometry on EMG both in normal and in pathological conditions.

Acknowledgements

Bibliography

Abramoff, M. D., P. J. Magelhaes, and S. J. Ram (2004) Image processing with ImageJ. Biophotonics Int. *11*:36–42.

Aquilonius, S. M., H. Askmark, P. G. Gillberg, S. Nandedkar, Y. Olsson, and E. Stalberg (1984) Topographical localization of motor endplates in cryosections of whole human muscles. Muscle Nerve *7*:287–293.

Bennett, M., S. Ho, and N. Lavidis (1986) Competition between segmental nerves at end-plates in rat gastrocnemius muscle during loss of polyneuronal innervation. J. Physiol. (Lond) *381*:351–376.

Bennett, M. R. and S. Ho (1988) The formation of topographical maps in developing rat gastrocnemius muscle during synapse elimination. J. Physiol. (Lond) *396*:471–496.

Brushart, T. M., J. Gerber, P. Kessens, Y. G. Chen, and R. M. Royall (1998) Contributions of pathway and neuron to preferential motor reinnervation. J. Neurosci. *18*:8674–8681.

Coërs, C. and A. L. Woolf (1959) Normal histology of the intramuscular nerves and nerve endings. Oxford: Blackwell Scientific Publications, pp. 12–41. 1st edn.

Dekhuijzen, A. J., P. A. van Koetsveld, G. C. Baan, R. D. Woittiez, and P. A. Huijing (1986) Motor endplate position of rat gastrocnemius muscle. Muscle Nerve *9*:642–647.

Dimitrova, N. A., C. Disselhorst-Klug, A. Trachterna, G. V. Dimitrov, and G. Rau (2002) Surface detected potentials of normal and reinnervated motor units: a simulation study for muscles consisted of short fibres. Electromyogr. Clin. Neurophysiol *42*:219–230.

English, A. W. and W. D. Letbetter (1982) Anatomy and innervation patterns of cat lateral gastrocnemius and plantaris muscles. Am. J. Anat. *164*:67–77.

Feirabend, H. K., P. Kok, H. Choufoer, and S. Ploeger (1994) Preservation of myelinated fibers for electron microscopy: a qualitative comparison of aldehyde fixation, microwave stabilisation and other procedures all completed by osmication. J. Neurosci. Methods *55*:137–153.

Fiala, J. C. and K. M. Harris (2002) Computer-based alignment and reconstruction of serial sections. Microsc. Anal. *52*:5–7.

Grottel, K., J. Celichowski, and K. Kowalski (1986) Spatial analysis of motor unit potentials of the rat medial gastrocnemius. Acta Physiol. Pol. *37*:219–227.

Hebel, R. and M. W. Stromberg (1986) Anatomy and embryology of the laboratory rat, Worthsee: BioMed Verlag, chap. Myology, pp. 25–44.

Holewijn, M., P. Plantinga, R. D. Woittiez, and P. A. Huijing (1984) The number of sarcomeres and architecture of the M. Gastrocnemius of the rat. Acta Morphol. Neerl. Scand. *22*:257–263.

Janjua, M. Z. and S. K. Leong (1981) Labelling of cervical and thoracic spinal neurones following injection of horseradish peroxidase in the leg muscles of rats. Brain Res. *223*:386–390.

Karnovsky, M. J. and L. Roots (1964) A "direct-coloring" thiocholine method for cholinesterase. J. Histochem. Cytochem. *12*:219–221.

Kobbert, C., R. Apps, I. Bechmann, J. L. Lanciego, J. Mey, and S. Thanos (2000) Current concepts in neuroanatomical tracing. Prog. Neurobiol. *62*:327–351.

Koelle, G. B. and J. S. Friedenwald (1949) A histochemical method for localizing cholinesterase activity. Proc. Soc. Exp. Biol. (N.Y.) *70*:617–622.

Liu, S., P. Damhieu, P. Devanze, G. Said, J. M. Heard, and M. Tadie (2003) Efficient reinnervation of hindlimb muscles by thoracic motor neurons after nerve cross-anastomosis in rats. J. Neurosurg. *99*:879–885.

Marani, E. (1981) Enzyme Histochemistry, New York: Plenum Press, chap. 9, pp. 481–581.

McHanwell, S. and T. J. Biscoe (1981) The localization of motoneurons supplying the hindlimb muscles of the mouse. Philos. Trans. R. Soc. Lond. B Biol. Sci. *293*:477–508.

Miller-Larsson, A. (1986) Motor unit action potential field–modelling results. Biol. Cybern. *53*:307–321.

Nandedkar, S. D., D. B. Sanders, E. V. Stalberg, and S. Andreassen (1988) Simulation of concentric needle EMG motor unit action potentials. Muscle Nerve *11*:151–159.

Popratiloff, A. S., W. F. Neiss, E. Skouras, M. Streppel, O. Guntinas-Lichius, and D. N. Angelov (2001) Evaluation of muscle re-innervation employing pre- and post-axotomy injections of fluorescent retrograde tracers. Brain Res. Bull. *54*:115–123.

Rafiuddin, A. M. and R. Jayakumar (2003) Peripheral nerve regeneration in RGD peptide incorporated collagen tubes. Brain Res. *993*:208–216.

Rosen, M., L. T. Malmgren, and R. R. Gacek (1983) Three-dimensional computer reconstruction of the distribution of neuromuscular junctions in the thyroarytenoid muscle. Ann. Otol. Rhinol. Laryngol. *92*:424–429.

Ruiter, C. J. D., A. de Haan, and A. J. Sargeant (1995) Physiological characteristics of two extreme muscle compartments in gastrocnemius medialis of the anaesthetized rat. Acta Physiol. Scand. *153*:313–324.

Stalberg, E. and L. Karlsson (2001a) The motor nerve simulator. Clin. Neurophysiol. *112*:2118–2132.

Stalberg, E. and L. Karlsson (2001b) Simulation of EMG in pathological situations. Clin. Neurophysiol. *112*:869–878.

Stalberg, E. and L. Karlsson (2001c) Simulation of the normal concentric needle electromyogram by using a muscle model. Clin. Neurophysiol. *112*:464–471.

Swett, J. E., R. P. Wikholm, R. H. Blanks, A. L. Swett, and L. C. Conley (1986) Motoneurons of the rat sciatic nerve. Exp. Neurol. *93*:227–252.

Thomas, C. K., S. Sesodia, D. E. Erb, and R. M. Grumbles (2003) Properties of medial gastrocnemius motor units and muscle fibers reinnervated by embryonic ventral spinal cord cells. Exp. Neurol. *180*:25–31.

Valero-Cabre, A., K. Tsironis, E. Skouras, X. Navarro, and W. F. Neiss (2004) Peripheral and spinal motor reorganization after nerve injury and repair. J. Neurotrauma *21*:95–108.

Varejao, A. S., P. Melo-Pinto, M. F. Meek, V. M. Filipe, and J. Bulas-Cruz (2004) Methods for the experimental functional assessment of rat sciatic nerve regeneration. Neurol. Res. *26*:186–194.

Zacks, S. I. (1964) The Motor Endplate, Philadelphia: W.B. Saunders, pp. 1–28.

Zalewska, E., I. Hausmanowa-Petrusewicz, and E. Stalberg (2004) Modeling studies on irregular motor unit potentials. Clin. Neurophysiol *115*:543–556.

CHAPTER **4**

Morphometric Analysis of the Fiber Populations of the Rat Sciatic Nerve, Its Spinal Roots, and Its Major Branches [†]

Abstract

Development of neural prostheses requires a number of quantitative morphological parameters to be established in the used experimental animals. To provide such information, extensive morphometric analysis was performed on the rat sciatic nerves, its founding dorsal and ventral spinal roots, and its major branches - the tibial, peroneal, and sural nerves. Tissue specimens from 4 female adult Albino-Wistar were collected, processed, and measured in semi-thin histological sections using microscopic image analysis software. Variation in the density of myelinated fibers, interspace, and tissue cross-sectional area was studied with respect to the individual roots and nerves. In the dorsal roots, fiber numbers and cross-sectional areas varied linearly with the spinal root level. Fiber diameter distributions were modeled statistically using multi-component lognormal models and an optimal model for every nerve or root was selected by the Schwartz-Bayesian information criterion. For the dorsal roots, the ventral roots, the sciatic nerve, and the peroneal nerve optimal models consisted of 3 components, while for the tibial and sural nerves 2 component models were optimal. Functional identities of the fiber populations described by the individual components were established using calculations of corresponding conduction velocities according to Arbuthnott et al. [J Physiol 1980; 308: 125-57] and anatomical considerations. The proximo-distal transitions between the fiber populations of different nerves were established by statistical comparisons of the model parameters. Obtained reference values of the rat morphometric parameters can be used in further theoretical and experimental research for neural prosthesis development.

4.1 Introduction

IN the rat, sciatic nerve originates form the spinal nerve L4 - L6 (Brunner et al., 1980; Swett et al., 1986). At the middle of the thigh, it splits into several fascicles, which further distally give rise to the tibial, peroneal, and sural nerves, and a cutaneous branch (Schmalbruch, 1986; Swett et al., 1986). The rat sciatic nerve and its tributary branches are frequently used as model systems for studying the mechanisms of regeneration of nerve fibers (Navarro and Kennedy, 1991; Vleggeert-Lankamp et al., 2004; Negredo et al., 2004), developmental and induced cell death (Greensmith et al., 1996; Prodanov et al., 1998; Puigdellivol-Sanchez et al., 2002; Iwasaki et al., 2004), and for establishing the performance of the implanted devices in the developing field of neural prostheses. Since optimal prosthetic function is still not achieved, a number of implantable electrodes for stimulation were proposed over the last 30 years (recent overviews in Heiduschka and Thanos (1998) and Prodanov et al. (2003) i.e. Chapter 2). Typically an electrode is placed surgically around the nerve (i.e. "cuff" - Rodriguez et al. (2000)) or is implanted inside a nerve, i.e. intrafascicular electrodes (Veltink et al., 1989; Malagodi et al., 1989), the Utah Microelectrode Array (Branner and Normann, 2000; McDonnall et al., 2004), the Twente Microelectrode Array (Rutten et al., 1991)) or a nerve stump is sutured to an electrode - i.e. sieve electrodes (Lago et al., 2005). For the optimal design of these electrodes one needs to establish a number of quantitative anatomical parameters for the used experimental nerves, such as their inter-nodal distances distribution and g-ratios, fiber density, fascicle configuration, and fiber diameter distribution. All of these parameters collectively influence obtained selectivity during stimulation (Veltink et al., 1989; Prodanov et al., 2003; Deurloo and Holsheimer, 2003). Due to the complex fasciculation pattern of the proximal parts of the peripheral nerves (Stewart, 2003) and the very long processing time in semi-automatic morphometric studies, quantitative descriptions of the rat lumbar spinal roots and nerves in the sciatic system are fragmentary (major studies in the rat are summarized in Appendix Table 4.A.1). Moreover, none of the mentioned extensive studies provides sufficient quantitative anatomical data needed for development of stimulation electrodes in the rat. To provide such information, we performed extensive morphometric analysis of the sciatic nerve, its founding spinal roots, and its major branches. In this study, we have focused on parameters such as numbers and density of fibers, fiber size distribution, nerve (root) area, and interspace (Table 4.1). Results of population modeling of the fiber diameter distributions of the studied nerves are also presented and the modeled fiber populations are related to electrophysiologically identifiable classes of fibers.

4.2 Materials and Methods

4.2.1 Animals

FOur female Wistar rats (HsdCpb), weighing on average 250 g, were obtained from the central animal care facility. Animal handling was carried out in accordance with the international (EU Directive 86/609/EEC) and national laws concerning the protection of the experimental animals[1].

---

[1]Leiden University Animal Care and Experimentation Commission UDEC 02076a

Table 4.1: Measured and derived morphological parameters of the myelinated fibers

Notation	Morphological parameter	Formula [dimension]
$N[f]_{sample}$	Number of fibers in sample	-
$N[f]_{total}$	Total number of fibers estimate	$(A[n]/A[s]) \cdot N[f]_{sample}$
$A[n]$	Area of the nerve profile	$[\mu m^2]$
$A[s]$	Area of the sample	$[\mu m^2]$
$A[f]$	Area of the fiber profile	$[\mu m^2]$
$d[f]$	Fiber diameter	$2\sqrt{A[f]/\pi}$ $[\mu m]$
$Dens[f]$	Density of fibers per 1000 μm^2	$N[f]/A[s] \cdot 1000$
$A[i]_{rel}$	Relative area of the interspace	$(1 - \Sigma A[f]/A[s]) \cdot 100$ [%]
$A[s]_{rel}$	Relative sampling area	$(\Sigma A[s]/A[n]) \cdot 100$ [%]
F[f]	Relative fiber frequency	[%]
Δ	Class width	$[\mu m]$
n	Number of samples	-

4.2.2 Preparation and Histological processing of samples

The animals were deeply anesthetized with 0.2 ml (i.e. 4.8 mg/100 g) Pentobarbital (Nembutal®, Ceva Sante Animale, Libourne, France) and then perfused transcardially with 250 ml 0.9% sodium chloride solution, followed by 250 ml modified Karnovsky fixative (1% paraformaldehyde, 1.25% glutaraldehyde, 0.1M phosphate buffer, pH 7.2) (Feirabend et al., 1998), and finally by 250 ml 0.1M phosphate buffered saline, pH 7.2. Before the onset of fixation, 0.1 ml 5,000 IU/ml Heparin (Leo Pharma, Breda, The Netherlands) was injected *i.c.* to prevent blood coagulation. The skin, superficial and deep hindlimb muscles were dissected under a surgical microscope and the sciatic nerve was exposed. The spinal canal was opened from vertebrae Th6 to S1. Lumbar dorsal and ventral spinal roots, and the hind limb nerves were identified according to the atlas of Hebel and Stromberg (1986). Tissue samples were dissected and stored in modified Karnovsky fixative until further processing. Collected material included samples of *ventral roots* of spinal levels L4 (n=8), L5 (n=7), and L6 (n=6); *dorsal roots* of spinal levels L4 (n=3), L5 (n=4), and L6 (n=6); and *nerves* - proximal sciatic (n=8), distal sciatic (n=8), tibial (n=8), common peroneal (n=7), sural (n=6), and the cutaneous branch of the sciatic (n=2). In most cases, both left and right sides were collected. Fixed tissue samples were incubated in a 1% solution of osmium tetraoxide for 2 h under constant agitation. Before and after incubation the tissue was rinsed 3 times x 5 min in 0.1 M phosphate buffer (pH 7.2). Samples were dehydrated in ascending series of ethanol and later embedded in Epon (Merck, Amsterdam, The Netherlands). Transverse 1 μm sections were cut on a Reichert ultramicrotome (Leica, Rijswijk, The Netherlands) and stained with a 1% toluidine blue and 1% borax solution according to Feirabend et al. (1998).

4.2.3 Morphometric evaluation

One to 6 microscopic images of subsamples, each with an area of 20,640 μm², together forming the total sample area $A[s]$, were taken at objective magnification of 40x. All light microscopically identifiable myelinated fibers in the subsamples were counted ($N[f]_{sample}$) and their profile areas $A[f]$ were measured using Zeiss Kontron Videoplan (semi-automatically) or Kontron KS-400 (automatically) image analyzers (Carl Zeiss, Weesp, The Netherlands) at a final magnification of

Ventral L5

Dorsal L5

Sciatic Proximal

Peroneal

Tibial

Sural
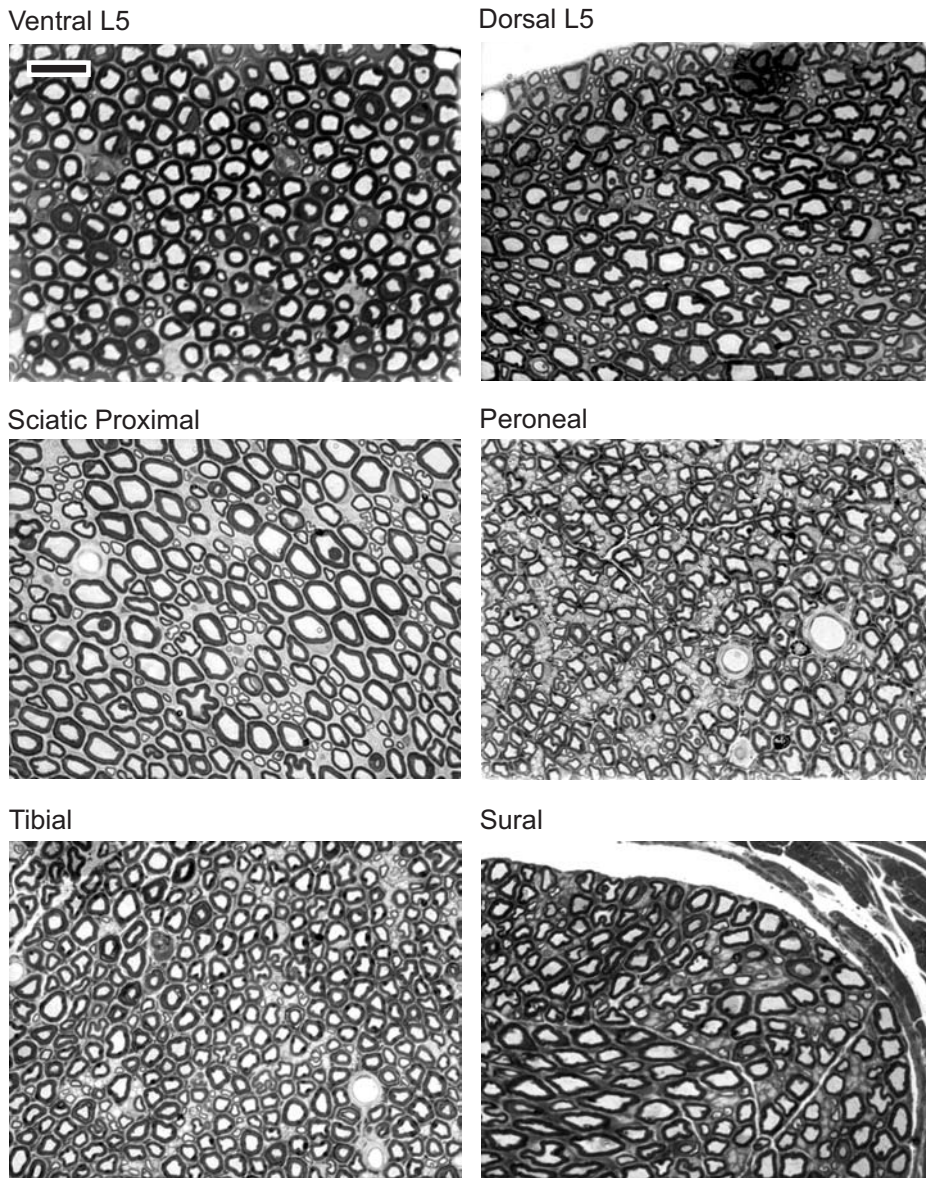
Figure 4.1: Histology of selected samples

Different ventral or dorsal root levels were difficult to distinguish visually; therefore only samples of L5 levels are shown. Dorsal root sample shows the typical picture of patches of small fibers interspaced among sparsely distributed large fibers (size grouping). Some of the fibers in the sural nerve had undulating course and were slightly obliquely sectioned. There was no clear-cut size grouping in the samples of the proximal sciatic, tibial, and peroneal nerves. All images were acquired with a 40x objective. Scale bar is 20 µm.

Table 4.2: Quantitative parameters of the roots and nerves

material	n	$d[f]$	$N[f]_{total}$	$A[i]_{rel}$	$A[n] \cdot 10^{-4}$	$A[s]_{rel}$
ventral roots						
L4	8	7.97 ± 1.07	$1{,}163 \pm 385$	34.4 ± 6.3	12.01 ± 3.58	58.8 ± 26.5
L5	7	7.65 ± 0.88	$1{,}611 \pm 636$	32.8 ± 4.7	11.93 ± 2.03	55.1 ± 21.9
L6	6	8.52 ± 0.79	$1{,}400 \pm 70$	32.1 ± 5.2	13.98 ± 2.32	45.3 ± 7.3
mean		8.05 ± 0.44	$1{,}391 \pm 224$	33.1 ± 1.2	12.64 ± 1.16	53.1 ± 7.0
dorsal roots						
L4	3	5.69 ± 0.73	$3{,}302 \pm 1{,}345$	31.2 ± 3.5	12.02 ± 3.62	39.6 ± 14.2
L5	4	5.75 ± 0.26	$3{,}645 \pm 725$	35.0 ± 5.7	18.41 ± 4.99	35.6 ± 9.7
L6	6	6.00 ± 0.83	$4{,}425 \pm 835$	34.1 ± 8.4	22.72 ± 2.00	29.0 ± 4.5
mean		5.81 ± 0.16	$3{,}791 \pm 576$	33.4 ± 2	17.72 ± 5.38	34.7 ± 2.4
proximal sciatic	8	6.61 ± 0.68	$7{,}599 \pm 1{,}331$	48.1 ± 9.8	59.03 ± 11.81	14.6 ± 3.9
distal sciatic	8	5.76 ± 0.87	$8{,}270 \pm 3{,}705$	50.3 ± 7.3	44.45 ± 7.32	21.1 ± 3.9
cutaneous	2	4.42 ± 0.11	439 ± 4	57.0 ± 1.1	1.80 ± 0.03	100.0 ± 0.0
peroneal	7	6.29 ± 0.41	$1{,}629 \pm 140$	53.8 ± 5.8	12.68 ± 1.71	49.6 ± 6.7
tibial	8	6.36 ± 0.92	$4{,}262 \pm 936$	46.2 ± 6.7	30.65 ± 5.53	26.4 ± 10.4
sural	6	5.26 ± 0.63	920 ± 572	49.3 ± 8.4	4.19 ± 2.02	100.0 ± 0.0

890x. Representative histological samples are depicted in Figure 4.1. The measured fiber profile area $A[f]$ included both axon and myelin sheath profiles. The entire area of the transverse nerve section $A[n]$ was also measured. For each measured fiber profile the corresponding diameter $d[f]$ was calculated as the diameter of the (imaginary) circle with the same profile area $A[f]$. Additional parameters were calculated including fiber density $Dens[f]$, relative area of the empty space between fiber profiles (further referred to as "interspace") $A[i]_{rel}$, total number of fibers $N[f]_{total}$, and relative sampling area $A[s]_{rel}$ (Table 4.1).

4.2.4 Statistical analysis of the data

Further computation, mathematical modeling, and statistical evaluation was performed using software the programs *Origin* 5.0 (Microcall Software Inc., Northampton, Massachusetts), *Statistica* 6.0 (StatSoft Inc., Tulsa, Oklahoma), and *Matlab* 6.5.1 (Mathsoft Inc., Nattic, Massachusetts). Data were analyzed using Student's t-tests (independent and paired) and analysis of variance (ANOVA). Frequency distributions of the various fiber samples were compared using the Kolmogorov-Smirnow (KS) test. For this purpose histograms with approximately $\sqrt{N[f]}$ diameter classes were used (de Jonge, 1963). Mixture modeling and the optimal statistical model selection procedure are described in Appendix B.

4.3 Results

4.3.1 Fiber morphometry

Table 4.2 summarizes the data obtained from the lumbar nerves and the spinal roots based on 72,604 individual fiber measurements. Due to the small number of collected samples from the
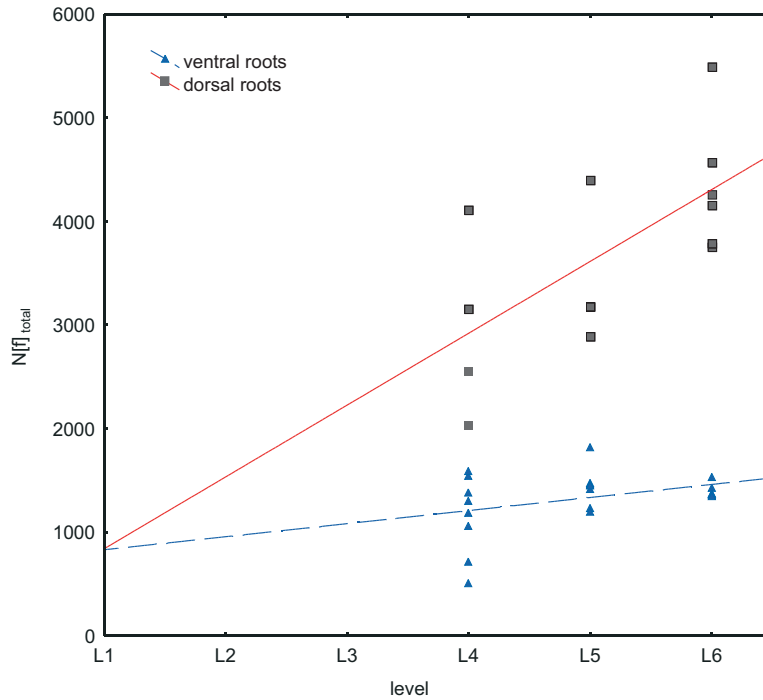
Figure 4.2: Level variation in the numbers of fibers in the lumbar spinal roots

cutaneous branch of the sciatic nerve (n=2) it was not compared statistically to other nerves or spinal roots.

4.3.2   Differences between animals

To establish possible differences between the individual animals, tissue samples were categorized by animal IDs and, additionally, by materials as ventral roots, dorsal roots, or distal nerves. In the ventral roots, differences between the different animals could be detected for each of the parameters fiber diameter, density, and interspace (one way ANOVA; $p < 0.05$). In the dorsal roots and the distal nerves, differences between the different animals could be detected only for the interspace (one way ANOVA; $p < 0.05$).

There were no animal differences for the sample-related parameters $A[s]_{rel}$ and $N[f]_{sample}$, and for $N[f]_{total}$ in any of the categories (one way ANOVA; $p > 0.05$). Therefore, observed differences were not due to the sampling.

4.3.3   Fiber numbers

Dorsal roots consistently contained more fibers than the ventral ones (all comparisons $p < 0.0001$; t-test, see also Fig. 4.2). In the dorsal roots, there was a positive correlation between the number of myelinated fibers and the lumbar level (r=0.68, $p < 0.05$). Fiber numbers varied linearly with the dorsal root level (General Regression Model; $p < 0.0001$). The following spinal

Figure 4.3: Density of fibers in roots and nerves

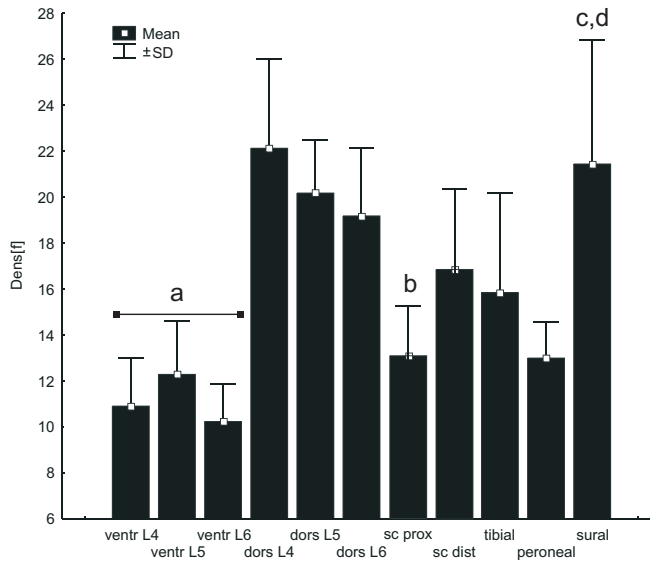Abbreviations: *ventr* - ventral, *dors* - dorsal, *sc dist* - distal sciatic nerve, *sc prox* - proximal sciatic nerve; notations: `a` - $p < 0.01$ compared to sensory nerves (roots), `b` - $p < 0.05$ compared to the proximal sciatic and the peroneal nerves, `c` - $p < 0.001$ compared to motor roots, `d` - $p < 0.01$ compared to mixed nerves.

level dependency was found for the fiber numbers in the dorsal roots $N[f] = 145.2 + 693.8 \cdot level$ ($p < 0.05$; $R^2 = 0.45$), where the level varied from 4 to 6 for L4 - L6, respectively. In contrast, in the ventral roots there was no level dependency for the fiber counts ($p > 0.05$; simple regression) and no statistically significant differences between different ventral root levels ($p > 0.05$; ANOVA) were found.

There were no differences in the fiber counts between the proximal sciatic and the distal sciatic nerves ($p > 0.05$; t-test). This allowed to use further the averaged total fiber count estimate of the two studied levels of the sciatic nerve. If this number is taken as 100% then the following ranking could be established for the fiber count estimates: the tibial had 58.8%, the peroneal had 22.5%, and the sural had 12.7% of the fibers (Table 4.2; $p < 0.05$ in all comparisons of the sequence). The cutaneous branch had 6.1% of the fibers. Altogether these distal nerves accounted for 91.4% of the averaged fiber counts of the sciatic nerve. One should note that small branches leave the sciatic nerve between proximal and distal levels.

4.3.4 Density of fibers

The density of the spinal roots and lumbar nerves was analyzed by means of univariate ANOVA. Differences in densities between the individual nerves or roots were analyzed by *post hoc* LSD tests (Fig. 4.3). Functional character (i.e. sensory, motor, or mixed) of the nerves or the roots could account for the encountered variability in density ($p < 0.00001$). Density did not vary significantly between the individual ventral roots or individual dorsal roots ($p > 0.05$, all intra
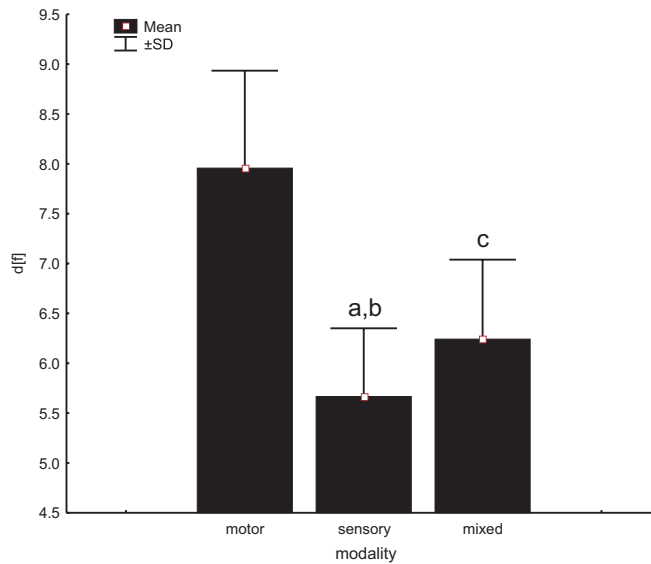
Figure 4.4: Fiber diameter variation with functional modality

Notations: *motor* includes data for the ventral roots, *sensory* includes the data for the dorsal roots and the sural nerve, *mixed* includes the data for the sciatic, tibial, and peroneal nerves. LSD tests: a, c - $p < 0.0001$ compared to motor; b - $p < 0.05$ compared to mixed.

group comparisons; Fig. 4.3). In contrast, in the *motor* ventral roots density was smaller than in the sensory dorsal roots (all comparisons $p < 0.001$; Fig. 4.3). The *sensory* sural nerve was comparable to the dorsal roots (all comparisons, $p > 0.21$) and markedly different from the motor ventral roots (all comparisons, $p < 0.0001$) and the mixed nerves (all comparisons, $p < 0.01$). Values of the density of the *mixed* nerves were between the values of the ventral and dorsal roots. The distal sciatic had a higher density compared to the proximal sciatic and peroneal nerves ($p < 0.05$; both comparisons) but not compared to the tibial nerve ($p > 0.05$). The proximal sciatic, the peroneal, and the tibial nerves were not different from each other with regard to the density ($p > 0.05$). Therefore, by their densities, the proximal sciatic and peroneal nerves were more "motor-like", while the distal sciatic was more "sensory-like".

The density of the spinal roots was additionally analyzed by means of regression analysis. In ventral or dorsal roots, there was no segmental dependency (from L4 to L6) of the fiber density (simple regression; $p > 0.05$).

4.3.5   Cross-sectional area of the nerve or root

The cross-sectional area of the spinal roots was analyzed by means of ANOVA and regression analysis. The segmental variation in the dorsal root cross-sectional area was tested by regression analysis. Dorsal root area varied linearly with the segmental level: $A[n] = -22,155 + 41,028 \cdot level$ [µm^2] where the level varied from 4 to 6 for L4 - L6, respectively ($p < 0.05$; $R^2 = 0.47$). In contrast, the ventral roots were not different from each other with regard to their area (in all comparisons $p > 0.05$; LSD post hoc test). The dorsal roots L5

and L6 were larger than the corresponding ventral roots ($p < 0.05$; LSD post hoc test). The distal sciatic nerve was not different from the proximal sciatic nerve ($p > 0.05$; LSD post hoc test). If the averaged area of the two studied levels of the sciatic nerve is taken as 100% then the following ranking could be established for the nerve cross-sectional area: the tibial had 54.2%, the peroneal had 24.3%, and the sural had 7.5% of the area (Table 4.2; $p < 0.05$ in all comparisons of the sequence). The cutaneous branch had 3.7% of the area. Altogether these distal nerves accounted for 89.7% of the averaged sciatic nerve area.

4.3.6 Interspace

In the spinal roots, there was no level variation in interspace. Ventral and dorsal roots were not different from each other, but had a smaller relative interspace than the nerves. Nerves were not different from each other with the only exception of the peroneal interspace, which was significantly larger than the tibial interspace ($p < 0.05$, t-test). Observed variation in the interspace could be explained on the basis of grouping by the functional modality of the nerves or roots (ANOVA, $p < 0.00001$). The mixed nerves had higher interspace than the motor ventral roots ($p < 0.0001$; LSD post hoc test) and sensory nerves and roots ($p < 0.0001$; LSD test post hoc test). There was no difference in the interspace between the (motor) ventral roots and the (sensory) dorsal roots and sural nerve ($p > 0.05$; LSD post hoc test).

4.3.7 Fiber diameter

Intra-sample heterogeneity with respect to fiber size

Table 4.3: Comparisons between subsamples constituting the studied materials

material	n	ANOVA [%]	t-test [%]	KS-test [%]
ventral roots				
L4	7	28.6	17.6	0
L5	7	28.6	13.9	0
L6	6	33.3	22.2	0
dorsal roots				
L4	3	100.0	77.8	33.3
L5	4	50.0	33.3	0
L6	3	83.3	63.9	8.3
distal nerves				
proximal sciatic	8	87.5	50.0	0
distal sciatic	8	100.0	77.8	33.3
tibial	8	87.5	71.7	25.0
peroneal	7	71.4	47.6	0
sural	5	80.0	49.3	0

Numbers denote the fraction of statistically significant outcomes among all tests performed. n - number of materials consisting of more than one subsample; Within each set of subsamples also t- and KS-tests were performed between all subsamples. The number of tests was given by ($N[subsamples]^2 - N[subsamples])/2$.

Sections containing more than one subsample were analyzed for their intra-sample heterogeneity. The subsamples within one section were compared using one-way ANOVA, Student's t-test, and Kolmogorov-Smirnow's test (KS). Frequencies of significant outcomes (i.e. positive tests) are presented in percents (Table 4.3). The outcomes of the 3 tests correlated strongly to each other (ANOVA and t - r=0.96, $p < 0.0001$; t and KS - r=0.82, $p < 0.01$; KS and ANOVA r=0.69, $p < 0.05$; where r denotes Pearson's correlation coefficient).

There were marked differences in t-test frequencies ($p < 0.05$, one way ANOVA) and intra-sample ANOVA frequencies ($p < 0.01$, one way ANOVA) between the categories ventral roots, dorsal roots, and distal nerves. Such effect was not found in the frequencies of the KS test ($p > 0.05$, one way ANOVA). Therefore, the shape of the diameter distribution histograms was not so sensitive in highlighting intra-sample heterogeneity, as was the mean diameter. For the sake of clarity, further in this section only t-tests' results are commented. Intra-sample heterogeneity was larger in the dorsal roots ($p < 0.05$; LSD post hoc test) and in the peripheral nerves ($p < 0.01$; LSD post hoc test) compared to ventral roots. This confirmed the visual impression of patchiness in the areas occupied by small fibers in the samples of dorsal roots (Fig. 4.1). In the dorsal roots, particularly, differences could be observed in L4 and to lesser extent in L6. In the peripheral nerves, differences could be observed in the distal sciatic and the tibial nerves.

Left-right differences

Table 4.4: Side differences with respect to the fiber diameter

material	n	Individual samples		Pooled samples
		t-test [%]	KS-test [%]	t-test
ventral roots				
L4	4	50.0 (R)	25.0	$p < 0.0001$
L5	3	33.3 (L)	33.3	$p > 0.05$
L6	3	66.7	35.0	$p > 0.05$
dorsal roots				
L4	1	100.0 (R)	100.0	$p < 0.0001$
L5	2	100.0 (L)	0.0	$p < 0.0001$
L6	3	66.7	33.3	$p < 0.0001$
distal nerves				
proximal sciatic	4	75.0 (R)	0.0	$p > 0.05$
distal sciatic	4	75.0 (R)	25.0	$p < 0.0001$
peroneal	3	33.3 (L)	0	$p > 0.05$
tibial	4	50.0	50.0	$p < 0.0001$
sural	3	66.7	33.3	$p < 0.0001$

Percentages denote the fraction of statistically significant outcomes among all tests performed; n - number of tests performed; R - prevalent $R > L$ disposition; L - prevalent $L > R$ disposition.

To test for the presence of side differences, series of t-tests and KS-tests were performed between the different samples of the individual animals (Table 4.4). Although left-right differences were encountered in a number of cases, no systematic prevalence of a side effect could be found. In addition, the data on fiber diameters were pooled for the left and the right side, respectively, and a t-test was performed. Pooling the data further reduced the number of

significant comparisons (Table 4.4). Further, frequencies of the tests were classified in three categories: ventral roots, dorsal roots, and distal nerves. No differences were encountered in the comparison between these categories for the outcomes of any of the tests ($p > 0.05$; one way ANOVA).

4.3.8 Segmental and proximo-distal differences in the means

The mean fiber diameters of the dorsal roots were not different from one another (ANOVA; $p > 0.05$ all post hoc comparisons by LSD test). Ventral roots were not different from one another (ANOVA, $p > 0.05$ all post hoc comparisons by LSD test). Per spinal level, ventral roots had larger mean diameters than the dorsal roots (ANOVA, $p < 0.05$ all post hoc comparisons by LSD test). From the peripheral nerves, the proximal sciatic was not different from the distal sciatic, peroneal, and tibial nerves ($p > 0.05$; t-test) but was different from the sural nerve ($p < 0.05$; t-test). The distal sciatic was not different from the peroneal, tibial, and the sural nerves ($p > 0.05$; t-test). The tibial nerve was not different from the peroneal nerve ($p > 0.05$; t-test) but was different from the sural nerve ($p < 0.05$; t-test). The peroneal nerve was different from the sural nerve ($p < 0.05$; t-test). Observed variation could be explained by classification according to the functional modality (ANOVA, $p < 0.0001$). The sensory nerves and roots had a smaller mean diameter than the motor ventral roots ($p < 0.0001$; LSD test) and mixed nerves ($p < 0.05$; LSD test) (see Fig. 4.4). Motor ventral roots in their turn were also different from the mixed nerves (LSD test, $p < 0.0001$; see Fig. 4.4). Level and segmental distinctions will be commented further in view of the population modeling.

4.3.9 Optimal population models of the size distributions

Population mixture modeling

To test for normal distribution of the fiber diameters we first modeled the fiber populations with a single component Gaussian model (Appendix eq. (B.1)). In all of the cases, the Gaussian model was ruled out by the Schwartz Bayesian Information Criterion (SBIC; Schwartz (1987)) in favor of a lognormal mixture model. Therefore, the normal distribution of the fiber diameters was rejected. Based on this we evaluated further the lognormal (LN1 - LN5) models (Fig. 4.5).

Based on its frequency of selection using SBIC, the optimal model for the dorsal roots, the ventral roots, and the peroneal nerve was LN3. Based on this model, three populations of fibers (noted further as $\mathbb{A}$, $\mathbb{B}$, and $\mathbb{C}$) were discerned in the ventral roots, the dorsal roots, the proximal sciatic, the distal sciatic, and the peroneal nerve (Table 4.5).

For the tibial and the sural nerves, the optimal model was LN2. Based on this model, two populations of fibers noted further as $\mathbb{A}'$ and $\mathbb{B}'$ were discerned in the tibial and the sural nerves (Table 4.5). An optimal model could not be selected for the sciatic nerve by the SBIC criterion only. In the distal sciatic, the most prevalent LN4 model consistently yielded population shares less than 5%, therefore LN3 was preferred. After inspection of the population histograms and the sections, LN3 was selected for the proximal sciatic nerve. For the cutaneous branch of the sciatic nerve one of the samples yielded LN2 and the other LN3. Inspection of the sections showed indeed differences between the two samples and an optimal model could not be selected. The LN3 model of the tibial nerve will be commented further in view of the proximo-distal analysis of the populations and is presented as well. Optimal models are presented in Table 4.5 and their parameter values in Appendix Table 4.C.1.
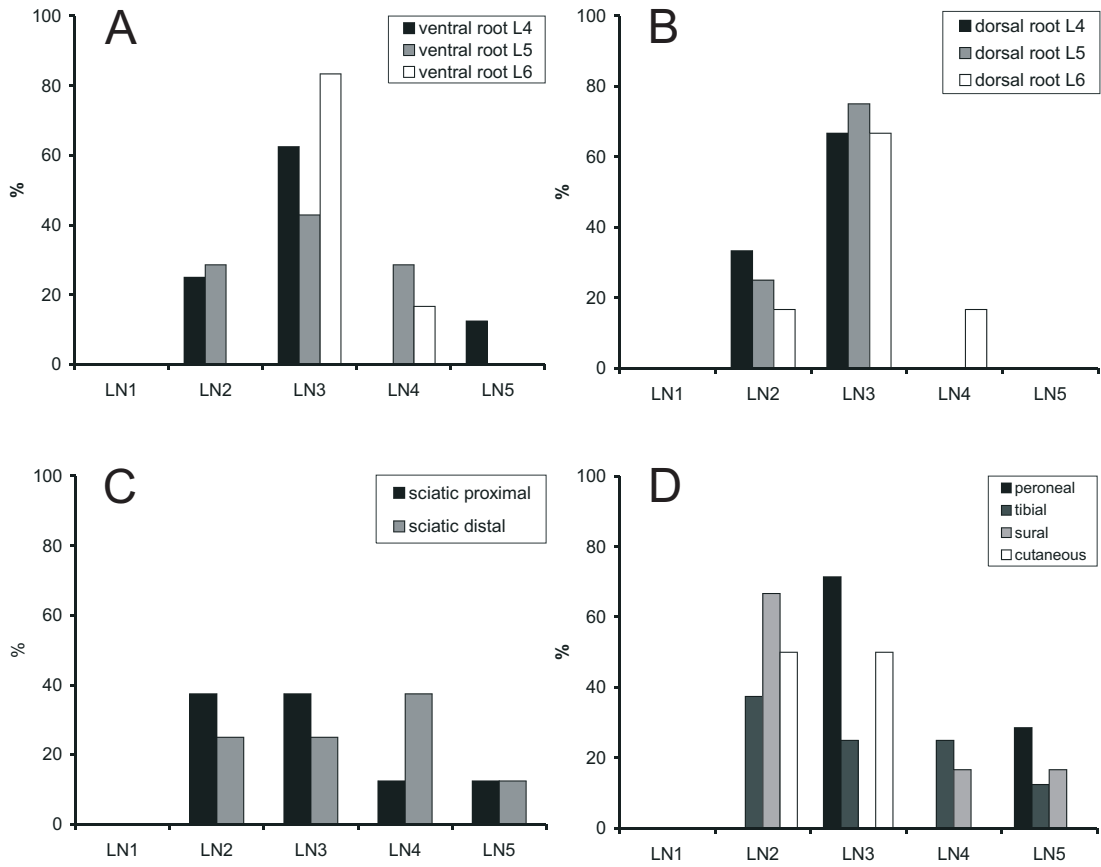
Figure 4.5: Prevalent models

Occurrences of models minimizing SBIC in the ventral roots, dorsal roots, and the peripheral nerves:
A - ventral roots; B - dorsal roots; C - sciatic nerve; D - tibial, peroneal, cutaneous, and sural nerves.

Table 4.5: Optimal model selection

material	model	criterion
ventral root L4	LN3	SBIC
ventral root L5	LN3	SBIC
ventral root L6	LN3	SBIC
dorsal root L4	LN3	SBIC
dorsal root L5	LN3	SBIC
dorsal root L6	LN3	SBIC
proximal sciatic	LN3	SBIC + Population shares
distal sciatic	LN3	SBIC + Population shares
peroneal	LN3	SBIC
tibial	LN2	SBIC
sural	LN2	SBIC

Motor ventral roots were characterized by a shift in the distribution towards larger fiber diameters as compared to the dorsal roots and the sciatic nerve (Fig. 4.5). This shift was most pronounced in the $\mathbb{C}$ population with a peak position around 12 μm (Fig. 4.6). Classified by the respective peak positions of the LN3 model (Table 4.C.1), *population* $\mathbb{A}$ comprised the small myelinated fibers, $\mathbb{B}$ - larger myelinated fibers and $\mathbb{C}$ - the largest myelinated fibers in each nerve or root (Fig. 4.6). Classified by the respective peak positions of the LN2 model (Table 4.C.1), population $\mathbb{A}'$ comprised the smaller myelinated fibers and $\mathbb{B}'$ the larger myelinated fibers in each nerve or root (Fig. 4.6). Comparisons using this classification are elaborated in the subsequent parts of this chapter.

Statistical analysis of the models

With respect to the positions of the peaks, there were no left-right differences for any of the materials (all t-tests, $p > 0.05$). With respect to the population shares, there were left-right differences only in the L6 ventral root for the populations $\mathbb{B}$ and $\mathbb{C}$ (t-test, $p < 0.05$) and in population $\mathbb{A}$ of the proximal sciatic (t-test, $p < 0.05$). There were inter-animal differences for the positions of the peak in the $\mathbb{A}$ (ANOVA, $p < 0.001$) and the $\mathbb{C}$ populations (ANOVA, $p < 0.0001$) in the ventral roots. Inter-animal differences were also found for the positions of the peak in $\mathbb{A}$ (ANOVA, $p < 0.05$) and $\mathbb{B}$ populations (ANOVA, $p < 0.05$) of the dorsal roots. Furthermore, inter-animal differences occurred in the positions of the peak for populations $\mathbb{A}$ and $\mathbb{C}$ (ANOVA, $p < 0.05$) in the peripheral nerves. With respect to the population shares there were no differences in the dorsal roots and only an occasional difference in population $\mathbb{A}$ of the ventral root L6 and of the sural nerve.

Inter-segmental and proximo-distal analysis of the lumbar nerves and the spinal roots

Further, we focused on analysis of the peripheral nerves and spinal roots using exclusively the LN3 model. The choice of model was based on its occurrence as the optimal model at the level of the spinal roots and the proposition to compare only analogous models to each other. Parametric comparisons of the peak positions and the population shares were performed using serial t-tests. Populations, described by the models, were considered equal if both their peak positions and their shares were not significantly different. Two models were considered equal if all of their corresponding populations were found equal.

Two dispositions were defined in the comparisons between the different roots or nerves: "mixing" if the peak positions were not significantly different but the shares were and "shifting" if the peak positions were significantly different regardless of the outcome of the shares' comparison.

Transitions from the spinal roots to the proximal sciatic nerve are depicted in Figure 4.8. In summary, ventral roots were more similar to the nerve than the dorsal roots were. By its composition, among the ventral roots L5 was the most similar to the nerve and L6 was least similar among the dorsal roots (Fig. 4.8A). The overall effect for the ventral root L5 was mixing, while for dorsal root L6 it was shifting. Population $\mathbb{A}$ in the ventral roots (L4 - L6) matched population $\mathbb{A}$ in the proximal sciatic nerve, whereas population $\mathbb{A}$ of the dorsal roots (L4 - L6) was shifted to the left (Fig. 4.8B) compared to population $\mathbb{A}$ of the proximal sciatic.

Transitions from the sciatic nerves to its major branches (i.e. tibial, peroneal, and sural nerves) are depicted in Figure 4.9. In general, during this transition most changes occurred in
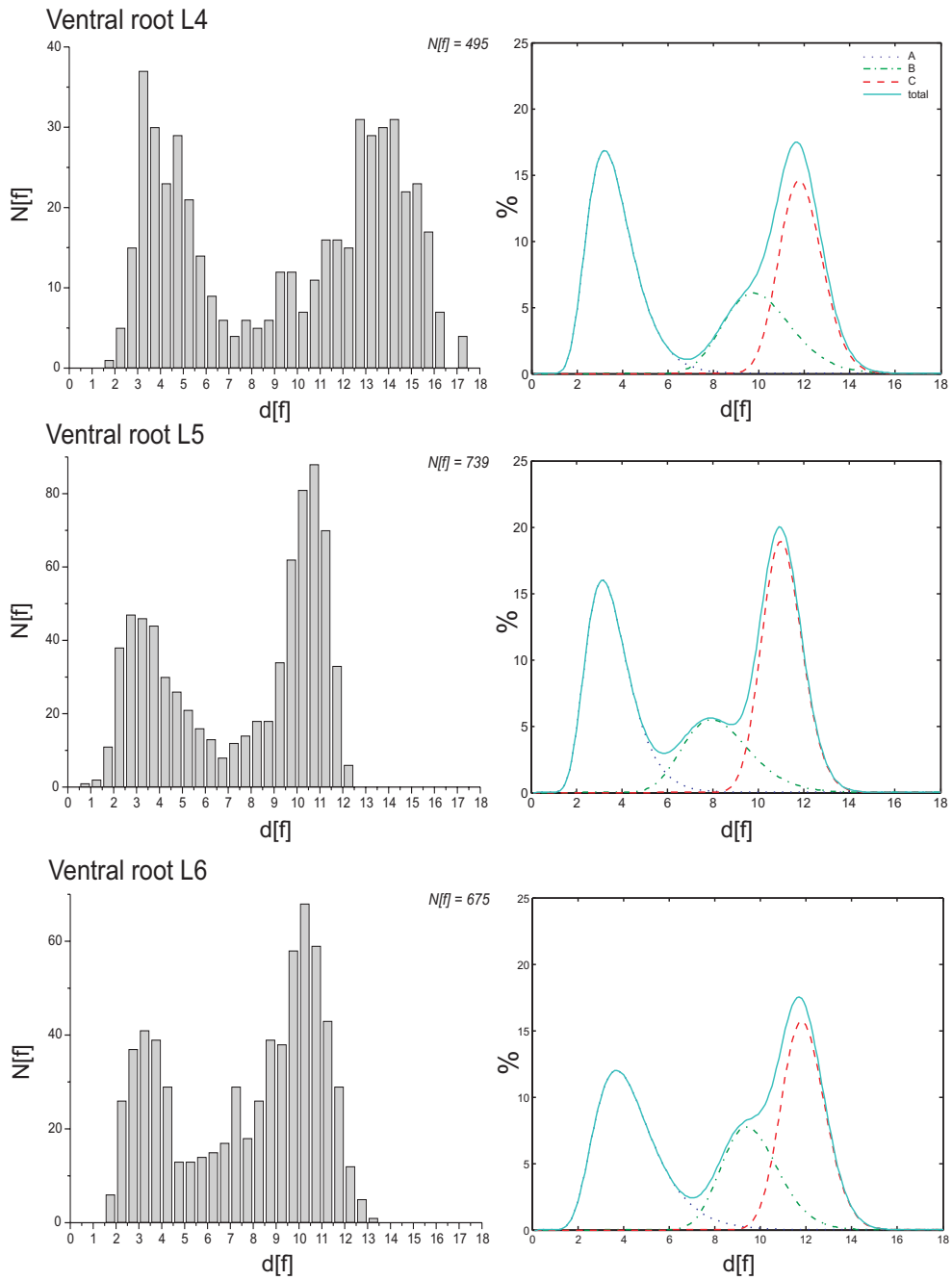
Figure 4.6: Representative cases with optimal models

Representative histograms (left) and corresponding averaged optimal models (right). Populations are shown separately and in superposition ("total").
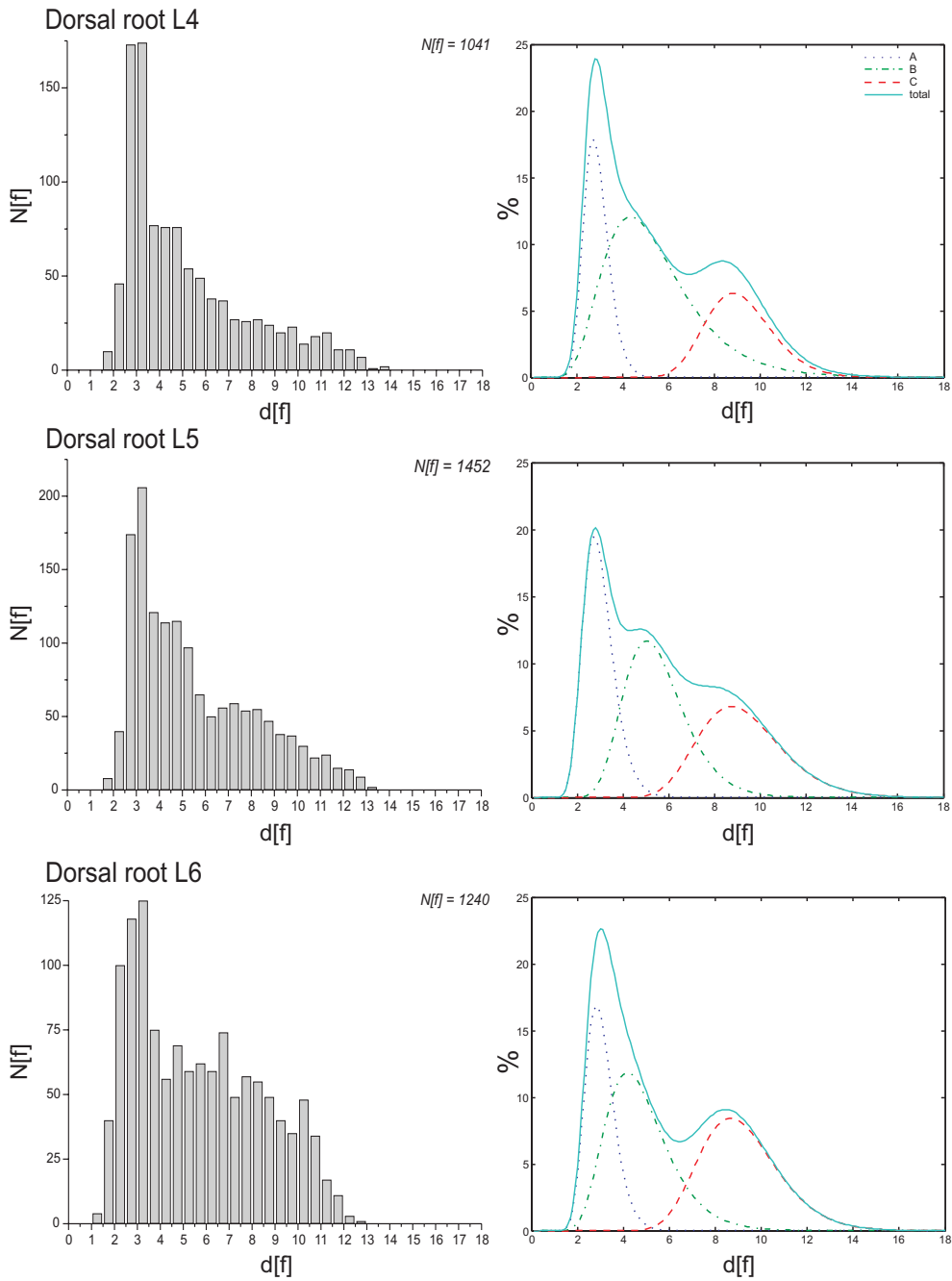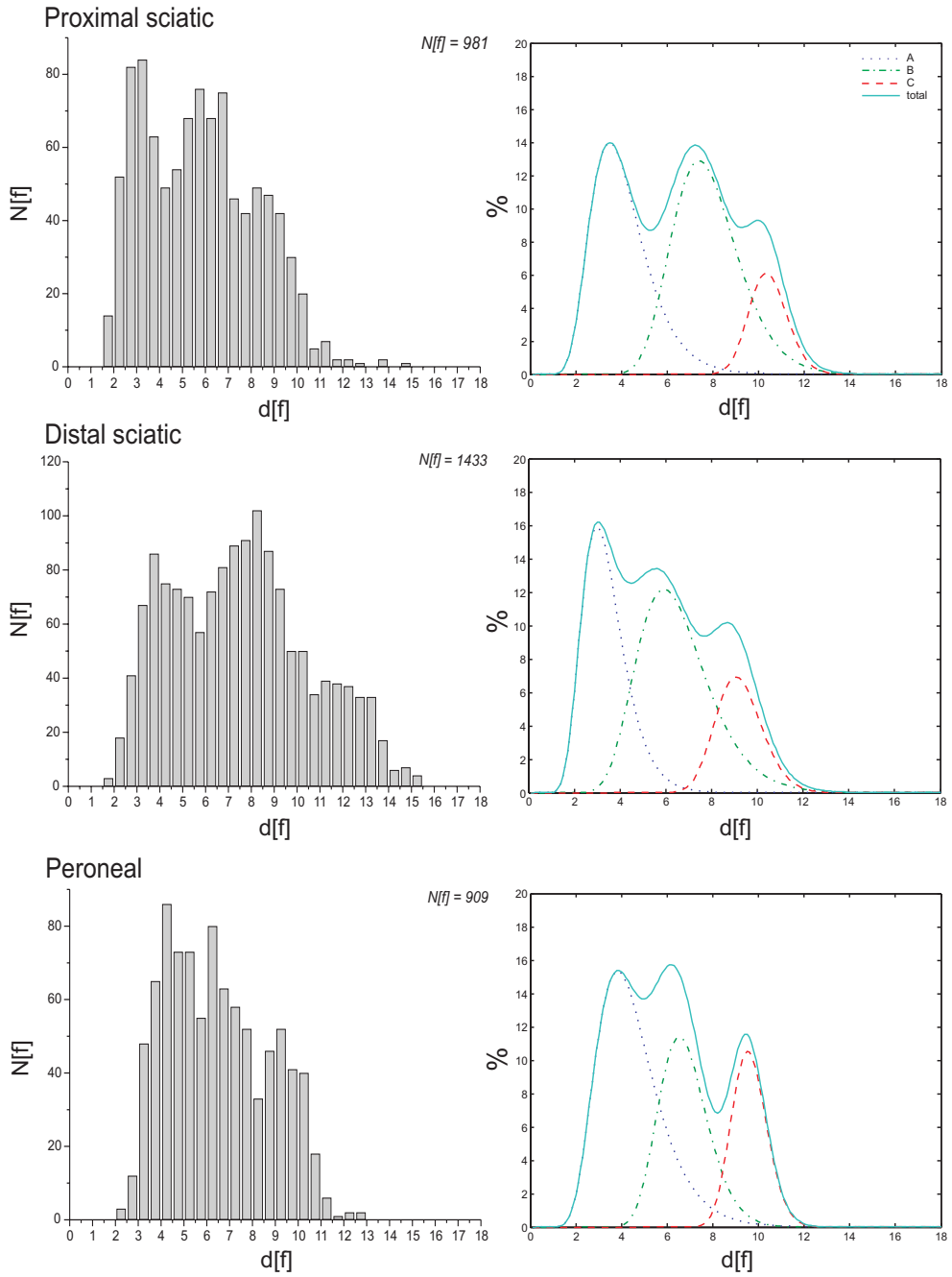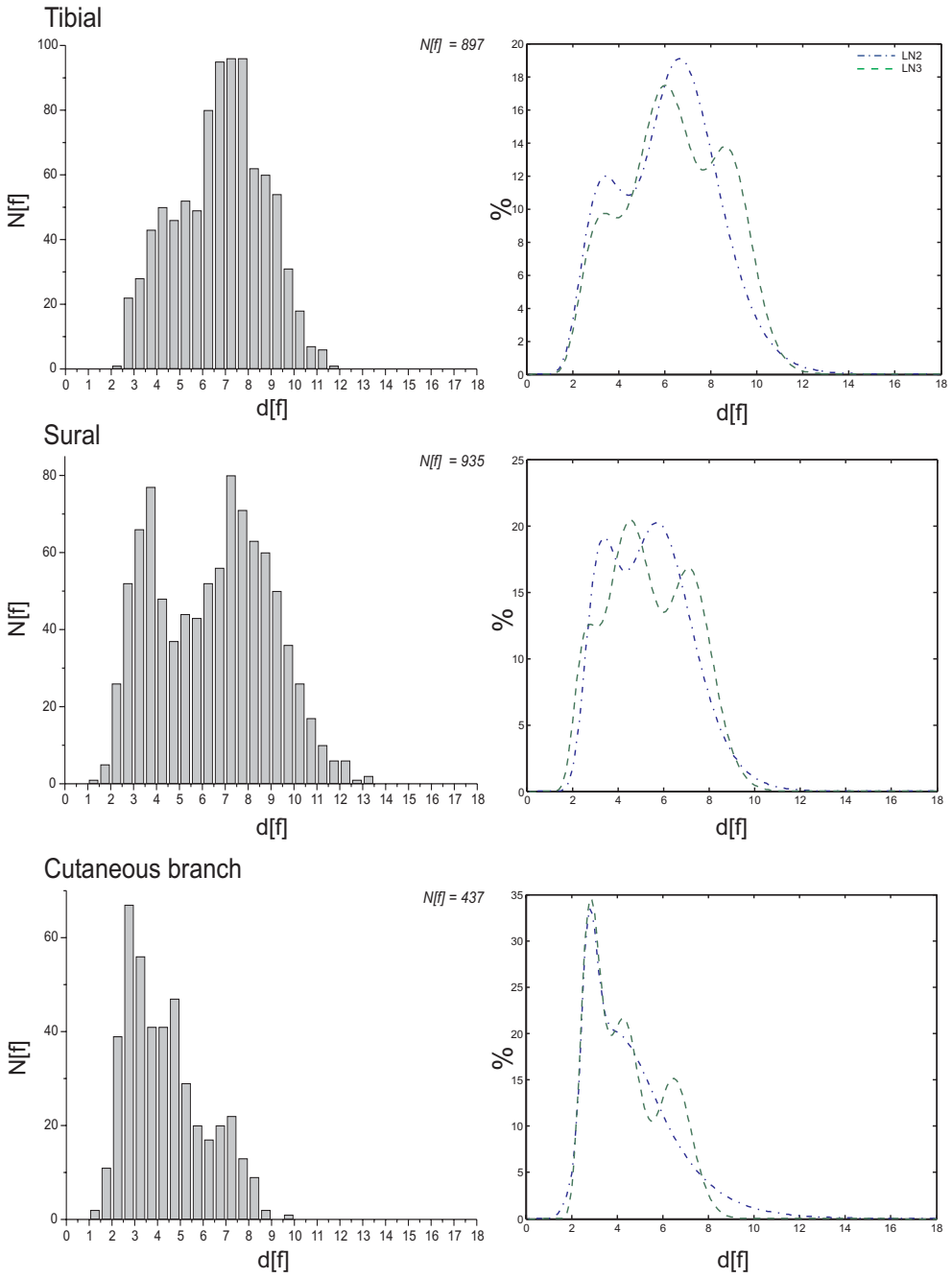
Figure 4.6 (continued)

Figure 4.6 (continued)

Figure 4.6 (continued)

Populations are shown in superposition for the LN2 and LN3 models (see text).
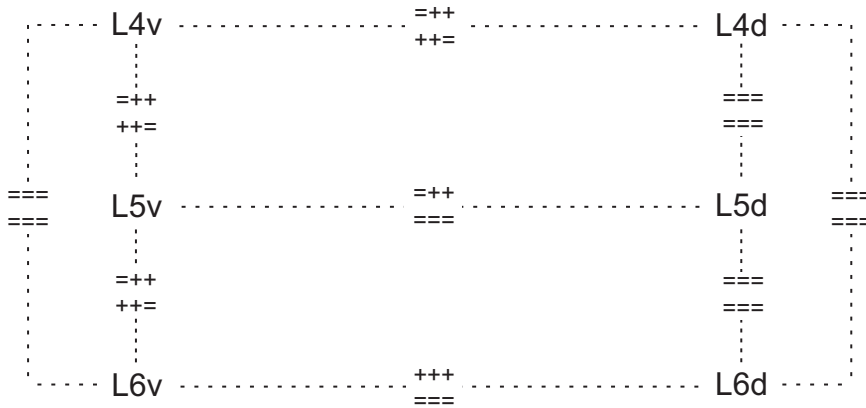
Figure 4.7: Comparisons of the spinal roots

Upper position indicates peak positions comparisons; lower position - shares comparisons. *Plus* signs denotes statistically significant test outcomes; left to right - $\mathbb{A}$, $\mathbb{B}$, and $\mathbb{C}$ populations. From the discerned populations, most changes occurred in population $\mathbb{B}$ of the ventral roots. The dorsal roots (L4 - L6) were found equal to each other but not equal to the ventral roots at the same levels. The differences were concentrated in population $\mathbb{B}$ but some dissimilarity was also noted in $\mathbb{C}$ and $\mathbb{A}$. Ventral root L6 was equal to L4. The peak position of population $\mathbb{B}$ was shifted to smaller values in ventral root L5 compared to ventral root L4 and L6 (see Fig. 4.6 and Table 4.C.1).

population $\mathbb{A}$. Population $\mathbb{B}$ made a shift to smaller sizes during the transition to the distal part of the sciatic nerve and was redistributed more to the tibial nerve. The observed effects were probably due to functional differences between the nerves. Population $\mathbb{C}$ did not change in the transition from the proximal sciatic to the peroneal and tibial nerves. The sural nerve was most different compared to the proximal sciatic, while the tibial nerve was the most similar. The tibial and peroneal nerves had equal populations $\mathbb{B}$ and $\mathbb{C}$ and showed mixing in $\mathbb{A}$ (Fig. 4.9A).

Based on the fiber number estimates for the different distal nerves as fractions of the fiber numbers of the sciatic nerve (p. 76) a compound LN3 model was computed to approximate the sciatic nerve according to the equation:

$$LN3_{compound} = 0.59LN3_{Tib} + 0.22LN3_{Per} + 0.13LN3_{Sur} + 0.06LN3_{Cut} \qquad (4.1)$$

Similarity between the compound model and the LN3 models of the sciatic nerves (Fig. 4.9B) was quantified using the Pierson's correlation coefficient r. Proximal sciatic was more similar to the compound model ($r = 0.92$, $p < 0.05$) than to the distal sciatic ($r = 0.89$, $p < 0.05$). Distal sciatic was also similar to the compound model ($r = 0.97$, $p < 0.05$) (ANOVA - overall goodness of fit, all $p < 0.0001$). From this, it can be concluded that the composition of the distal sciatic can be explained mostly by the composition of its constituting nerves.
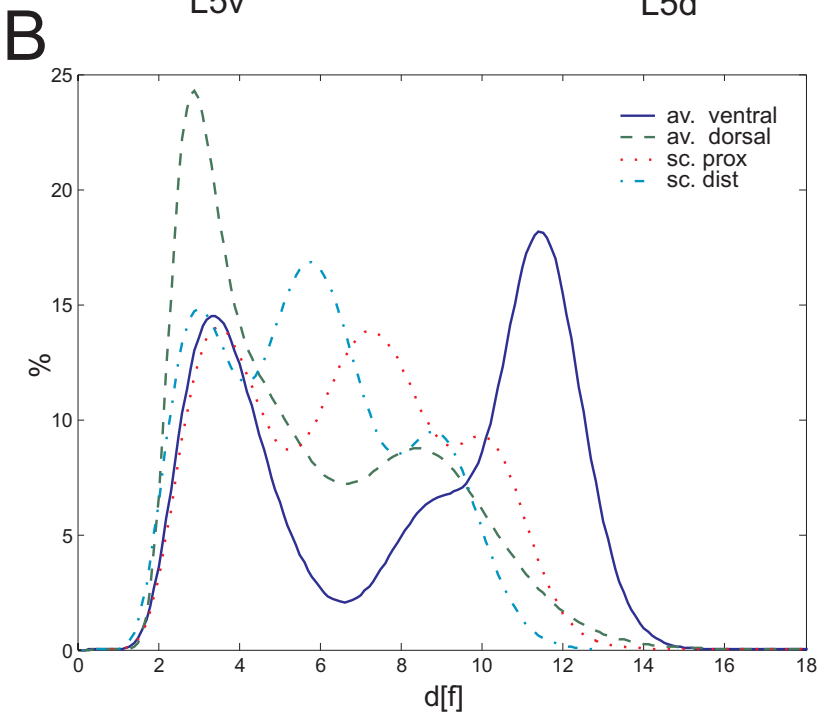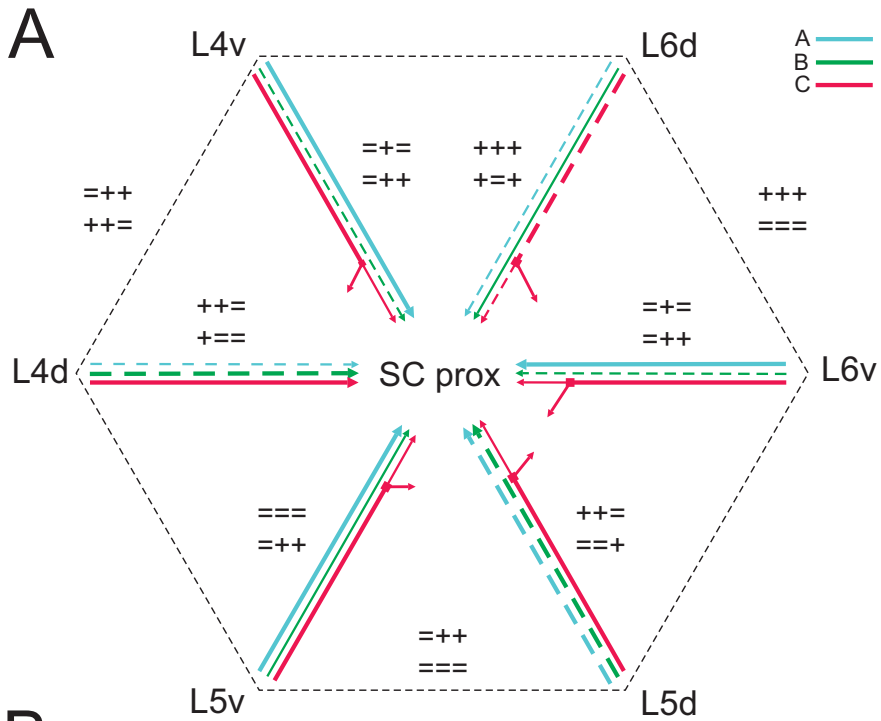
Figure 4.8: Transitions to the sciatic nerve

Figure 4.8 (continued): A - Population comparisons between the spinal roots and the proximal sciatic nerve; v - ventral, d - dorsal. Line thickness corresponds to population share comparison; line shape corresponds to population peak position comparison - dashed lines denote difference in the positions of the peak positions. *Plus* sign denotes significant difference; *equal* sign denotes non-difference. Upper position indicates peak positions comparisons; lower position - shares comparisons. Left to right - $\mathbb{A}$, $\mathbb{B}$, and $\mathbb{C}$ populations. Thin arrows indicate possible departure of fibers from *population* $\mathbb{C}$ into other nerves leaving the lumbar plexus. B - Interaction between the populations in the LN3 model; $av.$ - averaged, $sc.$ $prox$ - proximal sciatic, $sc.$ $dist$ - distal sciatic. The populations of the averaged ventral (solid line) and the averaged dorsal roots (dashed line) were plotted for comparison with the populations of the proximal (dotted line) and the distal sciatic (dash-dotted line) nerves.

4.3.10 Estimation of the conduction velocities of modeled fiber populations and the corresponding borders between the fiber classes

Table 4.6: Fiber conduction velocities estimation according to the ABK equations

	Fiber class	
Published data	$A\alpha$	$A\beta$
Peak position (m)	9.00 µm	4.36 µm
Share (a)	40.2 %	59.8 %
Spread (w)	0.23	0.46
MCV	38.7 ± 9.0 m/s	
Calculated	$A\alpha$	$A\beta$
FCV	51.3 m/s	20.1 m/s
MCV(LN2)	38.74 m/s	

Model notations are explained in Appendix B; FCV - peak fiber class conduction velocity estimate $FCV_{pop} = k_{pop}m_{pop}$; MCV - mean conduction velocity. $MCV(LN2)$ was estimated according to Appendix eq. (B.12) having p=1: $MCV(LN2) = k_{A\alpha}a_{A\alpha}m_{A\alpha}e^{\frac{3w_{A\alpha}^2}{2}} + k_{A\beta}a_{A\beta}m_{A\beta}e^{\frac{3w_{A\beta}^2}{2}}$

To establish the identities of the modeled fiber populations we used the relationship between the external diameter of a myelinated nerve fiber and its conduction velocity as established by the works of Arbuthnott, Boyd, and Kalu (Arbuthnott et al., 1977; Boyd and Kalu, 1979; Arbuthnott et al., 1980). In short, it was shown that the variation of the conduction velocity with the fiber diameter could be approximated by a piecewise linear regression function (referred to as the ABK equations). The authors calculated that for large fibers (e.g. $A\alpha$ fibers) in the cat, the overall diameter was related to fiber conduction velocity by a factor of 5.7, while for the smaller fibers ($A\beta$, $A\gamma$, and $A\delta$) the factor was 4.6.

Vleggeert-Lankamp et al. (2004) showed a functional correlation between a lognormal mixture model of the diameter distribution histograms in a peripheral nerve and its electrophysiologically identified $A\alpha$ and $A\beta$ fiber classes. To show applicability of this approach in the rat we reanalyzed their published data for the control nerves using the ABK equations (Table 4.6). Mean conduction velocity (MCV) and conduction velocities corresponding to the fiber class conduction velocity (FCV) at peak positions were estimated for the Vleggeert-Lankamp
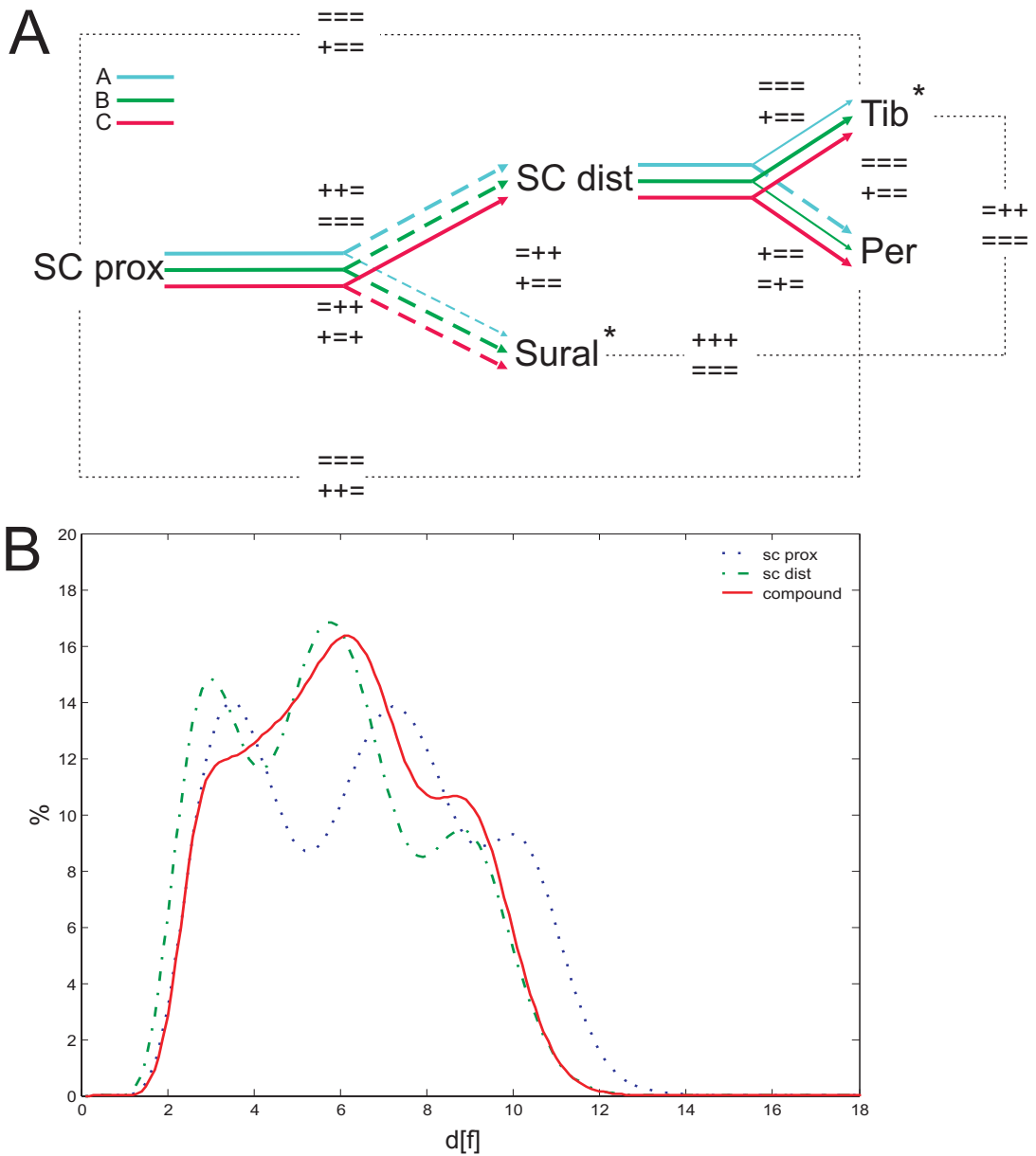
Figure 4.9: Comparisons of the sciatic nerve

A - Population comparisons in the system of the sciatic nerve. Line thickness corresponds to comparisons between population shares; line shape corresponds to comparisons between population peak positions - dashed lines denote difference in the positions of the peak positions. *Plus* sign denotes significant difference; *equal* sign denotes non-difference. Upper position indicates peak positions comparisons; lower position - shares comparisons; left to right - $\mathbb{A}$, $\mathbb{B}$, and $\mathbb{C}$ populations. * - optimal model - LN2. B - Composition of the sciatic nerve (*sc. prox* - proximal, *sc. dist* - distal) compared to a superposition of its tributary branch models noted as *compound*, see eq. (4.1).

et al. nerve model (Table 4.6). Calculations showed, that there was a quantitative agreement between the MCV estimates and the experimental data in the rat. Therefore, the use of the ABK equations in the rat was justified. Further, borders between the fiber populations in terms of diameters and corresponding conduction velocities were calculated (Fig. 4.10). To avoid the shifting and mixing effects already discerned in the peripheral nerve composition, we focused on the "pure" fiber populations in the ventral and dorsal roots in order to establish the functional identity of the populations in the distal nerves.

The smallest fibers that could be measured light-microscopically in our material were 1 μm in diameter that corresponded to conduction velocity of 4.6 m/s and it was taken as the lower border for the $A\delta$ and $A\gamma$ fiber classes. Calculated borders between the fiber populations matched well to the available literature data (Fig. 4.10). Therefore, the border between the $A\alpha$ and $A\gamma$ fibers was set to 31.2 m/s; the border between the $A\delta$ fibers and $A\beta$ fibers was set to 16.4 m/s; border between the $A\alpha$ and $A\beta$ fibers was set to 41.0 m/s. In the ventral roots, 2 sub-populations of $A\alpha$ fibers (termed $A\alpha^1$ and $A\alpha^2$) were distinguished with a border between them at 58.0 m/s.

4.3.11   Identities of the statistically modeled fiber populations
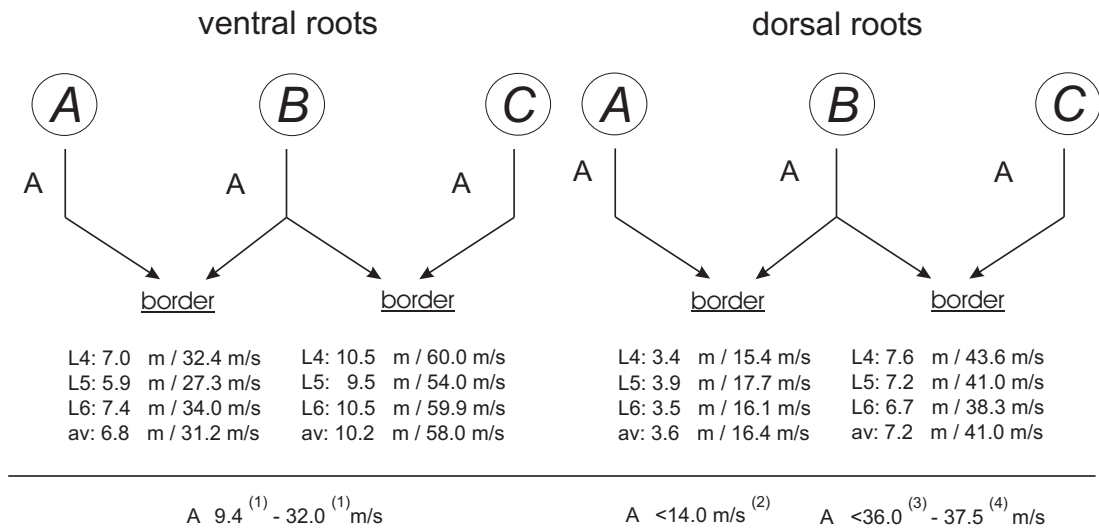
Figure 4.10: Calculated borders between the fiber populations compared to literature data

Borders are calculated according to Appendix eq. (B.15); corresponding conduction velocities (m/s) are estimated according to ABK equations; (1) - Gokin et al. (2001); (2) - Djouhri and Lawson (2004); (3) - Doncker et al. (2003); (4) - Lewin and McMahon (1991).

Borders between the $A\alpha$, $A\beta$, $A\gamma$, and $A\delta$ fiber classes identified in the previous section were used further in the identification of the fiber populations discerned in the peripheral nerves (Table 4.7). From the calculated borders between the fiber populations (Fig. 4.11A) and the correlation analysis of the population's shapes and positions it can be concluded that, in the

mixed nerves, $A\gamma$ fibers come from population A in the ventral roots and $A\delta$ fibers come from the population $\mathbb{A}$ of the dorsal roots to form population $\mathbb{A}$ of the mixed nerves (Fig. 4.11B). In order to form *population* $\mathbb{B}$ of the mixed nerves, $A\beta$ fibers come from population $\mathbb{B}$ of the dorsal root, while sensory $A\alpha$ fibers come from population $\mathbb{C}$ of the dorsal roots (Fig. 4.11B). In order to form *population* $\mathbb{C}$ of most mixed nerves, motor $A\alpha$ fibers come from ventral root populations $\mathbb{B}$ and $\mathbb{C}$ and intermingle with the sensory $A\alpha$ fibers from dorsal root population $\mathbb{C}$ (Fig. 4.11 A and B).

4.4 Discussion

4.4.1 Choice of the optimal statistical population models

Research on finite mixture distributions developed methods to estimate model parameters and statistical criteria to identify the optimal number of components in the mixed distribution underlying a particular set of data (Titterington, 1990). In this chapter, optimal models of the individual tissue samples were selected by the combined use of the SBIC criterion favoring the parsimony of modeling and an additional criterion restricting the minimal shares of the modeled fiber populations. Due to the variability encountered in the same root or nerve (i.e. that different samples were described by optimal models with different number of components) the optimal model at the level of all samples of a particular nerve or root (i.e. at population level) was selected based on its prevalent occurrence. Due to the limited number of available animals it is difficult to explore further the sources of variability in the optimal model selection. For the mixed nerves, three-component models were optimal (Fig. 4.6), while for the predominantly sensory sural nerve, two-component models were optimal. Bimodal distributions in the histogram of the sural nerve were described before for human (Jacobs and Love, 1985) and rat (Appendix Table 4.A.1 and Jeronimo et al. (2005)). Therefore, we can speculate that two-component models will be preferred for sensory nerves.

4.4.2 Relationship between nerve fiber dimensions and its conduction velocity

We suggest that the relationship between the conduction velocity and fiber diameter obtained in the cat can be used in the rat. This is also in agreement with corresponding measurements in quail (Sakaguchi et al., 1993), pigeon (Necker and Meinecke, 1984), and human nerves (Tackmann et al., 1976). Therefore, such relationship probably reflects structural laws optimizing the conduction in the myelinated fibers as suggested by Rushton (1951).

Initial studies in myelinated fibers suggested a linear relationship (Gasser and Erlanger, 1927) that was later disputed by Blair and Erlanger (1933). However, later observations (Gasser and Grundfest, 1939; Hursh, 1939) and theoretical considerations (Rushton, 1951) ruled in favor of a linear relationship between the diameter of a myelinated fiber and its conduction velocity. The extensive functional and morphometric studies performed in 1970-80 by Arbuthnott, Boyd and Kalu yielded the formulae for the different fiber classes used in this study (Arbuthnott et al., 1977; Boyd and Kalu, 1979; Arbuthnott et al., 1980). Nevertheless, as we have shown in Appendix B, the proposed statistical approach does not necessarily require a linear relationship. Similar analysis was also performed with the power law relationship proposed by Coppin and Jack (1972) (i.e. $V(d) = 1.5\,d^{3/2}$) and it gave comparable results (data not shown).

4.4.3   Identities of the statistically modeled fiber populations

Different myelinated fiber types can be discerned physiologically and anatomically by their conduction velocity and their diameter, respectively. This chapter addresses the different myelinated fiber types in terms of population mixture modeling of their fiber diameter distributions. We could assign functional identities to the so modeled fiber populations corresponding to existing physiological sub-divisions of the fiber types (Table 4.7). Based on this identification, 2 sub-populations of $A\alpha$ fibers were distinguished in the ventral roots. Such distinction can be seen in some of the histograms of Dyck et al. (1982) for the cat L5 ventral roots - i.e. 2 peaks in the $A\alpha$ spectrum.

Proposed identities correspond to previous morphometric studies. In the dorsal roots, the peak positions of the populations matched with peak positions of the fiber distribution histograms assembled by Sima (1974) for young rats (see Appendix Table 4.A.1). In the L5 ventral roots, the peak positions of the populations $\mathbb{A}$ (i.e. $A\gamma$/B fibers) and $\mathbb{C}$ (i.e. $A\alpha^2$ fibers) matched the corresponding peaks described by Sima (1974). In the proximal part of the sciatic nerve, the peak positions of populations $\mathbb{A}$ (i.e. $A\gamma/A\delta$ fibers) and B ($A\beta$ fibers) were also comparable. In the tibial nerve, the peak position of the afferent fiber diameter histogram described by Schmalbruch (1988) matched population $\mathbb{B}$ (e.g. $A\beta$ fibers) and the tail population $\mathbb{A}$ (e.g. $A\delta$ fibers). The peak positions of the reconstructed motor fiber histograms matched populations $\mathbb{A}$ (e. g. $A\gamma$ fibers) and $\mathbb{C}$ (e.g. $A\alpha^1$ fibers). In the sural nerve, the peak positions of populations $\mathbb{A}'$ (e.g. $A\delta$ fibers) and $\mathbb{B}'$ (e.g. $A\beta$ fibers) matched the peak positions in the histograms assembled by Jeronimo et al. (2005).

4.4.4   Segmental organization of the spinal roots

By means of regression analysis we showed that spinal level dependence was present in the dorsal roots. This held both for the cross-sectional area and for the total number of fibers. In contrast, level dependence was absent for the density of fibers and the relative interspace. The established linear relationship between the number of myelinated fibers and the lumbar level allowed to predict the number of fibers from the segmental level. Moreover, analysis of the previously published tabulated fiber counts of Langford and Coggeshall (1981) showed a similar but opposite trend for the dorsal sacral root segments: myelinated fiber numbers correlated negatively with the sacral level ($r = -0.96$; $p < 0.05$). Based on these observed correlations, we can conjecture that a rostro-caudal positive trend in the fiber counts should exist at cervical level but not at thoracic level. Therefore, fiber counts for the dorsal roots should be reported per single root and not as averages of several root levels. In contrast to the dorsal roots, no dependence for the fiber number was found in the ventral roots (Fig. 4.2). Ventral roots turned out to be more uniform also with respect to their density and area. On the other hand, there were segmental differences in their composition, which were not present in the dorsal roots.

Another testable conjecture of the regression model will be the presence of an increasing rostro-caudal trend in the numbers of fibers in L1 - L3 dorsal roots and absence of such a trend for the corresponding ventral root levels. The second part of this conjecture can be confirmed by statistical analysis of the data of Coggeshall et al. (1977) for the ventral roots L1 - L6, where a non-significant correlation was found ($r = 0.24$, p=0.64). At this stage, it is difficult to relate the observed phenomenon to variation in density of sensory innervation in the hind limb muscles or skin.
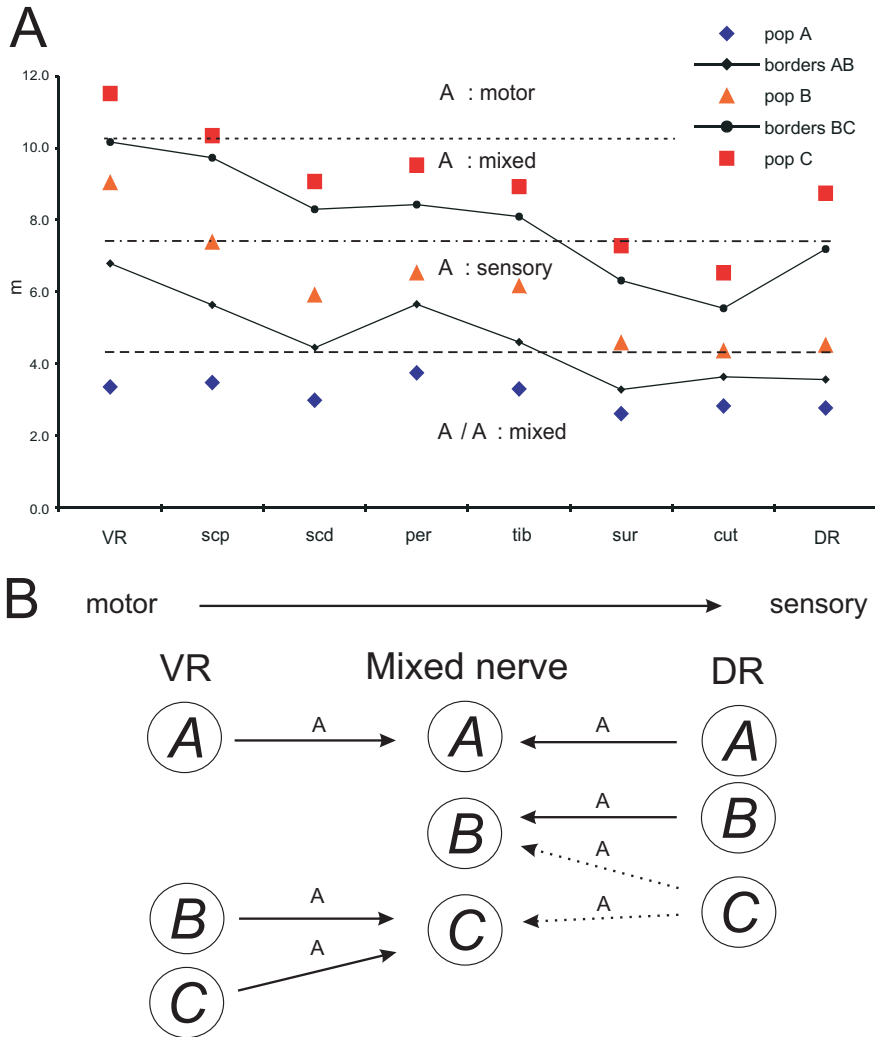
Figure 4.11: Borders (A) and identities (B) of the fiber populations in the roots and nerves

A - Border between the dorsal root $A\alpha$ sensory fibers and the ventral root $A\alpha^2$ (dotted line); border between $A\alpha$ sensory and $A\beta$ sensory fibers (dash-dotted line); border between the $A\gamma$ motor (ventral roots) and $A\beta$ sensory fibers (dorsal roots) (dashed line); *VR* - ventral root; *DR* - dorsal root; *scp* - proximal sciatic; *scd* - distal sciatic; *per* - peroneal; *tib* - tibial; *sur* - sural; *cut* - cutaneous branch. B - Contributions of the different populations in the spinal roots to the populations in the mixed nerves. Dotted arrows denote variable contribution.

Table 4.7: Identities of the $\mathbb{A}$, $\mathbb{B}$, and $\mathbb{C}$ populations in the peripheral nerves

Spinal roots			
	Populations		
	$\mathbb{A}$	$\mathbb{B}$	$\mathbb{C}$
Averaged ventral roots			
FCV [m/s]	15.3	51.6	65.7
Identity	$A\gamma/B$	$A\alpha^1$	$A\alpha^2$
Averaged dorsal roots			
FCV [m/s]	12.8	20.6	49.7
Identity	$A\delta/B$	$A\beta$	$A\alpha^1$

Mixed nerves			
Sciatic proximal			
FCV	16.0	34.0 - 42.1	58.9
Identity	$A\gamma/A\delta$	$A\beta/A\alpha^1$	$A\alpha^2$
Sciatic distal			
FCV	13.8	27.2 - 33.7	51.7
Identity	$A\gamma/A\delta$	$A\beta$	$A\alpha^1$
Peroneal			
FCV	17.6	30.0 - 37.2	54.3
Identity	$A\gamma/A\delta$	$A\beta$	$A\alpha^1$
Tibial			
FCV	15.2	28.3 - 35.1	50.9
Identity	$A\gamma/A\delta$	$A\beta$	$A\alpha^1$

Sensory nerves		
	Populations	
	$\mathbb{A}'$	$\mathbb{B}'$
Sural		
FCV [m/s]	15.2	21.1
Identity	$A\delta$	$A\beta$
Cutaneous		
FCV [m/s]	12.7	18.2
Identity	$A\delta$	$A\beta$

FCV is calculated according to ABK equations. Ranges correspond to estimates of FCV with factors for small and large fibers, respectively. Identities are assigned on the basis of the FCV.

4.4.5 Sampling and internal heterogeneity in the peripheral nerves and roots

Morphometric studies of peripheral nerves involve sampling of the myelinated fibers. Design based sampling (e.g. stereological approach) may be used to give accurate estimates of single parameters such as area, diameter, and density (Mayhew and Sharma, 1984; Mayhew, 1988; Larsen, 1998). However, spatial distribution of the myelinated fibers within a nerve is often non-uniform, therefore it is difficult to derive a good sampling scheme. This marked heterogeneity in the myelinated fiber size distribution imposes measurement of relatively large samples as a way to secure a reliable estimate of the density and the size distribution histograms (Torch et al.,

1989; Saxod et al., 1985). Based on these considerations we evaluated relatively large samples, i.e. $A[s]_{rel}$ varied from 15% to 100% of $A[n]$ (Table 4.2). The high intra-sample heterogeneity in the distal nerves and the dorsal roots can possibly account for the observed side differences for the same levels. Pooling the data on the left and the right sides considerably reduced the number of statistically significant differences. Moreover, with respect to $A[s]_{rel}$ and $N[f]_{sample}$ no inter-animal differences could be detected. Therefore, the sampling in the peripheral nerves and the spinal roots was adequate for the purposes of this study.

4.4.6 Branching and functional redistribution of the myelinated fibers

Encountered marked internal heterogeneity of the dorsal roots and the distal nerves is probably caused by size grouping of the nerve fibers (Fig. 4.1). Since different placements of the sampling frames will sample heterogeneous parts of tissue this will result in between-sample variation in the histograms and respectively in differences in the mean diameters. Observed proximo-distal differences in the peak positions and the shares in the modeled populations can be caused either by the functional redistribution of the fibers in the tributary branches formation or by the branching of fibers.

From Figures 4.8A, B and 4.11 it can be concluded that considerable changes in the composition of the nerves occur at the level of the lumbar plexus, while distally the observed effects on the populations can be explained mostly by redistribution of the fibers into following more distal nerves. Differences in $\mathbb{C}$ population (i.e. the thick fibers) between the ventral roots and the distal sciatic nerve (Fig. 4.8 and Table 4.2), which have presumably the same $A\alpha^2$ motor identity (Table 4.7), can be explained either by decrease in the fiber diameter of the $A\alpha^2$ motor fibers throughout their course or by their branching into smaller fibers or by redistribution to other nerves leaving the lumbar plexus. Studies in the rat ventral root C7 suggest absence of branching for the myelinated fibers at proximal level (Fraher and O'Sullivan, 1989). In addition, counts of the motor fibers in muscle nerve branches closely match that of motor neurons (Pamphlett and Sjarif, 2003). Therefore, probably there is no branching of the myelinated fibers in the ventral roots and the observed differences in the composition are due to departure of fibers into the pelvic nerves that were not included in the present study.

Moreover, at the level of the distal sciatic nerve, branching of the fibers was probably negligible since its tributary nerves summed up to 91% of the fiber numbers in the distal sciatic. In addition, as it was shown in Fig. 4.9B, the composition of the distal sciatic could be derived from its tributary nerves. Therefore, the observed difference between the proximal and the distal sciatic nerve can be attributed to the functional redistribution (Fig. 4.9) because it was not accompanied with corresponding differences between the proximal sciatic and the tibial and peroneal nerves.

Despite the similar composition of the different dorsal root levels it is probable that they do not participate with equal shares in the formation of the proximal sciatic nerve (regression model). Taking into account the contrasting redistribution in the proximal sciatic and the actual fiber counts it is most probable that the nerve is formed to a smaller extent by the dorsal root L6 in comparison with L4 and L5. This is in agreement with the observed segmental distribution of the sciatic nerve sensory neurons (Swett et al., 1991).

4.4.7   Anatomical parameters applicable in the design of implantable neural prostheses

With regard to the selective electrical stimulation using implantable neural prostheses several anatomical parameters can be of importance.

Fascicular structure of the nerve (root): If extra-fascicular stimulation is employed (i.e. a cuff electrode encompassing the nerve) the arrangement of the different fascicles of the nerve influence the selectivity of simulation (Deurloo and Holsheimer, 2003). Previous studies in the rat indicate that the distal part (i.e. at mid thigh) of the sciatic nerve is already divided into tibial and peroneal fascicles (Schmalbruch, 1988; Swett et al., 1986); therefore such anatomical considerations become relevant there. In our experience, in some cases, the fascicle division of the sciatic starts already at proximal levels, i.e. around the trochanter. In contrast, we observed fascicle division at the level of ventral roots only very rarely. Therefore, from anatomical point of view, ventral roots would provide more reproducible results during stimulation than the sciatic nerve.

Density and interspace: Another relevant parameter for the implantable neural prostheses is the fiber density (Feirabend et al., 2002). During the stimulation pulse, the product of the supra-threshold area and the fiber density will give the total number of fibers that will be stimulated. Therefore, in nerves having lower densities, higher stimulation currents should be used in order to recruit sufficient amount of fibers. In the ventral roots, in particular, the fiber densities were comparable for all studied levels; therefore it is possible to use the same stimulation protocol for all levels. The resistance of the interstitial space is different from the resistance of the fibers and the perineurium. In the presented study, an estimate for the interstitial space was given by the interspace parameter. This can eventually become an important parameter if the cross talk between myelinated nerve fibers is studied.

Fiber diameter distribution and population models: Quantitative parameters, such as numbers and sizes of fibers, are valuable for studying developmental, experimental, and pathological changes of the nerves (Pamphlett and Sjarif, 2003). The axonal atrophy and focal demyelination that can occur chronically after electrode implantation will result in reduction of the axonal density and changes of the size distribution and g-ratio of the nerve fibers (Agnew and McCreery, 1990) that can be evaluated morphometrically. From Table 4.7 it follows that target for motor stimulation are populations $\mathbb{B}$ and $\mathbb{C}$ in the ventral roots that form approximately 60% of the fibers and population $\mathbb{C}$ in the mixed nerves that forms between 13 and 23% of the fibers (i.e. the $A\alpha$ fibers). From the mutual disposition of the populations, it can be concluded that size selectivity of stimulation will be better in the peroneal nerve compared to the tibial and the sciatic nerves (Fig. 4.6). Moreover, since the fiber diameter is related to the firing threshold and to the refractory period (Blair and Erlanger, 1933), the strength of the injected current and the inter pulse duration used for optimal electrical stimulation of a given population of fibers by cuff electrodes can be calculated for the presented parametric models.

Additional geometric parameters can be also important for the electrical stimulation. These are the orientation of the fibers in the peripheral nerve and their size grouping in the cross-section. It was shown theoretically that the *orientation* can influence the

excitation and the blocking currents needed for certain modes of selective stimulation (Vučkovič et al., 2005). In our experience such undulation in the rat ventral roots is not pronounced. In contrast, in the peripheral nerves it can be substantial and probably should be considered for the design of electrodes for stimulation. *Size grouping* can be important for the desired size selectivity of stimulation. We did not address specifically the size grouping in the design of the morphometric study. From the analysis of the internal heterogeneity it follows that the ventral roots did not show pronounced size grouping. On the other hand, the dorsal roots and the peripheral nerves had some degree of size grouping (Fig. 4.1).

To summarize, with regard to motor neuroprostheses, from an anatomical point of view, ventral spinal roots can be a suitable target of electrical stimulation due to their moderate internal heterogeneity and the small variation in both their cross-sectional area and density. On the other hand, established segmental differences in their composition probably reflect the topographical organization of the hind limb innervation and should be taken into account for the purposes of electrical stimulation. Stimulation of the dorsal roots, for example, for pain suppression can be also considered from the findings in this study since the dorsal roots have similar composition in the lumbar region (L4 - L6). On the other hand, their marked internal heterogeneity can hamper the size selectivity of such stimulation if applied in a topographically inappropriate place.

4.5   Conclusions

Presented comprehensive study of the normal fiber morphometry of the lumbar nerves and their spinal roots established reference values of morphometric parameters such as fiber density, interspace, and cross-sectional area in the rat that can be used in further theoretical and experimental research in the field of the neural prosthesis development. Variation of the fiber numbers and cross-sectional areas in the dorsal roots could be explained by regression models. Functional modality (i.e. the sensory, motor, or mixed character) could classify the observed variability in the interspace, density, and composition of the nerves and roots. The nature of the fiber size distributions has been revealed by rigorous statistical modeling rather than by purely phenomenological descriptions that enabled us to establish the functional identities of the modeled fiber populations. Proposed approach can give a conceptual framework for understanding the comparative anatomy of the peripheral nerves and their spinal roots and can be further applied in other animal species or in men. Obtained results are important in view of the fiber size selectivity of stimulation (Chapter 2). However, to address the topical (e.g. muscle) selectivity of such stimulation additional studies are necessary (see Chapter 7).

Acknowledgements

Appendix

A   Morphometric literature data

Table 4.A.1: Literature morphometric data on the normal rat lumbar nerves and roots

Source	Material	Parameters determined
Sima (1974)	Sciatic nerve (N=3, 180 days)	range: 1 - 13 µm peak positions: 4 µm; 8.5 µm
	L5 ventral (N=3, 180 days)	range: 1 - 16 µm peak positions: 4 µm; 12 µm
	L5 dorsal (N=3, 180 days)	range: 1 - 15 µm peak positions: 3.5 µm; 6.5 µm; 8.5 µm
Jenq et al. (1986)	Sciatic nerve (N=4)	$N[f] = 7,938 \pm 182$ range: 1.5 - 12.5 µm
Rao and Krinke (1983)	L4 dorsal (N=4)	$N[f] = 2,731$
Schmalbruch (1986)	Sciatic (N=5)	$N[f] = 7,800$; Efferent: $N[f] = 1,600$
	Tibial (N=5)	$N[f] = 4,500$; Efferent: $N[f] = 1,014 \pm 106$ peak positions: 3.5 µm; 4.5 µm
	Peroneal (N=5)	$N[f] = 1,900$; Efferent: $N[f] = 588 \pm 79$
	Sural (N=5)	$N[f] = 1,050$
Jeronimo et al. (2005)	Sural (N=5, 180 days)	$N[f] = 951 \pm 76*(L); 961 \pm 70*(R);$ $d[f] = 5.34 \pm 0.15(R); 5.45 \pm 0.07(R)$ range: 2 - 10 µm peak positions: 3.5 µm; 4.5 µm

N - number of adult animals; L - left side; R - right side; * - standard error of the mean. Other notations are explained in Table 4.1; range and peak positions concern the range and the position of peaks in the respective diameter distribution histograms. Age is given in days if available.

B   Mixture modeling of the histograms

B.1   Optimal model selection

Normalized histograms of $d[f]$ were prepared for all nerve samples using n=180 diameter classes of equal width of Δ=0.1 µm covering the range of 0-18 µm. These histograms were further employed in the statistical mixture modeling. Data were fitted against a Gaussian model and five different lognormal mixture models - single (LN1), double (LN2), triple (LN3), quadruple (LN4), and quintuple (LN5) using the built-in curve fitting routine in *Origin*. The corresponding functions are described by the following equations:

Gaussian function model

$$N(x) = Fe^{-\frac{(x-m)^2}{2w^2}}$$

(B.1)

where m - mean; w - standard deviation; F - class frequency at the mode value (i.e. at m).

Lognormal function models

$$\text{LNn(x)} = \sum_{i=A,B,C,D,E}^{n} F_i e^{-\frac{(\ln x - \ln m_i)^2}{2w_i^2}} \tag{B.2}$$

Single (LN1) n=1; double (LN2) n=2; triple (LN3) n=3; quadruple (LN4) n=4; quintuple (LN5) n=5; m - peak position (i.e. mode value), w - spread parameter; F - class frequency at the mode value (i.e. population weight parameter). For each of the populations A - E, the actual share in the total $N[f]_{sample}$ was calculated numerically.

The optimal model was selected according to a combination of three criteria:

1. Schwartz-Bayesian information criterion

   SBIC (Schwartz, 1987) was computed according to:

   $$SBIC = n \ln SSR + p \ln n \tag{B.3}$$

   where n is the number of classes in the fitted histogram, p the number of free parameters (i.e. 3, 3, 6, 9, 12 and 15 for the Gaussian and LN1 - LN5 models, respectively), and SSR is the residual sum of squares computed as: $SSR = \frac{1}{n} \sum_{i}^{n} (F_i[d]_{obs} - F_i[d]_{fit})^2$ where "obs" denotes the observed, "fit" the fitted frequency in the sample histogram and i is the class. As could be seen from its formula, SBIC information criterion is a compromise between the minimization of the error and the numbers of the parameters employed to do so by inclusion of a penalizing term for the addition of new parameters. According to the general properties of SBIC, the optimal model minimizes the criterion value compared to all the other (non-optimal) models (Schwartz, 1987).

2. Occurrence of populations with less than 5% of share in the sample
   Due to the choice of the class size, such models exhibited sharp spikes that were not comparable with the actual histograms and were considered over-fitted independently of the value of SBIC. In this case, the model with the second smallest SBIC value was selected as optimal.

3. Quality of histology
   In case of unequivocal choice of model for a particular type of nerve or spinal root the histological sections were also inspected and the sample areas checked for tissue defects. In this case, the sections with some lower quality were excluded from the model selection scheme. However, they were still in the calculation of the parameter means and standard deviations and the subsequent statistical comparisons.

B.2   Parameters of the lognormal distribution

THE lognormal distribution is typically defined as:

$$P(x|\mu, w) = \frac{1}{\sqrt{2\pi}\, w\, x}\, e^{-\frac{1}{2w^2}\, \ln^2(\frac{x}{\mu})} \tag{B.4}$$

where w is the spread parameter and m is the scale parameter. Statistical properties of the lognormal distributions can be found in Weisstein (1999). The mode (i.e. the peak position) of the lognormal distribution is given by the expression:

$$m = \mu e^{-w^2} \tag{B.5}$$

For the purposes of performed curve fitting (see eq. (B.2)) the lognormal distribution was reformulated as:

$$P(x|m, w) = \frac{e^{-\frac{w^2}{2}}}{\sqrt{2\pi}\, w\, m}\, e^{-\frac{1}{2w^2}\, \ln^2(\frac{x}{m})} \tag{B.6}$$

Following this formulation, it can be shown that the expectation of an arbitrary power p of the variable x (i.e. x^p) is:

$$E[x^p] = m^p\, e^{\frac{p(p+2)}{2}\, w^2} \tag{B.7}$$

Therefore, the mean and the variance of the lognormal distribution can be expressed by:

$$E[x] = m\, e^{\frac{3}{2}\, w^2} \tag{B.8}$$

$$Var[x] = E^2[x](e^{w^2} - 1) \tag{B.9}$$

B.3   Estimation of parameters related to lognormal mixture distributions

The theory of mixture distributions can be found in Everitt and Hand (1981) and Titterington et al. (1985). If $F(X)$ is a function of a random variable $X \in \mathbf{R}$ having a normalized density distribution function $D(x)$ defined for $X \in W$ the expectation of $F(X)$ can be defined by:

$$E[F(x)] = \int_{X \in W} F(x)D(x)dx \tag{B.10}$$

In the case of a linear mixture distribution, $D(x) = \sum_i^n a_i D_i(x)$ and the weights of the individual components are normalized by $\sum_i^n a_i = 1$. Due to the additivity of integration: $E[F(x)] = \sum_i^n a_i E_i[F(x)]$ where $E_i[x]$ is the expectation of ith individual component. Therefore, in the case of a power function of the form $F_p(x) = kx^p + b$ holds:

$$E[F_p(x)] = k \sum_i^n a_i E_i[x^p] + b \tag{B.11}$$

Finally, after substitution with eq. (B.7) for the lognormal mixture distribution:

$$E[F_p(x)] = k \sum_i^n a_i \, m_i^p \, e^{\frac{p(p+2)}{2} \, w_i^2} + b \tag{B.12}$$

Intercepts of any two arbitrary components in a lognormal mixture distribution can be obtained by solving the equation:

$$\frac{a_a \, e^{-\frac{w_a^2}{2}}}{\sqrt{2\pi} \, w_a \, m_a} \cdot e^{-\frac{1}{2w_a^2} \ln^2 \frac{x}{m_a}} = \frac{a_b \, e^{-\frac{w_b^2}{2}}}{\sqrt{2\pi} \, w_b \, m_b} \cdot e^{-\frac{1}{2w_b^2} \ln^2 \frac{x}{m_b}} \tag{B.13}$$

where and a and b denote any 2 components of the mixture. After logarithmic transformation and grouping it can be shown that eq. (B.13) is equivalent to the elementary square equation

$$\left(\frac{1}{w_b^2} - \frac{1}{w_a^2} \right) \cdot z^2 - 2 \left(\frac{\ln m_b}{w_b^2} - \frac{\ln m_a}{w_a^2} \right) \cdot z + \frac{\ln^2 m_b}{w_b^2} - \frac{\ln^2 m_a}{w_a^2} + 2Q = 0 \tag{B.14}$$

where

$$Q = \ln \frac{a_a}{w_a m_a} - \ln \frac{a_b}{w_b m_b} + \frac{(w_b^2 - w_a^2)}{2}$$

and $x = e^z$. Therefore, the solution is given by:

$$z_{1,2} = \frac{\left(\frac{\ln m_b}{w_b^2} - \frac{\ln m_a}{w_a^2} \right) \pm \sqrt{\left(\frac{\ln m_b}{w_b^2} - \frac{\ln m_a}{w_a^2} \right)^2 + \left(\frac{1}{w_b^2} - \frac{1}{w_a^2} \right) \left(\frac{\ln^2 m_b}{w_b^2} - \frac{\ln^2 m_a}{w_a^2} + 2Q \right)}}{\frac{1}{w_b^2} - \frac{1}{w_a^2}}$$

and consequently

$$x_{1,2} = e^{z_{1,2}} \tag{B.15}$$

C   Parameters of the optimal models

THE non optimal LN3 model is given for the tibial nerve because of its further use in proximo-distal population analysis.

Table 4.C.1: Parameters of the optimal models

LN3		Populations		
ventral roots		$\mathbb{A}$	$\mathbb{B}$	$\mathbb{C}$
L4	m	3.21 ± 0.58 [µm]	9.76 ± 1.51 [µm]	11.77 ± 1.71 [µm]
	w	0.30 ± 0.06	0.15 ± 0.05	0.08 ± 0.02
	a	42.9 ± 6.8 [%]	22.6 ± 13.5 [%]	34.5 ± 13.3 [%]
L5	m	3.15 ± 0.42 [µm]	7.94 ± 2.02 [µm]	10.98 ± 1.25 [µm]
	w	0.29 ± 0.10	0.18 ± 0.10	0.08 ± 0.02
	a	38.2 ± 9.2 [%]	20.0 ± 12.3 [%]	41.8 ± 8.5 [%]
L6	m	3.69 ± 0.47 [µm]	9.41 ± 1.41 [µm]	11.81 ± 1.37 [µm]
	w	0.33 ± 0.06	0.13 ± 0.06	0.08 ± 0.04
	a	38.7 ± 3.3 [%]	24.0 ± 15.5 [%]	37.3 ± 15.4 [%]
average	m	3.36 ± 0.30 [µm]	9.04 ± 0.97 [µm]	11.52 ± 0.47 [µm]
	w	0.31 ± 0.14	0.15 ± 0.06	0.07 ± 0.03
	a	39.8 ± 2.4 [%]	22.2 ± 2.0 [%]	37.9 ± 3.7 [%]
dorsal roots				
L4	m	2.73 ± 0.25 [µm]	4.35 ± 0.62 [µm]	8.81 ± 0.82 [µm]
	w	0.19 ± 0.10	0.39 ± 0.09	0.16 ± 0.06
	a	23.7 ± 11.8 [%]	53.7±± 12.9 [%]	22.6 ± 23.7 [%]
L5	m	2.74 ± 0.31 [µm]	5.03 ± 1.29 [µm]	8.74 ± 1.53 [µm]
	w	0.23 ± 0.10	0.25 ± 0.08	0.20 ± 0.09
	a	31.6 ± 9.7 [%]	38.0±± 19.1 [%]	30.4 ± 19.1 [%]
L6	m	2.83 ± 0.43 [µm]	4.18 ± 1.43 [µm]	8.67 ± 1.29 [µm]
	w	0.21 ± 0.13	0.30 ± 0.14	0.19 ± 0.08
	a	25.7 ± 16.0 [%]	38.9 ± 17.8 [%]	35.4 ± 20.3 [%]
average	m	2.77 ± 0.06 [µm]	4.52 ± 0.45 [µm]	8.74 ± 0.07 [µm]
	w	0.21 ± 0.11	0.31 ± 0.10	0.1 ± 0.08
	a	31.3 ± 4.1 [%]	38.6 ± 8.8 [%]	30.1 ± 6.5 [%]
peripheral nerves				
proximal sciatic	m	3.48 ± 0.39 [µm]	7.39 ± 0.99 [µm]	10.34 ± 1.49 [µm]
	w	0.32 ± 0.07	0.19 ± 0.04	0.08 ± 0.03
	a	41.1 ± 7.7 [%]	46.2 ± 11.2 [%]	12.7 ± 7.7 [%]
distal sciatic	m	2.99 ± 0.43 [µm]	5.92 ± 1.39 [µm]	9.07 ± 1.86 [µm]
	w	0.29 ± 0.07	0.25 ± 0.09	0.11 ± 0.09
	a	36.0 ± 6.3 [%]	46.6 ± 13.6 [%]	17.4 ± 18.1 [%]
peroneal	m	3.83 ± 0.51 [µm]	6.53 ± 0.57 [µm]	9.53 ± 0.80 [µm]
	w	0.32 ± 0.11	0.16 ± 0.07	0.08 ± 0.02
	a	49.6 ± 14.0 [%]	30.2 ± 15.6 [%]	20.2 ± 6.1 [%]
tibial	m	3.30 ± 0.53 [µm]	6.16 ± 1.52 [µm]	8.93 ± 1.75 [µm]
	w	0.31 ± 0.11	0.20 ± 0.07	0.10 ± 0.06
	a	25.8 ± 11.1 [%]	50.8 ± 27.4 [%]	23.4 ± 29.6 [%]

Table 4.C.1 (continued)

material		Populations	
peripheral nerves		$\mathbb{A}'$	$\mathbb{B}'$
tibial	m	3.43 ± 0.33 [μm]	6.80 ± 1.18 [μm]
	w	0.33 ± 0.06	0.21 ± 0.03
	a	35.3 ± 22.1 [%]	64.7 ± 22.1 [%]
sural	m	3.30 ± 0.51 [μm]	5.87 ± 1.18 [μm]
	w	0.23 ± 0.07	0.22 ± 0.06
	a	35.9 ± 18.1 [%]	64.1 ± 18.1 [%]
cutaneous*	m	$2.76 \; 0.16$ [μm]	3.95 ± 0.01 [μm]
	w	0.12 ± 0.02	0.39 ± 0.02
	a	16.8 ± 4.0 [%]	83.2 ± 4.0 [%]

Parameters: m - peak position value (eq. B.5), w - spread value, a - population share (relative size); * - non-optimal model for comparison with the other sensory nerve.

Bibliography

Agnew, W. F. and D. B. McCreery (eds.) (1990) Neural Prostheses: Fundamental studies. Prentice Hall Advanced Reference Series. Englewood Cliffs: Prentice Hall.

Arbuthnott, E. R., I. A. Boyd, and K. U. Kalu (1977) The relation between axon area, axon circumference, total fibre circumference and number of myelin lamellae for different groups of fibres in cat hind-limb nerves [proceedings]. J. Physiol. (Lond) *273*:88P–89P.

Arbuthnott, E. R., I. A. Boyd, and K. U. Kalu (1980) Ultrastructural dimensions of myelinated peripheral nerve fibres in the cat and their relation to conduction velocity. J. Physiol. (Lond) *308*:125–157.

Blair, E. A. and J. Erlanger (1933) A comparison of the characteristics of axons through their individual electrical responces. Am. J. Physiol. *106*:524–564.

Boyd, I. A. and K. U. Kalu (1979) Scaling factor relating conduction velocity and diameter for myelinated afferent nerve fibres in the cat hind limb. J. Physiol. (Lond) *289*:277–297.

Branner, A. and R. A. Normann (2000) A multielectrode array for intrafascicular recording and stimulation in sciatic nerve of cats. Brain Res. Bull. *51*:293–306.

Brunner, R., P. Zimmermann, and F. W. Klussmann (1980) Localization and neurophysiological properties of motoneurones of the m. triceps surae of the rat after retrograde labelling with Evans blue. Cell Tissue Res. *212*:73–81.

Coggeshall, R. E., D. G. Emery, H. Ito, and C. W. Maynard (1977) Unmyelinated and small myelinated axons in rat ventral roots. J. Comp. Neurol. *173*:175–184.

Coppin, C. M. and J. J. Jack (1972) Internodal length and conduction velocity of cat muscle afferent nerve fibres. J. Physiol. (Lond) *222*:92P–93P.

de Jonge, H. (1963) Inleiding tot de medische statistiek. Tech. Rep. 65, Verhand. Ned. Inst. Praev. Gen.

Deurloo, K. and J. Holsheimer (2003) Fascicular selectivity in transverse stimulation with a nerve cuff electrode: A theoretical approach. Neuromodulation *6*:258–269.

Djouhri, L. and S. N. Lawson (2004) $A\beta$-fiber nociceptive primary afferent neurons: a review of incidence and properties in relation to other afferent a-fiber neurons in mammals. Brain Res. Brain Res. Rev. *46*:131–145.

Doncker, L. D., F. Picquet, J. Petit, and M. Falempin (2003) Characterization of spindle afferents in rat soleus muscle using ramp-and-hold and sinusoidal stretches. J. Neurophysiol. *89*:442–449.

Dyck, P. J., J. Karnes, M. Sparks, and P. A. Low (1982) The morphometric composition of myelinated fibres by nerve, level and species related to nerve microenvironment and ischaemia. Electroencephalogr. Clin. Neurophysiol. Suppl. *36*:39–55.

Everitt, B. S. and D. J. Hand (1981) Finite mixture distributions. London and New York: Chapman and Hall.

Feirabend, H. K., H. Choufoer, and S. Ploeger (1998) Preservation and staining of myelinated nerve fibers. Methods *15*:123–131.

Feirabend, H. K., H. Choufoer, S. Ploeger, J. Holsheimer, and J. D. van Gool (2002) Morphometry of human superficial dorsal and dorsolateral column fibres: significance to spinal cord stimulation. Brain *125*:1137–1149.

Fraher, J. P. and V. R. O'Sullivan (1989) Age changes in axon number along the cervical ventral spinal nerve roots in rats. J. Comp. Neurol. *280*:171–182.

Gasser, H. S. and J. Erlanger (1927) The role played by the sizes of the constituent fibers of a nerve trunk in determining the form of its action potential wave. Am. J. Physiol. *80*:527–547.

Gasser, H. S. and H. Grundfest (1939) Axon diameters in relation to the spike dimensions and the conduction velocity in mammalian nerves. Am. J. Physiol. *127*:393–414.

Gokin, A. P., B. Philip, and G. R. Strichartz (2001) Preferential block of small myelinated sensory and motor fibers by lidocaine: in vivo electrophysiology in the rat sciatic nerve. Anesthesiology *95*:1441–1454.

Greensmith, L., J. Dick, A. O. Emanuel, and G. Vrbova (1996) Induction of transmitter release at the neuromuscular junction prevents motoneuron death after axotomy in neonatal rats. Neuroscience *71*:213–220.

Hebel, R. and M. W. Stromberg (1986) Anatomy and Embryology of the Laboratory Rat. Worthsee: BioMed Verlag.

Heiduschka, P. and S. Thanos (1998) Implantable bioelectric interfaces for lost nerve functions. Prog. Neurobiol. *55*:433–461.

Hursh, J. B. (1939) Conduction velocity and diameter of nerve fibers. Am. J. Physiol. *127*:131–139.

Iwasaki, Y., Y. Ichikawa, O. Igarashi, S. Konno, J. Aoyagi, K. Ikeda, S. Marabuchi, S. Ono, H. Iguchi, K. Kawabe, and T. Fujioka (2004) T-588 protects motor neuron death following axotomy. Neurochem. Res. *29*:403–406.

Jacobs, J. M. and S. Love (1985) Qualitative and quantitative morphology of human sural nerve at different ages. Brain *108 (4)*:897–924.

Jenq, C. B., K. Chung, and R. E. Coggeshall (1986) Postnatal loss of axons in normal rat sciatic nerve. J. Comp. Neurol. *244*:445–450.

Jeronimo, A., C. A. Jeronimo, O. A. R. Filho, L. S. Sanada, and V. P. Fazan (2005) Microscopic anatomy of the sural nerve in the postnatal developing rat: a longitudinal and lateral symmetry study. J. Anat. *206*:93–99.

Lago, N., D. Ceballos, F. J. Rodriguez, T. Stieglitz, and X. Navarro (2005) Long term assessment of axonal regeneration through polyimide regenerative electrodes to interface the peripheral nerve. Biomaterials *26*:2021–2031.

Langford, L. A. and R. E. Coggeshall (1981) Branching of sensory axons in the peripheral nerve of the rat. J. Comp. Neurol *203*:745–750.

Larsen, J. O. (1998) Stereology of nerve cross sections. J. Neurosci. Methods *85*:107–118.

Lewin, G. R. and S. B. McMahon (1991) Physiological properties of primary sensory neurons appropriately and inappropriately innervating skeletal muscle in adult rats. J. Neurophysiol. *66*:1218–1231.

Malagodi, M. S., K. W. Horch, and A. A. Schoenberg (1989) An intrafascicular electrode for recording of action potentials in peripheral nerves. Ann. Biomed. Eng. *17*:397–410.

Mayhew, T. M. (1988) An efficient sampling scheme for estimating fibre number from nerve cross sections: the fractionator. J. Anat. *157*:127–134.

Mayhew, T. M. and A. K. Sharma (1984) Sampling schemes for estimating nerve fibre size. I. methods for nerve trunks of mixed fascicularity. J. Anat. *139 (Pt 1)*:45–58.

McDonnall, D., G. A. Clark, and R. A. Normann (2004) Selective motor unit recruitment via intrafascicular multielectrode stimulation. Can. J. Physiol. Pharmacol. *82*:599–609.

Navarro, X. and W. R. Kennedy (1991) The effects of autologous nerve transplants on motor and sudomotor reinnervation by regenerative axons. Brain Res. *565*:181–187.

Necker, R. and C. Meinecke (1984) Conduction velocities and fiber diameters in a cutaneous nerve of the pigeon. J. Comp. Physiol. A *154*:817–824.

Negredo, P., J. Castro, N. Lago, X. Navarro, and C. Avendano (2004) Differential growth of axons from sensory and motor neurons through a regenerative electrode: a stereological, retrograde tracer, and functional study in the rat. Neuroscience *128*:605–615.

Pamphlett, R. and A. Sjarif (2003) Is quantitation necessary for assessment of sural nerve biopsies? Muscle Nerve *27*:562–569.

Prodanov, D., G. Mantchev, A. Iliev, V. Traykov, K. Yakimova, R. Kaneva, and I. Krushkov (1998) Effects of Dexamethasone in rat neonatal model of axotomy-induced motoneuronal cell death. Arch. Physiol. Biochem. *106*:355–361.

Prodanov, D., E. Marani, and J. Holsheimer (2003) Functional Electric Stimulation for sensory and motor functions: progress and problems. Biomed. Rev. *14*:23–50.

Puigdellivol-Sanchez, A., A. Valero-Cabre, A. Prats-Galino, X. Navarro, and C. Molander (2002) On the use of Fast Blue, Fluoro-Gold, and Diamidino Yellow for retrograde tracing after peripheral nerve injury: uptake, fading, dye interactions, and toxicity. J. Neurosci. Methods *115*:115–127.

Rao, R. S. and G. Krinke (1983) Changes with age in the number and size of myelinated axons in the rat L4 dorsal spinal root. Acta Anat. (Basel) *117*:187–192.

Rodriguez, F. J., D. Ceballos, M. Schuttler, A. Valero, E. Valderrama, T. Stieglitz, and X. Navarro (2000) Polyimide cuff electrodes for peripheral nerve stimulation. J. Neurosci. Methods *98*:105–118.

Rushton, W. A. (1951) A theory of the effects of fibre size in medullated nerve. J. Physiol. (Lond) *115*:101–122.

Rutten, W. L., H. J. van Wier, and J. H. Put (1991) Sensitivity and selectivity of intraneural stimulation using a silicon electrode array. IEEE Trans. Biomed. Eng. *38*:192–198.

Sakaguchi, T., M. Okada, T. Kitamura, and K. Kawasaki (1993) Reduced diameter and conduction velocity of myelinated fibers in the sciatic nerve of a neurofilament-deficient mutant quail. Neurosci. Lett. *153*:65–68.

Saxod, R., S. Torch, A. Vila, A. Laurent, and P. Stoebner (1985) The density of myelinated fibres is related to the fascicle diameter in human superficial peroneal nerve. Statistical study of 41 normal samples. J. Neurol. Sci. *71*:49–64.

Schmalbruch, H. (1986) Fiber composition of the rat sciatic nerve. Anat. Rec. *215*:71–81.

Schmalbruch, H. (1988) The effect of peripheral nerve injury on immature motor and sensory neurons and on muscle fibres. Possible relation to the histogenesis of werdnig-hoffmann disease. Rev. Neurol. (Paris) *144*:721–729.

Schwartz, G. (1987) Estimating the dimensions of a model. Annals Stat. *6*:461–464.

Sima, A. (1974) Studies on fibre size in developing sciatic nerve and spinal roots in normal, undernourished, and rehabilitated rats. Acta Physiol. Scand. Suppl. *406*:1–55.

Stewart, J. D. (2003) Peripheral nerve fascicles: anatomy and clinical relevance. Muscle Nerve *28*:525–541.

Swett, J. E., Y. Torigoe, V. R. Elie, C. M. Bourassa, and P. G. Miller (1991) Sensory neurons of the rat sciatic nerve. Exp. Neurol. *114*:82–103.

Swett, J. E., R. P. Wikholm, R. H. Blanks, A. L. Swett, and L. C. Conley (1986) Motoneurons of the rat sciatic nerve. Exp. Neurol. *93*:227–252.

Tackmann, W., G. Spalke, and H. J. Oginszus (1976) Quantitative histometric studies and relation of number and diameter of myelinated fibres to electrophysiological parameters in normal sensory nerves of man. J. Neurol. *212*:71–84.

Titterington, D. M. (1990) Some recent research in the analysis of mixture distributions. Statistics *21*:619–641.

Titterington, D. M., A. F. Smith, and U. E. Makov (1985) Statistical analysis of finite mixture distributions. New York: Wiley.

Torch, S., P. Stoebner, Y. Usson, G. D. D'Aubigny, and R. Saxod (1989) There is no simple adequate sampling scheme for estimating the myelinated fibre size distribution in human peripheral nerve: a statistical ultrastructural study. J. Neurosci. Methods *27*:149–164.

Veltink, P. H., J. A. van Alste, and H. B. Boom (1989) Multielectrode intrafascicular and extraneural stimulation. Med. Biol. Eng. Comput. *27*:19–24.

Vleggeert-Lankamp, C. L., R. J. van den Berg, H. K. Feirabend, E. A. Lakke, M. J. Malessy, and R. T. Thomeer (2004) Electrophysiology and morphometry of the $A\alpha$- and $A\beta$-fiber populations in the normal and regenerating rat sciatic nerve. Exp. Neurol *187*:337–349.

Vučkovič, A., J. J. Struijk, and N. J. Rijkhoff (2005) Influence of variable nerve fibre geometry on the excitation and blocking threshold. a simulation study. Med. Biol. Eng. Comput. *43*:365–374.

Weisstein, E. W. (1999) Log normal distribution. In *A Wolfram Web Resource*, http://mathworld.wolfram.com/LogNormalDistribution.html: CRC Press.

CHAPTER 5

Automatic Morphometry of Synaptic Boutons of Cultured Cells Using Granulometric Analysis of Digital Images [†]

Abstract

Numbers, linear density, and surface area of synaptic boutons can be important parameters in studies on synaptic plasticity in cultured neurons. We present a method for automatic identification and morphometry of boutons based on filtering of digital images using granulometric analysis. Cultures of cortical neurons (DIV8 and DIV21) were fixed and marked with fluorescently labeled antibodies for synapsin I (a marker for synaptic boutons) and MAP-2 (a marker for dendrites). Images were acquired on a confocal microscope and automatically processed. Granulometry, a morphological operator sensitive to the geometry and size of objects, was used to construct a filter passing fuzzy fluorescent grains of a certain size. Next, the filter was overlaid with the original image (masking) and the positive pixels were identified by an integral intensity threshold (thresholding). Disjoint grains, representing individual boutons, were reconstructed from the connected pixels above the threshold, numbered and their area was measured. In total, 1498 boutons with a mean diameter of 1.63 μm ± 0.49 μm (SD) were measured. Comparisons with manual counts showed that the proposed method was capable of identifying boutons in a systematic manner at the light microscopic level and was a viable alternative to manual bouton counting.

5.1   Introduction

STudies of synaptic morphology can sometimes be greatly facilitated by the use of neuronal cell cultures (Boyer et al., 1998). In cultures, synaptic boutons are arrayed in a thin layer at relatively low densities. This allows individual measurements to be performed more easily. In studies concerning synaptic plasticity in cell cultures, morphological parameters such as linear density and number of synapses, and size of the boutons can be particularly important (Tarsa and Goda, 2002; Palizvan et al., 2004).

To establish the dose- or time- dependence of a specific pharmacological effect often a large number of different experimental groups are needed. This rapidly increases the number of individual samples to be evaluated. Because of the high variability of the localizations of synapses on dendrites and the clustering of boutons, the stereological assumption of homogeneity of spatial distribution is violated. Therefore, complete dendritic trees are counted. To facilitate counting in cell cultures we developed a reproducible and robust method for automatic identification and morphometry of synaptic boutons. The method was further applied to synaptic boutons marked for *synapsin I* immuno-fluoresecence from micro-island cultures of neocortical neurons.

5.2   Methods

5.2.1   Granulometric filtering

PErhaps the oldest and most frequently used technique in the empirical sciences to quantify the size of solid particles is to use a series of sieves with increasing mesh openings. To quantify the properties of discrete sets of objects Matheron (1975) theorized empirical sieving into the formal concept of mathematical granulometry (see Appendix A). Granulometry was later applied in image analysis to both binary and continuous tone images (Serra, 1982). In a way similar to sieving grains, pixels comprising an image are "sieved" according to their connectivity to similar pixels imposed by a certain primitive geometric body termed *Structuring Element* (SE) (for illustration of the principle see Fig. 5.1). An integral characteristic of granulometry is the distribution of pixels with respect to the diameters of the used SEs (Fig. 5.1). A local maximum in its normalized first derivative, the *granulometric size density G(d)*, indicates the presence of a number of objects matching the particular SE. Moreover, granulometry can act as a band-pass filter capable of discriminating grains of a certain size based on their similarity to a SE (Dougherty and Chen, 2001). By exploiting this property, images can be simplified substantially to successfully isolate various classes of objects (Fig. 5.1).

5.2.2   Outline of the algorithm

The algorithm employed in the study can be outlined in the following main steps:

1. Perform granulometry of the image and compute G(d) (Appendix, eq. A.8).

2. Identify the scale of interest by the pattern of the peaks in G(d); select low bound $I_{low} = S \circ E_{low}$ and high bound images $I_{high} = S \circ E_{high}$, where $\circ$ denotes the opening operation (Appendix eq. A.3), and subtract the images.
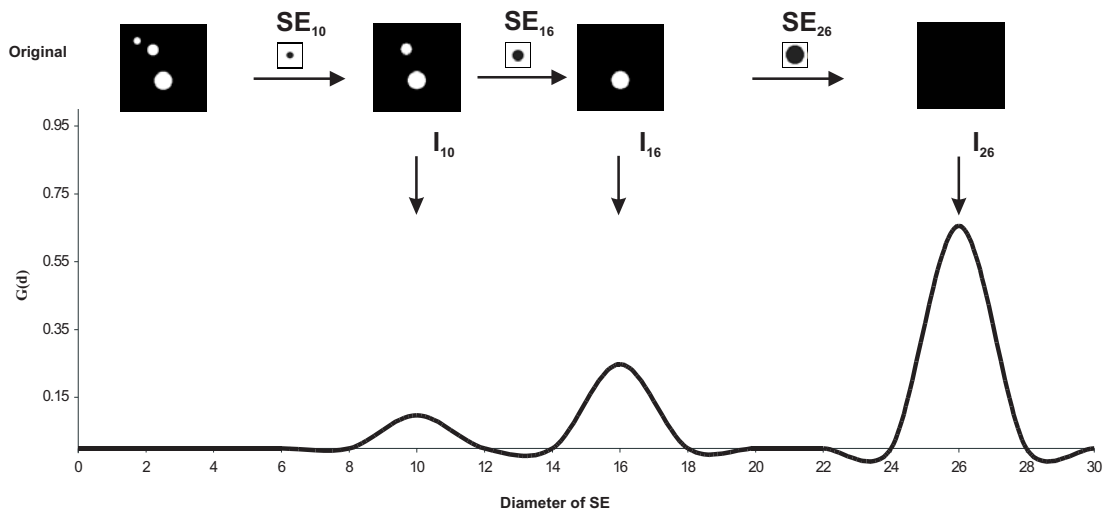
Figure 5.1: Granulometry of a binary image

An image containing 3 disks with diameters 10, 16 and 26 pixels is presented (noted "Original"). During granulometry, the image is successively sieved with a family of homothetic disk SEs of increasing diameters *d*. Each sieving step that removes a disk from the image results in a local maximum in *G(d)*. Derived images corresponding to the G(d) maxima - I_{10}, I_{16}, and I_{26} - are depicted together with the used SEs - SE_{10} (d=10), SE_{16} (d=16) and SE_{26} (d=26). By subtracting derived images, it is possible to isolate individual disks.

3. Construct the binary "mask" using the *k-means clustering* algorithm (Jain and Dubes, 1988) - a method that can overcome background autofluorescence of the studied cell structures more easily (see Discussion).

4. Delete irrelevant structures by superimposing the mask on the original image using bit-plane logical AND operation (masking). Threshold the resulting image using the integral thresholding (Appendix, eq. B.1) - a method that can reduce the variation in the area measurements (see Discussion).

5. Construct disjoint grains from the pixels that are above the threshold based on their 8-connected neighborhoods as implemented in *ImageJ*.

6. Enumerate and measure the grains constructed in this way.

5.2.3 Immuno-cytochemical procedures

Micro island cortical cultures were prepared from embryonic day 18 murine embryos (Heeroma et al., 2004). Neuronal cells were harvested on the 8th day (DIV8) and on the 21st day (DIV 21) of in vitro culturing (densities approx. 6000 neurons/cm^2). Cultures were stained with antibodies against a marker for dendrites, *microtubule-associated protein 2* (MAP-2) (Six et al., 1992), and a marker for synaptic vesicles, *synapsin I* (Huttner et al., 1983). Cultures were fixed

Table 5.1: Parameters and comparisons used in the validation studies

	Algorithm $\rightarrow N_a$	Observer 1 $\rightarrow N_1$	Observer 2 $\rightarrow N_2$
Algorithm	-	M_{m1}	M_{m2}
Observer 1	$D_{m1} = \frac{|N_a - M_{m1}|}{N_a}$	-	M_o
Observer 2	$D_{m2} = \frac{|N_a - M_{m2}|}{N_a}$	$D_o = \frac{|N_a - M_o|}{N_a}$	-

N_1 - number of objects detected by Observer 1; N_2 - number of objects detected by Observer 2; N_a - number of objects detected by the algorithm; M_m - number of matched objects between an observer and the method; D_m - method observer disagreement; M_o - number of matched objects between Observer 1 and Observer 2, D_o - inter-observer disagreement.

by 4% paraformaldehyde, washed 2 times for 15 min with 0.1M Phosphate buffered saline (PBS), and incubated in 0.1% Triton X-100 for 5 minutes followed by 4% fetal calf serum for 20 minutes. After washing with PBS, cultures were incubated for 1 hour at room temperature in a mixture containing 0.1% Triton X-100, mouse monoclonal anti-MAP-2, 1:200 (Boehringer, Alkmaar, The Netherlands) and rabbit polyclonal anti-synapsin I, 1:1000 (clone E028; Heeroma et al. (2004)) antibodies diluted in PBS. After washing 3 times with PBS, the cells were incubated for 1 hour at room temperature in secondary antibodies conjugated to anti-rabbit-Cy5 or anti-mouse-Alexa546 (Molecular Probes, Oregon, USA) (Heeroma et al., 2004). Finally, the slides were washed in PBS and cover-slipped with Dabco-Mowiol (Heimer and Taylor, 1974).

5.2.4   Imaging and Morphometric analysis

Cultures were analyzed on a Zeiss 510 Meta confocal microscope (Carl Zeiss, Heidelberg, Germany). A set of 57 high-resolution digital images of different cultures was recorded at a resolution of 4.45 pixels per μm. Images were acquired on 2 channels - *cyan*, comprising anti-synapsin staining and *red*, comprising anti-MAP-2 staining. In order to reduce the amount of debris, all but the area situated within 3 μm distance of any MAP-2 positive dendritic branches was blanked in the images.

Image processing and measurement steps were performed in the public domain software for image analysis *ImageJ* (NIH, Bethesda, Maryland, USA; http://rsb.info.nih.gov/ij/). The algorithm was run on the synapsin channel of every image. The identified boutons were numbered and their areas, equivalent diameters, and planar co-ordinates were measured and recorded. The derived images containing markings of detected objects were printed.

5.2.5   Validation by manual counts

Two experimental trials involving observers experienced in morphometry were performed: a "free" count trial and a "calibrated" count trial. During the "free" count trial, the observers had to mark each bouton they could identify in the images according to a size criterion (see Results). During the "calibrated" count trial, to reduce the variability coming from the "nature" of the observers (i.e. disagreement due to preferences to lower or higher counts) and to increase the statistical power, as an additional constraint, the expected number of boutons per image was preset to the number counted by the algorithm, i.e. "tea tasting lady experiment" design (Fisher, 1935).

To quantify the differences in identification of objects the notions of "method-observer disagreement" and "inter-observer disagreement" were used (see Table 5.1 for the formulae). This was necessary due to the absence of a "reference standard" method, a frequent situation in automated image analysis studies in the biological sciences. The synapsin channels of a representative set of images (n=9) were printed in continuous grey tone and divided in quadrants. The prints were presented independently to two observers to identify, mark, and count boutons. To evaluate the disagreement measures, objects marked either by the automatic procedure or by the human observers were matched and their counts were recorded per quadrant (see Table 5.1). To determine inter-trial disagreements, manually counted printouts in the trials were compared to each other by the same procedure.

Data were analyzed statistically by means of Student's t, χ^2, and Kolmogorov-Smirnow's tests, regression analysis, and analysis of variance (ANOVA) including post hoc comparisons by Scheffé, Neuman-Keuls, and LSD tests. Probability levels of less than 0.05 were considered significant.

5.3 Results

5.3.1 Synthetic image example

The working of the algorithm is illustrated in Figure 5.2. A synthetic image (Fig. 5.2A) was produced by painting randomly located circles using different brush sizes and varying degrees of fuzziness. Granulometry was performed with flat disk-shaped SEs. G(d) showed pronounced maxima that matched the brush diameters used for the drawing at d=4, 7, 10, and 13 pixels (Fig. 5.2D). The filtering procedure is exemplified further for the marked peak (Fig. 5.2D, asterisk). A total of 66 grains comprising 3.6% of the image area was identified (orange, Fig. 5.2C).

5.3.2 Determination of the filtering parameters for the cultured cells

As the fluorescent patches were round, granulometry was performed with a family of flat disk-shaped SEs ranging from d=1 to d=25 (0.2 μm - 5.6 μm). A consistent pattern could be discerned in the shape of the averaged G(d) (Fig. 5.3) - a peak region (P) in the range 0.7 - 1.6 μm, an intermediate region (shoulder - S) in the range 2.0 μm - 2.5 μm, and a decreasing region (tail - T) - from 2.9 μm on. The discerned regions were significantly different from each other ($p < 0.0001$, univariate ANOVA). Post hoc comparisons of the means showed significant differences by all tests ($p < 0.0001$). The *P-region* was larger than the tail (Fig. 5.3; asterisks, P) and the S-region (Fig. 5.3; double asterisks, P). The *S-region* was larger than the tail (Fig. 5.3; asterisks, S), but not larger than the origin. The *tail* was smaller than the origin.

The P-region corresponded to the presence of a large number of synapsin positive grains of matching sizes. The diameter range of these conformed to the size range of synaptic boutons described previously (Alsina et al., 2001). Accordingly, for the construction of I_{low} values of either d_{low}=3 or d_{low}=5 were selected depending on the individual G(d) and the amount of debris in an image. To construct I_{high}, the S-region was considered as well because in some images larger synaptic boutons were noticed. Accordingly, d_{high}=11 was selected as a parameter for I_{high}. An example is given in Figure 5.4D.
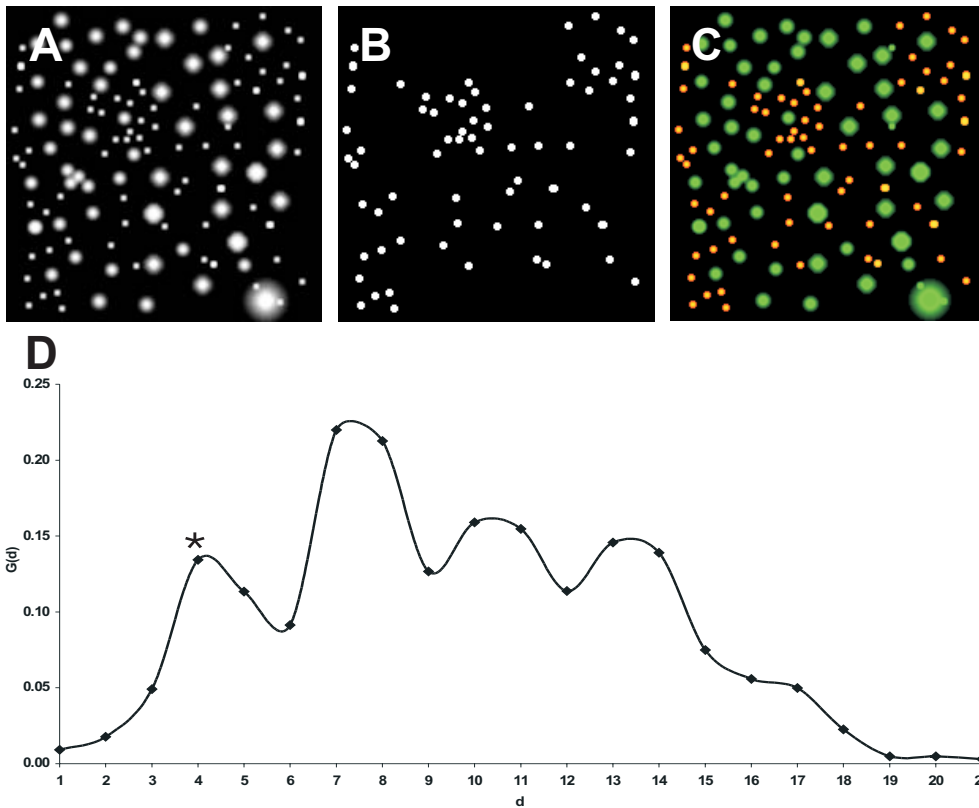
Figure 5.2: Granulometric filtering procedure of a synthetic image; full color p. 181

A - Synthetic image with dimensions 200 x 200 pixels containing 5 types of bright grains of varying grades of fuzziness. B - the mask derived from the marked peak in G(d) (asterisk, D). C - Co-localization of the mask (red) and the original image (green). Co-localized grains appear in orange color. D - Smoothed G(d) of the synthetic image (A).

Based on the discrimination of dark background, auto-fluorescing cell mass, and synapsin positive grains *three* brightness classes were used during k-means clustering. The brightest class was selected for the construction of the mask (Fig. 5.4E). During the integral thresholding, sufficient overlap of the thresholded particles with the actual synapsin grains was typically achieved for AF=0.8 (*Area Factor*, see Appendix B). An example outcome of the detection procedure is presented in Fig. 5.4F.

5.3.3   Morphometric analysis and comparisons with human observers

Measurements of the cultured cells are reported solely to illustrate the suitability of the method (Table 5.2). In total, 1498 boutons were automatically detected and measured in 57 images; 90% of them had diameters between 0.95 and 2.57 µm. Therefore, a simple size criterion for the manual validation could be formulated - boutons were defined as sharp synapsin-positive grains having diameters between 1 and 2.6 µm.
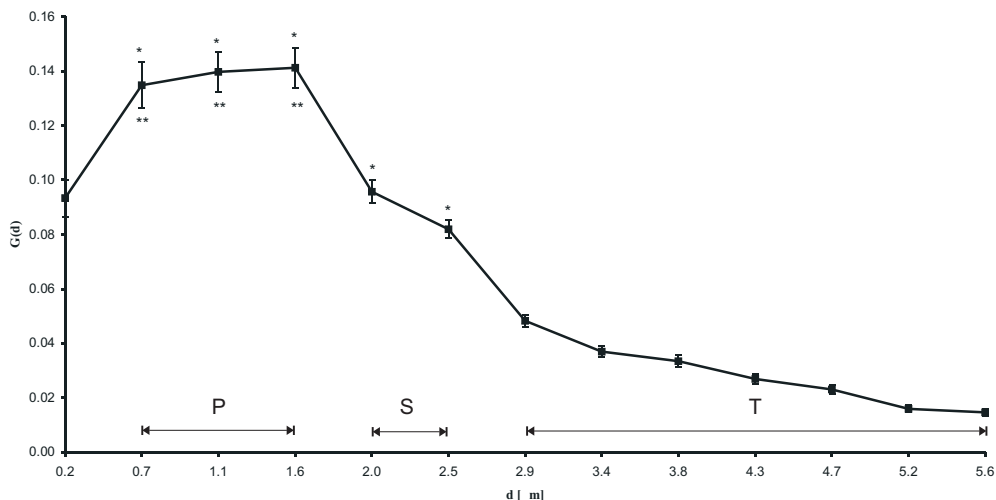
Figure 5.3: Averaged granulometric size density distribution of the entire image set

For descriptive purpose, we discerned peak (P), shoulder (S), and tail (T) regions (see text). Data are presented as means and confidence intervals.

Table 5.2: Descriptive statistics of the measured boutons

	Mean	Median	Mode	P5%	P95%	SD	Skewness	Kurtosis
Area [µm^2]	2.28	1.92	0.91	0.71	5.19	1.41	1.29	1.47
Diameter [µm]	1.63	1.56	1.075	0.95	2.57	0.49	0.66	-0.06

P5% - 5th percentile, P95% - 95th percentile, SD - standard deviation.

Table 5.3: Matched synapses and disagreements - free trial

	Algorithm	Observer 1	Observer 2
Algorithm	-	$M_{m1} = 10.33 \pm 11.19$	$M_{m2} = 12.67 \pm 13.06$
Observer 1	$D_{m1} = 47.21\% \pm 15.58\%$	-	$M_o = 9.50 \pm 6.39$
Observer 2	$D_{m2} = 30.62\% \pm 17.28\%$	$D_o = 56.12\% \pm 31.60\%$	-

Data are presented per image as mean $\pm$ standard deviation (see Table 5.1 for the notations).

5.3.3.1   Free count trial

The free count trial was performed on 451 quadrants (n=9 images, 422 µm^2 per quadrant on average). Summary of the trial is given in Table 5.3. The method-observer and the inter-observer disagreements did not differ significantly (Table 5.3; paired t-test, all comparisons gave $p > 0.05$). Observer 1 (O1), Observer 2 (O2), and the algorithm (A) identified the same mean number of synapses (paired t-test, in all comparisons $p > 0.30$). The counts correlated strongly among each other (A and O1 - $r = 0.99$, A and O2 - $r = 0.96$, O1 and O2 - $r = 0.95$; r denotes Pearson's correlation coefficient).

An important finding was the correlation between the number of mismatching objects of each observer and the number of objects counted by the algorithm in the same image (A and O1 - $r = 0.69$, A and O2 - $r = 0.71$). By using the "automatic" number as denominator in the
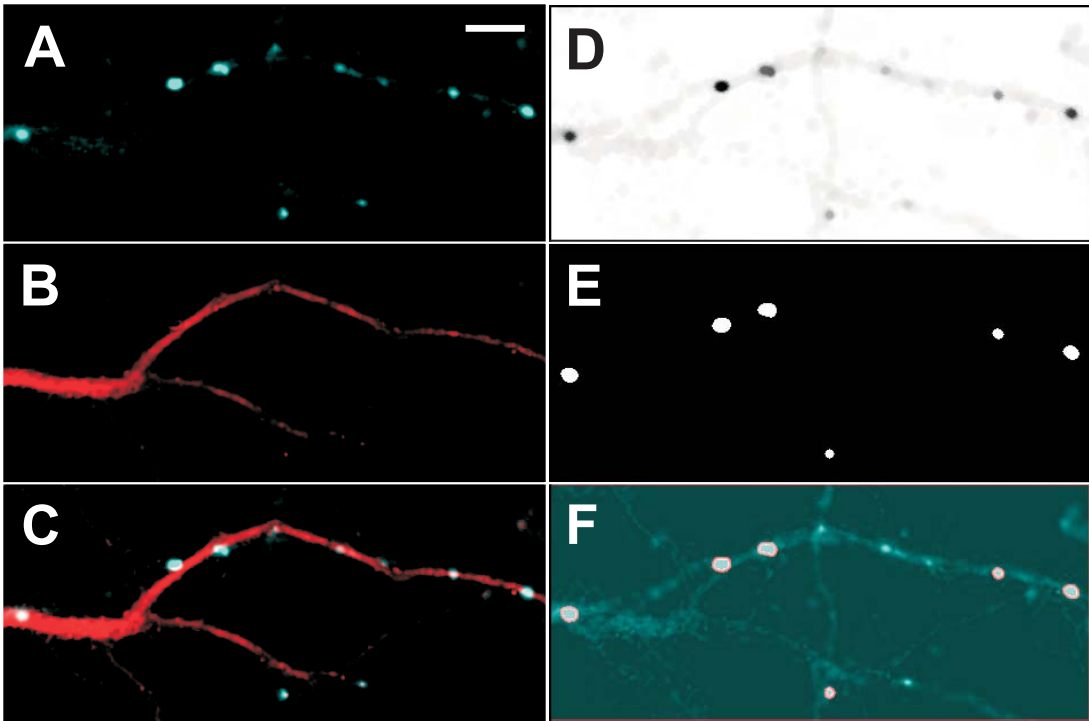
Figure 5.4: Illustration of the granulometric filtering technique on a real image; full color p. 182

A - High-resolution image of synapsin I staining; B - MAP-2 staining; C - Co-localization of synapsin I (cyan) and MAP-2 (red); D - inverted filtered image, *step 2* of the algorithm. E - mask image, *step 3*; F - co-localization of the detected synaptic boutons (red outline) with the original synapsin I image. Scale bar - 5 μm.

disagreement measure, we compensated for this effect in the statistical analysis. Based on this correlation, only the images with similar density of synapsin-positive grains were selected for the calibrated count trial.

5.3.3.2 Calibrated count trial

In the calibrated count trial, 77 objects in 348 quadrants (n=7 images; 380 μm^2 per quadrant on average) were counted (summary in Table 5.4). In total, 44 quadrants containing synaptic boutons were marked by either of the observers. The inter-observer and the method-observer disagreements did not differ significantly (Table 5.4; paired t-test, in all comparisons $p > 0.40$). The mean number of matched boutons per observer did not differ significantly from the expected number of boutons (Table 5.4; χ^2 test). Further, we examined the origins of the encountered method-observer disagreement. In 81.82% of the quadrants, there was a complete agreement between Observer 1, Observer 2 and the algorithm; in 4.55% of the quadrants, boutons identified by the observers were not present in the mask image. In 13.64% of the quadrants, the method-observer disagreement was due to the setting of the AF value.

Table 5.4: Matched synapses and disagreements - calibrated trial

	Algorithm	Observer 1	Observer 2
Algorithm	-	$M_{m1} = 8.14 \pm 2.79$ p= 0.42 (χ^2)	$M_{m2} = 8.00 \pm 2.77$ p= 0.29 (χ^2)
Observer 1	$D_{m1} = 21.73\% \pm 13.08\%$	-	$M_o = 8.86 \pm 3.09$
Observer 2	$D_{m2} = 22.57\% \pm 16.45\%$	$D_o = 15.48\% \pm 10.45\%$	-

Data are presented per image as mean $\pm$ standard deviation (see Table 5.1 for the notations).

5.3.3.3 Inter-trial comparisons

The inter-trial disagreement for Observer 1 was $31.90\% \pm 15.92\%$ and for Observer 2 was $13.66\% \pm 6.37\%$ compared for the same images. During the calibrated count trial, the averaged inter-observer disagreement was lowered 2.4 times and the method-observer disagreement was lowered 2.2 times compared to the free count trial.
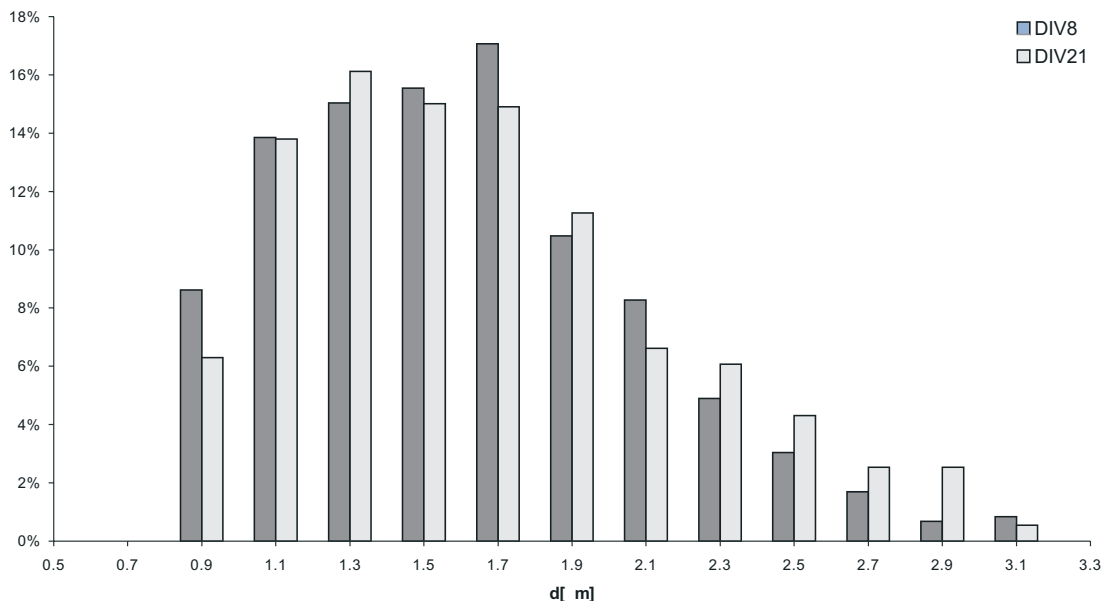
Figure 5.5: Effect on DIV on the size distribution of the synaptic boutons

5.3.4 Effects of the duration of culturing

Unexpectedly, the bouton counts per image at DIV8 (21.92 ± 26.41) were not significantly different from the bouton counts at DIV21 (31.24 ± 27.52) ($p > 0.05$, t-test). Bouton diameters were distributed uni-modally at both DIV8 and DIV21 (Fig. 5.5). The mean bouton area and the mean bouton diameter were larger at DIV21 (area 2.35 ± 1.47 μm^2; diameter 1.65 ± 0.51 μm; n=906) than at DIV8 (area 2.18 ± 1.31 μm^2; diameter 1.60 ± 0.47 μm; n=592)($p < 0.05$; t-test).

However, the distributions did not differ in shape ($p > 0.05$; Kolmogorov-Smirnow test). Days in vitro had a statistically significant influence on G(d) (ANOVA, $p < 0.0001$).

5.3.5 Sensitivity of the automatic bouton identification and measurements to parameter variation
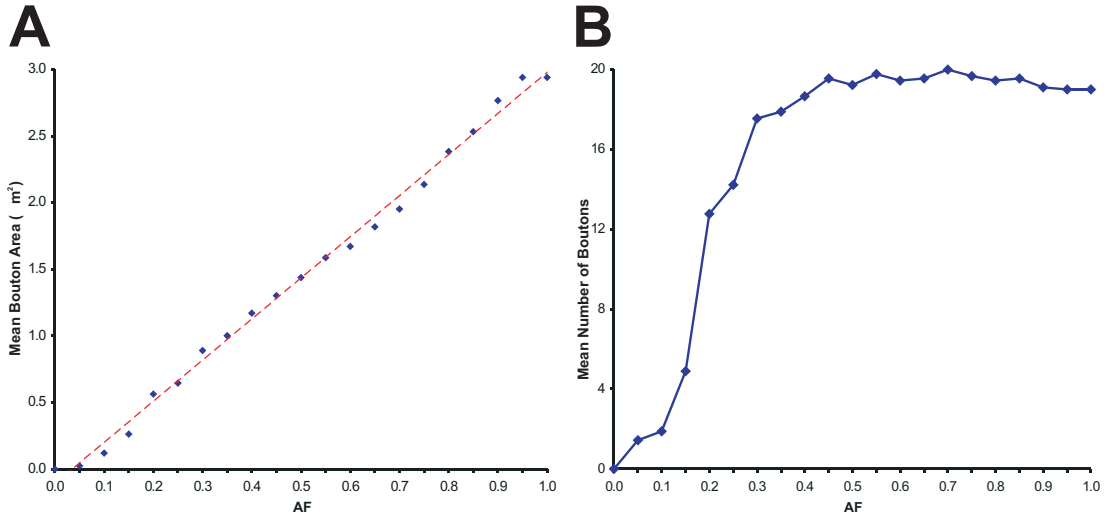

Figure 5.6: Sensitivity of the automatic area measurements and the counts to the variation of AF

The mean bouton area (A) varied linearly (dashed line) with AF while the mean number of boutons (B) rapidly reached saturation.

The variation in the numbers and the area of the automatically identified synaptic boutons, caused by the choice of parameter settings, was studied in the set of images used for the manual verification (n=9).

To study the influence of the area factor parameter the original granulometric filter settings were retained while the AF value was varied and the numbers and areas of the boutons were measured. As expected, both the numbers and the areas of the synaptic boutons depended on AF (Fig. 5.6 A and B). The mean bouton area (MA) varied linearly with AF (Fig. 5.6A) and obeyed the regression equation $MA = 3.09AF - 0.11$ ($R^2 = 0.995; \beta = 0.998; p < 0.0001$). In contrast, the mean number of boutons varied non-linearly with AF and reached saturation for values exceeding 0.4 (Fig. 5.6B).

The bandwidth settings used to count the image set (d_{low}=5, d_{high}=11), denoted as "original", were selected on the basis of literature data for the sizes of the synaptic boutons (Alsina et al., 2001). To study the influence of the granulometric filter bandwidth on the number of identified boutons, the algorithm was rerun using several different bandwidths: broader bandwidth (d_{low}=3, d_{high}=15), denoted "broad"; narrower bandwidth (d_{low}=5, d_{high}=9), denoted "narrow"; and shifted bandwidth (d_{low}=7, d_{high}=13), denoted "shifted" (Fig. 5.7). The AF
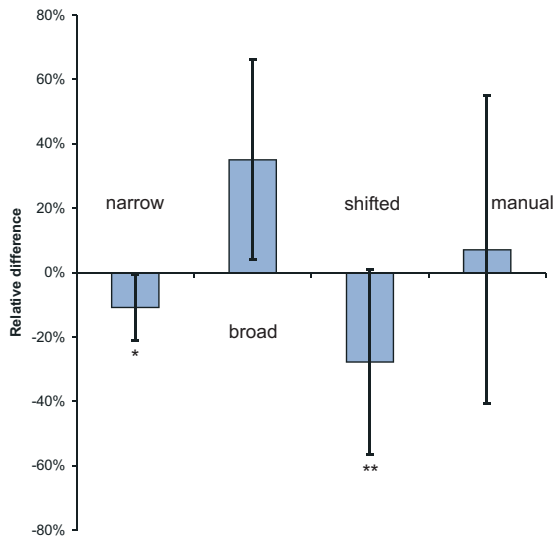
Figure 5.7: Sensitivity of the automatic counts to the variation of filtering bandwidth

Relative differences - $RD_i = 1 - N_i/N_{original}$; i denotes either of "broad", "narrow", or "shifted" bandwidth counts, or the averaged observer counts in the free count trial ("manual"); Noriginal denotes the "original" bandwidth (d_{low}=5, d_{high}=11) counts. Observer counts have the largest variation. Data are presented as means and confidence intervals.

was kept fixed to 0.8. In Figure 5.7, the relative count differences (RD, see legend) are depicted against the "original" bandwidth counts (baseline). Broad bandwidth counts were higher than narrow bandwidth counts ($p < 0.05$; paired t-test; Fig. 5.7, asterisk) and shifted bandwidth counts ($p < 0.001$; paired t-test; Fig. 5.7, double asterisks). There were no differences with the observer counts (all comparisons $p > 0.21$; paired t-test; Fig. 5.7). As expected, the narrow bandwidth counts were lower than the original and the broad bandwidth counts were higher than the original (0 was not in the 95% confidence interval of RD for either of them). The shifted bandwidth counts were marginally different from the original (0 was not in the 90% confidence interval of RD).

5.4 Discussion

Until now, analysis of images by granulometry was applied to the detection of fluorescent signals in *in situ* hybridization (Grigoryan et al., 2002), DNA micro-arrays (Angulo and Serra, 2003), and to the counting of blood cells (Ruberto et al., 2002), and parasites (Theera-Umpon et al., 2001). By means of similar granulometric analysis and filtering, we could successfully identify and perform measurements on synaptic boutons using specific immuno-fluorescence (Fig. 5.3).

The most common approach in automatic image analysis for identification of objects in a gray level image is to threshold the image and then to identify the objects based on *a priori* information of their size and shape. This approach has potentially two shortcomings. *First*, in fluorescence microscopy, the uneven illumination of the total field can result in a global intensity gradient across the acquired digital image caused by the emission of the mounting medium. If such an intensity gradient possesses intensity comparable to the objects of interest, a global threshold will introduce a bias towards the lighter intensities. Eventually, fusing of objects and overestimation of their area can occur. In contrast, an algorithm based on granulometry will have an advantage because intensity gradients may affect *G(d)* only at very large scales and

therefore will not interfere with the extraction of small objects. *Second*, if digital particles are classified by the circularity of their shapes, values exceeding the theoretical bonds for perfect continuous circles (i.e. larger than one) can be calculated for the small grains consisting of several pixels. This is caused by the digitization sampling resulting in underestimation of the particle perimeter, i.e. the pixel is an elementary measure of area and not of length. Therefore, the small digital particles will be misclassified resulting in bias in the identification procedure.

5.4.1   Choice of thresholding procedures

We used thresholding steps in two stages of the proposed algorithm. After the granulometric filtering of the original image, in step 3, the *k-means clustering* was used. This algorithm divides the image histogram in multiple classes of pixels that potentially discriminate between different objects (Jain and Dubes, 1988). The choice of multilevel thresholding was supported by the presence of cell structures having varying degrees of autofluorescence intermingled with the actual synapsin I signal. Such structures were not completely removed by the granulometric filter (Fig. 5.4A and D). The automatic thresholding, based on iterative sub-histogram average intensity decomposition as implemented in *ImageJ* (http://rsb.info.nih.gov/ij/docs/faqs.html), did not identify correctly the synaptic boutons in some of the filtered images. This was due to the overlapping distribution of the foreground pixels and the background gray levels as discussed in literature (Sezgin and Sankur, 2004).

In step 4 of the algorithm, an integral thresholding approach was used. By fixing AF, the estimate of the synaptic bouton area can be controlled (Fig. 5.6A) assuming the same conditions for image acquisition (i.e. same microscope optics, magnification, and camera). Moreover, values of AF greater than 0.4 did not affect the mean number of identified buttons (Fig. 5.6B).

5.4.2   Analysis of the manual counts

In both trials, human observers identified the same objects as the algorithm did (Tables 5.3 and 5.4). The method-observer disagreements indicated that the algorithm performed equally to a human observer. An unexpected finding in the "free" trial was the magnitude of the inter-observer disagreement. Presetting the expected outcome of identification (i.e. number of boutons to be detected by observers) reduced the inter-observer disagreement 2.4 times in the "calibrated" trial. Manual counts of anatomical structures can be tedious and error-prone, and result in a very long processing time (Benali et al., 2003). As demonstrated also in our study by the observed inter-trial disagreement, even experienced observers do not count exactly the same number of objects if the same picture is presented several times. In contrast, a deterministic algorithm will always count the same number of objects with the same parameter settings and is therefore preferable (Geuna et al., 2001; Benali et al., 2003).

5.4.3   Synaptic morphology

Within presynaptic terminals, synapsin I is concentrated in the compartment occupied by the synaptic vesicles (Südhof et al., 1989; Fletcher et al., 1991). It is considered an excellent marker for the synaptic terminal and is used routinely to estimate synaptic density (Camilli et al., 1983; Moore and Bernstein, 1989; Fletcher et al., 1991). Due to the prohibitive time expenditure

of electron microscopic morphometry, a number of studies were performed to correlate light microscopic measurements of synaptic structures to electron microscopic measurements (Papa et al., 1995; Boyer et al., 1998; Harata et al., 2001). It was found that the area occupied by synaptic vesicles loaded with fluorescent dye corresponded to the dimensions of the bouton on electron microscopic level (Harata et al., 2001). Therefore, we can correlate the area of the synapsin positive grain (i.e. the total projection area of the synaptic vesicles) to the area of the synaptic bouton. Reported subtle differences in the mean bouton area (i.e. four times smaller than the resolution of the image) and in the shape of $G(d)$ at DIV8 and DIV28 that do not reflect in corresponding differences in the bouton area histogram shapes probably correspond to slight differences either in the image acquisition conditions or in the performance of the immuno-cytochemical procedures.

5.5 Conclusions

A^N advantage of the proposed automated approach is that, apart from the number of synaptic boutons in a light microscopic image, it also allows to be measured morphological characteristics such as area, circularity, and maximal diameter. The proposed approach is not restricted solely to bouton detection. At different scales and using suitable labeling other cell structures, such as nuclei or axonal profiles, can also be identified and measured.

Acknowledgements

Appendix

A Mathematical morphology

M^{Athematical} morphology offers tools for analysis and processing of images based on the key set theory operations inclusion ($\subseteq, \subset$), union ($\cup$) and intersection ($\cap$)(Serra, 1982). Grey level images and SEs can be represented by 3D functions with their elevation indicating intensity (Sternberg, 1986). The associated sets are then the geometric bodies bellow the functions - so called "umbras". Principal operations in mathematical morphology are erosion, dilation, opening and closing. If $S(x)$ is the umbra of the image S and $E(x)$ is a SE set, *erosion* ($\ominus$) and *dilation* ($\oplus$) are defined by:

$$S \ominus E = \min_{b \in E} \{S(x+b) - E(b)\} \tag{A.1}$$

$$S \oplus E = \max_{b \in E} \{S(x-b) + E(b)\} \tag{A.2}$$

Opening of S by E is defined as:

$$S \circ E = (S \ominus E) \oplus E \tag{A.3}$$

and *closing* of S by E as

$$S \bullet E = (S \ominus E) \oplus E \tag{A.4}$$

Mathematically, granulometry is defined as a parameterised family of openings or closings characterized by the scale parameter d (Matheron, 1975). In the case of a homothetic family of SEs, granulometry can be represented by:

$$\Psi_d(S) = \bigcup_d S \circ dE \tag{A.5}$$

In the formula, d is the proportionality parameter of the homothety. By convention $\Psi_0(S) = S$ and for negative d *opening* is replaced by *closing*. For greyscale images, the measure of the interaction with SE is the volume $V[]$ removed by sieving. Its mapping onto the scale axis d is called granulometric size distribution:

$$W(d) = V[S] - V[\Psi_d(S)] \tag{A.6}$$

The granulometric size density is the normalized generalized derivative of W(d):

$$G(d) = \frac{1}{V[S]} \frac{\partial \Omega(d)}{\partial d} \tag{A.7}$$

The volume of image can be estimated from its histogram H by $V[S] = \sum_{g=0}^{255} H(g) \cdot g$ and the granulometric size density by

$$G(d) = \frac{V[S \circ dE] - V[S \circ (d-1)E]}{V[S]} \tag{A.8}$$

Gray-level morphological operations erosion, dilation, opening and closing were implemented as a sub-routine in *ImageJ* (http://rsb.info.nih.gov/ij/plugins/gray-morphology.html).

B   Integral thresholding

To produce binary particles we introduce $TrAF(T_{\min}, T_{\max})$, a parameterized integral threshold operator depending on the area factor parameter AF, which labels a pixel in the image if its intensity g falls between lower ($T_{\min}$) and upper threshold ($T_{\max}$) bounds constrained by the condition that the ratio between the area of the labeled pixels and the area of the non-black pixels equals AF:

$$\frac{A\left[g \in [T_{\min} \ T_{\max}]\right]}{A[g > 0]} = AF \tag{B.1}$$

In the formula, A[] denotes the area operator acting on the whole image. For the aims of the study, $T_{\max}$ was set to 255 while $T_{\min}$ was determined by varying its value until the condition was globally satisfied. The behavior of the threshold operator was studied in several simulated images having varying amounts of gaussian noise specified by its standard deviation (50, 100, 150, and 200; Fig. 5.B.1). The functional relationship between AF and T-min in the synthetic images is depicted in Figure 5.B.1.
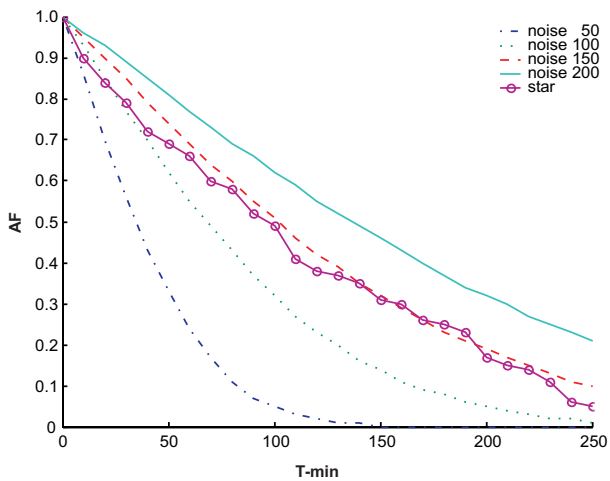
Figure 5.B.1: Dependence of the AF on the pixel intensity in synthetic images

AF is plotted versus T-min for 5 synthetic images - the image from Fig. 5.2A (denoted as "star"), and simulated images (dimensions 200 x 200) containing varying amounts of gaussian noise (σ=50, 100, 150 and 200) denoted as "noise σ" in the legend.

Bibliography

Alsina, B., T. Vu, and S. Cohen-Cory (2001) Visualizing synapse formation in arborizing optic axons in vivo: dynamics and modulation by BDNF. Nat. Neurosci. *4*:1093–1101.

Angulo, J. and J. Serra (2003) Automatic analysis of DNA microarray images using mathematical morphology. Bioinformatics. *19*:553–562.

Benali, A., I. Leefken, U. T. Eysel, and E. Weiler (2003) A computerized image analysis system for quantitative analysis of cells in histological brain sections. J. Neurosci. Methods *125*:33–43.

Boyer, C., T. Schikorski, and C. F. Stevens (1998) Comparison of hippocampal dendritic spines in culture and in brain. J. Neurosci. *18*:5294–5300.

Camilli, P. D., R. Cameron, and P. Greengard (1983) Synapsin I (protein I), a nerve terminal-specific phosphoprotein. I. Its general distribution in synapses of the central and peripheral nervous system demonstrated by immunofluorescence in frozen and plastic sections. J. Cell Biol. *96*:1337–1354.

Dougherty, E. R. and Y. Chen (2001) Robust optimal granulometric bandpass filters. Signal Proc. *81*:1357–1372.

Fisher, R. A. (1935) The Design of Experiments. Oliver and Boyd: Edinburgh.

Fletcher, T. L., P. Cameron, P. D. Camilli, and G. Banker (1991) The distribution of synapsin I and synaptophysin in hippocampal neurons developing in culture. J. Neurosci. *11*:1617–1626.

Geuna, S., P. Tos, R. Guglielmone, B. Battiston, and M. G. Giacobini-Robecchi (2001) Methodological issues in size estimation of myelinated nerve fibers in peripheral nerves. Anat. Embryol. (Berl) *204*:1–10.

Grigoryan, A. M., E. R. Dougherty, J. Kononen, L. Bubendorf, G. Hostetter, and O. Kallioniemi (2002) Morphological spot counting from stacked images for automated analysis of gene copy numbers by fluorescence in situ hybridization. J. Biomed. Opt. *7*:109–122.

Harata, N., T. A. Ryan, S. J. Smith, J. A. Buchanan, and R. W. Tsien (2001) Visualizing recycling synaptic vesicles in hippocampal neurons by FM 1-43 photoconversion. Proc. Natl. Acad. Sci. USA *98*:12748–12753.

Heeroma, J. H., M. Roelandse, K. Wierda, K. I. van Aerde, R. F. Toonen, R. A. Hensbroek, A. Brussaard, A. Matus, and M. Verhage (2004) Trophic support delays but does not prevent cell-intrinsic degeneration of neurons deficient for munc18-1. Eur. J. Neurosci. *20*:623–634.

Heimer, G. V. and C. E. Taylor (1974) Improved mountant for immunofluorescence preparations. J. Clin. Pathol. *27*:254–256.

Huttner, W. B., W. Schiebler, P. Greengard, and P. D. Camilli (1983) Synapsin I (protein I), a nerve terminal-specific phosphoprotein. III. Its association with synaptic vesicles studied in a highly purified synaptic vesicle preparation. J. Cell Biol. *96*:1374–1388.

Jain, A. K. and R. C. Dubes (1988) Algorithms for Clustering Data. Englewood Cliffs, New Jersey: Prentice Hall.

Matheron, G. (1975) Random Sets and Integral Geometry. Wiley series in probability and mathematical statistics. New York: Wiley, 2nd edn.

Moore, R. Y. and M. E. Bernstein (1989) Synaptogenesis in the rat suprachiasmatic nucleus demonstrated by electron microscopy and synapsin I immunoreactivity. J. Neurosci. *9*:2151–2162.

Palizvan, M. R., K. Sohya, K. Kohara, A. Maruyama, H. Yasuda, F. Kimura, and T. Tsumoto (2004) Brain-derived neurotrophic factor increases inhibitory synapses, revealed in solitary neurons cultured from rat visual cortex. Neuroscience *126*:955–966.

Papa, M., M. C. Bundman, V. Greenberger, and M. Segal (1995) Morphological analysis of dendritic spine development in primary cultures of hippocampal neurons. J. Neurosci. *15*:1–11.

Ruberto, C. D., A. Dempster, S. Khan, and B. Jarra (2002) Analysis of infected blood cell images using morphological operators. Image Vision Comput. *20*:133–146.

Serra, J. (1982) Image Analysis and Mathematical Morphology. London: Academic Press Ltd.

Sezgin, S. and B. Sankur (2004) Survey over image thresholding techniques and quantitative performance evaluation. J. Electron. Imaging *13*:146–165.

Six, J., U. Lubke, M. Mercken, M. Vandermeeren, C. Ceuterick, V. de Van, J. Boons, and J. Gheuens (1992) Specific monoclonal antibodies against normal microtubule-associated protein-2 (MAP2) epitopes present in Alzheimer pathological structures do not recognize paired helical filaments. Acta Neuropathol. (Berl) *83*:179–189.

Sternberg, S. R. (1986) Grayscale morphology. Comp. Vis. Graphic Inf. Proc. *29*:377–393.

Südhof, T. C., A. J. Czernik, H. T. Kao, K. Takei, P. A. Johnston, A. Horiuchi, S. D. Kanazir, M. A. Wagner, M. S. Perin, and P. D. Camilli (1989) Synapsins: mosaics of shared and individual domains in a family of synaptic vesicle phosphoproteins. Science *245*:1474–1480.

Tarsa, L. and Y. Goda (2002) Synaptophysin regulates activity-dependent synapse formation in cultured hippocampal neurons. Proc. Natl. Acad. Sci. USA *99*:1012–1016.

Theera-Umpon, N., E. R. Dougherty, and P. D. Gader (2001) Non-homothetic granulometric mixing theory with application to blood cell counting. Patt. Recogn. *34*:2547–2560.

Automated Morphometric Analysis of the Nerve Fiber Population Innervating the Rat Gastrocnemius Muscles [†]

Abstract

Muscle-selective stimulation by implantable neuroprostheses require a quantitative description of the nerve fiber populations in the ventral roots with regard to the muscle targets being innervated. Such descriptions can be obtained by means of retrograde axonal tracing from the relevant muscles. Here we present a quantitative description of the fiber population innervating the gastrocnemius muscle of the rat in samples of tibial and sciatic nerves, and L6 ventral roots. Gastrocnemius muscles of adult rats were injected with the retrograde tracer Fluoro-Gold and later on cross-sections of spinal cords, ventral roots, sciatic, and tibial nerves were imaged on a fluorescence microscope. To relate the area occupied by the tracer within an axonal profile to the area of the corresponding fiber (axon + myelin sheath) paired sets of measurements were performed on representative images. A linear regression relationship could be established for the equivalent diameter (i.e. $2\sqrt{Area/\pi}$ of the fiber and the equivalent diameter of the axonal signal according to the equation $d[fiber] = 6.86 + 0.38 \cdot d[signal]$. This allowed reconstruction of the total population of labeled fibers solely from the fluorescence measurements. Peaks in the population coincided with the $A\alpha$ fibers in both the L6 ventral root and the peripheral nerves. In contrast, the smaller $A\gamma$ fibers could not be detected. The presented method allows for the detection of the most prevalent class of labeled fibers in a tracing experiment, which can be instrumental in further topographical studies of the internal nerve topography.

6.1   Introduction

Lumbar spinal roots and the sciatic nerves in the rat are frequently used as model systems for studying: the *regeneration* of nerve fibers (Jenq and Coggeshall, 1985; Vleggeert-Lankamp et al., 2004), mechanisms of the developmental and induced neuronal *cell death* (Greensmith et al., 1996; Prodanov et al., 1998; Iwasaki et al., 2004) and for testing *neuroprosthetic interfaces* with the nervous system (Navarro and Kennedy, 1991). To restore locomotion in paraplegic patients a vast array of implantable neuroprosthetic devices have been tested in experimental animals (overviews in Agnew and McCreery (1990); Heiduschka and Thanos (1998)). Typically an electrode is placed surgically around the nerve (i.e. "cuff"- Rodriguez et al. (2000)) or is implanted inside a nerve (i.e. intrafascicular electrodes (Veltink et al., 1989; Malagodi et al., 1989), or microelectrode arrays (Rutten et al., 1995; Branner and Normann, 2000; McDonnall et al., 2004)) or a nerve stump is sutured to an electrode (i.e. sieve electrodes (Lago et al., 2005)). The internal topography of the motor fibers in the spinal roots and peripheral nerves can be instrumental for further improvement of the spatial selectivity of electrical stimulation obtained by implantable electrodes (Prodanov et al., 2003). Muscle-related internal topography (i.e. functional topography) of the motor axons can be investigated by injections of a tracer substance, such as hydroxystilbamidine (i.e. Fluoro-Gold) (Schmued and Fallon, 1986), into a muscle and subsequent mapping of the axons in the cross section of the relevant neural structure. If the morphological type of the retrogradely traced myelinated nerve fiber (i.e. the labeled axon and its encompassing myelin sheath) is identified in the same experiment this would allow to specify a mode of electrical stimulation tailored to the specific fiber type (i.e. size selective stimulation).

Morphological classification of structures is based either on a morphometric evaluation of the studied samples (objective approach) or on a qualitative assessment by expert observers (subjective approach) (Pamphlett and Sjarif, 2003). To reduce inter-observer disagreement and to increase inter-trial reproducibility the objective approach is preferable (Pamphlett and Sjarif, 2003; Prodanov et al., 2005a). Manual morphometry of anatomical structures is tedious and typically takes a very long processing time (Benali et al., 2003). In contrast, automated morphometry can greatly reduce processing time and is, therefore, preferable (Benali et al., 2003; Geuna et al., 2001).

In this study, we report automatic morphometric analysis of the nerve fiber populations that innervate rat gastrocnemius muscles as identified by retrograde tracing with Fluoro-Gold (FG). Some of the reported findings were presented in a preliminary form (Prodanov et al., 2004).

6.2   Methods

6.2.1   Animals

All experiments were performed in accordance with the international (EU Directive 86/ 609 /EEC) and national laws governing the protection of animals used for experimental purposes[1]. Three female Wistar rats (HsdCpb), weighing on average 250 g, were obtained from the central animal care facility.

---

[1]Leiden University Animal Care and Experimentation Commission UDEC 02076a

6.2.2   Operation

Under general anesthesia by isofluorane (1.5 - 2 %) and N_2O (1.0 l/min) and premedication with 0.1 ml(i.e. 0.4 mg/100 g Fentanyl citrate) Hypnorm[®] (Janssen Pharmaceutica, Beerse, Belgium) injected *i.p.* the skin of the animals and the superficial muscle layer were sectioned and the fascial surface of the gastrocnemius muscle was exposed. Muscles were injected with a 100 µl Hamilton microsyringe. Four per cent (m/v) aqueous solution of Fluoro-Gold (Fluorochrome Inc, Denver, Colorado) was applied in a quantity of 10 µl per injection in the gastrocnemius muscle: lateral head (2 injections) and medial head (1 injection). In order to achieve optimal deposition and maximal uptake the tracer injections were performed near the motor end-plate region of the muscles as previously determined (Prodanov et al., 2005b). To reduce tracer leakage the syringe was kept in the injection site for 2-3 minutes and the fascia was then washed thoroughly with sterile physiological saline solution. Finally, the skin was sutured and the animals were let to recover.

6.2.3   Preparation

After 3 days of survival, the animals were deeply anesthetized with 0.2 ml (i.e. 4.8 mg/100 g) Pentobarbital (Nembutal[®], Ceva Sante Animale, Libourne, France) and 0.2 ml Hypnorm (i.e. 0.8 mg/100 g Fentanyl citrate) and then perfused transcardially with 250 ml 0.9% sodium chloride solution, followed by 250 ml solution of 4% paraformaldehyde (PF) in 0.1M phosphate buffer, pH 7.2, and finally by 250 ml 0.1M phosphate buffered saline, pH 7.2. Under a surgical microscope, the skin, superficial and deep hind limb muscles were dissected and the sciatic nerve was exposed. The spinal canal was opened from its dorsal side from vertebrae Th6 to S1. Lumbar dorsal and ventral spinal roots were identified according to the atlas of Hebel and Stromberg (1986) by vertebrae counting from two landmarks - the *scapula* projecting at the level of Th6 vertebra and *os ilium* projecting at the level of L6 vertebra. The tissue samples included ventral roots L6, dorsal roots L6 (including the dorsal root ganglia), sciatic, peroneal, and tibial nerves from the operated side. Samples were stored in PF at 4 °C.

6.2.4   Tissue processing

Samples of the ventral and dorsal roots and the peripheral nerves were sectioned at a thickness of 14 µm on a Leica Jung cryotome (Leica Microsystems, Bensheim, Germany) and cover-slipped using Vectashield H-1000 aqueous mounting medium (Vector Laboratories, Peterborough, UK). Muscles and spinal cords were embedded in 13% gelatin and fixed in 4% PF. The gelatin blocks were serially sectioned on a freezing microtome (Leica Jung 1205, Leica Microsystems, Bensheim, Germany). Spinal cords were sectioned at a thickness of 40 µm coronally, or transversely. Muscles were transversely sectioned at a thickness of 120 µm. Sections were mounted, air-dried, and cover-slipped using aqueous mounting medium containing 10% (v/v) 0.1M phosphate buffer, pH 7.2, in glycerol.

6.2.5   Microscopy and Image processing

In order to assess the injection site and the amount of labeling, sections of the spinal cord and of the injected muscles were inspected on an Olympus IX-70 epi-fluorescence microscope (Olympus, Zoeterwoude, The Netherlands). Sections of the ventral roots were inspected on Axioplan
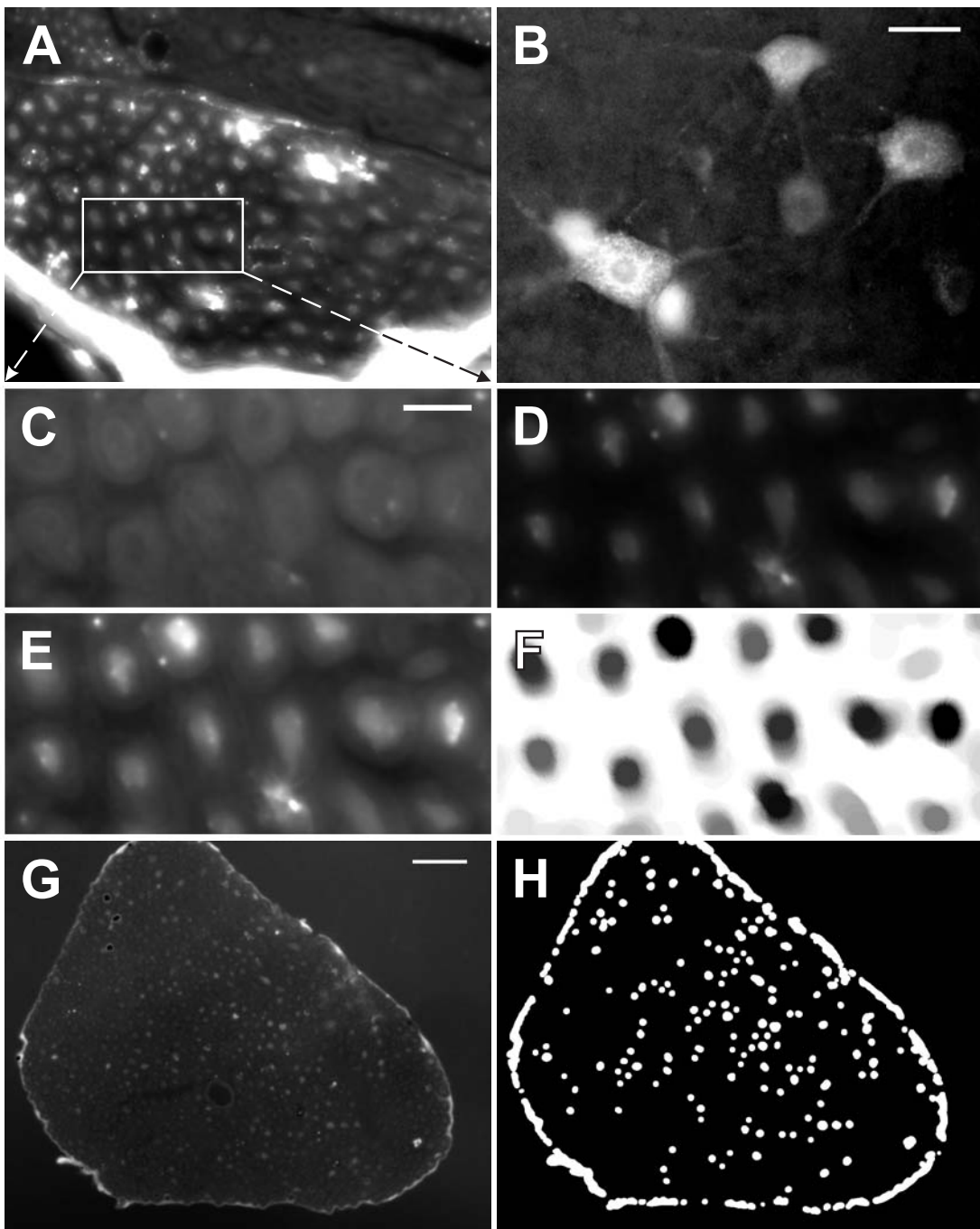
Figure 6.1: Tracing and fiber identification

Figure 6.1 (continued) A - A peripheral fascicle of the tibial nerve, FG channel. Note the autofluorescent perineurium and the variation in the filling of axons. The bright fussy blobs are dust particles. A ROI with dimensions 71 µm x 32 µm is marked onto the image. B - A group of FG-positive motoneurons in the lumbar spinal cord, FG channel, scale bar - 50 µm . Fuzzy spots are two other motoneurons that are not in the plane of focus. FG is situated in the cytoplasm, while the nuclei are negative. The dendrites show less fluorescence than the somas. C, D, E, F - the ROI is showed in greater detail and the working of the algorithm is demonstrated on it; C - FITC channel, scale bar is 10 µm, E - FG channel. Note that the positive axons are almost entirely filled with FG. D - channel-subtracted image; after recoloration the FITC channel was subtracted from the FG channel. Note the varying intensity of the residual labeling. F - granulometric filtering was applied to the D image to isolate the positive axons. The image is inverted and its brightness and contrast were adjusted to provide best observation. G - channel subtracted image of a L6 ventral root section, scale bar is 50 µm. Note the autofluorescence of the endoneurium. A blood vessel is situated pericentrally. H - granulometrically filtered and thresholded image.

(Carl Zeiss, Sliedrecht, The Netherlands) or Leica DM (Leica Microsystems, Bensheim, Germany) fluorescence microscopes equipped with CCD cameras. The fluorescent signal from the specimens was recorded on 2 channels using standard filter sets. FG signal was recorded using a standard filter set for DAPI (4',6-Diamidino-2-phenylindole) detection (excitation 320 - 370 nm) (i.e. Fig. 6.1 A, B, E). The signal from the myelin sheaths (comprising autofluorescence) was recorded using a filter set for FITC (Fluorescein) detection (excitation 450 - 490 nm) (Fig. 6.1C). Digital images (dimensions 528 µm x 407 µm) were acquired at resolution 2.46 pixels per µm using 20x objective and digitally stored. Image processing and measurement steps were performed using the public domain software for image analysis *ImageJ* (NIH, Bethesda, Massachusetts, http://rsb.info.nih.gov/ij/) (Abramoff et al., 2004). The following procedure was employed further to identify the FG-positive fibers:

Separation of channels

Due to the excitation characteristics of Fluoro-Gold its signal was absent from the FITC channel (Fig. 6.1 C, E). Therefore, it was possible to isolate the FG signal if the intensity of the FITC channel was subtracted from the intensity of the FG channel. A necessary condition to minimize the cut-off bias is that the overall resulting intensity is positive and therefore for the channels intensities should hold:

$$0 \notin Confidence[I(FG) - I(FITC)] \tag{6.1}$$

In the formula, $I()$ denotes channel intensity (i.e. gray value) and $Confidence$ - the confidence interval. For the optimal separation of channels images were recolored on the basis of the empirical statistics of a *Region Of Interest* (ROI). In short, a thin rectangle ROI was drawn across the image and the coefficient K was calculated as:

$$K = \frac{E[I(FG)]}{P_{95}[I(FITC)]} \tag{6.2}$$

where P95 denotes the 95th percentile of the empirical pixel intensity distribution and E[] denotes mathematical expectation estimate. Next, the FITC channel was multiplied by the coefficient:

$$FITC' = K \cdot FITC \tag{6.3}$$

Further, the resulting $FITC'$ channel was subtracted from the DAPI channel (Fig. 6.1D):

$$I = FG - FITC' \tag{6.4}$$

Granulometric filtering

Tracer-positive axonal profiles were isolated from the resulting images by means of granulometric filtering programmed as a subroutine in *ImageJ* (see web-site and Prodanov et al. (2005a)). The original image was transformed using morphological opening operations (Matheron, 1975; Serra, 1982) according to:

$$F = I \circ SE[d_{low}] - I \circ SE[d_{high}] \tag{6.5}$$

where $\circ$ denotes the opening operation and SE denotes *structuring element* image of a given size d (see 111). The granulometric size density distribution of several representative images was determined according to Prodanov et al. (2005a). Analysis of the granulometric size density distribution curves suggested the low bound for the filtering to be $d_{low}=9$ (comprising 3.7 μm) and the high bound of the filtering to be $d_{high}=25$ (10.2 μm). An example outcome of the filtering procedure (i.e. the F image) is presented in Fig. 6.1F.

6.2.6   Automatic morphometry

To avoid false detection of axons due to incomplete elimination of the endoneurium autofluorescence (Fig. 6.1G) the automatic detection and measurement of the FG-positive axons was performed in ROIs that excluded the endoneurium. In order to measure the area of each positive axon interactive intensity thresholds were set globally in the images. Binary grains representing FG-positive axonal profiles were constructed from the connected pixels having intensities within the threshold borders (as implemented in *ImageJ*). Identified FG-positive axonal profiles were automatically enumerated and outlined and their areas, corresponding diameters (computed as $2\sqrt{Area/\pi}$), and the Cartesian co-ordinates of their centers of mass were calculated and recorded in a database. During the measurement procedure derivative images were produced where the identification numbers of the positive fibers were visible. Resulting images with the numbered objects were overlaid onto the original image and inspected for the accuracy of FG-positive axons. In case of sub-optimal image processing resulting in false positive or false negative axons the operator repeated the processing and measurement procedure to eliminate them.

6.2.7   Matching of the fibers and semi-automatic morphometry

To associate the nerve fiber area measurement to a corresponding measurement of the area of fluorescent signal in the axon of the same fiber only fibers with clearly traceable borders, which had their axons filled with tracer were outlined. The derived images with the numbered axons produced during the previous step were combined with the FITC channels and the fibers that were clearly visible were manually outlined and automatically enumerated and their morphometric parameters were determined (see above). This procedure is further referred to as semi-automatic measurement. Thus, each measured fiber received 2 coupled identification numbers - one for the measurement of its FG axonal signal area and one for the measurement of its fiber area.

Table 6.1: Numbers of automatically measured FG-positive axons and corresponding manually outlined fibers

material	n	total axonal measurements (automatic)	matched fiber measurements (semi-automatic)
L6 ventral	3	355	116 (32.7%)
Sciatic	5	225	66 (29.3%)
Tibial	2	202	68 (33.7%)
Total	10	782	250 (31.9%)

In the ventral roots the whole root cross-section was measured. The peripheral nerves were measured within ROIs; n - number of images measured; numbers in brackets denote percentages of the matched fiber population from the total fiber population.

6.2.8 Reconstruction of the labeled fiber population and statistical analysis

The relationship between the size of the labeling $d[as]$ and the size of the overall nerve fiber $d[f]$ was studied in the matched sample of fibers (see Table 6.1) using multiple regression analysis and General Linear Model technique. Fiber populations were reconstructed from the axonal signal using the derived quantitative relationship. Properties of this reconstruction procedure were studied in the matched sample. For this purpose, the diameter distribution histograms of the matched sample and the reconstructed fiber populations were computed using class width of 0.5 μm corresponding to the resolution of the image (i.e. 1 pixel=0.41 μm). In every section in the sample, the histograms of the measured and the reconstructed fiber diameters were compared for each class using their relative difference $RD[d]$ as introduced in Prodanov et al. (2005a):

$$RD[d] = \frac{H_{rec}[d] - H_{mes}[d]}{N_{sample}} \tag{6.6}$$

where $H_{rec}[d]$ denotes the number of fibers in the reconstructed histogram for the fiber class d, $H_{mes}[d]$ - the number of fibers in the measured histogram for the fiber class d, and N_{sample} is the total number of fibers in the image.

Further statistical analysis was performed using ANOVA, Student's t-tests, and Kolmogorov - Smirnov (KS) tests. Probability levels of less than 0.05 were considered significant. Data are presented as means ± standard deviations.

6.3 Results

6.3.1 Tracer availability in the injection site and the spinal cord motoneurons

The injection sites in the injected muscles were clearly discernable. The spill towards adjacent muscles was minimal (data not shown). In all of the studied animals, the spinal cord motoneurons in the lumbar (L2 - L6) motoneuronal columns (Rexed laminae IX) were loaded with FG but not in the thoracic and sacral parts of the spinal cord. Due to the epi-fluorescence conditions and the incompatibility of the tracer with light-microscopic counter stains more

Table 6.2: Descriptive statistics of the automatic axonal measurements

	roots	nerves	t-test	KS-test
A[as] [μm^2]	19.89 ± 9.19	25.31 ± 13.18	$p < 0.0001$	$p < 0.001$
d[as] [μm]	4.90 ± 1.14	5.49 ± 1.43	$p < 0.0001$	$p < 0.001$
Sample size	355	427		

Data are presented as means $\pm$ SD. Dimensions of the parameters are shown in square brackets.

precise identification of the spinal levels was not possible. Tracer-positive motor neurons are depicted in Figure 6.1B. Some dorsal root ganglion neurons were tracer-positive as well but no tracer could be observed in the axonal profiles of the observed proximal parts of the dorsal roots (data not shown).

6.3.2 General microscopic observations

Collected ventral roots were unifascicular. Microscopically, on the cross-section they were of a roughly polygonal shape (Fig. 6.1G). Usually, there was one large clearly discernable blood vessel (vas radici) situated in varying locations. There were no other discernable landmarks that could allow further orientation. The shapes and sizes of the fibers in the peripheral nerves were more heterogeneous than in the ventral roots. The outer boundaries of nerve fibers were less sharp than in the ventral roots. Accordingly, fewer fibers could be measured reliably semi-automatically (see Table 6.1). The fluorescent signal was present in the cross-sections of the tibial (Fig. 6.1A) and sciatic nerves and the L6 ventral roots (Fig. 6.1G) but not in the peroneal nerves (data not shown). Tracer signal intensity was higher in the peripheral nerves (closer to the injection site) than in the L6 ventral root. The intensity of tracing signal in the sciatic and the peripheral nerves was beneficial for the automatic detection procedure.

6.3.3 Morphometric analysis

Results are derived from 782 automatically measured FG-positive axons and 250 semi-automatically (see Methods) measured FG-positive fibers (i.e. comprising FG-positive axon surrounded by a clearly discernable myelin sheath) (Table 6.1). The following notations of the morphometric parameters are used throughout the paper: $A[as]$ denotes the area of the axonal signal; $d[as]$ - the corresponding diameter of the axonal signal; $A[f]$ - the area of the fiber profile; and $d[f]$ - the corresponding fiber diameter. To relate the area occupied by tracer within an axonal profile to the area of the corresponding fiber (axon + myelin sheath) paired sets of measurements were performed on the fibers having clearly traceable borders and showing tracer fluorescence (see Methods). These fibers are further referred to as the matched sample.

Comparing the matched samples, $d[as]$ in the ventral roots was smaller than $d[as]$ in the peripheral nerves (Table 6.2). Comparing the matched sample to the total sample, in the ventral root samples, the axonal signal diameter $d[as]$ in the matched sample (4.97 ± 1.03 μm) was not significantly different from $d[as]$ in the total sample (4.90 ± 1.14 μm) ($p > 0.6$; t-test). Moreover, both samples had non-differing variances ($p > 0.18$; F-test) and distributions ($p > 0.8$; KS test). Therefore, matched ventral root axons comprised a representative sample from all automatically detected axons. In contrast, in the distal nerves $d[as]$ in the matched sample (5.18 ± 1.17 μm)

Table 6.3: Descriptive statistics of the matched fibers

	roots	nerves	t-test	F-test	KS-test
A[as][μm^2]	20.23 ± 8.23	22.16 ± 10.04	$p > 0.05$	$p > 0.6$	$p > 0.1$
A[f][μm^2]	59.43 ± 16.66	63.72 ± 16.87	$p < 0.05$	$p > 0.18$	$p < 0.05$
d[as] [μm]	4.97 ± 1.03	5.18 ± 1.17	$p > 0.1$	$p > 0.6$	$p > 0.1$
d[f] [μm]	8.61 ± 1.22	8.92 ± 1.20	$p < 0.05$	$p > 0.18$	$p < 0.05$
Sample size	116	134			

Data are presented as means $\pm$ SD. Dimensions of the parameters are shown in square brackets.

was significantly smaller than the total sample $d[as]$ (5.49 ± 1.43 μm)($p < 0.05$, t-test). The matched sample and the total population had also differing variances ($p < 0.01$; F-test) and distributions ($p < 0.05$; KS-test). Therefore, selection bias was possible for the axons of distal nerves.

In both the peripheral nerves and the ventral roots, matched fibers were distributed unimodally (Fig. 6.2B). The peaks in their size distributions were in range with the $A\alpha$ fibers in the rat as indicated in literature (Vleggeert-Lankamp et al., 2004). From the histogram it can be seen that in the periphery a larger amount of thick fibers was measured as compared to the ventral roots (Fig. 6.3B). This was also supported by the observed difference in the mean sizes (diameters or areas) and the distributions of the ventral roots compared to the peripheral nerves (Table 6.3). Axonal signal diameters correlated with the fiber diameters in the matched sample (Pearson's $r = 0.35$, $p < 0.0001$) (Fig. 6.2C). This allowed a full regression analysis to be performed. First, it was tested whether a non-linear dependency would fit better the data. For that purpose, polynomial models of 2$^{\mathrm{nd}}$ and 3$^{\mathrm{rd}}$ order and a logarithmic regression model were tested. However, none of them fitted the data adequately. Next, to study the relationship between the axonal signal and the fiber size, we used the General Linear Model technique and accounted for the type of the material (i.e. ventral root or peripheral nerve) as a categorical predictor. Both the intercept ($p < 0.0001$, t-test) and slope ($\beta = 0.33$, $p < 0.0001$, t-test) of the model were significantly different from 0. The type of material did not affect significantly either the slope ($p > 0.9$) or the intercept of the regression line ($p > 0.7$). Therefore the influence of the type of material was not considered in further modeling of the data. Finally, refitting the data with simple regression model yielded the following linear function (see also Fig. 6.2C):

$$d[f] = 6.86 + 0.38 \cdot d[as] \tag{6.7}$$

The standard errors of the intercept and the slope were 0.34 μm and 0.07 respectively.

6.3.4 Reconstruction of the fiber population in the matched sample

Fiber population of the matched sample was reconstructed from the axonal signal (Fig. 6.2A) using Eq. 6.7 and a size distribution histogram of the reconstructed fiber population was computed (Fig. 6.2D). In the ventral roots, the mean measured fiber diameter (8.61 ± 1.23 μm, n=116) was not significantly different from the mean reconstructed fiber diameter (8.74 ± 0.39 μm, n=116) ($p > 0.3$; t-test). In the peripheral nerves, the mean measured fiber diameter (8.92 ± 1.20 μm, n=134) was not significantly different from the mean reconstructed fiber diameter (8.82 ± 0.44 μm, n=134) ($p > 0.3$; t-test). In contrast to the semi-automatically measured
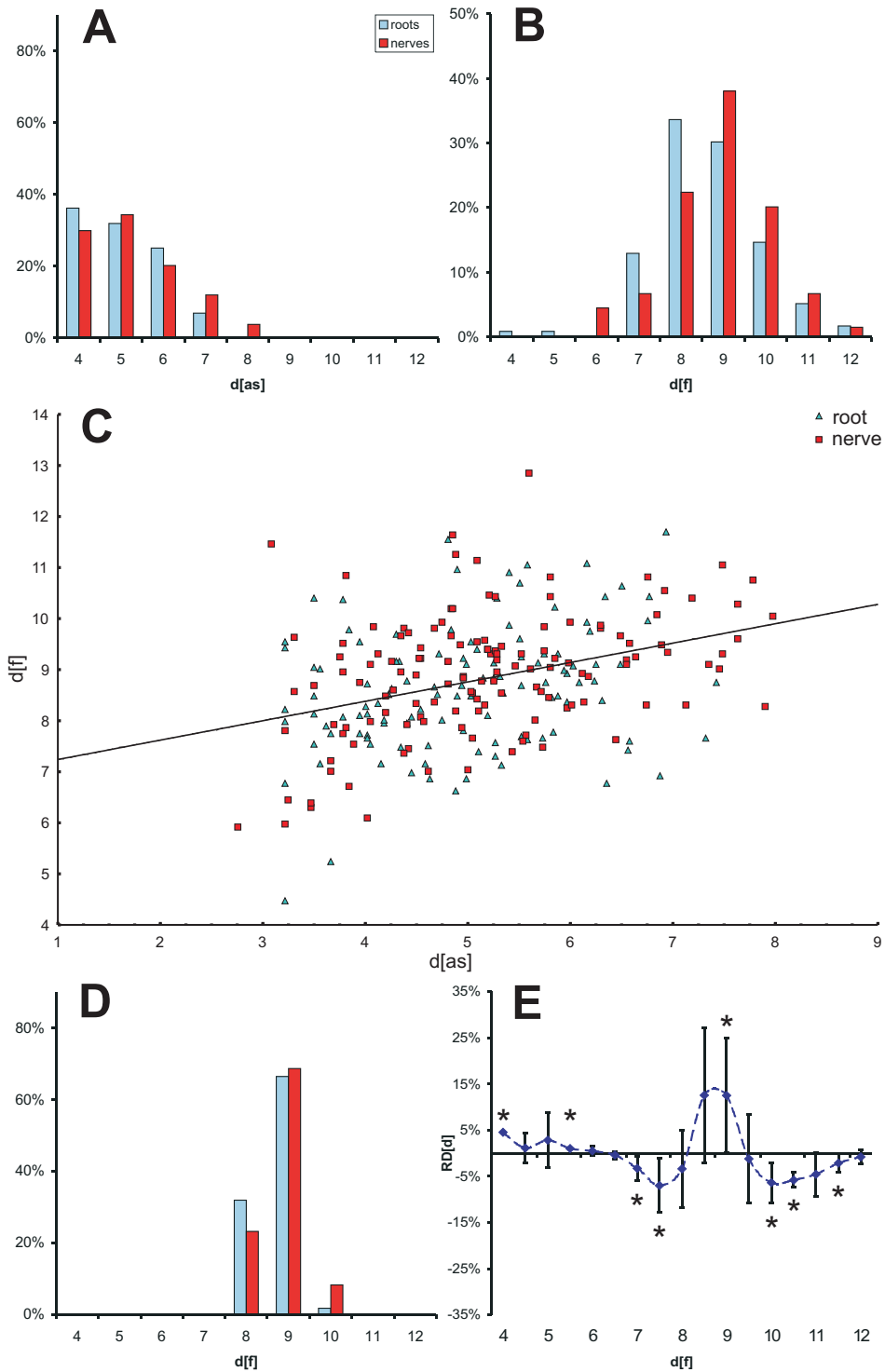
Figure 6.2: Reconstruction of the matched fiber populations

Figure 6.2 (continued) A - axonal signal size distribution. B - fiber diameters distribution. C - relationship between the $d[as]$ and $d[f]$. D - histogram of the reconstructed population. E - Relative difference, RD[d]; 95% confidence intervals are depicted; *root* denotes samples from the L6 ventral root; *nerve* denotes samples from the tibial and sciatic nerves. Class width (A-D) is 1.0 μm.
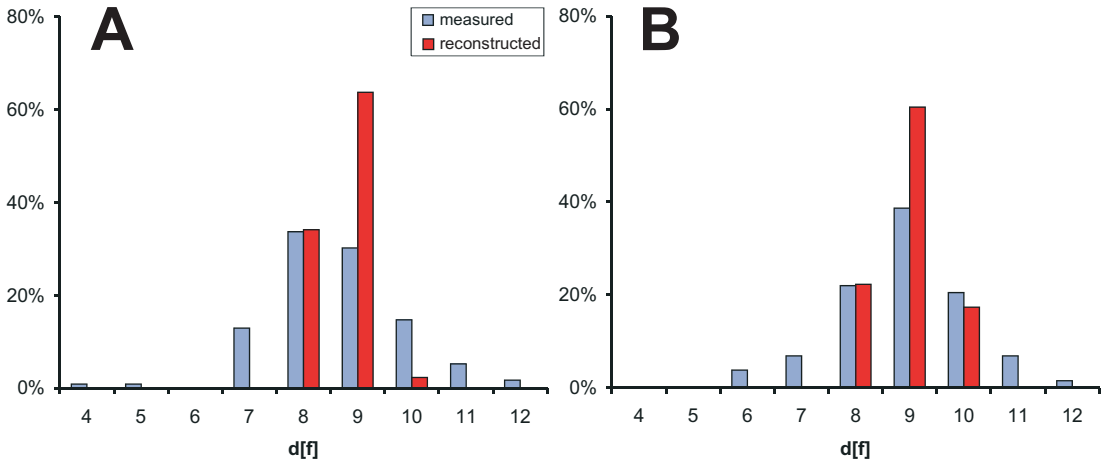

Figure 6.3: Reconstructed diameter distributions of total populations of detected fibers

A - ventral root L6; B - peripheral nerves; *measured* refers to the matched sample and *reconstructed* to the total sample population; class width - 1.0 μm.

populations (see Table 6.3) due to the similarities in the axonal signal in the peripheral nerves and the ventral roots the respective reconstructed populations did not differ in both means ($p > 0.13$; t-test) and distributions ($p > 0.7$; KS-test).

The performance of the reconstruction procedure was studied in the different fiber classes using the *relative difference RD[d]* (eq. 6.6) between the semi-automatically measured and reconstructed histograms. Compared to the semi-automatic measurements the automatic reconstruction procedure overestimated the fibers distributed around the mean diameter on average with up to 15% of the population and underestimated on average down to -9% the fibers in the larger and the smaller diameter groups (Fig. 6.2E).

6.3.5 Reconstruction of the total population of labeled fibers

To identify the type of fibers that were labeled in the experiment, the reconstruction procedure was extended to the total labeled axonal population. In both the ventral roots and the peripheral nerves, histograms of the reconstructed populations showed peaks that were in range with the $A\alpha$ motor fibers (Fig. 6.3)(Vleggeert-Lankamp et al., 2004). Comparing the matched and the total population of the reconstructed fibers there were no differences in the mean $d[f]$ in the ventral roots ($p > 0.5$; t-test) but there were statistically significant differences in the peripheral nerves ($p < 0.05$; t-test). Compared to the ventral roots, there was a shift towards larger diameters in the peripheral nerves. Accordingly, the mean diameter of the reconstructed fibers was larger in the peripheral nerves (8.94 ± 0.54 μm, n=427) than in the ventral roots (8.71 ± 0.43 μm, n=355) ($p < 0.0001$, t-test).

6.4   Discussion

6.4.1   Type of fibers that are predominantly labeled

IN the presented material, predominantly $A\alpha$ fibers were labeled and measured (Fig. 6.2). Measurements of entire fiber populations in the ventral root L6 showed that more than 30% of the fibers had diameters above 10.5 μm (see Chapter 4). Since the matched sample in the L6 was representative for the total population of labeled fibers, it can be concluded that the size distribution of the gastrocnemius motor fibers did not correspond to the size distribution of the entire $A\alpha$ fiber population in L6. Surprisingly, only a small amount of thick $A\alpha$ fibers was present in the gastrocnemius fiber population compared to the entire $A\alpha$ fiber population. The same pattern could be found for the axonal size distributions in the L6 ventral root: 42% of the axons described by Coggeshall et al. (1977) in L6 were larger than 8 μm while we did not find any of the axons innervating gastrocnemius to be larger than that size (Fig. 6.2A). Moreover, measurements of Peyronnard et al. (1986) showed absence of larger than 12 μm $A\alpha$ motor fibers in the rat medial gastrocnemius nerve branch and peaks of their histogram around 9 - 10 μm, which is in accordance with our measurements (Fig 6.2B). As already suggested in Chapter 4 (p. 97), reported differences can probably be caused by redistribution of the thick $A\alpha$ fibers to nerves innervating axial muscles of the tail and the pelvis, as suggested also by the branching pattern of the lumbar plexus (Hebel and Stromberg, 1986).

6.4.2   Choice of tracer and specificity of labeling

FG is a widely used retrograde fluorescent tracer for studying the connectivity in the nervous system because (i) it is not taken up by undamaged fibers of passage, (ii) it does not diffuse out of fixed retrogradely-labeled neurons and (iii) it can be applied in wide ranges of survival times by both iontophoretic or pressure injections; see for example Schmued (1990; 1994). In accordance with the mentioned properties, tracer signal was not observed in non-neuronal cells in the spinal cord cross-sections. Therefore, the detected tracer signal in the axonal profiles could be attributed to specific tracer transport from the injection site. Transport of FG in the proximal parts of the DRG axons cannot be excluded completely. However, due to the active centripetal nature of the FG transport it is unlikely. FG is associated with vesicular structures in the transporting axons (Schmued et al., 1989); therefore, it is likely that it is transported by the cytoskeletal motor proteins and these act mostly unidirectionally (Brown, 2003).

In the ventral roots, the number of motor nerve fibers innervating a muscle can be estimated from the counts of its motor neurons in the spinal cord since branching of the myelinated fibers in the ventral roots is very unlikely. Studies in the rat suggest that the myelinated fibers do not branch in the cervical ventral roots (Fraher and O'Sullivan, 1989) and counts of the motor fibers in some lumbar muscle nerve branches closely match the numbers of their motor neurons (Peyronnard et al., 1986). Studies using *i.m.* injections and variety of tracers, such as FG (Arasaki et al., 1997; Rotto-Percelay et al., 1992), Horeseradish peroxidase (HRP) (Burke et al., 1977), and Cholera toxin-HRP (Rotto-Percelay et al., 1992), suggest that a smaller number of γ motor neurons are labeled in comparison with α motor neurons. The number varying between 9% for Cholera toxin-HRP and 33% for FG. In contrast, using nerve transections, the number of detected α and γ motor neurons seemed comparable (Peyronnnard and Charron, 1983). All of the rat studies, however, estimate similar numbers of α motor neurons for the medial gastrocnemius giving an average of 109 and comprising 69% of the total number of motor

neurons (Arasaki et al., 1997; Rotto-Percelay et al., 1992). To our knowledge, there is only one available quantitative study for the rat lateral gastrocnemic muscle that estimated the number of motor neurons to be on average 101 (Tredici et al., 1996), which would imply 70 α motor neurons. This gives an overall estimate for both gastrocnemius muscles (medial and lateral) of 179 motor neurons (i.e. 109+70), which is approximately a half of the counts of Swett et al. (1986) and is in agreement with the findings of Peyronnnard and Charron (1983).

$A\gamma$ fibers are commonly discerned based on their size to have diameters less than 7 μm (Peyronnnard and Charron, 1983) or 6.8 μm (Chapter 4). Based on this, only 4% of the measured motor fibers in L6 (Fig. 6.3A) could be identified as $A\gamma$ fibers . The number of the $A\alpha$ motor fibers in the ventral root L6 could be estimated to be 116, which was 65% of the estimated numbers of the combined gastrocnemius α motor neurons. Therefore, probably there was no overestimation of the $A\alpha$ motor fiber count and no substantial unspecific axonal labeling originating from other muscles. Since the innervation of the gastrocnemius muscles stems from the L4 - L6 spinal levels (Brunner et al., 1980; Swett et al., 1986) and we reported here only data for L6, it is difficult to discuss further the magnitude of possible underestimation of the fiber counts. Since the three-dimensional spatial arrangements of the motor endplates (Prodanov et al., 2005b) (i.e. $A\alpha$ fibers endings) and the muscle spindles (Swett and Eldred, 1960) (i.e. $A\gamma$ fibers endings) in the gastrocnemius muscles are very similar the reported finding can be attributed to differences in the kinetics of tracer uptake from the endings of the $A\gamma$ fibers probably due to their encapsulation by the connective tissue sheath of the muscle spindle.

6.4.3 Reliability of measurement and reconstruction

Reported subtle variation of $d[as]$ in the ventral roots as compared to the peripheral nerves did not affect the relationship between $d[as]$ and $d[f]$. Moreover, it yielded an absolute difference of the means comparable to the image resolution (i.e. 0.41 μm). Therefore, it does not have a biological significance.

Empirical relationship derived in this study is strictly valid only when using similar tracing protocol, exposure time, microscope optics, and image resolution. Several factors could influence the used procedure. *First*, the image resolution (e.g. magnification) affects both the automatic identification and the semi-automatic measurements. Small axons (respectively fibers) could not be imaged in sufficient detail to be outlined reliably. In addition, the bandwidth setting of the granulometric filter could influence the identification especially of the small fibers (Prodanov et al., 2005a). The low bound setting used during filtering was equivalent to 3.46 μm, therefore fibers with diameters smaller than this could not have been reliably detected (i.e. the majority of $A\gamma$ fibers). *Second*, the orientation of fibers could affect the semiautomatic measurements. Distortions of the shapes of the fibers caused by changes in their orientation could increase their projection area onto the plane of sectioning and consequently lead to overestimation of their equivalent diameter. *Third*, the exposure time affects the intensity of the fluorescent signal in the image and thus the quantity of axons being detected. The optimal exposure time strongly depends on the built-in filtering capabilities of the CCD camera being used. In general, use of much shorter exposure time would heave resulted in fewer axons being detected due to underestimation of the signal intensity. In contrast, much longer exposure time would heave resulted in an increase of the overall intensity of the signal and overestimation of the amount of the labeling detected in the axons and eventually in fusing of axons (e.g. underestimation of their number).

Fluorescent tracers in combination with digital microscopy greatly facilitate the task of tracing axons. On the other hand, the microscopic conditions imposed by a fluorescence protocol are less than ideal for a manual mode of measurements. Although imperfect for morphometric purposes due to the thickness of the sections introducing fuzziness of the fiber borders, the use of a fluorescent tracing protocol provided a suitable compromise between the straightforwardness and reproducibility of detection from one hand, and the accuracy of fiber dimensions reconstruction from the other. A relationship between the size of the labeling in an axonal profile and the size of the overall fiber could be established. On the other hand, compared to the matched sample population there were some differences in the size distribution histograms of the reconstructed fiber population (Fig. 6.2E). This can probably be explained either by different behavior of the tracer in the thick $A\alpha$ fibers compared to smaller fibers or by different relationship between the dimensions of the axon and its myelin sheath for the different fiber classes (Arbuthnott et al., 1980; 1977). Careful inspection of the scatter plot (Fig. 6.2C) suggests that the amount of labeling did not correlate well with the fiber diameter for the very large fiber diameters. On the other hand, the positions of the peaks in the histograms of the matched and the reconstructed fiber populations matched well (Fig. 6.3) and the error of the reconstruction procedure, represented by $RD[d]$, was moderate (Fig. 6.2E).

6.5   Conclusions

An advantage of the used approach is that it allows for a simultaneous reconstruction of the size distribution of labeled population of fibers and construction of a map of their co-ordinates from a single experiment. This brings forward the opportunity to study also the spatial distribution of a particular population of labeled fibers in the same histological section, which is important for further studies of the functional topography of the ventral roots.

Acknowledgements

Bibliography

Abramoff, M. D., P. J. Magelhaes, and S. J. Ram (2004) Image processing with ImageJ. Biophotonics Int. *11*:36–42.

Agnew, W. and D. B. McCreery (eds.) (1990) Neural Prostheses: Fundamental studies. Prentice Hall Advanced Reference Series. Englewood Cliffs: Prentice Hall.

Arasaki, K., M. Tamaki, Y. Hosoya, and N. Kudo (1997) Validity of electromyograms and tension as a means of motor unit number estimation. Muscle Nerve *20*:552–560.

Arbuthnott, E. R., I. A. Boyd, and K. U. Kalu (1977) The relation between axon area, axon circumference, total fibre circumference and number of myelin lamellae for different groups of fibres in cat hind-limb nerves [proceedings]. J. Physiol. (Lond) *273*:88P–89P.

Arbuthnott, E. R., I. A. Boyd, and K. U. Kalu (1980) Ultrastructural dimensions of myelinated peripheral nerve fibres in the cat and their relation to conduction velocity. J. Physiol. (Lond) *308*:125–157.

Benali, A., I. Leefken, U. T. Eysel, and E. Weiler (2003) A computerized image analysis system for quantitative analysis of cells in histological brain sections. J. Neurosci. Methods *125*:33–43.

Branner, A. and R. A. Normann (2000) A multielectrode array for intrafascicular recording and stimulation in sciatic nerve of cats. Brain Res. Bull. *51*:293–306.

Brown, A. (2003) Axonal transport of membranous and nonmembranous cargoes: a unified perspective. J. Cell Biol. *160*:817–821.

Brunner, R., P. Zimmermann, and F. W. Klussmann (1980) Localization and neurophysiological properties of motoneurones of the m. triceps surae of the rat after retrograde labelling with Evans blue. Cell Tissue Res. *212*:73–81.

Burke, R., P. Strick, C. Kim, and B. Walsmmsley (1977) Anatomy of the gastrocnnemius and soleus motor nuclei in cat spinal cord. J. Neurophysiol. *40*:677–680.

Coggeshall, R. E., D. G. Emery, H. Ito, and C. W. Maynard (1977) Unmyelinated and small myelinated axons in rat ventral roots. J. Comp. Neurol. *173*:175–184.

Fraher, J. P. and V. R. O'Sullivan (1989) Age changes in axon number along the cervical ventral spinal nerve roots in rats. J. Comp. Neurol *280*:171–182.

Geuna, S., P. Tos, R. Guglielmone, B. Battiston, and M. G. Giacobini-Robecchi (2001) Methodological issues in size estimation of myelinated nerve fibers in peripheral nerves. Anat. Embryol. (Berl) *204*:1–10.

Greensmith, L., J. Dick, A. O. Emanuel, and G. Vrbova (1996) Induction of transmitter release at the neuromuscular junction prevents motoneuron death after axotomy in neonatal rats. Neuroscience *71*:213–220.

Hebel, R. and M. W. Stromberg (1986) Anatomy and Embryology of the Laboratory Rat. Worthsee: BioMed Verlag.

Heiduschka, P. and S. Thanos (1998) Implantable bioelectric interfaces for lost nerve functions. Prog. Neurobiol. *55*:433–461.

Iwasaki, Y., Y. Ichikawa, O. Igarashi, S. Konno, J. Aoyagi, K. Ikeda, S. Marabuchi, S. Ono, H. Iguchi, K. Kawabe, and T.Fujioka (2004) T-588 protects motor neuron death following axotomy. Neurochem. Res. *29*:403–406.

Jenq, C. B. and R. E. Coggeshall (1985) Numbers of regenerating axons in parent and tributary peripheral nerves in the rat. Brain Res. *326*:27–40.

Lago, N., D. Ceballos, F. J. Rodriguez, T. Stieglitz, and X. Navarro (2005) Long term assessment of axonal regeneration through polyimide regenerative electrodes to interface the peripheral nerve. Biomaterials *26*:2021–2031.

Malagodi, M. S., K. W. Horch, and A. A. Schoenberg (1989) An intrafascicular electrode for recording of action potentials in peripheral nerves. Ann. Biomed. Eng. *17*:397–410.

Matheron, G. (1975) Random Sets and Integral Geometry. Wiley series in probability and mathematical statistics. New York: Wiley, 2nd edn.

McDonnall, D., G. A. Clark, and R. A. Normann (2004) Selective motor unit recruitment via intrafascicular multielectrode stimulation. Can. J. Physiol. Pharmacol. *82*:599–609.

Navarro, X. and W. R. Kennedy (1991) The effects of autologous nerve transplants on motor and sudomotor reinnervation by regenerative axons. Brain Res. *565*:181–187.

Pamphlett, R. and A. Sjarif (2003) Is quantitation necessary for assessment of sural nerve biopsies? Muscle Nerve *27*:562–569.

Peyronnard, J. M., L. F. Charron, J. Lavoie, and J. P. Messier (1986) Motor, sympathetic, and sensory innervation of rat skeletal muscles. Brain Res. *373*:288–302.

Peyronnnard, J. and L. Charron (1983) Motoneuronal and motoraxonal innervation in the rat hindlimb: A comparative study using Horeseradish peroxidase. Exp. Brain Res. *50*:125–132.

Prodanov, D., J. H. Heeroma, and E. Marani (2005a) Automatic morphometry of synaptic boutons of cultured cells using granulometric analysis of digital images. J. Neurosci. Methods p. in press.

Prodanov, D., E. A. J. F. Lakke, H. K. P. Feirabend, N. N. J. Holsheimer, and E. Marani (2004) A direct fluorescence-based approach for elucidating the fiber diameter and spatial distribution of motor fibers innervating the rat gastrocnemic muscles. Bournemouth, UK, Proceedings of IFESS-FESnet 2004, pp. 48–50.

Prodanov, D., G. Mantchev, A. Iliev, V. Traykov, K. Y. R. Kaneva, and I. Krushkov (1998) Effects of dexamethasone in rat neonatal model of axotomy-induced motoneuronalcell death. Arch. Physiol. Biochem. *106*:355–361.

Prodanov, D., E. Marani, and J. Holsheimer (2003) Functional Electric Stimulation for sensory and motor functions: progress and problems. Biomed. Rev. *14*:23–50.

Prodanov, D., M. A. Thil, E. Marani, J. Delbeke, and J. Holsheimer (2005b) Three-dimensional topography of the motor endplates of the rat gastrocnemius muscle. Muscle Nerve *32*:292–302.

Rodriguez, F. J., D. Ceballos, M. Schuttler, A. Valero, E. Valderrama, T. Stieglitz, and X. Navarro (2000) Polyimide cuff electrodes for peripheral nerve stimulation. J. Neurosci. Methods *98*:105–118.

Rotto-Percelay, D., J. Wheeler, F. Osoriao, K. Platt, and A. Loewy (1992) Transneuronal labeling of spinal interneurons and sympathetic preganglionic neurons after pseudorabies virus injections in the rat medial gastrocnemius muscle. Brain Res. *574*:291–306.

Rutten, W. L., T. A. Frieswijk, J. P. Smit, T. H. Rozijn, and J. Meier (1995) 3D neuro-electronic interface devices for neuromuscular control: design studies and realisation steps. Biosens. Bioelectron. *10*:141–153.

Schmued, L. C. (1990) Fluoro-Gold and 4-acetamido-4'-isothiocyanostilbene-2,2'disulfonic acid: use of substituted stilbenes in neuroanatomical studies. Methods in Neurosciences *3*:317–330.

Schmued, L. C. (1994) Anterograde and retrograde neuroanatomical tract tracing with fluorescent compounds. Neuroscience Protocols *50*:1–15.

Schmued, L. C. and J. H. Fallon (1986) Fluoro-Gold: a new fluorescent retrograde axonal tracer with numerous unique properties. Brain Res. *377*:147–154.

Schmued, L. C., K. Kyriakidis, J. H. Fallon, and C. E. Ribak (1989) Neurons containing retrogradely transported Fluoro-Gold exhibit a variety of lysosomal profiles: a combined brightfield, fluorescence, and electron microscopic study. J. Neurocytol. *18*:333–343.

Serra, J. (1982) Image Analysis and Mathematical Morphology. London: Academic Press Ltd.

Swett, A. L. and E. Eldred (1960) Distribution and numbers of stretch rceptors in medial gastrocnemius and soleus muscles of the cat. Anat. Rec. *137*:453–460.

Swett, J. E., R. P. Wikholm, R. H. Blanks, A. L. Swett, and L. C. Conley (1986) Motoneurons of the rat sciatic nerve. Exp. Neurol. *93*:227–252.

Tredici, G., C. Migliorini, I. Barajon, G. Cavaletti, and R. Cece (1996) Anatomical organization of the spinal paths to the soleus and gastrocnemius muscles of the rat hind limb. J. Hirnforsch. *37*:81–89.

Veltink, P. H., J. A. van Alste, and H. B. Boom (1989) Multielectrode intrafascicular and extraneural stimulation. Med. Biol. Eng. Comput. *27*:19–24.

Vleggeert-Lankamp, C. L., R. J. van den Berg, H. K. Feirabend, E. Lakke, M. J. Malessy, and R. T. Thomeer (2004) Electrophysiology and morphometry of the $A\alpha$- and $A\beta$-fiber populations in the normal and regenerating rat sciatic nerve. Exp. Neurol. *187*:337–349.

CHAPTER 7

Local Spatial Analysis of the Motor Axonal Clustering in the Rat Ventral Spinal Roots [†]

Abstract

Internal neural topography of the motor axons in the ventral spinal roots can be studied using retrograde tracing. Gastrocnemius muscles of adult rats were injected with the retrograde tracer Fluoro-Gold and later on the ventral roots were harvested, sectioned, and inspected on a fluorescence microscope equipped with a CCD camera. Maps of the "positive" fibers' locations were automatically constructed. To analyze the maps, a local spatial statistical approach was devised to test for the occurrence of clusters and to reveal their locations. As a measure of the likelihood of a specific point in the mapped point pattern to be part of a cluster, a local clustering index function was introduced. Next, based on series of Monte-Carlo simulations, a cluster threshold function was constructed to compare against the clustering present in a *completely spatially random* point pattern at any given scale. Clusters above the computed threshold were then visualized by means of kernel smoothing and interpolation. Functions were tested on simulated data and applied to spatial data from the retrograde tracing experiments. Results revealed clustering of the motor fibers innervating the gastrocnemius muscle at the level of the L6 ventral spinal root.

7.1   Introduction

Normal spatial organization of the fibers in the peripheral nerves and ventral spinal roots is seldom studied. Studies on pathological nervous mechanisms compare only estimates of the numbers, density, and size distribution of the fibers at selected levels, such as roots, spinal tracts or peripheral nerves, to the pathological condition but not the spatial distribution of the nerve fibers (Dyck et al., 1984). Early microdissection studies did not reveal an organized pattern in the distribution of fibers in the peripheral nerves, therefore it was assumed that their topography was disorganized (Sunderland, 1945). However, contradicting evidence accumulated subsequently from anatomical tracing studies in amphibians (Brown et al., 1989) and primates (Brushart, 1991), and from microneurographical studies in man (Schady et al., 1983; Hallin, 1990). This organization, further referred to as *internal neural fiber topography* (Sunderland, 1945), may be particularly important for spatially selective electrical recording and stimulation of the ventral roots (Prodanov et al., 2003). Recently developed theoretical models predict that small regions of a nerve (e.g. spinal root) can be selectively stimulated (Deurloo and Holsheimer, 2003). Therefore, mapping of the ventral roots may streamline the development of more efficient neural prostheses that can be used to improve the posttraumatic clinical condition of patients with spinal cord injury.

In order to investigate the internal neural topography of motor fibers they should be specifically marked onto the cross section and their locations mapped. The resulting mapped pattern can be described and studied by spatial statistical analysis (Diggle, 1983). Two types of statistical descriptions are discerned to describe an observed pattern - first order statistics that are based on the counts of objects in different regions of the map and second order statistics that are based on functions of the distances between the objects (Diggle, 1983).

To describe the internal neural topography of nerve fibers in a cross section, we devised a local second order approach to test for the occurrence of clusters and to localize them if present. Our results revealed clustering of the motor fibers innervating gastrocnemius muscle at the level of the L6 ventral spinal root.

7.2   Methods

An overview of the concepts and methodology of spatial analysis is given in the Appendix. In brief, the observed spatial arrangements of structures are modeled as realizations of various stochastic processes. The simplest and best-described spatial arrangement of the objects, called Complete Spatial Randomness (CSR), is characterized by mutually independent and homogeneous distribution of the studied objects. Upon comparison with CSR, the other arrangements of objects fall in two categories of "departures from randomness": clustering of the objects, if the objects are locally denser than in CSR; and repulsion, if the objects are locally sparser than in CSR (see Fig. 7.1 for examples).

7.2.1   Cluster Index Function

One of the difficulties in analyzing clustering in the context of nerve fibers is the finite geometry of the cross section, which makes many of the methods devised for infinite space irrelevant. Therefore, local descriptors of the spatial pattern of fibers are preferable. To measure the likelihood of an arbitrary point p belonging to point pattern P to be part of a cluster, we
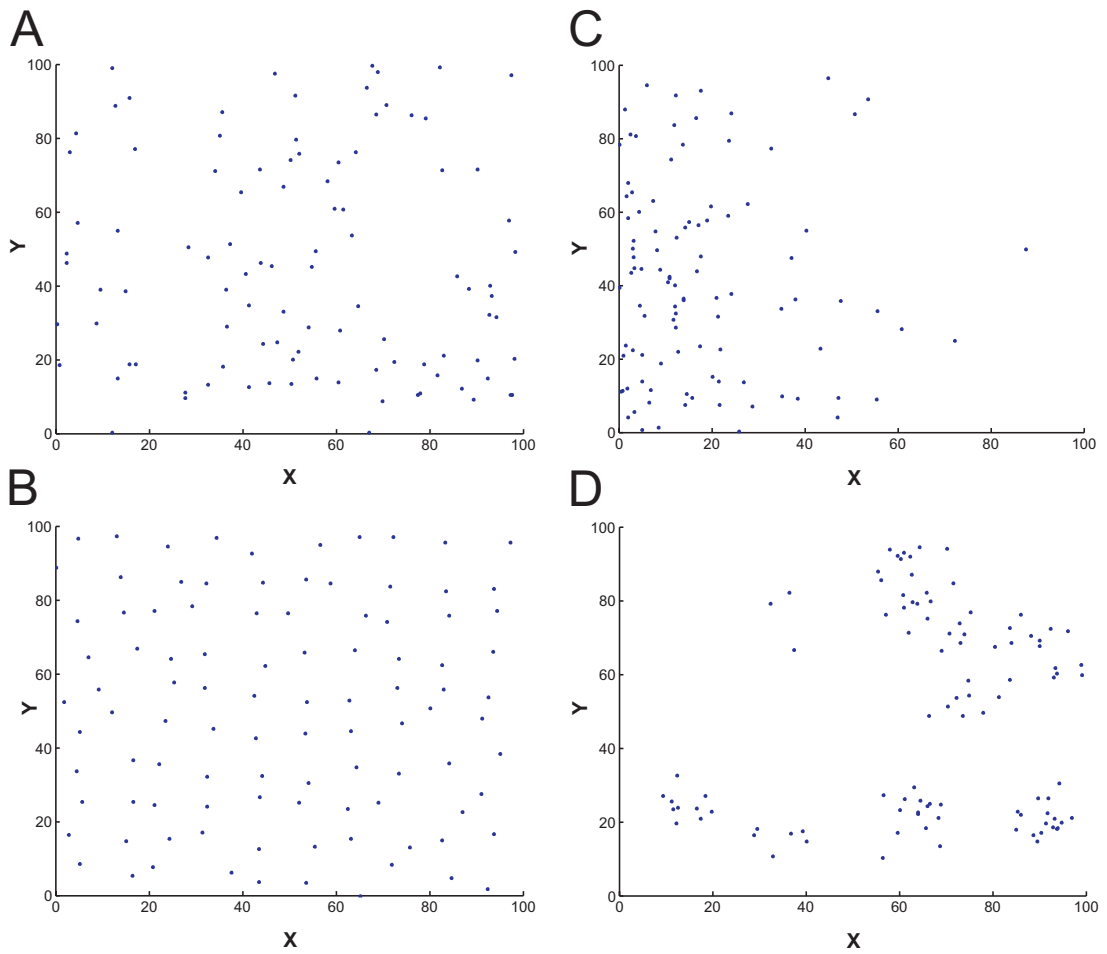
Figure 7.1: Simulations of different types of point processes

All of the point processes were simulated on a 100 x 100 square with 100 points: A - CSR; B - regular point pattern; C - inhomogeneous Poisson process; D - Neyman-Scott cluster process (see Data). Points are represented by dots.

introduce a local descriptor of the "amount" of clustering, the Local Clustering function $LC_p(h)$ defined as the number of points within the radius h from the point p:

$$LC_p(h) = N[(x_j, y_j) \in P \mid (d_{p,j} \leq h)] \qquad (7.1)$$

where $N[]$ denotes the number of the points and $d_{p,j}$ is the distance of an arbitrary point (x_j, y_j) to p. The definition of $LC_p(h)$ is illustrated in Figure 7.2. Since the observed point pattern is viewed as a realization of a random point process, $LC_p(h)$ can be related to the Ripley's K-function (see Appendix A.3).
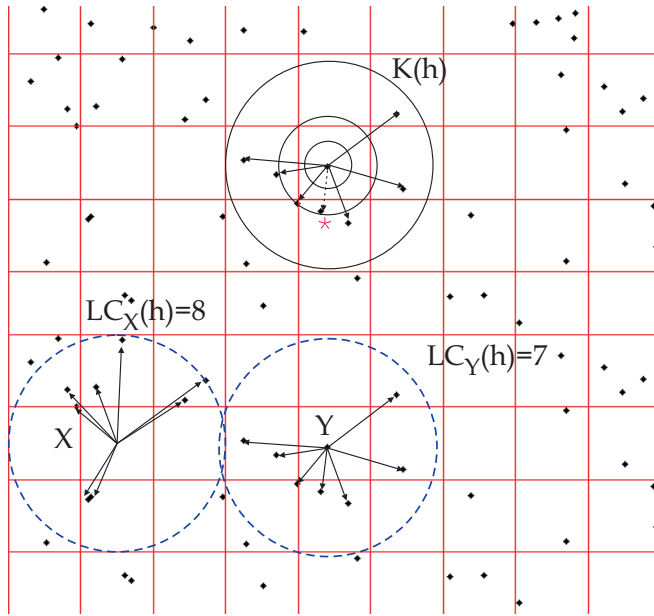
Figure 7.2: Definition of $LC_p(h)$

$LC_p(h)$ is evaluated for 2 other randomly selected points - X and Y. Relationship between $LC_p(h)$ and $K(h)$ is demonstarated in the Appendix. The points used to estimate $K(h)$ at the indicated scale are pointed by arrows. The nearest neighbor of the selected point is indicated with an asterisk and is pointed by a dashed arrow.

7.2.2 Clustering Threshold function

In order to test locally wether the observed pattern of fiber locations is more clustered than a CSR pattern (an obvious H_0 hypothesis) we introduce a parameterized clustering threshold function $T_\alpha(h)$ depending on the significance parameter α and the scale parameter h. To attain locality, $T_\alpha(h)$ should express the probability that the local descriptor of the 'amount' of clustering $LC_p(h)$ exceeds a certain threshold value in an associated CSR point process:

$$P\{LC_p(h) > T_\alpha(h) \,|\, p \sim CSR\} = \alpha \tag{7.2}$$

Accordingly, if the "amount" of clustering of the observed pattern exceeds the 'amount' present in CSR ($LC_p(h) > T_\alpha(h)$ e.g. H_0 is locally rejected) one can infer the existence of clustering in the local neighborhood h around the particular point p. In infinite isotropic space, $T_\alpha(h)$ can be computed analytically. However, in the cross section the tissue borders and tissue defects (App. Fig. 7.A.1) introduce distortions that are intractable analytically. Therefore, $T_\alpha(h)$ was calculated for series of simulated CSR point patterns Q with the same intensity inside the nerve tissue borders. $T_\alpha(h)$ was numerically estimated as the expected value of the inverse of the α-quantile of the empirical probability distribution function $F_a[LC_p(h)]$:

$$T_\alpha(h) = E\{F_\alpha^{-1}[LC_p(h) \,|\, p \in Q]\} \tag{7.3}$$

In the performed simulations, α was conventionally set to 0.95; consequently, only 5% of the points were expected to exceed the threshold $T_{0.95}$.

7.2.3 Exploratory analysis of the detected clustering

An extension of the local description to the entire point pattern can be defined as the set of all local clustering functions: $GC(h) = \{LC_p(h) \,|\, p \in P\}$. An important property of $GC(h)$ is that it preserves the information of the individual point coordinates. The subset of supra-threshold points, termed Global Clustering Set, can be defined as:

$$S(h) = \{p \in P \mid LC_p(h) > T_\alpha(h)\} \tag{7.4}$$

$S(h)$ then can be used to describe the detected clustering. For the current application an important parameter of $S(h)$ is its number of points $N(h) = N[S(h)]$.

   If we consider clustering to be generated by a certain localized mechanism, the regions of most likely occurrences of the clusters should be discerned in the section. To delineate these regions we can associate $S(h)$ to a continuous two-dimensional (2D) kernel function of the coordinates. A conventional choice then is the 2D Gaussian kernel, $\Phi(x,y)$ (see for example Silverman (1986); Wand and Jones (1995). Then the bandwidth of the kernel M should be related to the intensity λ. For CSR pattern, such bandwidth can simply be $1/\lambda$; e.g. $\Phi(x,y) \approx exp\left[-\lambda(x^2 + y^2)\right]$. For an arbitrary pattern, the bandwidth should be related also to the studied scale of clustering h. In the simplest case, M can be taken as the ratio:

$$M = \frac{\pi h^2}{E[LC_p(h)]}$$

In this way, for the special case of CSR is retained $M = 1/\lambda$ (see Appendix eq. (A.6)). Accordingly, to visualize the detected clusters, $S(h)$ was associated to the sum of the Gaussian kernels centered in the locations of each supra-threshold point

$$\Phi_h(x,y) = \frac{1}{N_s 2\pi M} \sum_{s \in S(h)} LC_s(h) \, e^{-\frac{(x-x_s)^2 + (y-y_s)^2}{2M}} \tag{7.5}$$

It can be shown that $\int\limits_{-\infty}^{+\infty} \int\limits_{-\infty}^{+\infty} \Phi_h(x,y) \, dx \, dy = E[LC_s(h)]$. Therefore, the quantity

$$P\{(x,y) \in A\} = \frac{1}{E[LC_s(h)]} \int\limits_{x,y \in A} \int \Phi_h(x,y) \, dx \, dy$$

can be interpreted as the probability to localize a clustered point in the region A.

7.2.4 Data

7.2.4.1 Simulated data

Series of simulations were performed with 4 types of *point processes* (for the definition see Appendix) - a homogenous Poisson process; an inhomogeneous Poisson process (IPP) with

exponential decay of intensity; a grid process; and a Neyman-Scott clustering process. All of the point processes were simulated on a 100x100 square with 100 points. In Figure 7.1 are presented typical instances of the simulated point processes. The inhomogeneous Poisson process was simulated using the intensity function: $\lambda(x, y) = 0.01 \exp(-0.05x - 0.02y)$ as described by Diggle (1983). The grid process was simulated by a two-stage approach. First, seed points were situated onto the coordinates' gird with spacing d. Then, each point was perturbed by a random isotropic translation with a spread σ distributed like $N(0, \sigma)$. For the particular example, parameter values were $d=10$ and $\sigma=2$. The Neyman-Scott process was generated by a 2 stage approach Diggle (1983). First, a parent Poisson process with intensity ρ was generated. Then, around each parent point were randomly assigned children points isotropically scattered around its location with a spread σ distributed like $N(0, \sigma)$. For the particular example, parameter values were $\rho=0.001$ (10 cluster centers) and $\sigma=5$.

7.2.4.2 Spatial data from tracing experiments

Animal experimentation procedures were reported in Chapter 6. In short, to visualize motor axons in the ventral roots, the gastrocnemius muscle (both heads) of adult male albino Glaxo-Wistar rats were injected in the motor endplate regions with the retrograde tracer Fluoro-Gold (Fluorochrome Inc, Denver, Colorado) (Schmued and Fallon, 1986) aided by a topographical map of the these regions (Prodanov et al., 2005b). The roots were harvested from the rats after 3 days of survival, sectioned, and inspected on a Leica epi-fluorescence microscope equipped with a CCD camera. Image processing and measurement steps were performed using the public domain software for image analysis *ImageJ* (NIH, Bethesda, Massachusetts; http://rsb.info.nih.gov/ij/). Fibers were automatically identified using granulometric filtering (Prodanov et al., 2005a) as described in Chapter 6. Their coordinates were recorded in a database and imported for further analysis in *Matlab*. To illustrate the approach, we report the analysis of several representative samples from our database of images of the cross sections of the L6 ventral spinal root.

Table 7.1: Summary statistics of the reported cases

Section ID	Count	Average cluster size	E[H]	SD[H]	p-value	E[G]	SD[G]	p-value
N1233[a]	110	20.21%	187.84	97.84	0.0000	18.94	11.64	0.2924
N1208[a]	149	36.24%	152.21	91.80	0.0000	14.00	10.38	0.0033
N1230[b]	158	16.86%	149.22	74.96	0.0000	11.54	5.87	0.0100
N1268[b]	149	24.94%	140.32	69.78	0.0000	12.88	5.12	0.0456
N1431[c]	97	26.36%	182.15	100.75	0.0000	18.18	10.60	0.0000
N1376[c]	90	18.16%	186.66	94.67	0.0000	18.68	10.14	0.0033
Average	126	23.80%	166.40			15.70		

a - animal A1119; b - animal A1120; c - animal A1121; *E[]* expected value (first moment), *SD* - standard deviation (second moment of the distribution), all expressed in µm. Average cluster size is given in relative terms: $N_s/Number\ of\ points$, where N_s is estimated from Eq. (7.6)

7.2.5 Data analysis and testing

Programming and data analysis were carried out in the *Matlab* computational environment (version 6.5; The Mathworks Inc, Natick, Massachusetts). In each image, 300 simulations were sampled from a pool of 2000 simulated points. Tissue defects and blood vessels were avoided by simulating points only onto the foreground area (App. Fig. 7.A.1). The Inter-point distance distribution function - *H(h)* and the Nearest Neighbor distance distribution function - *G(h)* were used as conventional analytical tools to infer the type of spatial distribution of the fibers (see Appendix). Since simulated patterns were performed on the same images as where the observed patterns were recorded, border effects had the same direction and magnitude and would not affect comparisons. Therefore, no corrections for border effects were applied.

According to Diggle (1983), one-sided test for significance was introduced; p-values less than 0.05 were considered significant.

7.3 Results

7.3.1 Behavior of $T_\alpha(h)$ and $S(h)$ for the simulated point processes

In order to apply the proposed functions to observed point patterns we studied first the behavior of the functions in well-defined simulation conditions. Four instances of point processes were used in the simulations - a homogenous Poisson process, representing CSR; an inhomogeneous Poisson process with exponential decay of intensity, representing clustering tendency with no specific scale of interaction; a grid process, as an opposite to clustering; and a Neyman-Scott process, representing a well characterized type of a cluster process (see Simulated data and Fig. 7.1). All of the statistical descriptor functions ($G(h)$, $H(h)$, and $T_\alpha(h)$) were estimated from 100 Monte-Carlo simulations of CSR patterns with the same number of points. Conventional spatial analysis of the simulated patterns is presented in Appendix Figure 7.A.2. The behavior of $T_\alpha(h)$ for the simulated patterns is presented in Fig. 7.3. $T_\alpha(h)$ showed saturation near $h = 60$. For $h > 70$ border effects started to play a significant role; therefore, data points were not displayed in the graphs. $T_\alpha(h)$ proved to be a robust cluster discriminator for the clustered patterns at the studied scales (note the similarities in the shape of the functional graphs for the clustered patterns in Fig. 7.3 and App. Fig. 7.A.2).

Clustered points in the simulated patterns could be discriminated by the Gaussian envelope associated to $S(h)$ at different scales (Fig. 7.4). However, with the increase of the scale parameter h, individual clusters started to merge.

7.3.2 Observed and Simulated H and G-functions in the ventral roots

To illustrate the proposed approach, six different sections of L6 ventral spinal roots from three different animals from our database are presented (Table 7.1). The spatial distribution of fibers showed clustering, which allowed further analysis of the data by means of the cluster index functions. The analysis of cases N1268 (Fig. 7.5) and N1230 (Fig. 7.6) is presented in detail. Both patterns of fibers showed departures from randomness most pronounced at 150 - 200 μm (i.e. at mesoscopic scale) (Figs. 7.5B, 7.6B). As expected, *H(h)* was more sensitive than *G(h)* in the detection of departures towards clustering at large scales (compare B to E in Figs. 7.5 and 7.6).
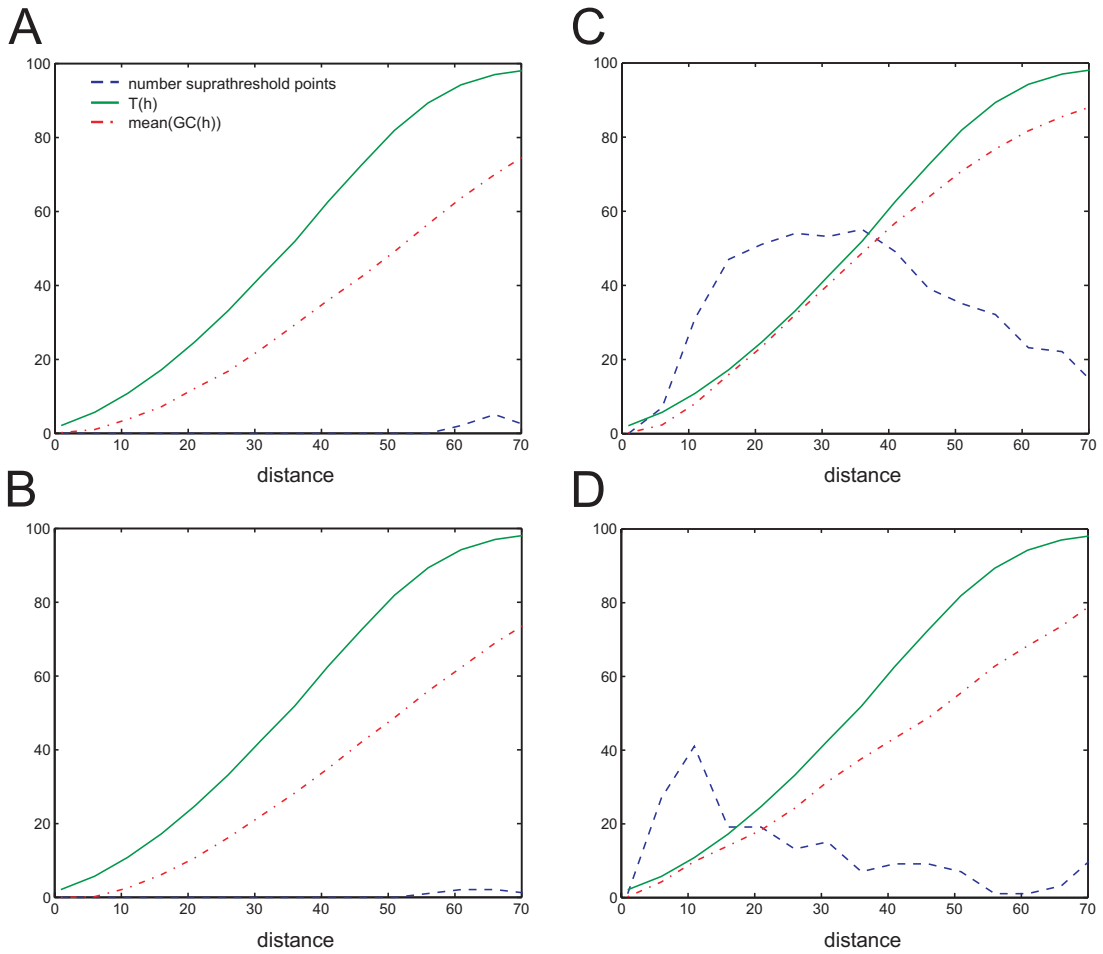
Figure 7.3: Influence of the scale on $T_{0.95}(h)$ for simulated patterns

$T_{0.95}(h)$, $N(h)$ denoted as *suprathreshold points*, and $E[GC(h)]$ estimated by the mean $GC(h)$, were computed for simulated point processes: A - CSR process; B - grid process - no clusters are detected ; C - IPP, large number of clustered points having no characteristic scale of clustering; D - Neyman-Scott process, the peak around $h=10$ corresponds to 2σ (see Data).
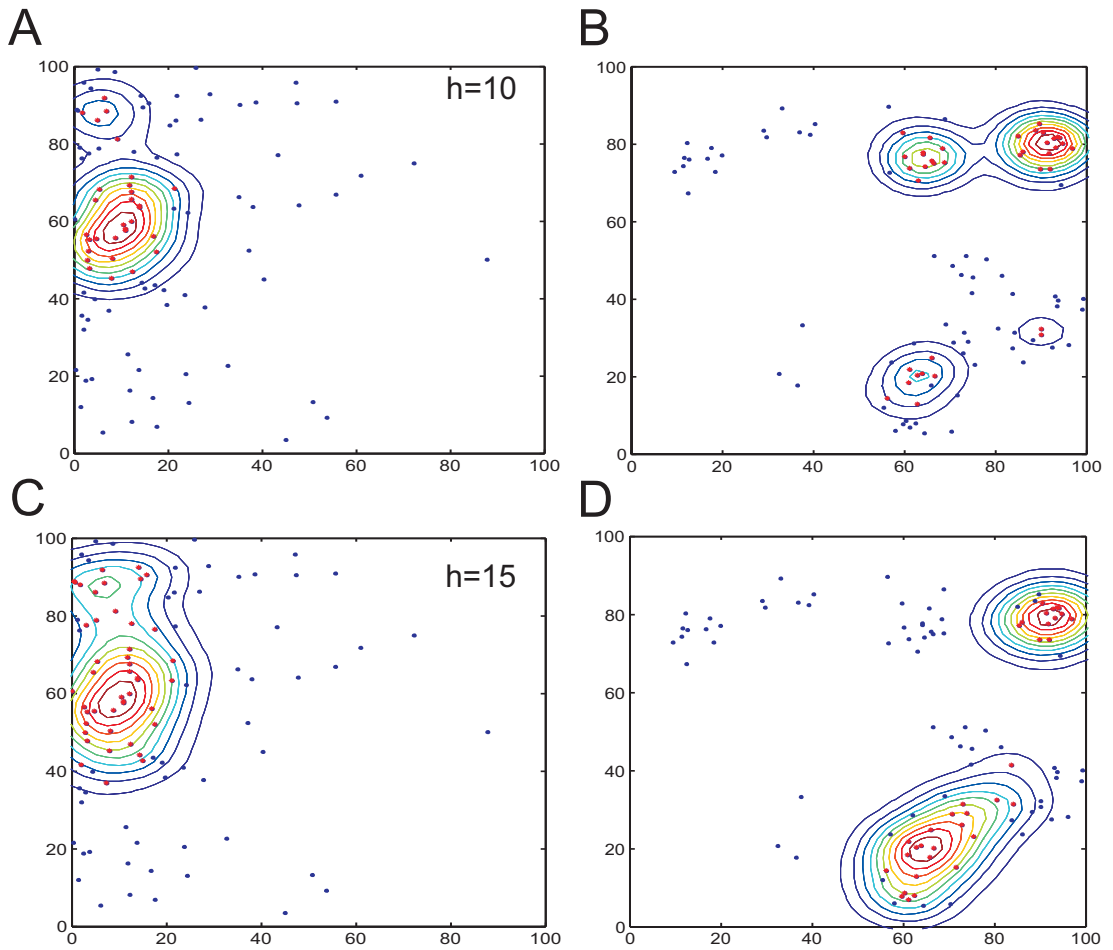
Figure 7.4: Behavior of the contour map $\Psi_h(x, y)$ at two different scales of study; full color p. 183

A, C - IPP; B, D - Neyman-Scott process; A, B h=10; C, D h=15. Suprathreshold points are depicted in different color.

Figure 7.5: Inter-point and nearest neighbor distribution functions, case N1230

A, B, C - Observed and simulated *H(h)*; D, E, F - Observed and simulated *G(h)*. *G(h)* of the fibers shows attraction at scales below 30 (E) while *H(h)* shows attraction at all scales (B). Base line is taken as the mean of all simulated functions (B,E).
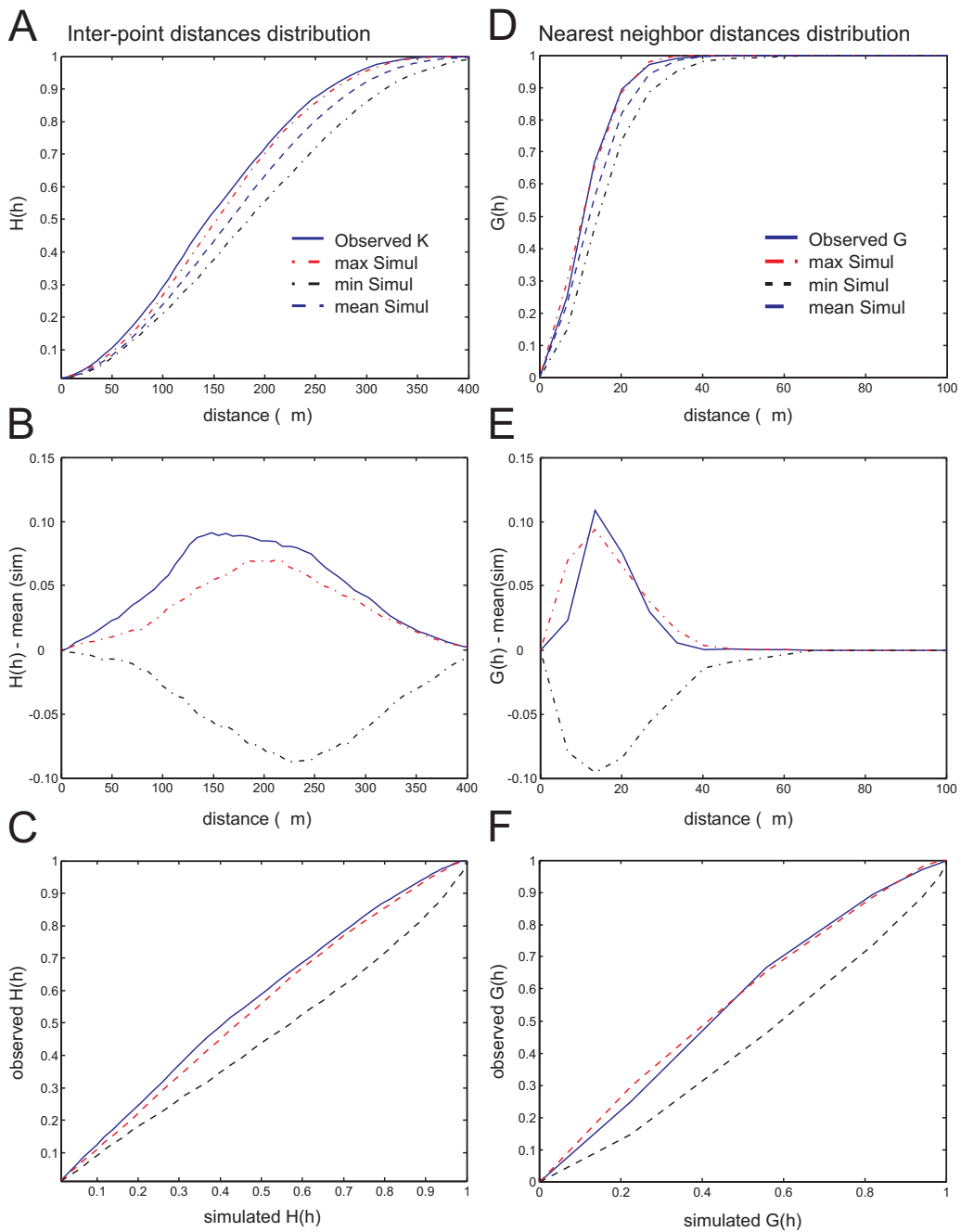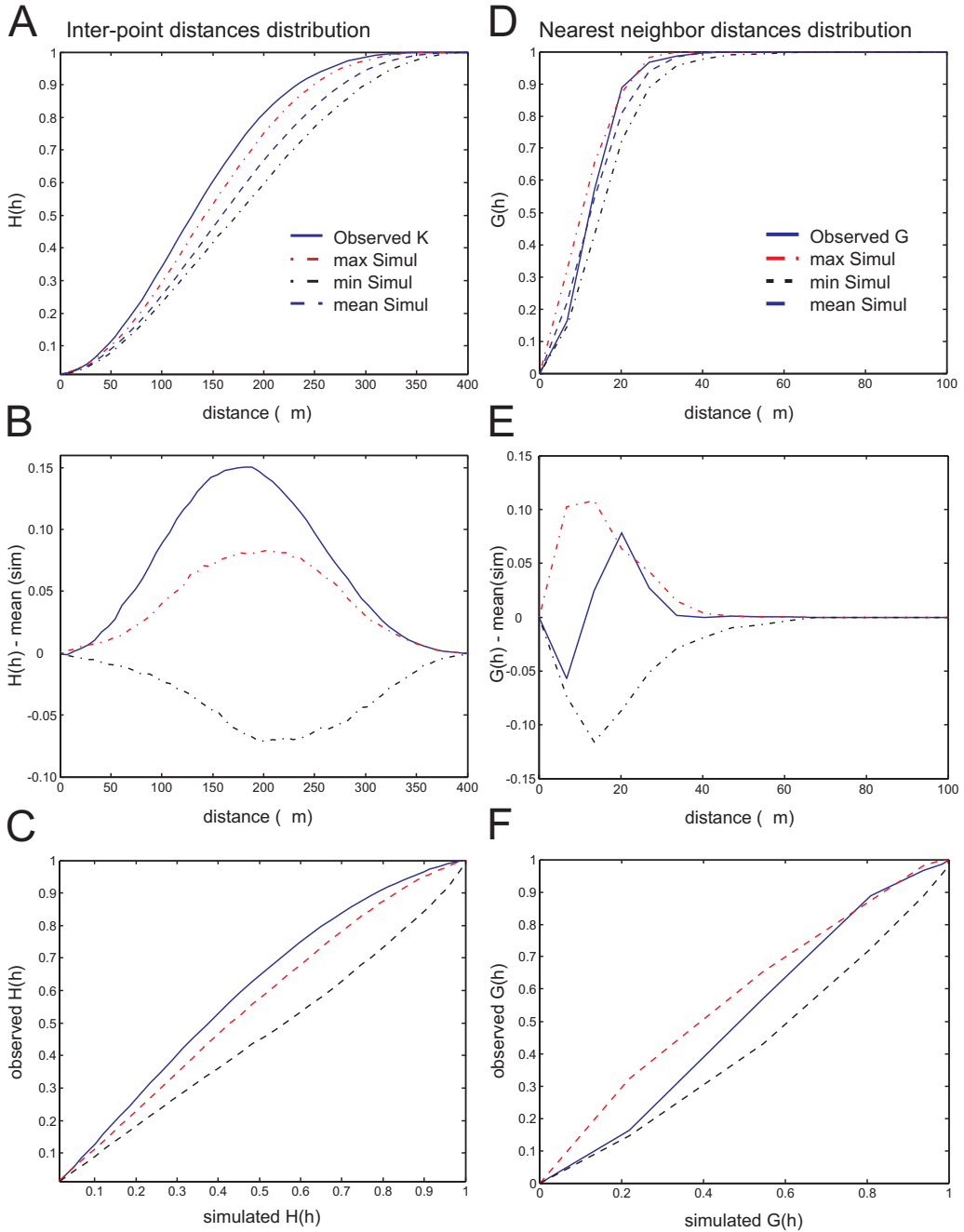
Figure 7.6: Inter-point and nearest neighbor distribution functions, case *N1268*

A, B, C - Observed and simulated *H(h)*; D, E, F - Observed and simulated *G(h)*. *G(h)* of the fibers shows repulsion at small scales ($h < 10$) and attraction at larger scales ($h > 15$) (E, F) while *H(h)* shows attraction at all scales (B, C). Base line is taken as the mean of all simulated functions (B,E).

7.3.3   Influence of the scale parameter on the amount and localization of clustering

The influence of the scale parameter h on the amount of detected clustering is presented in Figure 7.7. The average number of the clustered fibers with regard to the scale was calculated as

$$N_s = \frac{1}{R} \int_0^R N[S(h)]dh \tag{7.6}$$

where R is a sufficiently large scale. Simulated data showed that to avoid large edge effects R should be less than 70% of the minimal side of the study window (Fig. 3); therefore, R was set to 286 μm. The averaged number of the clustered fibers is presented in Table 7.1. $N(h)$ of both studied cases had peaks around $h = 100$ μm and tails around 200 μm (Fig. 7.7 A and D). Therefore, to determine the influence of the scale parameter h on the localization and the configuration of clustering, detected clusters were displayed for both $h = 100$ μm (Fig. 7.7 B and E) and $h = 200$ μm (Fig. 7.7 C and F). While varying h, the configuration of the detected clusters shifted only slightly in the cross-section, while the position of the cluster centers remained approximately the same.

7.3.4   Localization of detected clusters

Cluster dimensions, which may be particularly important for the anatomical interpretation of the results, are difficult to infer from the data. To study the relation of the clustering to the tissue borders, the Gaussian surfaces computed at $h = 100$ μm were superimposed on the borders of the ventral roots in the cross-sections (Fig. 7.8). From Figures 7.8B and E it can be seen that during histological processing random rotation of the tissue had occurred and that the clusters of fibers innervating the gastrocnemius muscle are confined to a particular region of the studied ventral roots.

7.4   Discussion

7.4.1   Anatomical significance of the findings

Our data cast light on the old problem of the internal topographical organization of nerves. We showed that clusters were a robust feature of the observed tracing patterns and the locations of cluster cores varied only slightly with scale (Fig. 7.7). As discussed in Chapter 6 (p. 136), 96% of the fiberes that were automatically identified belongetd to the $A\alpha$ fiber class; and those were estimated to be approx. 180 for both gastrocnemius muscles. Reported number of axons here corresponds, therefore, to 121 $A\alpha$ fibers, which is 67% of the total estimate and is 38% of the total number of motor neurons for both gastrocnemius muscles found by Swett et al. (1986). As part of the triceps surae muscle, the innervation of the gastrocnemius muscles is considered to come primarily from the L5 and L6 levels (Brunner et al., 1980; Tredici et al., 1996). Taken together, these findings mean that gastrocnemius motor fibers were topographically organized in the studied examples (n=6; three different animals) of the L6 ventral root.

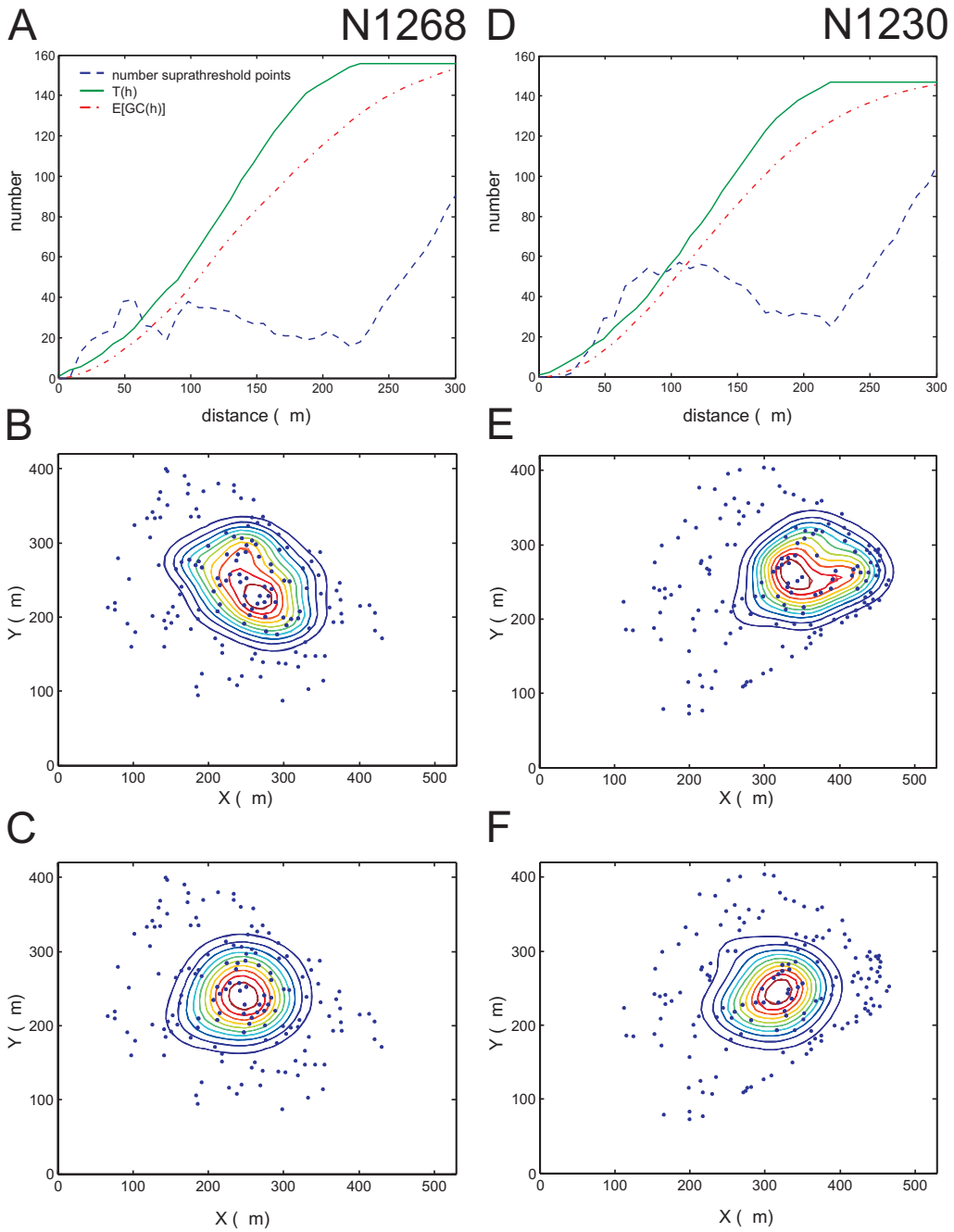Figure 7.7: Influence of the scale parameter on the observed clustering; full color p. 184

A, D - $T_\alpha(h)$ is plotted together with the E$[GC(h)]$ and the number of *suprathreshold* points *N(h)*; B, E - clustering detected at h=100 μm; C, F - clustering detected at h=200 μm; iso-level surfaces are connected by contours and plotted on top of the detected Fluoro-Gold positive fibers (filled circles).

Internal neural topography has implications for the development of neural prostheses. In order to restore the locomotor functions lost after spinal cord injury, cuff electrodes can be implanted around spinal roots distal to the affected level (Agnew and McCreery, 1990). However, the protocols of stimulation at the level of the ventral roots lack sufficient spatial selectivity to stimulate synergistic muscle groups (Prodanov et al., 2003). In the presented examples of the L6 ventral root, only part of the labeled motor fibers was clustered (on average 23.8%; Table 7.1). To test wether the elicited force in the gastrocnemius muscle is sufficient to regain muscle function and to establish optimal stimulation parameters cluster density maps can be incorporated into mathematical models of stimulation of the ventral roots and muscle recruitment resulting from such stimulation be estimated.

Spatial organization of the neuroanatomical structures can be understood better with the help of spatial data analysis. For example, spatial analysis revealed the mechanistic rules of cellular pattern formation in the retina during development (Sunderland, 1945) and regeneration (Schmued and Fallon, 1986). Spatial studies proved fruitful also in understanding pathology of CNS and sense organs (Diaz et al., 2001). Studies in a variety of neurodegenerative disorders suggested that brain lesions often exhibit common spatial patterns that reflect their pathogenesis, for example in *Creutzfeldt-Jakob disease* (Armstrong et al., 2003; Armstrong and Cairns, 2003), *Alzheimer's disease* (Pearson et al., 1985; Armstrong, 1993), and *Lewy Body dementia* (Armstrong et al., 1997).

7.4.2   Spatial data analysis and neuroscience

Local second-order descriptions, as used in this paper, were initially proposed for ecological applications in the 1980s (Dyck et al., 1984). However due to the limitations in the then available computation power these techniques did not get enough recognition. Only few spatial methods were applied so far for neuroanatomical data. Among them were the quadrant counts variance method of Greig-Smith (Armstrong, 1997) and a method based on the correlation of the counts in adjacent quadrants (Armstrong, 2000). Common limitations of these first order methods are that the sampling and aggregation procedures are not translation-invariant and, therefore, sliding of the window could alter the detection. Next, the inferred scale of clustering could be a measure for the spacing between the clusters and therefore ambiguous. Finally, it is not possible to locate the inferred clusters precisely due to the coarseness of the quadrant separation.

Descriptions of the cross-sections of peripheral nerves and spinal roots have some particularities. It is difficult to orient the tissue once it was dissected, because neither the peripheral nerves nor the spinal roots have clear anatomical landmarks. Next, sectioning of the tissue introduces a random rotation. Moreover, shape of the ventral roots and nerves can vary (round, flat, undulating) depending on the distance from the spinal cord. All this precludes from using a local coordinate system based on landmarks and consequently first order methods and rules strongly for a distance-based description (i.e. translation and rotation invariant).

To address these problems, we developed a local distance-based description that is easy to apply and straightforward to interpret. Its major advantages are that (i) individual clusters can be localized and studied with regard to the tissue borders or, if present, other anatomical landmarks of the studied organ, (ii) the approach can deal with arbitrary patterns since the homogeneity assumption is not necessary and (iii) maps of the cluster density can be constructed for different scales of interest.
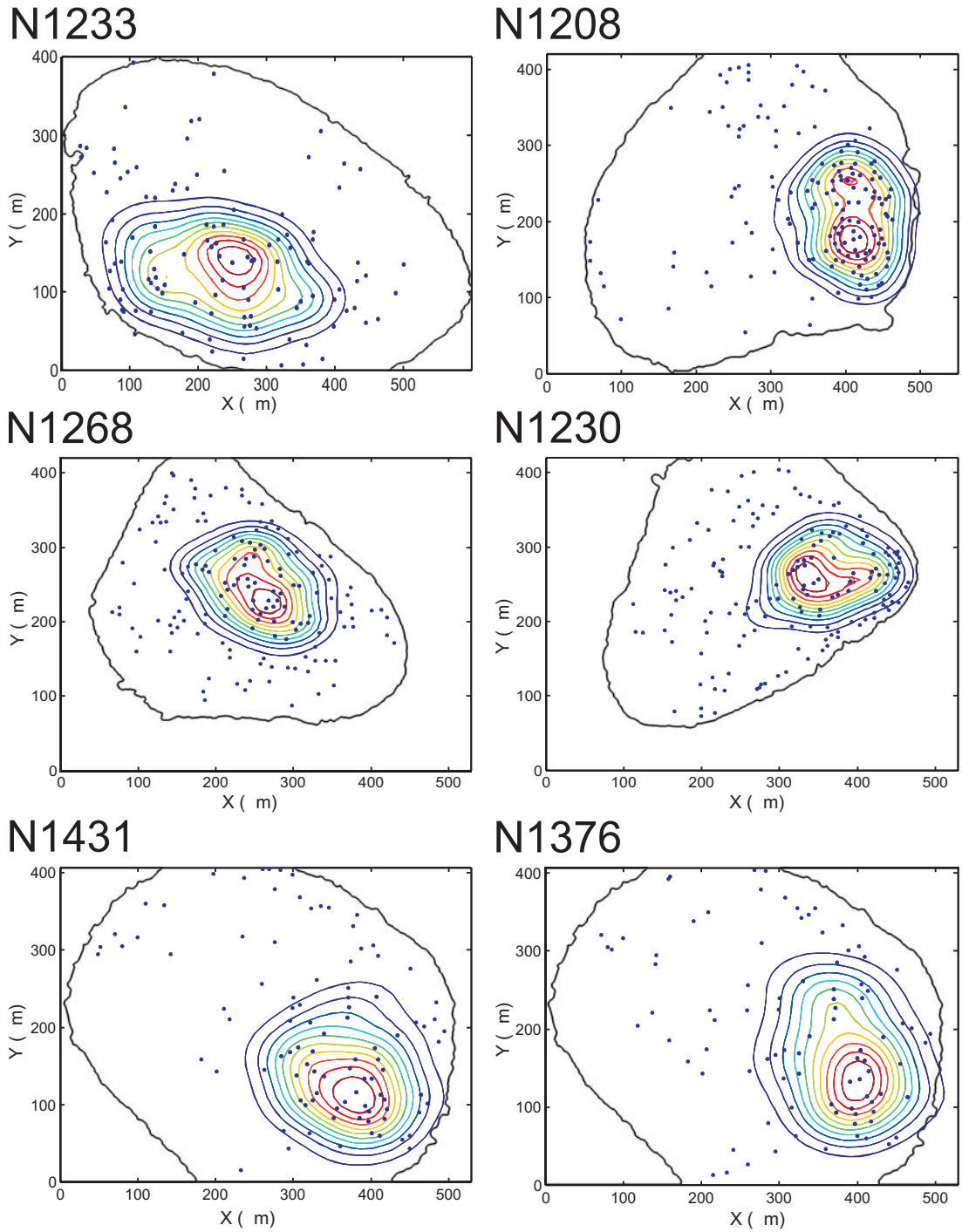
Figure 7.8: Detected clusters related to the cross-sections at $h=100$ µm; full color p. 185

Figure 7.8 (continued): Opposing plots are different sections of the L6 ventral root from the same animal (see Table 7.1). Sections were rotated during histological processing. Clusters are superimposed on the tissue borders; iso-level surfaces are connected by contours and plotted on top of the observed point patterns (filled circles).

Appendix

A   Statistical descriptions of Spatial Point Patterns

A.1   The spatial point process in the plane

THE term spatial analysis has a pedigree in geography that can be traced back to at least the 1950s. According to Haining (2003), "*spatial analysis represents a collection of techniques and models that explicitly use the spatial referencing associated with each data value or object that is specified within the system under study*". Mapped distribution of events in the plane (i.e. the nerve fibers in the cross-section), called spatial point pattern (SPP), can be modeled mathematically by the stochastic mechanism of spatial point process. According to Diggle, spatial point process is "*any stochastic mechanism, which generates a countable set of events in the plane*"(Diggle, 1983, p. 47). Mathematical descriptions of SPPs are very sensitive to the shape of the region of study and to the interactions among the points at global scale and therefore, analytical descriptions are possible in a very limited number of cases (Ripley, 1991).

The simplest and best-characterized spatial process is the Poisson process in the plane. It has 2 important properties, referenced together by the concept of Complete Spatial Randomness: (i) homogeneity - the intensity of the process is constant over the region of study; (ii) spatial independence in the occurrence of the events - there is no correlation in the numbers of events in neighboring regions. Conditioned on the number of points k, the Poisson process obeys the probability distribution law:

$$P\{N(S) = k\} = \frac{[\lambda A(S)]^k}{k!}\, e^{-\lambda A(S)} \tag{A.1}$$

where λ is the intensity of the process and $N(S)$ is the number of points contained is the area $A(S)$ of the bounded region of study S.

A.2   Exploratory second order analysis

A number of methods were developed in different disciplines for analysis of spatial data (for comprehensive descriptions see Diggle (1983); Ripley (1991); Cressie (1993); Stoyan et al. (1996); and Haining (2003). Here we focus on several basic exploratory descriptors that can be computed from the data.

Nearest neighbor distance distribution - $G(h)$ is defined as the probability that the distance from an arbitrary point to its nearest neighboring point is at most h. Values of this function at short distances are a crude measure of the degree of clustering and its values at long distances indicate the fraction of points that are greatly isolated from each other. $G(h)$ can be estimated by

$$G(h) = \frac{N[d_{i,j} \leq h]}{n} \tag{A.2}$$

where N denotes the number of points having $d_{i,j} \leq h$ ($d_{i,j}$ - distance between any point and its nearest neighbor) and n is the total number of points in the area of the study.

Inter-event distance distribution - $H(h)$ is defined as the probability that the distance from an arbitrary point to any other point is at most h. The form of this function depends strongly on the shape of the region of study. It can be expressed in closed analytical form only for simple planar figures. $H(h)$ is more sensitive than $G(h)$ to the large scale organization of the point pattern. $H(h)$ can be estimated by

$$H(h) = \frac{N[d_{i,j} \leq h]}{n(n-1)/2} \tag{A.3}$$

where N denotes the number of points having $d_{i,j} \leq h$

A.3 The Ripley's K-function and its relation to $LC_p(h)$

Ripley's K-function (recent overview in Ripley (1991)) measures the expected number of points that are within a given distance to a randomly chosen point divided by the intensity of the process:

$$K(h) = \frac{E\{N[i, j \in P \mid (d_{i,j} \leq h)]\}}{\lambda} \tag{A.4}$$

If the border effects are neglected, it can be shown that for a Poisson process (CSR) $E[K(h)] = \pi h^2$. If there is repulsion between the points, like in a regular pattern, $K(h) < \pi h^2$ and if there is attraction between the points, like in a clustered pattern, $K(h) > \pi h^2$. For a random process from the definition of $LC_p(h)$ it follows that

$$E[LC_p(h)] = E\{p \in P | N[j \in P| (d_{p,j} \leq h) \Rightarrow$$
$$E[LC_p(h)] = E\{N[p, j \in P|(d_{p,j} \leq h)]\} \Rightarrow E[LC_p(h)] = \lambda \cdot K(h) \tag{A.5}$$

Therefore, for a CSR point pattern with intensity λ holds

$$E[LC_p(h)] = \lambda \pi h^2 \tag{A.6}$$

Conditioned on the observed number of points N, holds $E[LC_p(h)] = (N-1)A_h/A_s$, where A_h is the area within a radius h (πh^2 in the absence of edge effects) and A_s is the area of the region of study.

A.4 Formal statistical tests

In general, only few statistical tests are available for comparing different point patterns. The most general approach for comparison against a SPP with known generation mechanism is by means of Monte-Carlo simulations. For example, if one aims to compare against CSR as the simplest alternative, N_s series of CSR Monte-Carlo simulations are performed and for each of them some exploratory descriptor function is calculated. Without diminishing generality we can give an example by $H(h)$. The lower simulation envelope

$$L(h) = \min\{H_s(h); s \leq N_s\} \tag{A.7}$$

Figure 7.A.1: Examples of the simulation masks

Tissue borders of cases N1268 (A) and N1230 (B); points were simulated on the white area only. The black areas within the tissue (white) are distortions such as tissue defects, blood vessels etc.

and the upper simulation envelope

$$U(h) = \max\{H_s(h); s \leq N_s\} \tag{A.8}$$

are computed and the observed *H(h)* is compared against them. For point patterns with repulsion between the points generally holds $H_{observed}(h) < L(h)$, while for point patterns that show clustering holds $H_{observed}(h) > U(h)$. Accordingly, CSR is rejected for the interval of distances where either of the inequalities holds.

A p-value of a formal one-sided statistical test can also be introduced (Diggle, 1983). The integrals

$$u_i = \int\limits_0^{R_{\max}} \left[H_i(r) - \frac{1}{N_s - 1} \sum_{j \neq i}^{N_s - 1} H_j(r) \right]^2 dr \tag{A.9}$$

are calculated and ranked for the stimulations, then
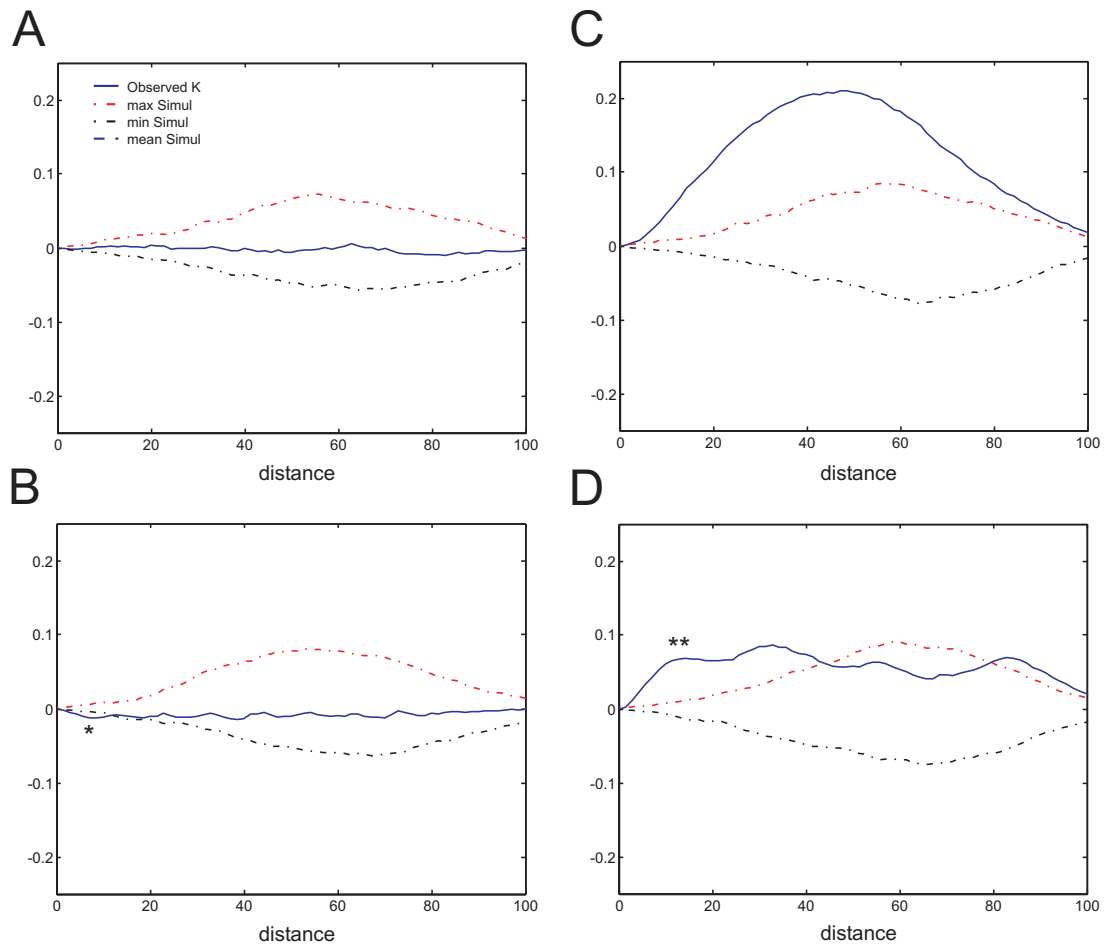
$$p = 1 - \frac{rank(u_{observed})}{N_s} \tag{A.10}$$

Figure 7.A.2: Inter-point distance analysis of the simulated patterns

A - CSR process; B - grid process, the dip around h=10 corresponds to the grid spacing (see Data); C - IPP, clustering is present at all scales; D - Neyman-Scott process, clustering is present at several scales, the peak around $h=10$ corresponds to 2σ (see Data). Base line is taken as the mean $H(h)$ of all simulations.

Bibliography

Agnew, W. F. and D. B. McCreery (1990) Neural Prostheses: Fundamental studies. Prentice Hall Advanced Reference Series. Englewood Cliffs: Prentice Hall.

Armstrong, R. A. (1993) Is the clustering of neurofibrillary tangles in Alzheimer's patients related to the cells of origin of specific cortico-cortical projections? Neurosci. Lett. *160*:57–60.

Armstrong, R. A. (1997) Analysis of spatial patterns in histological sections of brain tissue. J. Neurosci. Methods *73*:141–147.

Armstrong, R. A. (2000) Analysis of spatial patterns in histological sections of brain tissue using a method based on regression. J. Neurosci. Methods *95*:39–45.

Armstrong, R. A. and N. J. Cairns (2003) Spatial patterns of the pathological changes in the cerebellar cortex in sporadic Creutzfeldt-Jakob disease (sCJD). Folia Neuropathol. *41*:183–189.

Armstrong, R. A., N. J. Cairns, and P. L. Lantos (1997) Dementia with Lewy bodies: clustering of Lewy bodies in human patients. Neurosci. Lett. *224*:41–44.

Armstrong, R. A., P. L. Lantos, J. W. Ironside, and N. J. Cairns (2003) Spatial correlation between the vacuolation, prion protein, deposition and surviving neurons in patients with Creutzfeldt-Jakob disease (vCJD). J. Neural. Transm. *110*:1303–1311.

Brown, D. R., A. W. Everett, and M. R. Bennett (1989) Compartmental and topographical distributions of axons in nerves to the amphibian (Bufo marinus) glutaeus muscle. J. Comp Neurol. *284*:231–241.

Brunner, R., P. Zimmermann, and F. W. Klussmann (1980) Localization and neurophysiological properties of motoneurones of the M. triceps surae of the rat after retrograde labelling with Evans blue. Cell Tissue Res. *212*:73–81.

Brushart, T. M. (1991) Central course of digital axons within the median nerve of macaca mulatta. J. Comp. Neurol. *311*:197–209.

Cressie, N. A. (1993) Statistics for Spatial Data. Wiley Series in Probability and Statistics. Wiley-Interscience.

Deurloo, K. and J. Holsheimer (2003) Fascicular selectivity in transverse stimulation with a nerve cuff electrode: A theoretical approach. Neuromodulation *6*:258–269.

Diaz, M. E., G. Ayala, S. Quesada, and L. Martinez-Costa (2001) Testing abnormality in the spatial arrangement of cells in the corneal endothelium using spatial point processes. Stat. Med *20*:3429–3439.

Diggle, P. J. (1983) Statistical Analysis of Spatial Point Patterns. London: Academic Press.

Dyck, P. J., J. Karnes, P. O'Brien, H. Nukada, A. Lais, and P. Low (1984) Spatial pattern of nerve fiber abnormality indicative of pathologic mechanism. Am. J. Pathol. *117*:225–238.

Haining, R. (2003) Spatial Data Analysis: Theory and Practice. Cambridge: Cambridge University Press.

Hallin, R. G. (1990) Microneurography in relation to intraneural topography: somatotopic organisation of median nerve fascicles in humans. J. Neurol. Neurosurg. Psychiatry *53*:736–744.

Pearson, R. C., M. M. Esiri, R. W. Hiorns, G. K. Wilcock, and T. P. Powell (1985) Anatomical correlates of the distribution of the pathological changes in the neocortex in Alzheimer disease. Proc. Natl. Acad. Sci. USA *82*:4531–4534.

Prodanov, D., J. H. Heeroma, and E. Marani (2005a) Automatic morphometry of synaptic boutons of cultured cells using granulometric analysis of digital images. J. Neurosci. Methods (in press) .

Prodanov, D., E. Marani, and J. Holsheimer (2003) Functional Electric Stimulation for sensory and motor functions: Progress and problems. Biomed. Rev. *14*.

Prodanov, D., M. A. Thil, E. Marani, J. Delbeke, and J. Holsheimer (2005b) Three-dimensional topography of the motor endplates of the rat gastrocnemius muscle. Muscle Nerve *32*:292–302.

Ripley, B. D. (1991) Statistical inference for spatial processes. Cambridge: Cambridge University Press, 1st edn.

Schady, W., J. L. Ochoa, H. E. Torebjork, and L. S. Chen (1983) Peripheral projections of fascicles in the human median nerve. Brain *106 (Pt 3)*:745–760.

Schmued, L. C. and J. H. Fallon (1986) Fluoro-Gold: a new fluorescent retrograde axonal tracer with numerous unique properties. Brain Res. *377*:147–154.

Silverman, B. W. (1986) Density estimation for statistics and data analysis. Chapman and Hall/CRC, Monographs on Statistics and Applied Probability, pp. 1–22.

Stoyan, D., W. Kendall, and J. Mecke (1996) Stochastic geometry and its applications. John Wiley & Sons, 2nd edn.

Sunderland, S. (1945) The intraneural topography of the radial, median, and ulnar nerves. Brain *68*:243–299.

Swett, J. E., R. P. Wikholm, R. H. Blanks, A. L. Swett, and L. C. Conley (1986) Motoneurons of the rat sciatic nerve. Exp. Neurol. *93*:227–252.

Tredici, G., C. Migliorini, I. Barajon, G. Cavaletti, and R. Cece (1996) Anatomical organization of the spinal paths to the soleus and gastrocnemius muscles of the rat hind limb. J. Hirnforsch. *37*:81–89.

Wand, M. P. and M. C. Jones (1995) Kernel smoothing. Boca Raton, Florida: CRC Press.

General Discussion

8.1 The gastrocnemius muscle

After careful review of previous research studies on the lumbar spinal cord, the gastrocnemius muscle of the rat was selected as a starting point for the tracing experiments. This choice was made for two reasons: *first*, its innervation stems from L4 - L6 ventral roots (Brunner et al., 1980; Tredici et al., 1996) that were the target for the aimed investigations and *second*, it is widely used in physiological experiments (Chapters 3 - 5). It was conjectured that a topographic map of the motor endplates would allow placement of tracer injections in a more specific and reproducible manner, which would increase the reproducibility of the observed labeling (Chapter 3, Introduction). To this end, based on the assembled 3D map and microscopic observations performed during dissections, we provided guidelines for the best approach of the medial and lateral gastrocnemius muscles for tracer injections (Prodanov et al., 2005). Proposed 3D map is a useful contribution to the fields of muscle physiology and anatomy. More realistic modeling of EMG can be achieved if the 3D geometry of the motor endplate zones is incorporated into available models (for references, see Chapter 3). Moreover, sampling or excluding parts of datasets can simulate pathological conditions, such as partial denervation. In such a way, the influence of the motor endplate geometry on EMG of the gastrocnemius muscle can be studied in greater detail.

8.2 Morphometric and spatial analysis of neuronal structures

Expert identification of cell structures can suffer from poor reproducibility (Geuna et al., 2001; Benali et al., 2003). To accelerate the process of morphometry, we developed a reproducible automatic object identification and measurement technique and implemented it in an "open source" software program for image analysis. Human observers successfully verified the technique in a task of synapse bouton identification in two trials (Chapter 5). This automatic

technique was further developed to encompass fluorescent retrograde tracer identification in noisy microscopic images (Chapter 6). Dimensions of axons loaded with the retrograde tracer Fluoro-Gold were measured automatically and related to the full nerve fiber dimensions (axon and myelin sheath) using a linear regression relationship. This allowed reconstructing the total labeled fiber population from the fluorescence picture. Using the technique, it was shown that in both L6 ventral roots and peripheral nerves, primarily $A\alpha$ fibers were detected (Chapter 6).

Moreover, there was only a small fraction of thick fibers (i.e. $A\alpha^2$ in the nomenclature of Chapter 4) that were labeled and consequently measured. Apart from a methodological bias, observed difference can be caused by redistribution of these fibers to the nerves innervating axial muscles. Before reaching the trochanter and the mid-thigh, where samples of the proximal and distal sciatic nerve were collected, respectively, the sciatic nerve gives branches to the tail and the pelvic muscles (i.e. *nn. glutei caudalis et cranialis; n pudendus; n. cutaneus femoris caudalis*); see Figure 1.4 and Hebel and Stromberg (1986). Therefore, it is possible that the $A\alpha^2$ fibers segregate and channel through these nerves. To address this conjecture, a similar morphometric study should be performed in the pelvic nerves. We further conjectured that using this approach both the type and the spatial distribution of the labeled fibers could be determined in the same histological section (Chapter 6) and developed a statistical technique to analyze the spatial arrangement of the labeled fibers (Chapter 7). Using this technique, it was established that part of the motor fibers innervating the gastrocnemius muscle form a cluster at the level of the L6 ventral spinal root.

8.3 Proper targets of stimulation in view of the structural organization of the lumbar nerves and roots

A Number of quantitative morphological parameters, such as the cross-sectional dimensions of nerves and roots, the density of fibers, and their size distribution were established in Chapter 4. Obtained results have the following implications for further development of neuroprostheses.

From an anatomical point of view, *ventral spinal roots* can be suitable targets for electrical stimulation due to their moderate internal heterogeneity and the small variation in their cross-sectional areas and density. The extent to which encountered internal heterogeneity in the ventral roots can influence the electrical stimulation cannot be addressed at this stage. On the other hand, encountered segmental differences in their composition probably reflect the topographical organization of the hind limb innervation and should be taken into account when applying electrical stimulation. Stimulation of the *dorsal roots*, for example for pain suppression, can also be considered from the findings in Chapter 4, since the studied dorsal roots (L4 - L6) had a similar composition. On the other hand, their marked internal heterogeneity can hamper the size selectivity of such stimulation if applied at a topographically inappropriate place.

The *(common) peroneal nerve* is also a suitable target for stimulation because of the relatively large separation between its $A\alpha$ and $A\beta$ fiber populations as reflected in the shape of the optimal LN3 model of the nerve (Fig. 4.6, p. 86). This apposition can be beneficial for the size-selectivity of stimulation. Therefore, further development of devices, such as the Finetech implantable peroneal drop-foot stimulator (Kenney et al., 2002), should be based on the outcome of morphometric studies in human material. The tibial nerve, on the other hand, is less suitable for stimulation because of the overlap between the $A\alpha$ and $A\beta$ populations of fibers

(Fig. 4.6, p. 86).

An array of techniques for fiber size selective stimulation has been proposed in literature (for a detailed overview see Chapter 2). They can be classified in: (i) anodal blocking of the large fibers (Fang and Mortimer, 1991); (ii) reshaping the profile of extracellular potential along axons using multiple electrodes in a cuff (Lertmanorat and Durand, 2004); and (iii) altering the stimulation pulse shape (i.e. pre-pulses (Deurloo et al., 2001)). In most cases, an insulating cuff surrounding the nerve is utilized and because the cuff has the tendency to make the electrical field homogenous in each cross-section plane of the nerve this would yield lowest dependency on location of a fiber in the cross-section. Therefore, such techniques are suitable for nerves (e.g. fascicles) innervating only few different muscles. A good example for this is the diaphragm, where neural prostheses proved to be very successful (Chapter 2 and Prodanov et al. (2003)).

In contrast, due to its marked proximo-distal heterogeneity and multi-fascicular structure, the sciatic nerve is not suitable for electrical stimulation with cuff electrodes. Stimulation using intraneural electrodes could provide some selectivity at the muscle level - for example, with 3D microelectrode arrays, such as the Utah Slanted Microelectrode Array (Branner and Normann, 2000; Branner et al., 2001). Obtained muscle selectivity of the medial and lateral gastrocnemic muscles could readily be explained by the fascicle division of the nerve muscle branches present at that level. It should be noted that the recruitment characteristics of intrafascicular electrodes are very different from the extrafascicular electrodes. The nodes of Ranvier nearest to the electrodes will be excited first, and these could belong to different size classes of fibers (Frieswijk et al., 1998; Rutten et al., 1999; Veltink et al., 1988; 1989).

8.4 The composition of the nerves and the roots

Analysis of the fiber populations performed in Chapter 4 showed that, in the majority of the studied nerves and roots, three fiber populations could be identified statistically and they remained conserved in composition throughout their course from the spinal roots to the muscles. The physiological types of the individual components in the fiber populations were established using calculations of conduction velocities arising from the measurements of Boyd and Kalu (1979) and Arbuthnott et al. (1980) according to the previous theoretical considerations of Rushton (1951). Moreover, it was possible to assign a functional modality (i.e. sensory, motor, or mixed character) to each of the populations in the studied lumbar nerves (Chapter 4). The approach proposed in Chapter 4 can give a conceptual framework for comparisons in the anatomy and physiology of the peripheral nerves and their spinal roots across different species. For example, the similarity and dissimilarity between the human and the rat peroneal nerves can be further explored for the purposes of foot drop stimulator development. The internal microscopic organization of the lumbar nerves and roots was addressed further in Chapter 7. Obtained results cast light on the discussion on the internal organization of the nerves.

8.5 Is the nerve a plexus or a cable?

The fascicular organization of human peripheral nerves was recognized as early as XVIIIth century by Van Leeuwenhoek (1719) and Prochaska (1779). In the early XXth century, two contradicting views were promoted for the organization of nerves. While several investigators promoted "cable-like" nerve organization (Stoffel, 1913; 1915; Putti, 1916; Barile, 1917), others

described a "plexiform arrangement" of the fascicles within a nerve (Heinemann, 1916; Dustin, 1918; Compton, 1917; Langley and Hashimoto, 1917). By studying the clinical manifestations of the partial nerve injuries caused by nerve injuries from bullet wounds, Dejerine et al. (1915) were able to attribute motor or sensory groups of fibers to specific fascicles of the ulnar nerve at the elbow (review in Stewart (2003)). Peripheral neuropathies associated with war injuries were also investigated using electrical stimulation by Marie et al. (1915) and Kraus and Ingham (1920), who also concluded in favor of cable organization. The results of intraneural stimulation experiments in the pioneer animal studies varied with the technique and the proximo-distal localization and were not conclusive. For example, stimulation of cat single peroneal fascicles at the knee level resulted in contraction of individual muscles (Langley and Hashimoto, 1917), whereas stimulation at the level of the ischial tuberosity resulted in contraction of all muscles supplied by the sciatic nerve (McKinley, 1921). Using an anatomical microdissection technique, Sunderland attempted to reconstruct the longitudinal course of fascicles. His basic tenet was that the complexity of fascicular rearrangements in the mid and proximal segments of nerves "*excluded the possibility of groups of nerve fibers being confined throughout their course to a particular funiculus (fascicle)*"(Sunderland, 1945). This became a widely accepted view of the internal structure of the nerves. Precise as they were, Sunderlands's observations were limited by his gross anatomical technique. His views were contested by the advent of modern microneurographical and tracing techniques.

Using a microneurographical technique, Schady et al. (1983) could discriminate a fraction of the fascicles studied in the upper arm that projected to a single digital interspace and Hallin (1990) was able to demonstrate intrafascicular concentration of the sensory axons. Evidence supporting a more-organized view of some nerves is accumulated primarily from retrograde tracing studies in various animal species. Musculotopic organization of the motor axons was demonstrated in the *recurrent laringeal nerve* in the cat (Malmgren et al., 1977); the *oculomotor* (Atasever et al., 1993) and *hypoglossal* nerves in the rat (Lee et al., 1996) and in the segmental nerves for the gluteal muscle fibers in the frog (Brown et al., 1989). Cable-like fascicular anatomy was described also in the *median nerve* of the macaque (Brushart, 1991) and the *musculocutaneous nerve* in the rat (Bertelli et al., 1995). It was suggested that, in the rat *sciatic nerve*, segregation of the fibers was present depending of the spinal level of origin (Montoya et al., 2002).

Results from Chapter 7 advance further the musculotopical view of organization of peripheral nerves by showing that at least some muscles in the rat are represented topographically at the L6 spinal root level.

8.6 Observed clustering can be caused by a positional gradient in the spinal root

MAny projections within the nervous system are topographically organized. Within the motor system of man, motor neuron pools for different muscles form a roughly topographical map onto the limb (Sherrington, 1892). Musculotopic organization for the motor neuronal columns in the spinal cord was proposed by Romanes (see for example Romanes (1964) and Jacobson (1991)). This organization was explained by the concept of a spatio-temporal correlation between the growth of the axons from the ventral horn and the order of innervation in proximo-distal sequence in the limbs. Distally, limb muscles also receive topographically

organized innervation from the peripheral nerves (Swett et al., 1970; Brown and Booth, 1983; Bennett and Lavidis, 1984; Laskowski and Sanes, 1987; Bennett and Ho, 1988). For some motor nuclei, it was demonstrated that they form topographical projections onto their motor targets during the embryonic development that are refined after birth (Bennett and Lavidis, 1981; Brown and Booth, 1983; Bennett et al., 1989) and are disrupted if the nerve had regenerated (Brown and Everett, 1990; Everett and Brown, 1996). In most cases, the rostro-caudal location of the axis of motoneuronal cell bodies is mapped onto either the rostro-caudal axis (Laskowski and Sanes, 1987) or the antero-posterior axis of a muscle (Hardman and Brown, 1985). Taken together, these studies suggest that during development, spinal cord motoneurons project within a particular muscle to predictable locations according to their position in the motor nucleus.

During development, motor axons are able to grow to their correct muscle targets because they respond to specific limb-associated cues (Landmesser, 1978; Lance-Jones and Landmesser, 1980; 1981; Honig, 1982; Lance-Jones and Dias, 1991), while the path finding choices of sensory axons depend on the motor axons (Honig et al., 1998). Different positional cues and mechanical interactions inside the nerve are thought to play a role in this process (for overview see Landmesser (1992) and Goodman (1996)). Actions of positional gradients of substances, such as the cell-adhesion molecules (CAM), have been implied in development and regeneration of the amphibian (Maden, 2002) and in the development of the avian limbs (Honig et al., 1998). It is plausible to go one step further and hypothesize that observed clustering of the motor fibers is caused by the action of a similar gradient of positional cues within the spinal root that groups motor axons during growth to innervate their target muscles in a topographical manner.

8.7 Electrical stimulation in view of the spatial organization of motor fibers in the roots

Previous research on selective stimulation using implantable neuroprostheses was based on the assumption that the target motor nerve fibers were either uniformly or completely randomly (i.e. CSR, see Chapter 7) distributed in the nerves, respectively ventral roots (Smit, 1996). In contrast, we showed that the $A\alpha$ fibers were organized in one or several clusters in the ventral root L6 (Chapter 7).

Labeling in the $A\gamma$ fibers from the gastrocnemius muscle could not be detected in the L6 ventral root (Chapter 6). Nevertheless, it is plausible to consider that $A\gamma$ fibers are also interspaced together with the clustered $A\alpha$ fibers. In this case, the size selectivity arises as an important issue for the efficiency of stimulation of the cluster. Findings described in Chapter 7 provide a solid basis for future research on how exactly a cluster of nerve fibers can be effectively stimulated. To reiterate the relevant findings from Chapter 7: on average, 23.8 % of the labeled $A\alpha$ motor fibers were clustered and they were densely arranged at distances of about 1.5 - 2 fiber diameters (Table 7.1). Therefore, the density of the fibers can be appropriate for selective stimulation of the cluster. The average nearest-neighbor distance is related to the expected number of fibers in a given volume and, therefore, can be an important parameter for the design of intrafascicular micro-electrode arrays.

Observations in cats suggest that the flexor groups of motoneurons in the spinal cord are arranged in such a way that each main mass of cells tends to be concerned with the innervation of muscles, which move the same joint (Romanes, 1964). In the rat spinal cord, the flexor muscles

have different motor nuclei from the extensors (Nicolopoulos-Stournaras and Iles, 1983). If arrangement of the motor nuclei corresponds to the map in the ventral root then, by analogy with the separate location of the flexor and extensor motor columns, it can be conjectured that the motor fibers innervating flexor and extensor muscles would have separate representations at the level of the ventral root. Performing additional tracing experiments with simultaneous differential marking of flexor and extensor muscle groups can test this conjecture. If true, it can be further speculated that even if other fibers interspaced with the clustered ones are stimulated they will be of synergistic muscles, so functional movement would be gained rather than decreased.

8.8 Future outlooks: which way of stimulation is better?

THe configuration of the observed clusters (Chapter 7) taken together with the findings in Chapter 4 suggests that ventral roots are confirmed as a target for selective stimulation by implantable neuroprostheses. When considering their applicability for neural prosthesis development both highlighted aspects of the organization of the spinal roots should be taken into account. At this stage it is difficult to make a definitive choice for "the best" electrode or "the best" protocol for stimulation. As mentioned before, for a topically selective stimulation (e.g. stimulation of a cluster of motor fibers), the use of an insulating cuff around the nerve is not optimal, although some position selectivity can be achieved with multiple electrodes surrounding the nerve or the root. Among the other available options for selective stimulations are: (i) subepineural electrodes using non-complete cuffs (Goodall et al., 1996); (ii) slowly penetrating intrafascicular nerve electrodes (Tyler and Durand, 1997); (iii) flat interface nerve electrodes (Leventhal and Durand, 2004)) and (iv) penetrating electrodes, such as the flexible intrafasicular electrodes (Yoshida and Horch, 1993) and the 3D microelectrode arrays (Rutten, 2002; Branner and Normann, 2000). Still, the chronic biocompatibility of these electrodes has not been sufficiently tested (Prodanov et al., 2003). To test whether the elicited force in the studied muscle (in this case, the gastrocnemius) is large enough to regain muscle function and to establish optimal stimulation parameters cluster density maps should be incorporated into mathematical models of stimulation of the ventral roots.

Bibliography

Arbuthnott, E. R., I. A. Boyd, and K. U. Kalu (1980) Ultrastructural dimensions of myelinated peripheral nerve fibres in the cat and their relation to conduction velocity. J. Physiol. (Lond) *308*:125–157.

Atasever, A., B. Durgun, H. H. Celik, and E. Yilmaz (1993) Somatotopic organization of the axons innervating the superior rectus muscle in the oculomotor nerve of the rat. Acta Anat. (Basel) *146*:251–254.

Barile, C. (1917) Sul reale valoro practico della topografia fascicolare dei nervi periferici (secondo Stoffel) per l'esecuzione dell anastomosi dei nervi degli arti. Policlinico *24*:1177–1180.

Benali, A., I. Leefken, U. T. Eysel, and E. Weiler (2003) A computerized image analysis system for quantitative analysis of cells in histological brain sections. J. Neurosci. Methods *125*:33–43.

Bennett, M. R., A. M. Davies, and A. W. Everett (1989) The development of topographical maps and fibre types in toad (bufo marinus) glutaeus muscle during synapse elimination. J. Physiol. (Lond) *409*:43–61.

Bennett, M. R. and S. Ho (1988) The formation of topographical maps in developing rat gastrocnemius muscle during synapse elimination. J. Physiol. (Lond) *396*:471–496.

Bennett, M. R. and N. A. Lavidis (1981) Development of the topographical projection of motor neurons to amphibian muscle accompanies motor neuron death. Brain Res. *254*:448–452.

Bennett, M. R. and N. A. Lavidis (1984) Development of the topographical projection of motor neurons to a rat muscle accompanies loss of polyneuronal innervation. J. Neurosci. *4*:2204–2212.

Bertelli, J. A., M. Taleb, A. Saadi, J. C. Mira, and M. Pecot-Dechavassine (1995) The rat brachial plexus and its terminal branches: an experimental model for the study of peripheral nerve regeneration. Microsurgery *16*:77–85.

Boyd, I. A. and K. U. Kalu (1979) Scaling factor relating conduction velocity and diameter for myelinated afferent nerve fibres in the cat hind limb. J. Physiol. (Lond) *289*:277–297.

Branner, A. and R. A. Normann (2000) A multielectrode array for intrafascicular recording and stimulation in sciatic nerve of cats. Brain Res. Bull. *51*:293–306.

Branner, A., R. B. Stein, and R. A. Normann (2001) Selective stimulation of cat sciatic nerve using an array of varying-length microelectrodes. J. Neurophysiol. *85*:1585–1594.

Brown, D. R. and A. W. Everett (1990) Compartmental and topographical specificity of reinnervation of the glutaeus muscle in the adult toad (bufo marinus). J. Comp. Neurol. *292*:363–372.

Brown, D. R., A. W. Everett, and M. R. Bennett (1989) Compartmental and topographical distributions of axons in nerves to the amphibian (bufo marinus) glutaeus muscle. J. Comp Neurol. *284*:231–241.

Brown, M. C. and C. M. Booth (1983) Postnatal development of the adult pattern of motor axon distribution in rat muscle. Nature *304*:741–742.

Brunner, R., P. Zimmermann, and F. W. Klussmann (1980) Localization and neurophysiological properties of motoneurones of the m. triceps surae of the rat after retrograde labelling with Evans blue. Cell Tissue Res. *212*:73–81.

Brushart, T. M. (1991) Central course of digital axons within the median nerve of macaca mulatta. J. Comp. Neurol. *311*:197–209.

Compton, A. T. (1917) The intrinsic anatomy of the large nerve truncs of limbs. J. Anat. *51*:103–117.

Dejerine, J., A. Dejerine, and J. Mouzon (1915) Les lésions de gros troncs nerveux des membres par projectiles de guerre. Presse Med. *40*:321–328.

Deurloo, K. E., J. Holsheimer, and P. Bergveld (2001) The effect of subthreshold prepulses on the recruitment order in a nerve trunk analyzed in a simple and a realistic volume conductor model. Biol. Cybern. *85*:281–291.

Dustin, A. P. (1918) La fasciculation des nerfs. Ambul. Ocean *2*:135–154.

Everett, A. W. and D. R. Brown (1996) Loss of the position-dependent reinnervation of regenerated toad (bufo marinus) glutaeus muscle. J. Comp. Neurol. *366*:293–302.

Fang, Z. P. and J. T. Mortimer (1991) Selective activation of small motor axons by quasi-trapezoidal current pulses. IEEE Trans. Biomed. Eng. *38*:168–174.

Frieswijk, T. A., J. P. Smit, W. L. Rutten, and H. B. Boom (1998) Force-current relationships in intraneural stimulation: role of extraneural medium and motor fibre clustering. Med. Biol. Eng. Comput. *36*:422–430.

Geuna, S., P. Tos, R. Guglielmone, B. Battiston, and M. G. Giacobini-Robecchi (2001) Methodological issues in size estimation of myelinated nerve fibers in peripheral nerves. Anat. Embryol. (Berl) *204*:1–10.

Goodall, E. V., J. F. de Breij, and J. Holsheimer (1996) Position-selective activation of peripheral nerve fibers with a cuff electrode. IEEE Trans. Biomed. Eng. *43*:851–856.

Goodman, C. S. (1996) Mechanisms and molecules that control growth cone guidance. Ann. Rev. Neurosci. *19*:341–377.

Hallin, R. G. (1990) Microneurography in relation to intraneural topography: somatotopic organisation of median nerve fascicles in humans. J. Neurol. Neurosurg. Psychiatry *53*:736–744.

Hardman, V. J. and M. C. Brown (1985) Spatial organization within rat motoneuron pools. Neurosci. Lett. *60*:325–329.

Hebel, R. and M. W. Stromberg (1986) Anatomy and Embryology of the Laboratory Rat. Worthsee: BioMed Verlag.

Heinemann, O. (1916) Ueber Schutzverletzungen der peripheren Nerven. Nebst anatomischen Untersuchungen über den inneren Bau der grossen Nervenstamme. Arch. klin. Chir. *108*:107–150.

Honig, M. G. (1982) The development of sensory projection patterns in embryonic chick hind limb. J. Physiol. (Lond) *330*:175–202.

Honig, M. G., P. A. Frase, and S. J. Camilli (1998) The spatial relationships among cutaneous, muscle sensory and motoneuron axons during development of the chick hindlimb. Development *125*:995–1004.

Jacobson, M. (1991) Development of nerve connections with muscle and peripheral sense organs. In *Developmental Neurobiology*, Plenum press, book chapter 9, pp. 359–400. 3rd edn.

Kenney, L., G. Bultstra, R. Buschman, P. Taylor, G. Mann, H. Hermens, J. Holsheimer, A. Nene, M. Tenniglo, H. van der Aa, and J. Hobby (2002) An implantable two channel drop foot stimulator: initial clinical results. Artif. Organs *26*:267–270.

Kraus, W. M. and S. D. Ingham (1920) Peripheral nerve topography. Arch Neurol Psychiatry *4*:259–296.

Lance-Jones, C. and M. Dias (1991) The influence of presumptive limb connective tissue on motoneuron axon guidance. Dev. Biol. *143*:93–110.

Lance-Jones, C. and L. Landmesser (1980) Motoneurone projection patterns in the chick hind limb following early partial reversals of the spinal cord. J. Physiol. (Lond) *302*:581–602.

Lance-Jones, C. and L. Landmesser (1981) Pathway selection by embryonic chick motoneurons in an experimentally altered environment. Proc. R. Soc. Lond B Biol. Sci. *214*:19–52.

Landmesser, L. (1978) The development of motor projection patterns in the chick hind limb. J. Physiol. (Lond) *284*:391–414.

Landmesser, L. (1992) Growth cone guidance in the avian limb: a search for cellular and molecular mechanisms. In P. C. Letourneau, S. B. Kater, and E. R. Macagano (eds.), *The nerve growth cone*, Raven, pp. 373–385.

Langley, J. N. and M. Hashimoto (1917) On the structure of separate nerve bundles in a nerve trunc and on internal nerve plexuses. J. Physiol. (Lond) *51*:318–345.

Laskowski, M. B. and J. R. Sanes (1987) Topographic mapping of motor pools onto skeletal muscles. J. Neurosci. 7:252–260.

Lee, S., D. W. Eisele, A. R. Schwartz, and D. K. Ryugo (1996) Peripheral course of genioglossal motor axons within the hypoglossal nerve of the rat. Laryngoscope *106*:1274–1279.

Lertmanorat, Z. and D. M. Durand (2004) A novel electrode array for diameter-dependent control of axonal excitability: a simulation study. IEEE Trans. Biomed Eng. *51*:1242–1250.

Leventhal, D. K. and D. M. Durand (2004) Chronic measurement of the stimulation selectivity of the flat interface nerve electrode. IEEE Trans. Biomed Eng. *51*:1649–1658.

Maden, M. (2002) Positional information: knowing where you are in a limb. Curr. Biol. *12*:R773–R775.

Malmgren, L. T., M. J. Lyon, and R. R. Gacek (1977) Localization of abductor and adductor fibers in the kitten recurrent laryngeal nerve: use of a variation of the horseradish peroxidase tracer technique. Exp. Neurol *55*:187–198.

Marie, P., H. Meige, and A. Gosset (1915) Les localisations motrices dans les nerfs périphériques. Bull. Acad. Méd (Paris) *74*:789–810.

McKinley, J. C. (1921) The intraneural plexus of fasciculi and fibers in the sciatic nerve. Arch. Neurol. Psychiatry *6*:377–399.

Montoya, G. J., J. Ariza, J. J. Sutachan, and H. Hurtado (2002) Relationship between functional deficiencies and the contribution of myelin nerve fibers derived from l-4, l-5, and l-6 spinolumbar branches in adult rat sciatic nerve. Exp. Neurol *173*:266–274.

Nicolopoulos-Stournaras, S. and J. F. Iles (1983) Motor neuron columns in the lumbar spinal cord of the rat. J. Comp. Neurol. *217*:75–85.

Prochaska, G. (1779) De structura nervorum. Vienna: R. Graeffer.

Prodanov, D., E. Marani, and J. Holsheimer (2003) Functional Electric Stimulation for sensory and motor functions: Progress and problems. Biomed. Rev. *14*:23–50.

Prodanov, D., M. A. Thil, E. Marani, J. Delbeke, and J. Holsheimer (2005) Three-dimensional topography of the motor endplates of the rat gastrocnemius muscle. Muscle Nerve *32*:292–302.

Putti, V. (1916) Sulla topografia fascicolare dei nervi periferici e piu specialmente dello sciatic popliteo externo. Clinica Chir. *24*:1021–1035.

Romanes, G. J. (1964) The motor pools of the spinal cord. In *Organization of the spinal cord*, Elsevier, Progress in brain research, book chapter 11, pp. 93–119.

Rushton, W. A. (1951) A theory of the effects of fibre size in medullated nerve. J. Physiol. (Lond) *115*:101–122.

Rutten, W. L. (2002) Selective electrical interfaces with the nervous system. Ann. Rev. Biomed. Eng. *4*:407–452.

Rutten, W. L., J. P. Smit, T. A. Frieswijk, J. A. Bielen, A. L. Brouwer, J. R. Buitenweg, and C. Heida (1999) Neuro-electronic interfacing with multielectrode arrays. IEEE Eng. Med. Biol. Mag. *18*:47–55.

Schady, W., J. L. Ochoa, H. E. Torebjork, and L. S. Chen (1983) Peripheral projections of fascicles in the human median nerve. Brain *106 (Pt 3)*:745–760.

Sherrington, C. S. (1892) Notes on the arrangement of some motor fibers in the lumbo-sacral plexus. J. Physiol. (Lond) *13*:621–722.

Smit, J. P. A. (1996) Selective Motor Stimulation using Endoneural Prostheses. Ph.D. thesis, Twente University.

Stewart, J. D. (2003) Peripheral nerve fascicles: anatomy and clinical relevance. Muscle Nerve *28*:525–541.

Stoffel, A. (1913) Beitrage zu einer rationellen Nervenchirurgie. München Med. Wehnschr *60*:175–179.

Stoffel, A. (1915) Ueber die Behandlung verletzter Nerven im Kriege. München Med. Wehnschr *62*:201–203.

Sunderland, S. (1945) The intraneural topography of the radial, median and ulnar nerves. Brain *68*:243–299.

Swett, J. E., E. Eldred, and J. S. Buchwald (1970) Somatotopic cord-to-muscle relations in efferent innervation of cat gastrocnemius. Am. J. Physiol. *219*:762–766.

Tredici, G., C. Migliorini, I. Barajon, G. Cavaletti, and R. Cece (1996) Anatomical organization of the spinal paths to the soleus and gastrocnemius muscles of the rat hind limb. J. Hirnforsch. *37*:81–89.

Tyler, D. J. and D. M. Durand (1997) A slowly penetrating interfascicular nerve electrode for selective activation of peripheral nerves. IEEE Trans. Rehabil. Eng. *5*:51–61.

Veltink, P. H., J. A. van Alste, and H. B. Boom (1988) Influences of stimulation conditions on recruitment of myelinated nerve fibers: a model study. IEEE Trans. Biomed Eng. *35*:917–924.

Veltink, P. H., J. A. van Alste, and H. B. Boom (1989) Multielectrode intrafascicular and extraneural stimulation. Med. Biol. Eng. Comput. *27*:19–24.

Yoshida, K. and K. Horch (1993) Selective stimulation of peripheral nerve fibers using dual intrafascicular electrodes. IEEE Trans. Biomed. Eng. *40*:492–494.

CHAPTER 9

Summaries and Appendices

Summary

This thesis provides morphological and functional information needed for further development of the implantable neural prostheses for locomotion. Data obtained from series of morphometric studies and retrograde tracing experiments were analyzed using novel statistical and imaging approaches developed to study the organization of the myelinated nerve fibers in the peripheral nervous system. Research findings can be summarized in two propositions concerning the organization of the peripheral nerves and spinal roots in the lumbar region. By means of statistical modeling of the size distributions enabling to discriminate different populations of fibers in an otherwise "continuous" size spectrum of fibers, it was found that fiber populations have a conserved and readily discernable composition throughout their course along the peripheral nerves. Moreover, it was possible to discern the functional modality of these populations - i.e. their sensory or motor character. With regard to neuroprostheses, it is shown that the peroneal nerve is a suitable target for electric stimulation due to the separation of its large motor fibers from the smaller ones. This composition can explain the empirical efficiency of the implantable drop-foot stimulator. In contrast, solely from a structural point of view, the tibial and sciatic nerves are difficult targets for stimulation due to the worse separation of the large motor fibers from the smaller presumably sensory fibers. Using spatial statistical technique developed to delineate regions of clustered fibers, it is demonstrated that the $A\alpha$ motor fiber populations, which innervate gastrocnemius muscles are topographically organized (i.e. forming a clustered pattern in the spatial statistical sense) from the level of the ventral roots and remain in this state as they form dedicated motor muscle branches. A hypothesis describing the origin of the observed clustering of the motor axons is proposed. In view of the findings described in this thesis, the ventral spinal roots L4 - L6 are proper targets for electrical stimulation due to their musculotopical organization.

Samenvatting van het proefschrift

HET onderzoek zoals beschreven in dit proefschrift verschaft de morfologische en functionele gegevens, die nodig zijn voor verdere ontwikkeling van implanteerbare neurale prothesen. In Hoofdstuk 2 werd een overzicht gegeven van Fuctionele Electrische Stimulatie (FES) en het gebied van neuroprothesen. Ter vastelling van de functionele anatomische gegevens die nodig zijn voor de verdere ontwikkeling van neurale prothesen voor het herstel van de bewegingsfucties werden de gangbare toepassingen aan een kritisch onderzoek onderworpen. De gewenste gegevens werden verkregen met behulp van morfometrie en retrograde tracer experimenten. De verzamelde gegevens werden geanalyseerd met nieuwe statistische en beeldverwerkingstechnieken, ontwikkeld voor de bestudering van de organisatie van gemyeliniseerde zenuwvezels in het perifere zenuwstelsel. De onderzoeksresultaten zoals beschreven in dit proefschrift kunnen samengevat worden in twee voorstellen betreffende de organisatie van de lumbale perifere zenuwen en spinale wortels. Met behulp van statistiche modellering van de groottedistributies die het mogelijk maakte om verschillende vezelpopulaties te onderscheiden in een overigens 'continu' kaliberspectrum, werd ontdekt, dat vezelpopulaties een vaste en eenvoudig te onderscheiden samenstelling bezitten bij hun verloop door de perifere zenuwen. Bovendien was het mogelijk om de functionele modaliteit (sensibel of motorisch) van deze populaties vast te stellen. Wat betreft neuroprothesen wordt aangetoond, dat de nervus peroneus een geschikt doelwit is voor electrische stimulatie en wel op grond van de (statistische) scheiding tussen de dikke motorische vezels en de dunnere vezels in deze zenuw. Deze samenstelling kan een verklaring zijn voor de empirisch vastgestelde doelmatigheid van de implanteerbare drop-foot stimulator. Hiertegenover staat dat vanuit een puur structureel oogpunt de nervus tibialis en ischiadicus moeilijk te stimuleren zijn gezien de slechtere (statistische) scheiding tussen de dikke motorische vezels en de dunnere, vermoedelijk sensibele, vezels. Met gebruikmaking van een spatiële statistische techniek, die ontwikkeld was om gebieden van vezelclustering af te grenzen, wordt aangetoond dat de $A\alpha$ motor vezelpopulaties, die de *musculus gastrocnemius* innerveren topografisch georganiseerd zijn (dwz een ruimtelijk statistisch cluster-patroon vormen) vanaf het niveau van de voorwortels en zo georganiseerd blijven tot in de uiteindelijke spiertakken. Voor het ontstaan van de waargenomen clustering van de motorische axonen wordt een hypothese voorgesteld. Op grond van de resultaten beschreven in dit proefschrift zijn de ventrale ruggenmergswortels L4 - L6 een geschikte doelwit voor electrische stimulatie, en wel dankzij hun musculotopische organisatie.

List of Publications Related to the Thesis

Journal Articles

Prodanov, D., E. Marani, and J. Holsheimer (2003) Functional Electric Stimulation for sensory and motor functions: Progress and problems. Biomed. Rev. *14*:23–50.

Prodanov, D., M. A. Thil, E. Marani, J. Delbeke, and J. Holsheimer (2005) Three-dimensional topography of the motor endplates of the rat gastrocnemius muscle. Muscle Nerve *32*:292–302.

Prodanov, D., J. H. Heeroma, and E. Marani (2005) Automatic morphometry of synaptic boutons of cultured cells using granulometric analysis of digital images. J. Neurosci. Methods (in press).

Prodanov, D., N. Nagelkerke, and E. Marani (2005) Local spatial analysis of the motor axonal clustering in rat ventral spinal roots. Submitted to J. Neurosci. Methods.

Prodanov, D. and H. K. P. Feirabend (2005) Automated morphometric analysis of the nerve fiber population innervating the rat gastrocnemius muscles. Submitted to BMC Neuroscience.

Conference Proceedings

Prodanov, D., E.A.J.F. Lakke, H.K.P. Feirabend, J. Holsheimer, and E. Marani (2002) Distribution of the motor nerve fibers in the ventral lumbo-sacral roots: Significance for functional electrical stimulation, Papendal, The Netherlands, Proceedings of the Dutch Annual Conference on Biomedical Engineering, pp. 107–110

Prodanov, D., E. A. J. F. Lakke, H. K. P. Feirabend, J. Holsheimer, and E. Marani (2003) Distribution of the nerve fibers in the ventral lumbar roots and peripheral nerves: Rat and baboon morphometric study. Proceedings of the Dutch Annual Conference on Biomedical Engineering, pp. 134–137.

Prodanov, D., M.-A. Thil, J. Holsheimer, J. Delbeke, D. Ypey and E. Marani (2003) 3D-map of the motor end-plate regions in the rat gastrocnemic muscle as an aid for localized application of retrograde tracers, Papendal, The Netherlands, Proceedings of the Dutch Annual Conference on Biomedical Engineering, pp. 138–141

Prodanov, D., E. A. J. F. Lakke, H. K. P. Feirabend, N. Nagelkerke, J. Holsheimer, and E. Marani (2004) A direct fluorescence-based approach for elucidating the fiber diameter and spatial distribution of motor fibers innervating the rat gastrocnemic muscles. Bournemouth, UK, Proceedings of IFESS-FESnet 2004, pp. 48–50.

Prodanov, D., N. Nagelkerke, and E. A. J. F. Lakke (2004) K-function based approach for topographical description of the peripheral nerve fibers, Proceedings of the Dutch Annual Conference on Biomedical Engineering, Papendal, The Netherlands pp. 114–116

Curriculum vitae

Dimiter Petkov Prodanov

Personal details

date of birth: 16 March 1975   **place of birth:** Sofia, Bulgaria

Education

May 2002 – Jan 2006   Leiden University Medical Center, Leiden, The Netherlands
Research training in the Neuroregulation group, Department of Neurosurgery
and
Twente University, Enschede, The Netherlands
PhD training program in the Biomedical Signals and Systems group, Faculty of Electrical Engineering, Mathematics, and Informatics

2000 – 2002   Medical University - Sofia, Sofia, Bulgaria
post-graduate training in Clinical Pharmacology, Department of Pharmacology and Toxicology, Medical Faculty

1993 – 1999   Medical University - Sofia, Sofia, Bulgaria
graduated as a Medical Doctor with *Master degree*
research training in the Department of Pharmacology and Toxicology, Medical Faculty

1989 – 1993   National Gymnasium for Natural sciences and Mathematics, Sofia, Bulgaria
graduated *cum laude* with profile Biotechnology

Memberships

International Brain Research Organization (IBRO), Dutch Society for Experimental and Clinical Neuroscience, Dutch Institute for Biomedical Technology (BMTI), Editorial board member of *Head and Face Medicine*, Development team of *ImageJ*

Research Interests

Anatomy of the Central and the Peripheral nervous system; Pharmacology and Physiology of the neurodegenerative disorders and programed cell death; Image Analysis and fluorescent microscopy; Spatial Statistics; Computer modeling

Words of thanks (Благодарности)

> *One of the symptoms of an approaching nervous breakdown is the belief that one's work is terribly important.*

> *Bertrand Russell*

Uɴbelievably I am here. Of course, I could not have done anything without the NeuralPRO, but the financial support I already mentioned earlier. Here is the place to thank for the Oscar. So this is the account for the thanks giving:

I'd like to thank to my (former) colleagues for the support which I got from them on numerous occasions: especially to Marga, Herman and Egbert for helping me settle in Leiden back in 2002. I'd like to apologize to Jantine for occupying many of Enrico's evenings and half of his last vacation in France. I'd like to thank also to Bert, my late office mate, for the numerous funny conversations and helpful advice and especially to Enrico and Hans for their patience and timely feedback on our manuscripts.

I would like to acknowledge Dr. Jan Holsheimer, Prof. K. Usunoff and Prof. N. Boyadjieva who were very much involved in the critical phases of my doctorate. I also want to outline the contributions of my collaborators and friends Joost Heeroma and Nico Nagelkerke who trusted my intuition long enough so we reached working solutions. Here is the place to mention Prof. H. Uylings, who pointed out the works of P. Diggle in spatial statistics and also gave me an assignment to complete together with a tall Dutch guy called Joost at the morphometry course in Amsterdam. I'd like to acknowledge also Prof. D. Ypey for the early literature on the motor endplates; Dr Ruud van den Berg for the critical reading of Chapter 4; Jelle Goeman for giving me advice on LaTeX and checking some of my calculations and Jérémie Lebrec for challenging my ideas on regression and anova in Chapters 4 and 6. I'd like to thank also to Dr. Katya Jordanova and Karen Kleiwerda, who provided me access to the fluorescence microscope in the Pathology Department.

Finally thanks go to my friends who made me enjoy my stay in the Netherlands. Thanks go to Кети, Пешо, Дежо, Jack, and Vincent!

Thank you Иво – for the loooong phone calls during funny times of the day and night; you Стела – for talking me into LaTeX-ing and you Luc – for the life, universe and everything! I'd like also to thank to the people from the *LUSV* fencing club and the *Hong-Ying* Tai-Chi club and to my friends (especially the "old students" Chow, Maas, Jornas, Niels and Martijn) from the proud house of *Palmzicht* in Leiden.

Dear friends, you all have contributions to my peace of mind, mornings, days and evenings and I feel honored by your company. Without you Netherlands wouldn't have been such fun experience. And let me finish with the thought of the philosopher Nietzsche that every day without dance and laughter is a lost one.

Dimiter Prodanov
Leiden, 28 Nov 2005

Appendix: Color Figures

Figures from Chapter 3

Figure 9.A.1 (legend): Section planes are perpendicular to the longitudinal axis of muscle (Z-axis). Sections are 1.2 mm apart. The X-axis points in a medial direction; the Y-axis, to the tibial side of the muscle; the Z- axis, to the Achilles tendon. Boundaries of the muscle tissue are represented by planar contours. The motor endplate clusters are represented by spheres. A - Isometric projection of the 3D map (dorsal view). Three columns of motor endplates, boundaries indicated by blue space filling, are present within the muscle. The map is rotated so that the N-shaped figure is best seen (compare to Fig. 3.1C). B - Coronal projection. Top, tibial surface; bottom, dorsolateral surface. C - Frontal projection from the side of the tibia. The angle between the lateral and the central column is $18°$. The angle between the medial and the central column is $20°$. Scale bars are 2 mm.

Figure 9.A.2 (legend): Motor endplate clusters are represented by spheres. Boundaries of the muscle tissue are represented by planar contours. Section planes are perpendicular to the longitudinal axis of the muscle (z-axis). Sections are 1.2 mm apart. The X-axis points in a medial direction; the Y-axis, to the tibial side of the muscle and the Z-axis, to the Achilles tendon. A - Isometric projection of the 3D map (medial view). The motor endplates form a leaf-like structure. The 3D map is rotated so that the configuration of the motor endplates in space is best observed. B - Coronal projection. C - Frontal projection from the side of the tibia. Scale bars are 2 mm.
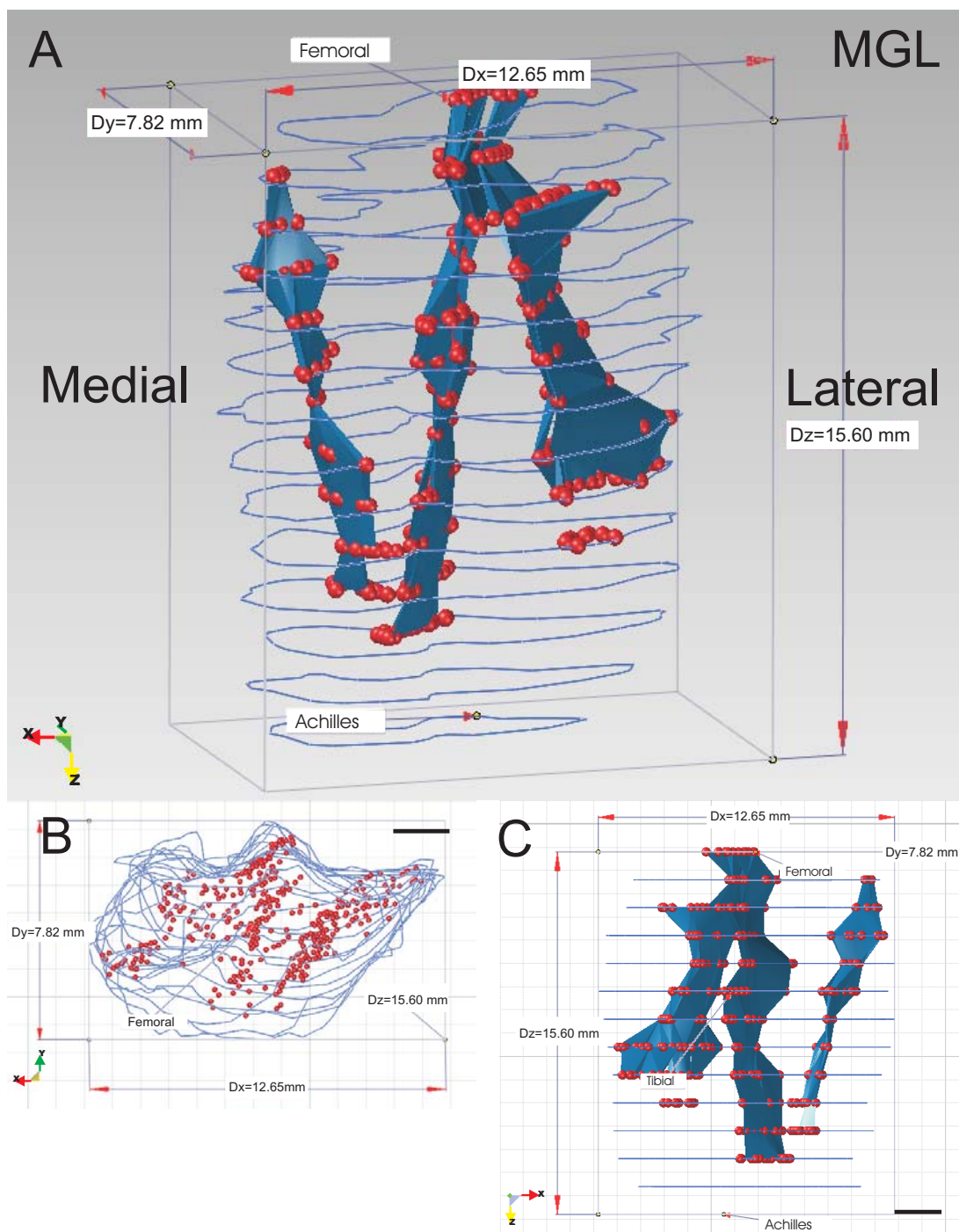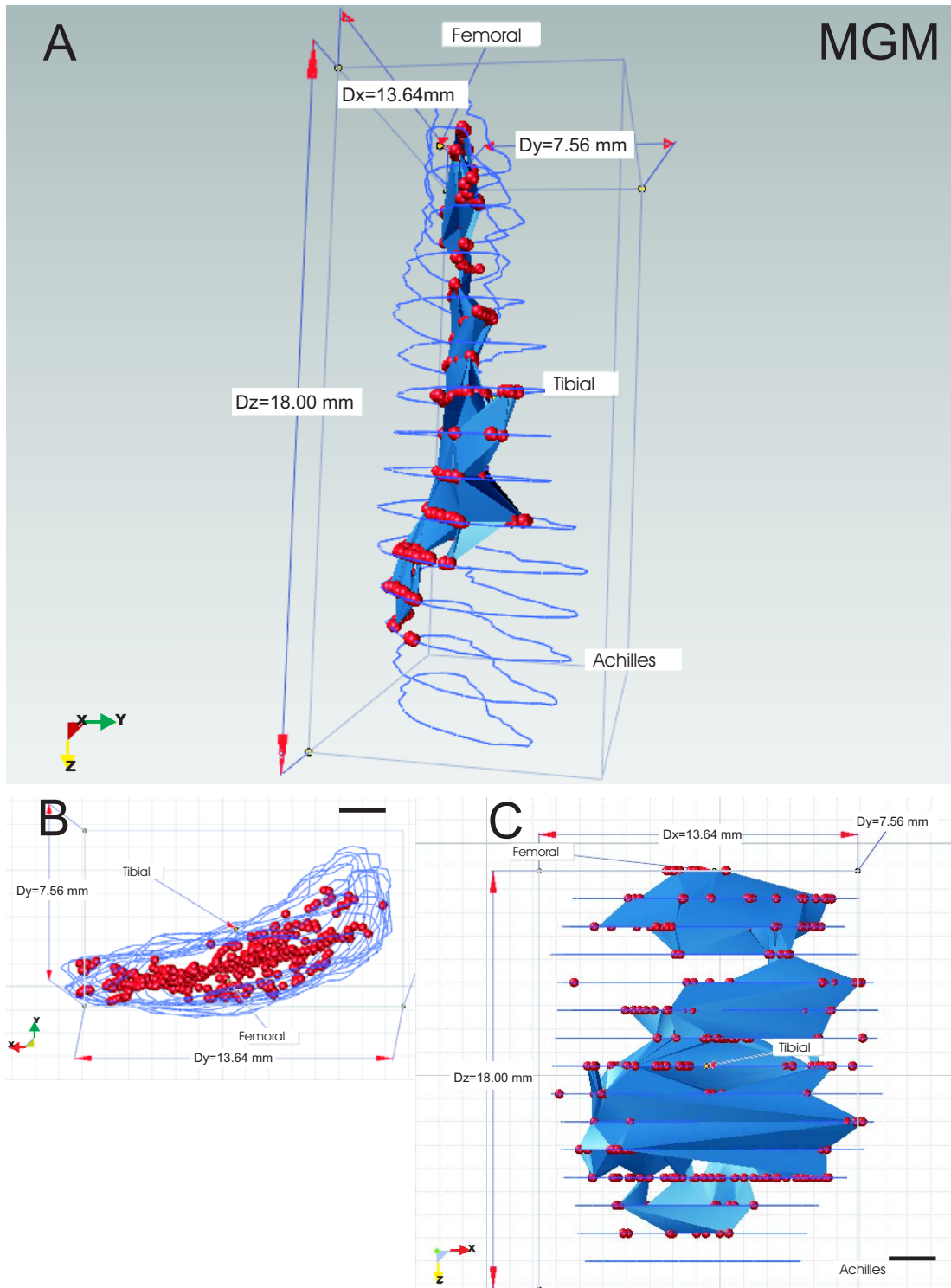
Figure 9.A.1: 3D map of MGL; Fig. 3.3

Figure 9.A.2: 3D map of MGM; Fig. 3.4
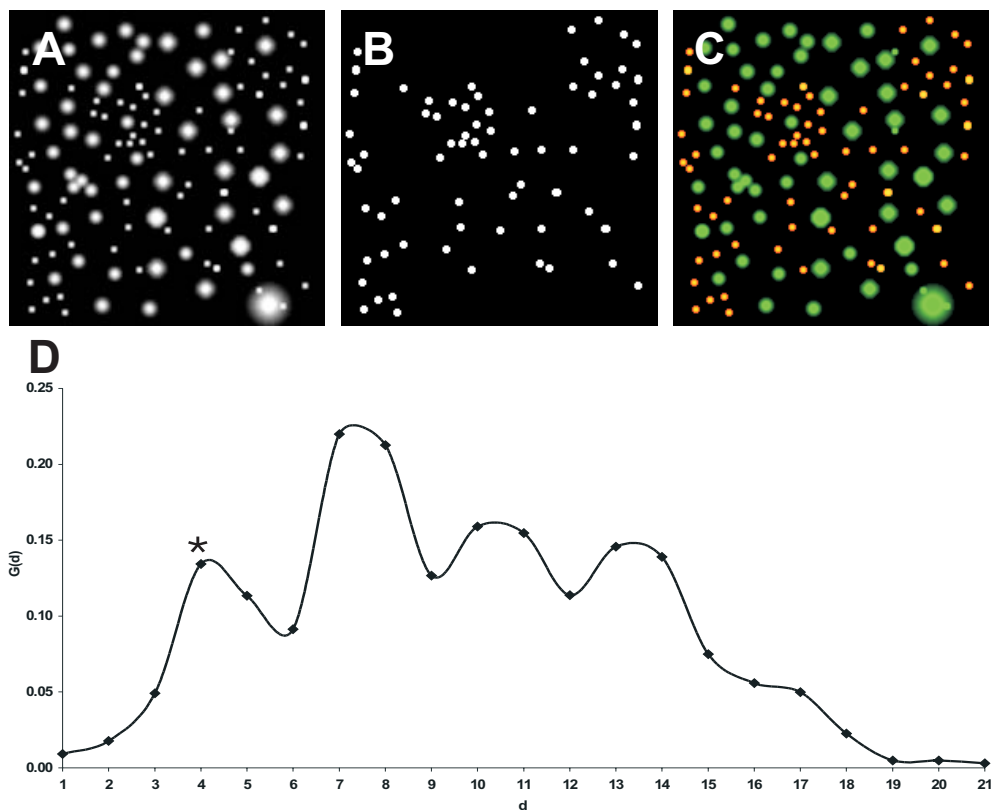
Figures from Chapter 5

Figure 9.A.3: Granulometric filtering procedure of a synthetic image; Fig. 5.2

A - Synthetic image with dimensions 200 x 200 pixels containing 5 types of bright grains of varying grades of fuzziness. B - the mask derived from the marked peak in G(d) (asterisk, D). C - Co-localization of the mask (red) and the original image (green). Co-localized grains appear in orange color. D - Smoothed G(d) of the synthetic image (A).
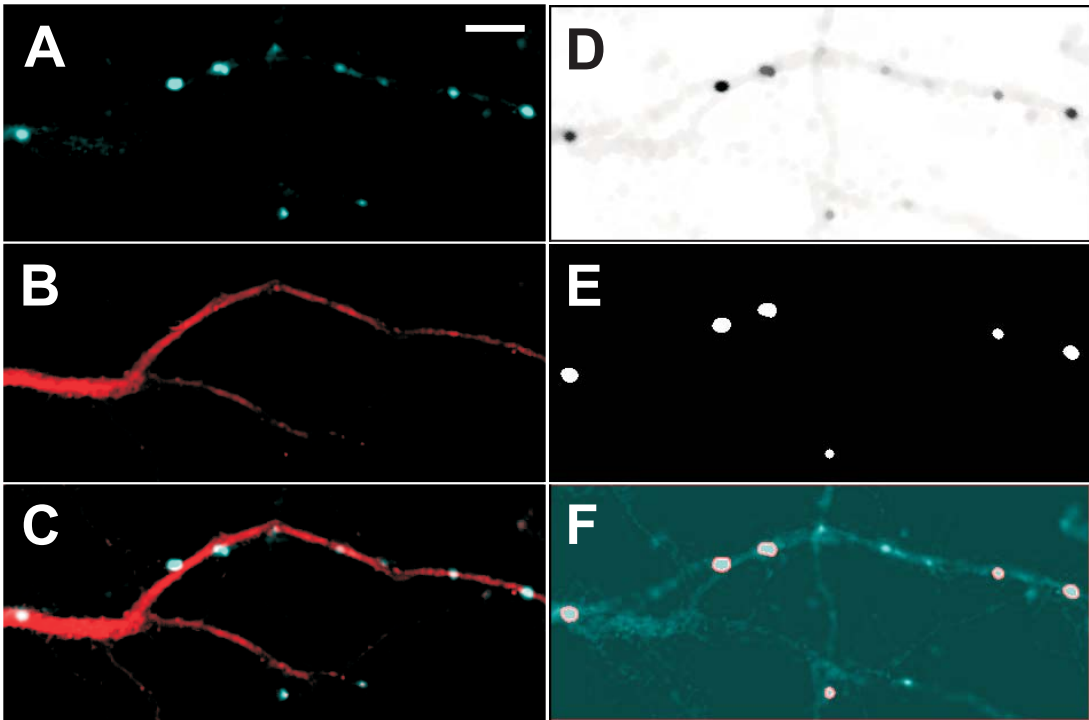
Figure 9.A.4: Illustration of the granulometric filtering technique on a real image; Fig. 5.4

A - High-resolution image of synapsin I staining; B - MAP-2 staining; C - Co-localization of synapsin I (cyan) and MAP-2 (red); D - inverted filtered image, step 2 of the algorithm. E - mask image, step 3; F - co-localization of the detected synaptic boutons (red outline) with the original synapsin I image. Scale bar - 5 μm.
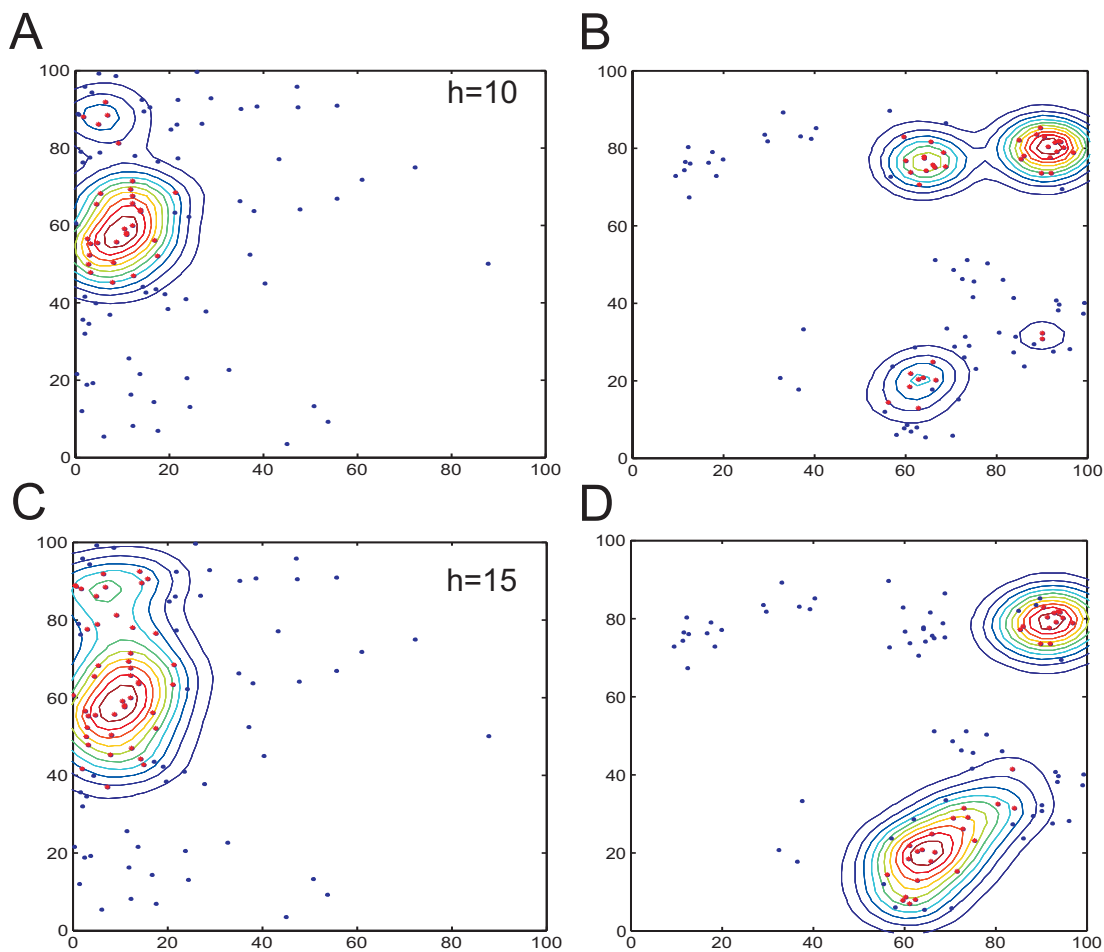
Figures from Chapter 7

Figure 9.A.5: Behavior of the contour map $\Psi_h(x, y)$ at two different scales of study; Fig. 7.4

A, C - IPP; B, D - Neyman-Scott process; A, B h=10; C, D h=15. Suprathreshold points are depicted in different color.
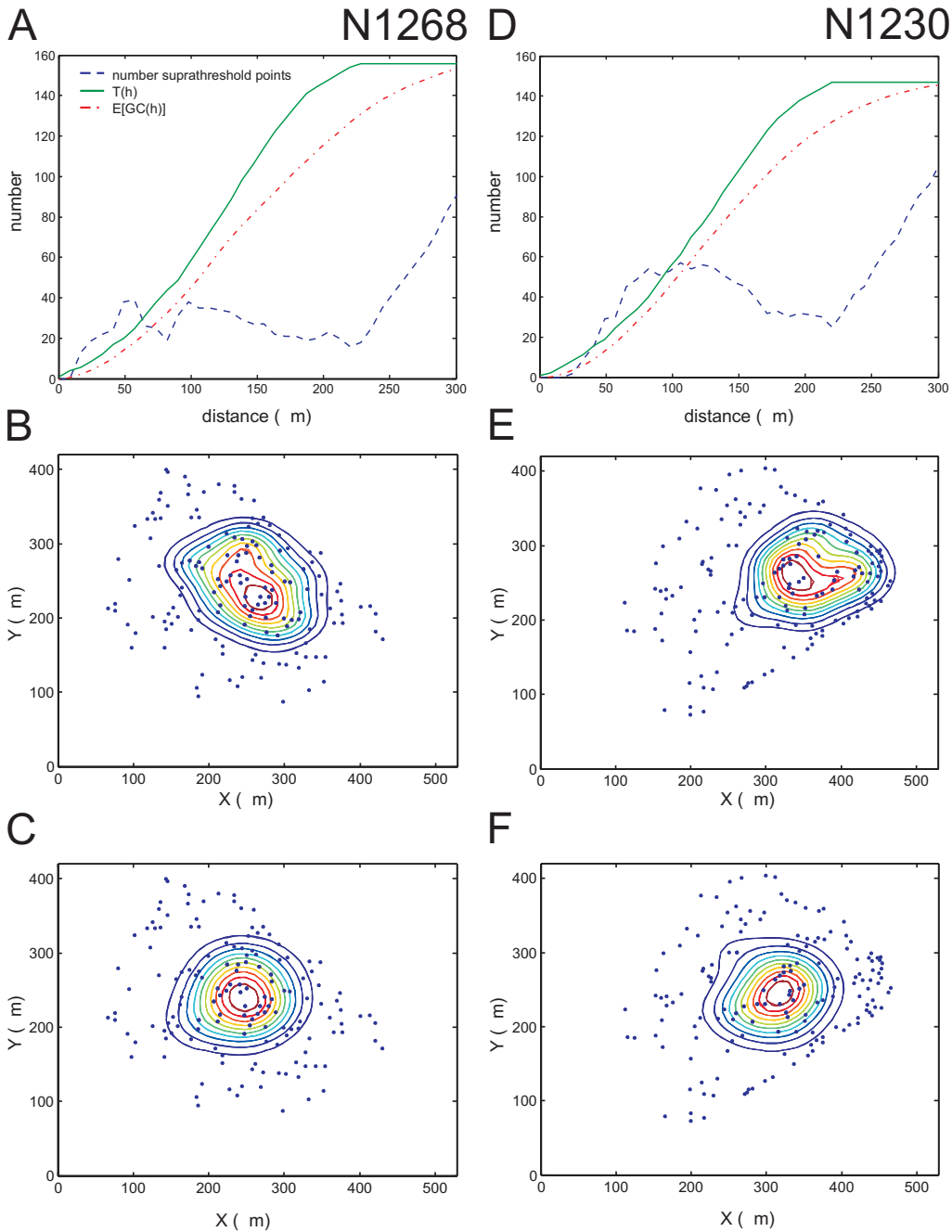
Figure 9.A.6: Influence of the scale parameter on the observed clustering; Fig. 7.7

A, D - $T_\alpha(h)$ is plotted together with the $\mathrm{E}[GC(h)]$ and the number of *suprathreshold* points *N(h)*; B, E - clustering detected at $h=100$ µm; C, F - clustering detected at $h=200$ µm; iso-level surfaces are connected by contours and plotted on top of the detected Fluoro-Gold positive fibers (filled circles).
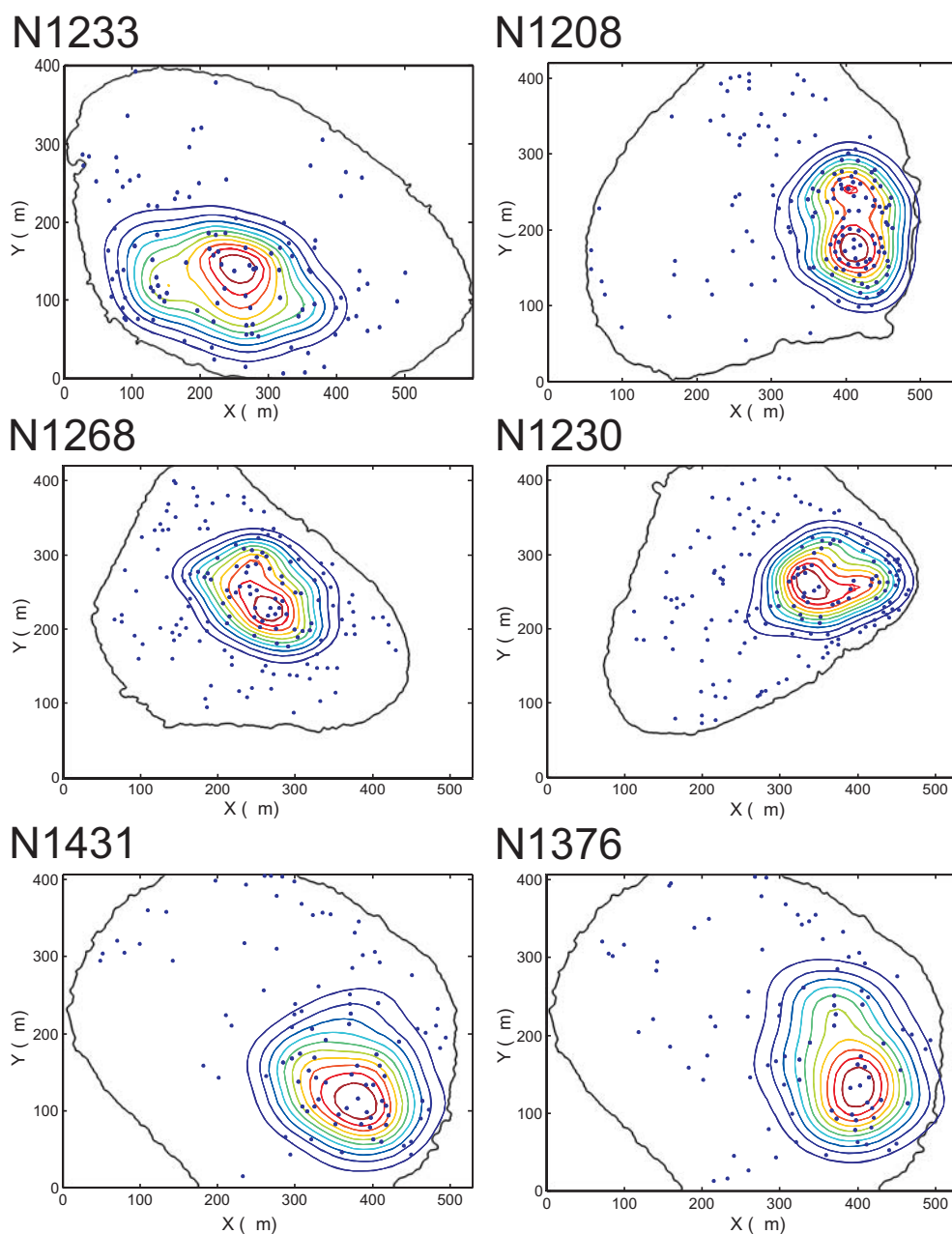
Figure 9.A.7: Detected clusters related to the cross-sections at h=100 µm; Fig. 7.8

Figure 7.8 (continued): Opposing plots are different sections of the L6 ventral root from the same animal (see Table 7.1). Sections were rotated during histological processing. Clusters are superimposed on the tissue borders; iso-level surfaces are connected by contours and plotted on top of the observed point patterns (filled circles).